Tracking and analysis of flamelet structures in turbulent non-premixed combustion

Verfolgung und Analyse von Flameletstrukturen in turbulenter nicht-vorgemischter Verbrennung

Zur Erlangung des akademischen Grades Doktor-Ingenieur (Dr.-Ing.)
genehmigte Dissertation von Dipl.-Ing. Felix Dietzsch aus Weimar
Tag der Einreichung: 13.11.2017, Tag der Prüfung: 10.01.2018
Darmstadt 2018 — D 17

1. Gutachten: Prof. Dr.-Ing. Christian Hasse
2. Gutachten: Prof. Dr.-Ing. habil. Dominique Thévenin

TECHNISCHE UNIVERSITÄT DARMSTADT

Fachbereich Maschinenbau
Simulation reaktiver Thermo-Fluid Systeme

Tracking and analysis of flamelet structures in turbulent non-premixed combustion
Verfolgung und Analyse von Flameletstrukturen in turbulenter nicht-vorgemischter Verbrennung

Genehmigte Dissertation von Dipl.-Ing. Felix Dietzsch aus Weimar

1. Gutachten: Prof. Dr.-Ing. Christian Hasse
2. Gutachten: Prof. Dr.-Ing. habil. Dominique Thévenin

Tag der Einreichung: 13.11.2017
Tag der Prüfung: 10.01.2018

Darmstadt 2018 — D 17

Erklärung zur Dissertation

Hiermit versichere ich, die vorliegende Dissertation ohne Hilfe Dritter nur mit den angegebenen Quellen und Hilfsmitteln angefertigt zu haben. Alle Stellen, die aus Quellen entnommen wurden, sind als solche kenntlich gemacht. Diese Arbeit hat in gleicher oder ähnlicher Form noch keiner Prüfungsbehörde vorgelegen.

Darmstadt, den 12. November, 2017

(Felix Dietzsch)

Danksagung

Die vorliegende Arbeit wurde während meiner Zeit als wissenschaftlicher Mitarbeiter am Institut für Energieverfahrenstechnik und Chemieingenieurwesen an der Professur für Numerische Thermofluiddynamik im Rahmen des Zentrums für Innovationskompetenz Virtuhcon begonnen.
Mein besonderer Dank gilt an erster Stelle meinem Doktorvater Prof. Dr.-Ing. Christian Hasse, der mir die Möglichkeit gab mich ausgiebig mit unterschiedlichsten Aspekten der numerischen Strömungsmechanik zu beschäftigen. Speziell möchte ich mich für sein hohes Engagement und die wissenschaftliche und methodische Unterstützung während der gesamten Zeit bedanken. Ein nicht minder großer Dank gilt Herrn Prof. Dr.-Ing. habil. Dominique Thévenin der die direkten numerischen Simulationscodes, die an seinem Lehrstuhl entwickelt wurden mit uns geteilt hat und ohne diese die vorliegende Arbeit nicht hätte entstehen können. Weiterhin möchte ich ihm für die zahlreichen Diskussionen über reaktive Strömungssimulationen danken und das er das zweite Gutachten für die vorliegende Arbeit erstellt hat.
Now I have to switch to English because I would like to express my deepest gratitude to Dr.-Ing. Abouelmagd Abdelsamie who developed the direct numerical simulation code I was using. You continuously supported me when I had questions regarding *DINO* and you were always open for discussions. Thank you so much!
Ein ebenso großer Dank gilt Dr.-Ing. Michael Gauding der immer ein offens Ohr für mich hatte, wenn ich Fragen bezüglich der DNS turbulenter Strömungen hatte. Die unzähligen Diskussionen über Turbulenztheorie, HPC-Themen und der Austausch von Codes haben entscheidend zum Gelingen der Arbeit beigetragen. Michael, vielen Dank! Arne, auch dir gilt mein größter Dank für die unzähligen Diskussionen zur Flamelettheorie und für die Bereitstellung des Flameletlösers.
Weiterhin möchte ich mich bei Dr.-Ing. Steffen Weise und Dr.-Ing. Danny Messig für die zahlreichen Diskussionen über IT-Themen bedanken. Steffen, ohne deine Bereitschaft mich in die Untiefen der Linux- und Clusteradministration einzuführen, wäre ich heute um sehr viele Erfahrungen und Erkenntisse ärmer. Danny, in deiner Eigenschaft als Kollege und “Lehrstuhlmutti” hattest du immer ein offenes Ohr und mir durch manche schwierige Zeit geholfen. Das verdient einen besonders großen Dank!
Unter all meinen Kollegen und Wegbegleitern, denen ich ebenfalls zu großem Dank für die sehr gut Zusammenarbeit verpflichtet bin, möchte ich noch Martin Pollack und Steffen Salenbauch hervorheben. Martin, die Kaffeerunden zusammen mit Danny waren immer eine sehr willkommene Abwechslung im Arbeitsalltag. Steffen, wenn du mich nicht zum Bouldern gebracht hättest wären die Wochen vor der Abgabe sehr eintönig gewesen.
Leider habe ich an dieser Stelle nur Worte zur Verfügung um meine unendliche Dankbarkeit meiner Familie gegenüber auszusprechen. Ohne euer undermüdliches Interesse an meinem Fortkommen und die bedingungslose Unterstützung wäre das alles nicht möglich gewesen. Stephie, über dies hinaus, falls das überhaupt geht, verdienst du eigentlich sehr viel mehr als ein Danke! Du hast mich tagtäglich durch die Höhen und Tiefen begleitet und warst stets für mich da. Ohne dich hätte ich das nicht geschafft!

Abstract

In this thesis, two approaches to analyze flamelet structures in turbulent non-premixed combustion are presented. The analyses are based on a highly resolved direct numerical simulation (DNS) of a temporally evolving turbulent syngas jet flame that was conducted to this end. First, the simulation is analyzed by means of a novel on-the-fly tracking procedure to assess the model assumptions of a recently published extended flamelet formulation, which in contrast to the classical flamelet model, explicitly accounts for flame-tangential transport effects. After the extended model is modified to describe flamelets in a Lagrangian manner, flamelets are tracked in the DNS with the help of tracer particles that are attached to the iso-surface of stoichiometric mixture fraction. At each time step, gradient trajectories (flamelets) are emitted from these particles and are traced along the ascending and descending gradient until a local extremal point is reached. The on-the-fly tracking procedure thus allows a detailed analysis of single flamelets in turbulent flames and a full reconstruction of flamelet histories for the first time.

In a second step, the history of flamelet identities is recomputed by means of a flamelet solver and a distinction is made between three different approaches (i) the classical flamelet (FLT), (ii) the curvature-affected flamelet (FLT-C) and (iii) the multi-dimensional flamelet (FLT-MD). Comparing the results of the recomputed histories with the DNS, it turns out that the FLT and FLT-C approaches mostly fail to reproduce the DNS results. On the other hand, the full extended FLT-MD approach agrees very well with the DNS for all identities considered, indicating that curvature-induced flame-tangential transport is an important aspect to consider in flamelet modeling. The study is complemented by a budget analysis of instantaneous flamelet identities, with which it is possible to quantify transient effects for the first time.

The second approach analyzing flamelet structures consists in decomposing the mixture fraction field into small subunits called “dissipation elements”. Dissipation elements are defined as the ensemble of all gradient trajectories that end at the same local extremal points (minimum and maximum). However, in contrast to the on-the-fly tracking this procedure is applied during the postprocessing of the DNS and allows to identify all gradient trajectories. Originally developed for the statistical analysis of non-reacting flows, this methodology promotes novel flamelet-based modeling strategies. Classifying dissipation elements according to the location of their extremal points, statistics are computed and analyzed for two instants of time, considering the Euclidean distance ℓ of the extremal points, the scalar difference ΔZ, the arithmetic mean Z_{m} and an approximate gradient $g = \Delta Z/\ell$. These statistics lead to further conclusions regarding the location of dissipation elements in mixture fraction space and how they are affected by turbulent mixing. Last, joint statistics of the temperature and the species mass fraction of OH with respect to g are inspected. It turns out, that there exists a strong correlation between the approximated gradient g and the quantities T and Y_{OH}, respectively.

Kurzfassung

In der vorliegenden Arbeit werden zwei Methoden zur Analyse von Flamelet-Strukturen in turbulenter nicht-vorgemischter Verbrennung vorgestellt. Die Analysen basieren auf einer eigens hierfür durchgeführten hoch aufgelösten direkten numerischen Simulation (DNS) einer sich zeitlich entwickelnden turbulenten Syngas Jetflamme. Zunächst wird die Simulation mittels einer neuartigen on-the-fly Trackingprozedur analysiert und Modellannahmen eines kürzlich veröffentlichten erweiterten Flameletmodells, das im Gegensatz zum klassischen Flameletmodell flammentangentialen Transport berücksichtigt, werden bewertet. Nachdem das erweiterte Modell hinsichtlich einer Lagrangen Beschreibungsweise modifiziert wurde, werden Flamelets mit Hilfe von Tracerpartikeln, die mit der Isofläche stoichiometrischer Mischung verknüpft sind, verfolgt. Ausgehend von diesen Partikeln werden in jedem Zeitschritt Gradiententrajektorien (Flamelets) emittiert und entlang des aufsteigenden und abfallenden Gradienten verfolgt bis ein lokaler Extrempunkt erreicht wird. Damit ermöglicht die on-the-fly Trackingprozedur erstmals eine detaillierte Analyse einzelner Flamelets in turbulenten Flammen und eine vollständige Rekonstruktion von Flamelethistorien.
In einem zweiten Schritt, wird die Historie einiger Flameletidentitäten mittels eines Flameletlösers nachberechnet, wobei zwischen folgenden 3 Methoden unterschieden wird: (i) das klassische Flamelet (FLT), (ii) krümmungsbeeinflusstes Flamelet (FLT-C) und (iii) multi-dimensionales Flamelet (FLT-MD). Vergleicht man die Ergebnisse der nachberechneten Historien mit der DNS, zeigt sich, dass die FLT und FLT-C Methode in den meisten Fällen die DNS Ergebnisse nicht reproduzieren können. Im Gegensatz dazu stimmt die FLT-MD Methode mit der DNS für alle Flameletidentitäten sehr gut überein, was beckräftigt, dass krümmungsinduzierter flammentangentialer Transport bei der Flameletmodellierung berücksichtigt werden sollte. Ergänzt wird diese Studie durch eine Budgetanalyse instantaner Flameletidentitäten, wobei mit Hilfe der Trackingprozedur zum ersten mal der Einfluss transienter Effekte quantifiziert werden kann.
Die zweite Methode zur Analyse von Flamelet-Strukturen basiert auf der Zerlegung des Mischungsbruchfeldes in kleine Elemente, die Dissipationselemente genannt werden. Dissipationselemente sind definiert als die Menge alle Gradiententrajektorien, die an den selben lokalen Extrempunkten (Minimum und Maximum) enden. Im Gegensatz zur on-the-fly Trackingprozedur wird diese Methode während der Auswertung der DNS zur Identifikation aller Gradiententrajektorien angewendet. Ursprünglich entwickelt für die statistische Analyse nicht-reaktiver Strömungen, ermöglicht diese Methodik neueartige flameletbasierte Modellierungsstrategien. Basierend auf einer Regimezerlegung der Dissipationselemente, bezogen auf die Lage der Extrempunkte, werden Statistiken hinsichtlich des Euklidischen Abstands ℓ der Extrempunkte, der skalaren Differenz ΔZ, des arithmetischen Mittels Z_{m} und eines approximierten Gradienten $g = \Delta Z/\ell$ für 2 Zeitpunkte ausgewertet und diskutiert. Diese Statistiken lassen weitere Rückschlüsse hinsichtlich der Lage der Dissipationselemente im Mischungsbruchraum zu und wie diese durch turbulente Mischung beeinflusst werden. Abschließend werden die gemeinsamen Wahrscheinlichkeitsdichtefunktionen der Temperatur T und des Speziesmassenbruchs Y_{OH} hinsichtlich g betrachtet. Es zeigt sich, dass ein enger Zusammenhang zwischen dem approximierten Gradienten g und den Größen T beziehungsweise Y_{OH} besteht.

Contents

1. Introduction **1**

1.1. Motivation 1
1.2. A valuable tool - Computational Fluid Dynamics 2
1.3. Modeling turbulent non-premixed flows 4
1.4. Objectives and outline of the thesis 6

2. Mathematical description of turbulent reactive flows **9**

2.1. Governing Equations for Reacting Flows 9
2.1.1. Conservation of mass 9
2.1.2. Conservation of momentum 10
2.1.3. Conservation of energy 11
2.2. Thermodynamic relations 11
2.2.1. Ideal-gas law 11
2.2.2. Specific enthalpies and heat capacities 12
2.2.3. Compressibility and speed of sound 13
2.3. Low-Mach number approach 14
2.3.1. Relation between Mach number and compressibility 14
2.3.2. Low-Mach number flow equations 15
2.4. Summary of governing equations 17
2.5. Transport relations 17
2.5.1. Shear viscosity 18
2.5.2. Diffusion velocities 19
2.5.3. Thermal Conductivity 21
2.6. Chemical kinetics relations 21

3. Flamelet modeling **25**

3.1. The mixture fraction variable 25
3.2. The flamelet model for non-premixed combustion 27
3.2.1. Steady laminar flamelet model 27
3.2.2. Extended flamelet formulation 28

4. Direct numerical simulation of turbulent reactive flows **39**

4.1. DNS code DINO 40
4.1.1. Spatial discretization - finite differences 41
4.1.2. Runge-Kutta time integration 41
4.1.3. Evaluation of the Jacobian matrix and chemical kinetics 44
4.1.4. Numerical timestep 45
4.1.5. Coupling of pressure and velocity 45

4.1.6. Poisson solver . . . 47
4.1.7. Parallelization and parallel efficiency . . . 48
4.2. Reactive temporally evolving jet flame . . . 50
4.2.1. General setup . . . 50
4.2.2. Initialization of mean profiles . . . 51
4.2.3. Initialization of chemistry . . . 52
4.2.4. Initialization of turbulence . . . 54
4.2.5. Results of the DNS . . . 55

5. On-The-Fly tracking of flamelet structures 65
5.1. Tracking algorithm . . . 65
5.1.1. Principles behind the algorithm . . . 65
5.2. Application to the reactive syngas jet . . . 72
5.2.1. Analysis of flamelet histories . . . 75
5.2.2. Budget analysis of flamelet equations . . . 82

6. Dissipation element analysis of turbulent non-premixed combustion 87
6.1. Numerical method . . . 89
6.2. Parametrization of dissipation elements . . . 90
6.3. Application to the reactive syngas jet . . . 91
6.3.1. Regime classification . . . 91
6.3.2. Joint statistics of Z_{m}^* and ΔZ^* . . . 93
6.3.3. Joint statistics of ΔZ^* and ℓ^* . . . 96
6.3.4. Joint statistics of g^* and ℓ^* . . . 99
6.3.5. Inner structure of dissipation elements . . . 99

7. Summary and conclusion 103

References 107

A. Additional chemical kinetic relations 121
A.1. Reverse rate coefficient . . . 121
A.2. Falloff reactions . . . 121

B. Validation cases 123
B.1. Decaying homogeneous isotropic turbulence . . . 123
B.2. Homogeneous reactor . . . 124

C. Code listings 127
C.1. Fortran interface to *pyJac* . . . 127

List of Figures

1.1. World energy consumption in quadrillions of BTUs by primary fuel from year 2010 to 2050. The vertical dashed line denotes the current year and separates historical records from projections [1]. 1

1.2. Schematic picture of differences between the RANS, LES and DNS approaches for numerical simulations of turbulent flows for (a) a signal in physical space and (b) the turbulent kinetic energy spectrum $E(\kappa)$. 3

3.1. Illustration of the orthogonal coordinate system (Z, ξ_2, ξ_3) attached to the stoichiometric mixture fraction iso-surface. 27

3.2. Illustration of the orthogonal coordinate system $n(t,\mathbf{x}), \xi_2(t,\mathbf{x}), \xi_3(t,\mathbf{x})$ attached to the stoichiometric mixture fraction iso-surface. The schematic shows a hypothetical evolution of the surface sheet from Lagrangian time τ_1 to τ_2. 31

4.1. Example of a two dimensional pencil decomposition used in *DINO* . The data is distributed between processors in the y and z direction. 48

4.2. Strong and weak scaling of the Runge-Kutta solvers presented in section 4.1.2. . . . 49

4.3. Setup of the direct numerical simulation together with a sketch of the initial profiles of $\langle Z \rangle$ and $\langle U \rangle$. The domain size is denoted by L_x, L_y and L_z. The contours show the logarithm of the scalar dissipation rate χ normalized by its value near extinction χ_q. 51

4.4. Evolution of two different resolution criteria: (a) $\Delta x/\eta$ and (b) $\kappa_{max}\eta$. For resolutions $\Delta x/\eta < 2.1$ and $\kappa_{max}\eta > 1.5$ the simulation can be considered as well resolved [137]. 52

4.5. Initial mean profile of mixture fraction and stream-wise velocity, for $U_{fuel} = 1$. 53

4.6. Evolution of temperature with scalar dissipation rate at stoichiometric conditions. The temperature near extinction (T_q) is estimated at the point where the temperature abruptly drops. At the same time this also states the scalar dissipation rate near extinction (χ_q). The scalar dissipation rate χ_{init} is assumed to be representative for the conditions under which the turbulent flame resides and it was set to $\chi_{init} = 0.67\chi_q$. 53

4.7. Initial profiles of temperature, Y_{H_2}, Y_{OH}, Y_{CO} and Y_{O_2} in: (a) flamelet space and (b) physical space. Note that for the sake of clarity not all initial profiles are shown. . . 54

4.8. Evolution of the temporally evolving syngas jet for $t/t_{jet} = 10, 20, 30, 40$ for: (a), (c), (e), (g) the mixture fraction and (b), (d), (f), (h) $\log_{10}(\chi/\chi_q)$ 57

4.9. Evolution of the temporally evolving syngas jet for $t/t_{jet} = 10, 20, 30, 40$ for: (a), (c), (e), (g) the temperature and (b), (d), (f), (h) the mass fraction of OH. 58

4.10. View on top of the center-plane xOz. The causal chain that leads to local extinction is visualized. Compressive (negative) strain ($a = \mathbf{n} \cdot \nabla\mathbf{u} \cdot \mathbf{n}$) causes increased scalar dissipation rates which inturn causes a decrease in temperature. 59

4.11. Temporal evolution of important flow quantities. After $t/t_{\text{jet}} \approx 10$ the jet shows evidence of self-similarity since $\langle k \rangle_{\text{st}}$ and $\langle \varepsilon \rangle_{\text{st}}$ start to gradually decay while the jet width exhibits a linear growth, which is to be expected for self-similarly evolving mixing layers [221]. 60
4.12. Profiles of the mean stream-wise velocity normalized by the streamwise mean center-line velocity. After $t/t_{\text{jet}} \approx 10$ the jet shows evidence of self-similarity as the profiles collapse. 60
4.13. Temporal evolution of the mean temperature around stoichiometry normalized by the temperature near extinction T_{q}. The jet exhibits significant local extinction between $t/t_{\text{jet}} \approx 12$ and $t/t_{\text{jet}} \approx 40$. 61
4.14. Joint probability density functions for $t/t_{\text{jet}} = 10, 20, 30, 40$ for: (a), (c), (e), (g) temperature and mixture fraction and (b), (d), (f), (h) OH mass fraction and mixture fraction. The black solid line and red dashed line indicate the conditional mean and quenching value, respectively. The vertical dash-dotted line indicates Z_{st}. 62
4.15. Flame structure statistics for $t/t_{\text{jet}} = 10, 20, 30, 40$ for: (a), (c), (e), (g) the joint pdf of $\log_{10}(\chi/\chi_q)$ and mixture fraction and (b), (d), (f), (h) the mean values of Y_{H_2}, Y_{CO}, Y_{OH}, Y_{O_2} conditioned on mixture fraction. The vertical dash-dotted line indicates Z_{st}. 63

5.1. Illustration of the orthogonal coordinate system $n(t, \mathbf{x}), \xi_2(t, \mathbf{x}), \xi_3(t, \mathbf{x})$ attached to the stoichiometric mixture fraction iso-surface. The schematic shows a hypothetical evolution of the surface sheet from Lagrangian time τ_1 to τ_2 together with the corresponding path of the reference point P', marked by the black dashed line. . . 66
5.2. Snapshot of the stoichiometric iso-scalar surface of mixture fraction together with randomly distributed particles. These particles are used during the on-the-fly tracking procedure. 68
5.3. Illustration of ghost cell communication patterns. The schematic illustrates the difference between the approaches for finite difference computations and the particle tracking algorithm employed here. The processors are marked by their location with respect to the sending processor. Arrows indicate possible communication patterns. 69
5.4. Schematic of the gradient trajectory tracking algorithm. The particle, that emits the trajectory, is marked with a black dot. Local maxima and minima are represented by a red plus and blue minus, respectively. Furthermore, hypothetical trajectories are shown for five different instants in time. 71
5.5. Simplified illustration of a splitting and reconnection event in one-dimensional space. 72
5.6. Top: Snapshot of the direct numerical simulation conducted in [127] together with the stoichiometric mixture fraction iso-surface ($Z = Z_{st}$). Bottom left: gradient trajectories (flamelets) that intersect the stoichiometric mixture fraction iso-surface. Bottom right: realization of a single flamelet. 73
5.7. Two exemplary trajectories that were tracked in a direct numerical simulation [127]. While both trajectories intersect the surface of stoichiometric mixture fraction, they are colored according to the temperature field. 73

5.8. Evolution of temperature T_P of the tracer particle for three exemplary trajectories T-I, T-II and T-III. Along these trajectories, five flamelet identities F_I to F_V are identified, which are examined in detail in this section. One marker represents at least 30 data points, to improve clarity in the figure. The dash-dotted line marks the temperature near extinction obtained from a representative steady laminar flamelet calculation. 74

5.9. Time history of the seed point temperature of the gradient trajectories T-I, T-II and T-III. Recomputed flamelet identities are marked by symbols, where squares and pluses mark the flamelet solution according to scenarios 1 and 2, respectively. The circles indicate solutions that were obtained with the complete set of extended flamelet equations. 76

5.10. Flame structures and regime classification for the two flamelet identities F_I (left) and F_{II} (right) of the gradient trajectory T-I. Each plot shows two instants in time, marked by the solid and dash-dotted vertical line in figure 5.9a, where the solid line corresponds to an early stage of the corresponding flamelet identity and the dash-dotted line to a later one. In all plots the vertical dashed line marks Z_{st}. 79

5.11. Flame structures and regime classification for the two flamelet identities F_{III} (left) and F_{IV} (right) of the gradient trajectory T-II. Each plot shows two instants in time, marked by the solid and dash-dotted vertical line in figure 5.9b, where the solid line corresponds to an early stage of the corresponding flamelet identity and the dash-dotted line to a later one. In all plots the vertical dashed line marks Z_{st}. 80

5.12. Flame structures and regime classification for the flamelet identity F_V of the gradient trajectory T-III. The plot shows two instants in time, marked by the solid and dash-dotted vertical line in figure 5.9c, where the solid line corresponds to an early stage of the flamelet identity and the dash-dotted line to a later one. In all plots the vertical dashed line marks Z_{st}. 81

5.13. Budgets of the extended flamelet temperature equation for two instants in time: early (left) and late (right). The budgets are evaluated for the flamelet identity F_V according to the time instants marked in figure 5.9c. All budgets are normalized by the maximum of all terms and “balance” (black line) denotes the sum of all budget terms. 82

5.14. Budgets of the extended flamelet species equations of CO_2, CO and O_2 for two instants in time: early (left) and late (right). The budgets are evaluated for the flamelet identity F_V according to the time instants marked in figure 5.9c. All budgets are normalized by the maximum of all terms and “balance” (black line) denotes the sum of all budget terms. 83

5.15. Budgets of the extended flamelet species equations of H_2O, H_2 and OH for two instants in time: early (left) and late (right). The budgets are evaluated for the flamelet identity F_V according to the time instants marked in figure 5.9c. All budgets are normalized by the maximum of all terms and “balance” (black line) denotes the sum of all budget terms. 84

6.1. Schematic of a scalar field including two hypothetical trajectories (orange) originating from an initial point to their respective minimum and maximum points. The green solid lines correspond to dissipation elements, enclosing all trajectories that end at the same minimum and maximum point. 88
6.2. Exemplary representation of a dissipation element within a three-dimensional direct numerical simulation. The blue bullet constitutes a local minimum, while the red bullet is a local maximum. The local extrema are connected through gradient trajectories which are colored with respect to the underlying scalar field. 88
6.3. Marginal probability distribution of the mixture fraction P(Z) at three instants in time. All pdfs exhibit a bimodal shape with minima located at $Z = 0.13$, $Z = 0.09$ and $Z = 0.07$ for ascending t/t_{jet}, respectively. 91
6.4. Two-dimensional slice of the instantaneous mixture fraction field Z in the xOz plane at $t/t_{\mathrm{ref}} \approx 20$. Gradient trajectories are schematically shown in the different regimes by colored solid lines. The white line indicates the location of stoichiometric mixture fraction and the black line indicates the location of the turbulent/non-turbulent interface. 93
6.5. Joint probability density function of Z^*_{m} and ΔZ^* for three dimensionless times. The different regimes and also their corresponding regime boundaries are highlighted. The probability is indicated by colors and scaled logarithmically. 95
6.6. Joint distribution of ΔZ^* and ℓ^* together with the conditional mean $\langle \Delta Z^* | \ell^* \rangle$ (black circles) for two instants of time $t/t_{\mathrm{jet}} = 20$ (left) and $t/t_{\mathrm{jet}} = 40$ (right). From top to bottom the different regimes are shown with $P(\Delta Z^*, \ell^*)$ of all trajectories at the bottom. The probability is indicated by colors and scaled logarithmically. 97
6.7. Joint distribution of g^* and ℓ^* together with the conditional mean $\langle g^* | \ell^* \rangle$ (black circles) for two instants of time $t/t_{\mathrm{jet}} = 20$ (left) and $t/t_{\mathrm{jet}} = 40$ (right). From top to bottom the different regimes are shown with $P(g^*, \ell^*)$ of all trajectories at the bottom. The probability is indicated by colors and scaled logarithmically. 98
6.8. Joint distributions of $T_{\mathrm{max}}/T_{\mathrm{q}}$ (top) and $Y_{\mathrm{OH,max}}/Y_{\mathrm{OH,q}}$ (bottom) with respect g^* for two instants of time $t/t_{\mathrm{jet}} = 20$ (left) and $t/t_{\mathrm{jet}} = 40$ (right), together with their conditional mean values $\left\langle T_{\mathrm{max}}/T_{\mathrm{q}} | g^* \right\rangle$ and $\left\langle Y_{\mathrm{OH,max}}/Y_{\mathrm{OH,q}} | g^* \right\rangle$, indicated by black circles. The probability is indicated by colors and scaled logarithmically. 100

B.1. Illustration of the initial three dimensional energy spectrum (a) and evolution of the spectrum b computed from velocity fluctuations generated with (B.1). The initial spectrum peaks at the prescribed wavenumber $\kappa_0 = 10$. 123
B.2. Self similar decay of mean kinetic energy $\langle k \rangle$ (solid line) and mean dissipation $\langle \varepsilon \rangle$ (dash-dotted line). In addition the theoretical decay rates are illustrated by the dotted lines. 124
B.3. Solutions of equations (B.4) and (B.5) obtained with different time integration strategies, cf. section 4.1.2. 125

List of Tables

3.1. The three flamelet regimes identified by Scholtissek et al. [47] for the extended flamelet model with differential diffusion ($\mathrm{Le}_i \neq 1$). 38

4.1. Finite difference weights for first and second derivatives used in DINO [139]. Note, the values listed in the table should be divided by Δx^m, where Δx denotes the uniform grid spacing. 41
4.2. Weights of the fourth-order five-stage explicit Runge-Kutta scheme [169, 170]. . . . 43
4.3. Weights of the third-order low-storage semi-implicit Runge-Kutta scheme [165]. . . 44
4.4. Strong scaling and strong scaling efficiency of the Runge-Kutta solvers presented in section 4.1.2. The scaling runs were performed on SuperMUC phase 1 at Leibniz Supercomputing Centre. Each island of phase 1 of SuperMUC consists of 512 nodes each of which is equipped with 2 Intel Xeon E5-2680 (8 cores at 2.7GHz). 49

Nomenclature

Abbreviations

Symbol	*Meaning*
CFD	Computational Fluid Dynamics
CFL	Courant-Friedrich-Lewy number
DE	Dissipation element
DNS	Direct Numerical Simulation
FFT	(forward) Fast Fourier Transform
FGM	Flamelet generated manifold
GHG	Greenhouse gas
GT	Gradient trajectory
HIT	Homogenous Isotropic Turbulence
IFFT	Inverse Fast Fourier Transform
IPCC	Intergovernmental Panel on Climate Change
jpdf	Joint propability density function
LES	Large Eddy Simulation
MPI	Message Passing interface
NSE	Navier-Stokes equations
pdf	Probability density function
RANS	Reynolds Averaged Navier-Stokes simulation
SuperMUC	Supercomputer at Leibniz Supercomputing Center in Munich
T/NT	Turbulent/Non-turbulent
TCI	Turbulence Chemistry Interaction

Symbol	*Meaning*	*Unit*
α	Thermal diffusivity	$\mathrm{m^2\,s^{-1}}$
β_i	Temperature exponent of reaction i	–
χ	Scalar dissipation rate	$\mathrm{s^{-1}}$
χ_q	Scalar dissipation rate at which the flame quenches	$\mathrm{s^{-1}}$
χ_st	Scalar dissipation rate at stoichiometric conditions	$\mathrm{s^{-1}}$
δ_{ij}	Kronecker delta	–
$\dot{\omega}_i$	Reaction rate of species i	$\mathrm{kg\,m^{-3}\,s^{-1}}$
$\dot{\omega}'_T$	Source term of the temperature equation	$\mathrm{J\,m^{-3}\,s^{-1}}$
ϵ	Dissipation rate of turbulent kinetic energy	$\mathrm{m^2\,s^{-3}}$
η	Kolmogorov length scale	m
γ	Isentropic expansion factor	–
$\kappa_{2,3}$	Principal curvatures of a mixture fraction iso-surface	$\mathrm{m^{-1}}$
κ	Wavenumber vector	$\mathrm{m^{-1}}$
κ_0	Wavenumber at which spectrum peaks	$\mathrm{m^{-1}}$
κ_Z	Total curvature of a mixture fraction iso-surface	$\mathrm{m^{-1}}$
$\kappa_{(1,2,3)}$	Components of the wavenumber vector	$\mathrm{m^{-1}}$
κ_0	Wavenumber corresponding to the integral scales of the flow	$\mathrm{m^{-1}}$
λ	Thermal conductivity of the mixture	$\mathrm{W\,K^{-1}\,m^{-1}}$
μ	Dynamic viscosity of the mixture	$\mathrm{kg\,m^{-1}\,s^{-1}}$
μ_i	Dynamic viscosity of species i	$\mathrm{kg\,m^{-1}\,s^{-1}}$
ν''_{ki}	Product stoichiometric coefficient for species k in reaction i	–

ν'_{ki}	Reactant stoichiometric coefficient for species k in reaction i	–
ν_{ki}	Overall stoichiometric coefficient for species k in reaction i	–
ρ	Density	$\mathrm{kg\,m^{-3}}$
ρ^*	Dimensionless density	–
ρ_0	Reference density	$\mathrm{kg\,m^{-3}}$
σ_{ij}	Momentum stress tensor	$\mathrm{kg\,m^{-1}\,s^{-2}}$
τ_η	Kolmogorov time scale	s
τ	Lagrangian time	s
$\xi_{2,3}$	Curvilinear surface coordinates	m
ζ	Bulk (volume) viscosity of the mixture	$\mathrm{kg\,m^{-1}\,s^{-1}}$

LATIN SYMBOLS

Symbol	*Meaning*	*Unit*
$(\Delta Z)_\mathrm{R}$	Reaction zone thickness	$\mathrm{m^{-1}}$
$[X_i]$	Molar concentration of species i	$\mathrm{mol\,m^{-3}}$
c_p	Heat capacity of the mixture at constant pressure	$\mathrm{J\,kg^{-1}\,K^{-1}}$
$c_{\mathrm{p},i}$	Heat capacity at constant pressure of species i	$\mathrm{J\,kg^{-1}\,K^{-1}}$
c_v	Heat capacity of the mixture at constant volume	$\mathrm{J\,kg^{-1}\,K^{-1}}$
$c_{\mathrm{v},i}$	Heat capacity at constant volume of species i	$\mathrm{J\,kg^{-1}\,K^{-1}}$
$\dot{\mathcal{Q}}$	Heat source	$\mathrm{J\,m^{-3}}$
e_t	Total energy per unit mass	$\mathrm{J\,kg^{-1}}$
$\mathbf{J}$	Jacobian matrix	–
$\mathcal{D}_{kl}$	Binary diffusion coefficient	$\mathrm{m^2\,s^{-1}}$
$\mathcal{K}_B$	Boltzmann constant	$\mathrm{J\,K^{-1}}$
$\mathcal{I}$	Identity matrix	–

$\mathbf{e}_{2,3}$	Unit tangent vectors	–
$\mathbf{n}$	Normal vector of a mixture fraction iso-surface	–
$\mathbf{r}$	Position vector of a point P	m
$\mathbf{r}_f$	Position of the projection of a point onto a surface	m
$\mathbf{u}_s$	Velocity of a point on a surface	$\mathrm{m\,s^{-1}}$
$\langle W \rangle$	Mean molecular weight	$\mathrm{kg\,mol^{-1}}$
$\mathcal{R} = 8.3144$	Universal gas constant	$\mathrm{J\,mol^{-1}\,K^{-1}}$
$V_{i,j}$	Diffusion velocity of species i in direction j	$\mathrm{m\,s^{-1}}$
Z_{st}	Mixture fraction at stoichiometric conditions	–
A_0	Prefactor of energy spectrum	$\mathrm{m\,s^{-2}}$
a_i	Rate of progress of reaction i	$\mathrm{mol\,m^{-3}\,s^{-1}}$
A_i	Pre-exponential factor of reaction i	$\mathrm{mol}^{-(1-\Sigma_{j=1}^{N_S}\nu_{ji})}\mathrm{K}^{-\beta_i}$
c	Speed of sound	$\mathrm{m\,s^{-1}}$
c_0	Reference speed of sound	$\mathrm{m\,s^{-1}}$
c_i	Third-body pressure modification factor	–
$C^\circ_{p,i}$	Standard-state heat capacity of species i at constant pressure	$\mathrm{J\,mol^{-1}\,K^{-1}}$
D_i^T	Thermo-diffusion coefficient of species i	$\mathrm{m^2\,s^{-1}}$
D_Z	Diffusion coefficient of the mixture fraction Z	$\mathrm{m^2\,s^{-1}}$
D_{ik}	Multi-component diffusion coefficients	$\mathrm{m^2\,s^{-1}}$
d_{kj}	Diffusion driving force	$\mathrm{m^{-1}}$
E	Prescribed energy spectrum	$\mathrm{m^2\,s^{-2}}$
$E_{a,i}$	Activation energy	$\mathrm{J\,mol^{-1}}$
F_i	Falloff blending factor	–
h	Enthalpy of the mixture	$\mathrm{J\,kg^{-1}}$

h_i	Enthalpy of species i	$\mathrm{J\,kg^{-1}}$
h_t	Total enthalpy per unit mass	$\mathrm{J\,kg^{-1}}$
H_i°	Standard-state enthalpy of species i	$\mathrm{J\,mol^{-1}}$
$k_{0,i}$	Low-pressure reaction rate coefficient of reaction i	$\mathrm{mol}^{-(1-\Sigma_{j=1}^{N_s}\nu'_{ji})}$
$k_{\infty,i}$	High-pressure reaction rate coefficient of reaction i	$\mathrm{mol}^{-(1-\Sigma_{j=1}^{N_s}\nu'_{ji})}$
$k_{b,i}$	Backward reaction rate coefficient of reaction i	$\mathrm{mol}^{-(1-\Sigma_{j=1}^{N_s}\nu''_{ji})}$
$k_{f,i}$	Forward reaction rate coefficient of reaction i	$\mathrm{mol}^{-(1-\Sigma_{j=1}^{N_s}\nu'_{ji})}$
l_0	Reference length	m
l_t	Integral length scale	m
l_χ	Length scale related to the reaction zone thickness	m
l_κ	Curvature related length scale	m
l_m	Mixing length	m
m_{ij}	Third-body efficiency of species j in reaction i	–
p	Total pressure	Pa
p^*	Dimensionless pressure	–
p_0	Reference pressure	Pa
$P_{r,i}$	Reduced pressure factor	–
q_j	Heat flux in direction j	$\mathrm{W\,m^{-2}}$
$R_{f,i}$	Forward rate of progress of reaction i	$\mathrm{mol\,m^{-3}\,s^{-1}}$
R_i	Base rate of progress of reaction i	$\mathrm{mol\,m^{-3}\,s^{-1}}$
$R_{r,i}$	Backward rate of progress of reaction i	$\mathrm{mol\,m^{-3}\,s^{-1}}$
s_d	Displacement speed of a surface	$\mathrm{m\,s^{-1}}$
S_i°	Standard-state entropy of species i	$\mathrm{J\,K^{-1}\,mol^{-1}}$
T	Temperature	K
t	Eulerian time	s

t^*	Dimensionless time	–
T_{fuel}	Temperature of the fuel stream	K
T_{odxizier}	Temperature of the oxidizer stream	K
$T_{a,i}$	Activation temperature	K
u^*	Dimensionless velocity	–
u'	Turbulence intensity	$\mathrm{m\,s^{-1}}$
u_0	Reference velocity	$\mathrm{m\,s^{-1}}$
u_j	Velocity vector	$\mathrm{m\,s^{-1}}$
u_η	Kolmogorov velocity scale	$\mathrm{m\,s^{-1}}$
$V_{c,j}$	Diffusion correction velocity in direction j	$\mathrm{m\,s^{-1}}$
W_i	Molecular weight of species i	$\mathrm{kg\,mol^{-1}}$
x^*	Dimensionless coordinate	–
X_i	Mole fraction of species i	–
Y_i	Mass fraction of species i	–
Z	Mixture fraction	–
Z_j	Mass fraction of element j	–

Miscellaneous

Symbol	*Meaning*
$\mathcal{O}(\bullet)$	Order of $(\bullet)$
$\mathrm{N_e}$	Number of chemical elements of the chemical kinetic scheme
$\mathrm{N_r}$	Number of reactions of the chemical kinetic scheme
$\mathrm{N_s}$	Number of species of the chemical kinetic scheme

Characteristic Numbers

Symbol	*Meaning*
Le_i	Lewis number of species i
Ma	Mach number
Re_t	Reynolds number according to integral scales

1 Introduction

1.1 Motivation

In today's industrialized world, energy requirements have constantly increased over recent decades, and they will still do so in the foreseeable future. The U.S. Energy Information Administration has forecasted that the world's energy consumption by the year 2050 will be 814 quadrillion British thermal units (BTUs), which is an increase of nearly 56 % compared to the year 2010, cf. figure 1.1. Although the amount of renewable energies will have increased by more than 150 % by the year 2050 , fossil fuels such as petroleum, coal and natural gas are still market-dominating. The primary process of power generation from fossil fuels is combustion. Therefore, the importance of combustion is obvious, and will possibly be unchallenged even after the year 2050.

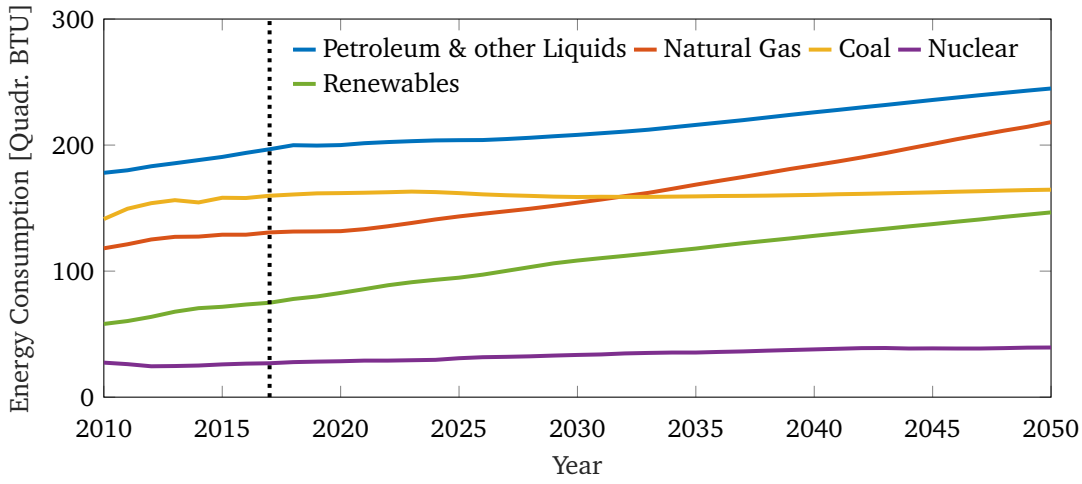

Figure 1.1.: World energy consumption in quadrillions of BTUs by primary fuel from year 2010 to 2050. The vertical dashed line denotes the current year and separates historical records from projections [1].

However, the conversion of chemical energy to thermal energy by combusting fossil fuels has adverse effects. The two most debated effects are air pollution and global warming [2]. For instance, the release of pollutants, such as carbon monoxide, sulfur dioxide, nitrogen dioxide and particulates, during the conversion process has adverse effects on human health, e.g. causing bronchial irritations, lung inflammation and reduced lung function, asthma, lung cancer or heart arrhythmia [2]. The second effect, global warming, is mostly caused by the emission of greenhouse gases (GHGs) such as CO_2, CH_4 or N_2O, and total anthropogenic GHG emissions continued to increase between 1970 and 2010, with larger absolute increases between 2000 and 2010 [3]. As stated by the Intergovernmental Panel on Climate Change (IPCC) [3], emissions of CO_2 from fossil fuel combustion and industrial processes contributed to about 78 % of the total increase in GHG emissions from 1970 to 2010.

To address these issues the, European Commission is looking at cost-efficient ways to make the European economy more climate-friendly and less energy-consuming [4] and has defined a low-carbon economy roadmap. The European Commission's strategy until the year 2050 is to cut greenhouse gases by 80 % compared to 1990, and has proposed several actions for the sectors: power generation, industry, transport, buildings and agriculture. While working to achieve these goals, a recurring claim made in all sectors is that energy and fuel-efficiency will be improved and pollutant emissions reduced.
To keep up with these ambitious goals, novel concepts and new design patterns are required for future combustion devices. While admission procedures are often interminable for new devices and are still largely based on laboratory experiments, such developments could be achieved faster and at lower costs if accurate, robust, and truly predictive computational design tools were available, so that testing could be conducted largely on the computer [5]. Then, parameter studies or geometry variations could be transferred to numerical simulation approaches, while the final admission could be based on a few laboratory experiments. Furthermore, detailed three-dimensional simulations that resolve all spatial and temporal scales could offer insights into various phenomena which otherwise would not be accessible by laboratory experiments. In recent years, computational fluid dynamics (CFD) have proven to be a valuable tool in situations where experiments are not feasible or could even be dangerous.

1.2 A valuable tool - Computational Fluid Dynamics

The term CFD refers to a branch of fluid mechanics which is not specifically designed for the analysis of combustion, but instead comprises tools for the analysis of flows from various areas of application, e.g. biomedical flows, ocean currents and atmospheric flows. The foundation of all CFD applications are the Navier-Stokes equations (NSE), which constitute a system of partial differential equations describing the motion of viscous fluids and whose solution is the velocity vector. Analytical solutions of the NSE only exist for very simple problems but for the majority of flows, they have to be solved numerically. Numerical solutions of the NSE are obtained by means of a computational domain which constitutes a discretized representation of the actual problem in conjunction with proper conditions defined at the boundary of the computational domain.

Reacting flows are one of the most difficult flow scenarios, since many highly complex physical processes are involved, e.g. turbulence, chemical kinetics, radiation, multi-component diffusion, soot formation and flame-acoustic interactions, which have to be coupled nonlinearly to describe the behavior of the overall system. Furthermore, chemical reacting flows are multi-scale problems, meaning that a fully coupled description involves various time and length scales, which additionally stresses a numerical treatment. Therefore, different numerical procedures have been developed in the past, which are tailored to deal with the numerical complexity of the various physical processes involved.
One of the most important phenomena found in almost all practical combustion devices is turbulence. There exist three established methodologies for analyzing turbulent flows:

- Direct numerical simulation (DNS),

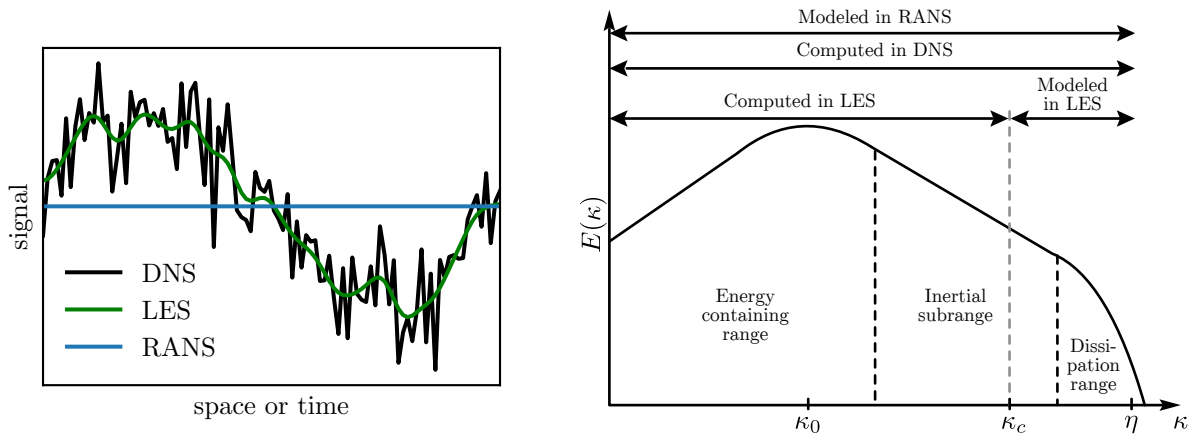

(a) physical space **(b)** spectral space

Figure 1.2.: Schematic picture of differences between the RANS, LES and DNS approaches for numerical simulations of turbulent flows for (a) a signal in physical space and (b) the turbulent kinetic energy spectrum $E(\kappa)$.

- Reynolds averaged Navier-Stokes simulation (RANS) and
- Large eddy simulation (LES).

The main difference between these approaches is the level of detail preserved in the simulation, which can best be illustrated by comparing an exemplary signal in physical space, see figure 1.2a. While DNS resolves all spatial and temporal scales, LES and RANS approaches only preserve details of the flow field up to a certain length scale. The important difference between LES and RANS is that Reynolds-averaged simulations deliver time-averaged solutions, thereby providing information about mean quantities only, whereas LES resolves the quantities up to a certain length scale specified by a filter width l_c.

Direct numerical simulations are unrivaled in the level of detail, but this comes at the expense of extremely high computational costs. While even moderately sized DNSs have roughly $\mathcal{O}(10^8)$ grid points and must be run on hundreds of processors to have an acceptable response time, today's high-fidelity simulations require nearly seven billion grid points and are run on more than 100,000 computing cores [6]. As a result, the amount of data generated by such simulations can be overwhelmingly huge and typically lies in the range of $\mathcal{O}(10^0)$ TB to $\mathcal{O}(10^2)$ TB for a single simulation [7], which in turn can only be postprocessed by $\mathcal{O}(10^3)$ computing cores. Due to the resolution requirements of DNSs and available computational resources, they are often limited to fairly low Reynolds numbers, which makes them impractical to simulate laboratory-scale combustion devices. Also, the preferably short response times are difficult to achieve using DNSs. Rather, direct numerical simulations are a tool of academic interest and often applied in benchmark cases focusing on single aspects of a turbulent reactive flow, e.g. turbulence chemistry interaction. The insights gained from these simulations are then often used to develop and validate closure models for LES or RANS approaches, which, by design, do not resolve all scales.

The closure problem can best be illustrated by looking at figure 1.2b, which shows an example of a turbulent kinetic energy spectrum plotted as a function of the wavenumber κ. According to Richardson [8], turbulent flows are composed of eddies of different sizes, with eddies at the

largest scales containing most of the kinetic energy and are being characterized by a wavenumber $\kappa_0 = 1/l_0$, where l_0 is comparable to the size of the problem. This energy is then successively transferred to smaller scales until the energy is finally dissipated by viscous action at the smallest scales. The smallest length scales denoted by η are determined due to Kolmogorov's first similarity hypothesis [9]. As indicated by the arrows in figure 1.2b, all spatial frequencies are resolved by DNS, whereas LES only resolves frequencies up to the cut-off wavenumber $\kappa_c = 1/l_c$. Turbulent motions associated with frequencies larger than κ_c have to be modeled in order to properly capture the flow physics. In RANS approaches this is even more pronounced since no turbulence frequencies are resolved. Although the above discussion is solely conducted in the context of turbulent motion, combustion-related phenomena such as chemical reactions and multi-species diffusion also pertain to the smallest scales. In fact, there is a strong interaction between turbulence and chemistry at these scales, which is referred to as turbulence-chemistry interaction (TCI) and which constitutes a closure problem for approaches such as RANS and LES, where the resolution is inadequate to resolve combustion phenomena.

1.3 Modeling turbulent non-premixed flows

This work focuses on the analysis of turbulent non-premixed combustion, where "non-premixed" refers to the initial state of the reactants. In a non-premixed flame, the reactants are initially separated and reactions occur only at the interface between fuel and oxidizer, where mixing and reaction both take place [10]. Since time scales of reactions are usually much shorter than time scales for diffusion, the latter processes is rate-determining. Non-premixed flames are therefore also often termed "diffusion flames", where "diffusion" applies strictly to the molecular diffusion of chemical species, driven by species gradients. In contrast, in a premixed flame, fuel and oxidizer are mixed at the molecular level prior to the occurrence of any significant chemical reaction [10].

In the past, different classes of models have been proposed for the prediction of turbulent non-premixed combustion processes. The closure problem of the subgrid-scale turbulent fluctuations is usually addressed by approaches such as RANS or LES; excellent reviews about existing closures are given in [11–13]. However, as stated earlier, in reactive flows a second closure problem emerges due to the interaction of turbulence with chemical reactions and molecular diffusion at the smallest scales. A range of approaches exist, but in an attempt to classify the closure strategies Pope [14] proposed two categories, which are referred to as flamelet-like and PDF-like models. Besides the review paper by Pope [14], other excellent reviews of combustion models are given in [15–19].
The core concept of PDF-like models is to solve a modeled conservation equation for the joint probability density function (jpdf) of fluid properties, including species mass fractions and enthalpy. As such, they provide a complete statistical representation of the thermo-chemical state [14]. A common approach to represent the joint distribution of fluid properties is the Lagrangian particle method [20], which uses a large number of particles, each with its own position and thermo-chemical state and possible other properties, if required. The transient behavior of the flow field including combustion is then described through the temporal evolution of the jpdf. One significant advantage of PDF-like methods over flamelet-like methods is that the chemical source term appears

in closed form. However, closure models are required for the molecular mixing term, since it relies on multi-point information [15]. A second drawback of pdf-like approaches is their high computational costs compared to flamelet-like models. According to Pope [14], computational efforts could easily increase by a factor of 17 in LES/PDF approaches with 38 chemical species. A detailed review of recent work in the field of LES/PDF, including several applications, is given by Haworth [21].

Flamelet models could be derived from an asymptotic view of reactive-diffusive layers located around the reaction zone [22, 23]. Assuming that chemical reactions are fast and at sufficiently large Damköhler numbers reaction zones are thin, and if the characteristic length scale of the reaction zone is smaller than that of the surrounding eddies, turbulence is unable to penetrate the reaction zone and the flame is assumed to be embedded in a quasi-laminar flow field [19]. With this notion, turbulent eddies can only cause deformation and stretching of the reaction zone. This view of flame structures allows the complex chemical structures of the flame to be decoupled from the flow dynamics, which can be modeled independently. This decoupling of scales constitutes an important advantage of flamelet models compared to pdf models, as it allows for a pre-tabulation of thermo-chemical states based on a small number of independent parameters. These parameters are referred to as look-up parameters. Having efficient tabulation and look-up strategies at hand [24–26] allows significant computational resources to be saved, compared to pdf methods. However, a drawback of this procedure is that, in order to account for the turbulence-chemistry interaction, pre-tabulating thermo-chemical states for LES or RANS requires assumptions about the joint distribution of the quantities used to parameterize the flamelet table [14].
In order to compile flamelet look-up tables, a set of one-dimensional equations, called flamelet equations, is solved. The classical form of the flamelet equations, as proposed by Peters [22] and Peters [23], is self-contained except for the flamelet parameter scalar dissipation rate, which links the chemistry and flow fields. The scalar dissipation rate plays a central role in non-premixed combustion modeling and is related to the gradient of the mixture fraction, which in turn represents the independent coordinate for non-premixed flamelet models. The mixture fraction is defined as zero in the pure oxidizer stream and one in the pure fuel stream.
In their classical form, as proposed by Peters [22], the flamelet equations describe one-dimensional reactive-diffusive structures , where transport is assumed to occur predominantly along flame-normal directions, i.e. along the gradient normal to mixture fraction iso-surfaces (in three dimensions). Since the early work of Peters [22], many extensions have been proposed to account for different complex flame features, e.g. differential diffusion [27, 28], unsteady effects [29–31], multi-feed combustion [32–34], local extinction and autoignition [35–38], pollutant formation [39], thermal and mixture stratification [40], radiation [41–43] and curvature [44–47].

Novel insights into flamelet-based modeling strategies might be promoted by a recent theory by Wang and Peters [48]. By means of the theory of “dissipation elements” further insights into fine-scale scalar mixing processes can be obtained by decomposing the mixture fraction field into small subunits called “dissipation elements”. The essence of this theory is to trace gradient trajectories along the ascending and descending gradient until a local extremal point is reached. The ensemble of all trajectories that end at the same local extremal points form a dissipation element, eventually

leading to a geometrical decomposition of the mixture fraction field. Wang and Peters [48] applied their theory to non-reactive flows, and were able to reconstruct statistical properties of the scalar field by solely knowing information at the endpoints of dissipation elements. In the context of turbulent reactive flows, dissipation element analysis seems to be an interesting opportunity to provide further insights into flamelet-relevant quantities, keeping in mind that gradient trajectories traced on the mixture fraction field constitute flamelets in terms of the flamelet theory.

1.4 Objectives and outline of the thesis

In order to develop and test models that account for the various aspects of turbulent combustion, detailed validation data are required. Although many high quality experimental data sets exist, they often lack the level of detail required to rigorously analyze model deficiencies [49]. In this regard direct numerical simulations have become increasingly important over recent years to complement theory and experiment [50]. Direct numerical simulations yield first-principle solutions free from turbulence modeling errors and with utmost realism regarding fine-scale physics [51]. Hence, they provide the most comprehensive data sets, which may then be used to assess model assumptions and to develop new modeling strategies. In this sense, DNS can be regarded as a (numerical) experiment under controlled conditions which allows an in-depth analysis of certain physical aspects of turbulent reactive flows. Although DNS are mostly limited to simple geometries and fairly low Reynolds numbers, the rapid advancements in the field of high-performance computing [52] have enabled some highly interesting DNS studies of practical relevance [6, 53–56].

In this thesis, a direct numerical simulation is conducted to analyze turbulent flamelets in detail and to assess the latest formulation of flamelet equations [47]. While the classical flamelet model [22, 23] neglects tangential effects, the extended model [47] explicitly accounts for the multi-dimensionality of flame physics and requires additional structure information of the underlying mixture fraction field, e.g. curvature of the mixture fraction field.
To this end, the extended flamelet model is modified to describe flamelets in a Lagrangian manner, which allows to track them in time and space facilitated by an on-the-fly tracking algorithm. Apart from a rigorous analysis of singly tracked flamelets, revealing insights into the behavior of flamelet related parameters are obtained by the method of dissipation elements [48].

The objectives of the thesis can summarized as follows:

- Conduct a highly resolved direct numerical simulation including detailed chemistry and transport properties. To facilitate the subsequent analyses, an additional transport equation must be solved for the mixture fraction.
- Develop a framework that allows for on-the-fly tracking of flamelet structures in space and time in a direct numerical simulation.
- Couple the on-the-fly tracking framework to the DNS solver. Use the extracted data to assess the latest formulation of non-premixed flamelet equations [47], which also account for curvature-induced transport processes and additionally require structure information on the

underlying mixture fraction field. Based on the on-the-fly tracking, reconstruct full flamelet histories from the DNS.

- Transfer the dissipation element concept to the turbulent reactive DNS. Introduce a regime classification that allows a distinction to be made between dissipation elements that are subject to chemical reactions and those that are mainly subject to turbulent mixing. By means of this regime classification, analyze the inner structure of dissipation elements.

This closes the introductory part of this thesis. Chapter 2 presents the mathematical formulae used to describe turbulent reactive flows. After a description of the governing equations and thermodynamic relations, important implications for low-Mach number flows are presented. The chapter closes with details about transport relations for multi-component mixtures and chemical kinetic expressions used to formulate chemical source terms.
Chapter 3 explains the fundamental concepts of flamelet modeling. First, the mixture fraction variable, which is a key quantity for all flamelet models, is introduced. Next, the steady laminar flamelet model is introduced, after which the extended formulation is presented in detail.
Chapter 4 deals with the direct numerical simulation conducted in this thesis. After a brief introduction, the core of the direct numerical simulation code is explained, presenting two newly implemented solvers together with their corresponding strong and weak scaling behavior. The chapter closes with an in-depth description of the direct numerical simulation setup used for the analyses, and statistical results obtained from the DNS are discussed.
Chapter 5 presents results from the on-the-fly tracking procedure. After a detailed description of the tracking algorithm that was used in conjunction with the DNS solver, results in terms of recomputed flamelet histories are presented. After that, budget analyses of the extended flamelet equations are conducted, where the transient nature of the tracked flamelets is explicitly taken into account.
In chapter 6 the concept of dissipation elements is applied to the direct numerical simulation outlined in chapter 4. After explaining the core principles of the dissipation element method, the numerical procedure is briefly outlined. Next, a parametrization of dissipation elements is introduced which is used for a statistical analysis, presented in the last section of chapter 6. Chapter 6 closes with the presentation of a regime classification suitable for characterizing the dissipation elements found in the DNS of turbulent reactive flows, and statistics obtained in the context of this classification are discussed. Chapter 7 closes the thesis by giving a summary and presenting conclusions.

2 Mathematical description of turbulent reactive flows

2.1 Governing Equations for Reacting Flows

The governing equations that are used to describe a multicomponent reacting flow system are given by the *conservation of mass*, the *conservation of momentum* and *the conservation of energy*. In the remainder, all equations are formulated in an Eulerian frame of reference and summation of repeated indices is implied, i. e.

$$M_{ij}\,v_j \equiv \sum_j M_{ij}\,v_j\,. \tag{2.1}$$

The chapter outlines the most important aspects required for the simulation of compressible turbulent reacting flows including explanations of possible simplifications of the governing equations. After a general introduction to turbulent combustion, the complete set of governing equations required for the simulation of turbulent reacting flows is described. Next, the most important thermodynamic and transport relations necessary for the description of multicomponent flow systems are presented. The chapter closes with principal explanations regarding chemical kinetic expressions important for the formulation of the source terms appearing in the governing equations of the chemical reacting species.

2.1.1 Conservation of mass

The conservation of mass follows the form for non-reacting flows and is given by

$$\frac{\partial}{\partial t}\rho + \frac{\partial}{\partial x_j}\rho u_j = 0\,. \tag{2.2}$$

In contrast to the field of classical aerodynamics, fluids considered in this work consist of a multitude of reacting species, each of which has to satisfy a transport equation. To this end, the mass fraction of each species i in the mixture, which has total mass m, is defined as

$$Y_i = \frac{m_i}{m}\,, \tag{2.3}$$

where m_i is the mass of species i. It is obvious that for N species $\sum_{i=1}^{\mathrm{N_s}} m_i = m$. Hence,

$$\sum_{i=1}^{\mathrm{N_s}} Y_i = \sum_{i=1}^{\mathrm{N_s}} \frac{m_i}{m} = 1\,. \tag{2.4}$$

The transport equation for each species mass fraction reads

$$\frac{\partial}{\partial t}\rho Y_i + \frac{\partial}{\partial x_j}\rho u_j Y_i = -\frac{\partial}{\partial x_j}\rho Y_i V_{i,j} + \dot{\omega}_i \,, \tag{2.5}$$

where $V_{i,j}$ denotes the diffusion velocity of species i in direction j and $\dot{\omega}_i$ describes the reaction rate of species i. Summation over all species, considering $\sum_{i=1}^{\mathrm{N_s}} \dot{\omega}_i = 0$ gives [57]

$$\frac{\partial}{\partial t}\rho + \frac{\partial}{\partial x_j}\rho u_j = -\frac{\partial}{\partial x_j}\rho \sum_{i=1}^{\mathrm{N_s}} Y_i V_{i,j} + \sum_{i=1}^{\mathrm{N_s}} \dot{\omega}_i = -\frac{\partial}{\partial x_j}\rho \sum_{i=1}^{\mathrm{N_s}} Y_i V_{i,j} \,, \tag{2.6}$$

which can be used to formulate a constraint for the species diffusion velocities

$$\sum_{i=1}^{\mathrm{N_s}} Y_i V_{i,j} = 0 \,. \tag{2.7}$$

2.1.2 Conservation of momentum

Assuming a compressible Newtonian fluid and neglecting volume forces, the general conservation of momentum reads

$$\frac{\partial}{\partial t}\rho u_i + \frac{\partial}{\partial x_j}\rho u_i u_j = \frac{\partial}{\partial x_j}\sigma_{ij} \,, \tag{2.8}$$

where u_i denotes the Eulerian velocity field, which depends on the spatial position x_j and time t. The stress tensor σ_{ij} can be split into isotropic stresses, caused by pressure, and viscous stresses

$$\sigma_{ij} = \tau_{ij} - p\delta_{ij} = -p\delta_{ij} + \left(\zeta - \frac{2}{3}\mu\right)\frac{\partial u_k}{\partial x_k}\delta_{ij} + \mu\left(\frac{\partial u_i}{\partial x_j} + \frac{\partial u_j}{\partial x_i}\right). \tag{2.9}$$

Here, τ_{ij} is the viscous stress tensor, δ_{ij} denotes the Kronecker delta, p the total pressure and μ and ζ are the dynamic (or shear) viscosity and the bulk viscosity, respectively. The dynamic viscosity is related to the kinematic viscosity by $\nu = \mu/\rho$. In contrast to the dynamic viscosity, the bulk viscosity (or volume viscosity) usually has been neglected in numerical studies [58]. It is produced by viscous forces that arise when a volume of fluid is compressed or dilated without a change in shape. While for monoatomic gas mixtures kinetic theory shows that the bulk viscosity is zero, the influence of bulk viscosity for polyatomic mixtures is not yet fully understood [58–64]. Although a few studies [63, 65] have shown that the volume viscosity might be of the same order than the shear viscosity for polyatomic gases, the whole term

$$\frac{\partial}{\partial x_i}\left(\zeta\frac{\partial u_k}{\partial x_k}\delta_{ij}\right) \tag{2.10}$$

generally has a weak influence for low-speed flows [63, 64, 66] and is therefore neglected in this work. Thus, the stress tensor σ_{ij} reduces to

$$\sigma_{ij} = \tau_{ij} - p\delta_{ij} = -p\delta_{ij} + \mu\left(2S_{ij} - \frac{2}{3}\frac{\partial u_k}{\partial x_k}\delta_{ij}\right), \tag{2.11}$$

where S_{ij} denotes the rate-of-strain tensor and is defined as

$$S_{ij} = \frac{1}{2}\left(\frac{\partial u_i}{\partial x_j} + \frac{\partial u_j}{\partial x_i}\right). \tag{2.12}$$

2.1.3 Conservation of energy

Several equations describing energy conservation exist [57] and all can be derived from the balance of total energy e_t. Neglecting volumetric forces, the principal conservation equation for total energy reads

$$\frac{\partial}{\partial t}\rho e_\mathrm{t} + \frac{\partial}{\partial x_j}\rho u_j e_\mathrm{t} = -\frac{\partial}{\partial x_j}q_j + \frac{\partial}{\partial x_j}\left(\sigma_{ij}u_i\right) + \dot{\mathcal{Q}}, \tag{2.13}$$

where $\dot{\mathcal{Q}}$ is a heat source term, e. g. due to an electric spark or radiative fluxes, and q_j is the heat flux,

$$q_j = -\lambda\frac{\partial}{\partial x_j}T + \rho\sum_{i=1}^{N} h_i Y_i V_{i,j}. \tag{2.14}$$

The first term of equation (2.14) accounts for heat diffusion according to Fourier's Law, where λ denotes the thermal conductivity of the mixture and T the temperature. The second term is specific for multicomponent mixtures and describes the energy flux due to diffusion of species having different enthalpies h_i.

2.2 Thermodynamic relations

2.2.1 Ideal-gas law

For multicomponent mixtures, an equation relating pressure, temperature and density is given by the ideal gas law [67, 68],

$$p = \rho\frac{\mathcal{R}}{\langle W\rangle}T. \tag{2.15}$$

Here, $\mathcal{R}$ is the universal gas constant and $\langle W\rangle$ denotes the molar mass of the mixture. The latter is computed by

$$\langle W\rangle = \left(\sum_{i=1}^{\mathrm{N_s}}\frac{Y_i}{W_i}\right)^{-1} = \sum_{i=1}^{\mathrm{N_s}} X_i W_i, \tag{2.16}$$

where species mole fraction X_i and species mass fraction Y_i are related by

$$\frac{Y_i}{X_i} = \frac{W_i}{\langle W \rangle} . \tag{2.17}$$

In equations (2.16) and (2.17), W_i represents the molar mass of species i.

2.2.2 Specific enthalpies and heat capacities

The conservation of total chemical energy, see equation (2.13), is related to the total chemical enthalpy h_t by

$$e_\mathrm{t} = h_\mathrm{t} - \frac{p}{\rho} = h + \frac{1}{2} u_i u_i - \frac{p}{\rho} , \tag{2.18}$$

where h denotes the chemical enthalpy of the mixture defined by

$$h = \sum_i^{\mathrm{N_s}} h_i Y_i . \tag{2.19}$$

The evaluation of the species enthalpies h_i requires the definition of a thermo-chemical reference state which is prescribed through a reference temperature T_0 (usually $T_0 = 298\,\mathrm{K}$) and the enthalpies of formation of each species $h^0_{\mathrm{r}ef,i}$ (determined at T_0). Then, the enthalpy of species i can be split into a sensible part, related to temperature changes, and a chemical part, related to the enthalpy of formation of species i,

$$h_i = \underbrace{\int_{T_0}^{T} c_{\mathrm{p},i} \, \mathrm{d}T}_{\text{sensible}} + \underbrace{h^0_{\mathrm{r}ef,i}}_{\text{chemical}} . \tag{2.20}$$

Here, $c_{\mathrm{p},i}$ is the heat capacity of species i at constant pressure. It is related to the heat capacity at constant volume by

$$c_{\mathrm{v},i} = c_{\mathrm{p},i} - \frac{\mathcal{R}}{W_i} . \tag{2.21}$$

Similar to equation (2.19) the mixture-averaged, mass-based specific heat at constant pressure, c_p, and at constant volume, c_v, are

$$c_\mathrm{p} = \sum_{i=1}^{\mathrm{N_s}} Y_i c_{\mathrm{p},i} , \tag{2.22}$$

$$c_\mathrm{v} = \sum_{i=1}^{\mathrm{N_s}} Y_i c_{\mathrm{v},i} . \tag{2.23}$$

Usually, for numerical simulations, the temperature dependence of species heat capacities and enthalpies is tabulated in polynomial forms [69–71]. In this work, the thermodynamic properties

for species i are tabulated (in molar units) using the seven-coefficient polynomials of Gordon and McBride [71]

$$\frac{C_{p,i}^{\circ}}{\mathcal{R}} = a_{0,i} + T\left(a_{1,i} + T\left(a_{2,i} + T\left(a_{3,i} + a_{4,i}T\right)\right)\right) \tag{2.24}$$

$$\frac{H_i^{\circ}}{\mathcal{R}} = T\left(a_{0,i} + T\left(\frac{a_{1,i}}{2} + T\left(\frac{a_{2,i}}{3} + T\left(\frac{a_{3,i}}{4} + \frac{a_{4,i}}{5}T\right)\right)\right)\right) + a_{5,i} \tag{2.25}$$

$$\frac{S_i^{\circ}}{\mathcal{R}} = a_{0,i}\ln T + T\left(a_{1,i} + T\left(\frac{a_{2,i}}{2} + T\left(\frac{a_{3,i}}{3} + \frac{a_{4,i}}{4}T\right)\right)\right) + a_{6,k} \tag{2.26}$$

where S_i is the entropy in molar units, and $()^{\circ}$ indicates a standard-state property at one atmosphere. The mass-based specific heat and enthalpy are then defined as

$$c_{\mathrm{p},i} = \frac{C_{p,i}}{W_i} \quad \text{and} \quad h_i = \frac{H_i}{W_i}\,. \tag{2.27}$$

It can be shown, that for ideal gases, equations (2.24) and (2.25) are also valid for pressures above one atmosphere, i.e. [72, 73]

$$\left(\frac{\partial c_{\mathrm{p}}}{\partial p}\right)_T = 0 \tag{2.28}$$

$$\left(\frac{\partial h}{\partial p}\right)_T = 0\,. \tag{2.29}$$

2.2.3 Compressibility and speed of sound

The term *compressible flow* implies variations in density throughout the flow field. In many cases these variations are caused by pressure changes between adjacent locations in the flow field. Thus, the rate of change of density with respect to pressure is an important parameter in the analysis of compressible flows and it is closely connected to the speed of propagation of small pressure disturbances, i.e. the speed of sound [67]. For ideal gases, the speed of sound c, is expressed by

$$c = \sqrt{\gamma\frac{p}{\rho}} = \sqrt{\gamma\frac{\mathcal{R}T}{\langle W\rangle}}, \tag{2.30}$$

where γ denotes the isentropic expansion factor

$$\gamma = \frac{c_{\mathrm{p}}}{c_{\mathrm{v}}}\,. \tag{2.31}$$

The principal nature of the flow field, e.g. occurrence of sonic shock waves, and thereby the computational treatment strongly depends on the ratio of magnitudes of the flow velocity and the

speed of sound. In order to measure compressibility effects, the ratio of a characteristic velocity of the flow field and the speed of sound is used, which is denoted by the Mach number and reads

$$\mathrm{Ma} = \frac{u_{ref}}{c}. \tag{2.32}$$

Flows that fall into a regime of low Mach numbers are also often referred to as “low-Mach” number flows. As will be seen in the next section, the governing equations (2.8) and (2.13) can be simplified and more efficient solutions algorithms (compared to a “fully compressible” formulation) can be applied.

2.3 Low-Mach number approach

Two principal strategies for the solution of the governing equations of reacting flows exist, where the distinction is made based on the considered compressibility of the fluid. In case of a fully-compressible formulation, the dispersion of acoustic waves is considered, while for weakly-compressible flows a decoupling of fluid dynamics and thermodynamics is pursued.
Many practical combustion applications, including the case discussed later, are operated under conditions where acoustic waves can be neglected and detailed simulations of such systems using a fully-compressible approach is then particularly inefficient [74, 75] and would impose prohibitive numerical costs. This partly results from the requirement that all relevant time scales have to be resolved. The characteristic time scale of acoustic wave propagation may be several orders of magnitude smaller than those important for convective and diffusive transport processes or chemical reactions.
It is therefore advantageous to seek for simplification of the governing equations by introducing the concept of low-Mach number flows which is based on an analysis of the order of magnitude of the various terms in the conservation equations [59, 66, 76]. Before going into detail on the low-Mach number version of the governing equations the relation between compressibility effects and the Mach number is explored.

2.3.1 Relation between Mach number and compressibility

The numerical solution of governing equations can be considerably simplified if compressibility effects and hence acoustic waves are neglected. In order to study the influence of compressibility, an order of magnitude analysis of the momentum equation is conducted. For the sake of convenience and without loosing the validity for general three-dimensional flows, the analysis is carried out for the one-dimensional inviscid Euler equations

$$\rho \frac{\partial}{\partial t} u + \rho u \frac{\partial}{\partial x} u = -\frac{\partial}{\partial x} p\,. \tag{2.33}$$

Therefor, dimensionless variables are introduced as

$$t^* = t\frac{u_0}{l_0}, \quad x^* = \frac{x}{l_0}, \quad u^* = \frac{u}{u_0}, \quad \rho^* = \frac{\rho}{\rho_0}, \quad p^* = \frac{p}{p_0}, \tag{2.34}$$

where $(\cdot)_0$ is a corresponding reference quantity. Using both, the relation $c_0^2 = \gamma p_0/\rho_0$, where c_0 denotes a reference speed of sound, and the Mach number given by $\mathrm{Ma} = u_0/c_0$, equation (2.33) becomes

$$-\frac{1}{\gamma \mathrm{Ma}^2 \rho^*}\frac{\partial}{\partial x^*}p^* = \left(\frac{\partial}{\partial t^*}u^* + u^*\frac{\partial}{\partial x^*}u^*\right). \tag{2.35}$$

Since the terms in equation (2.35) must balance each other, equation (2.35) implies that a change of $\mathcal{O}(1)$ in the right-hand side of equation (2.35) will produce a small change, $\mathcal{O}(\mathrm{Ma}^2)$, in the pressure gradient. In terms of physics, this means that the propagation of small, isentropic disturbances (e.g. pressure waves) is much faster than the advection of the flow. Thus, the pressure is leveled out more rapidly throughout the domain of interest. Due to this effect, differences within the velocity field are not able to create pressure fluctuations and, hence, no density fluctuations can arise. Therefore, it can be argued that for small Mach numbers compressibility effects are negligible. It is generally accepted that for $\mathrm{Ma} \leq 0.3$ a flow can be considered as weakly compressible. The implications of this assumption onto the governing equations is discussed next.

2.3.2 Low-Mach number flow equations

As a result of the discussion in section 2.3.1, for flows at low-Mach numbers, gradients in the fluid velocity cannot generate pressure gradients that lead to changes in density. Since the Mach number explicitly appears in equation (2.35) an asymptotic expansion in powers of the Mach number is a good choice to get insights into the physical behavior. A rigorous mathematical justification of such an analysis is given in [76, 77].
The low-Mach number asymptotic analysis is conducted by means of non-dimensional variables ψ^* that are expanded according to [78]

$$\psi^* = \psi_0^* + \mathrm{Ma}^2\tilde{\psi}^*, \tag{2.36}$$

where ψ^* represents any of the variables ρ, p, u that have been made dimensionless according to equation (2.34). In terms of the pressure, equation (2.36) can be interpreted as decomposing the pressure into a background (or thermodynamic) pressure p_0^* and a hydrodynamic fluctuation $\tilde{p}^*$. After introducing the expansions into the dimensionless momentum equation, cf. equation (2.35) and matching equal powers of Ma, yields a hierarchy of equations for the different powers of Ma. An important result of this decomposition is

$$\frac{\partial}{\partial x_i}p_0^* = 0. \tag{2.37}$$

Thus, to leading order the background pressure is a function of time only. For simplicity, it is furthermore assumed that flames occur in an open environment under constant pressure such that the leading order pressure term is, in fact, a constant. Only the $\mathcal{O}(\mathrm{Ma}^2)$ part of the pressure remains in the momentum equation which therefore becomes (in dimensional variables)

$$\frac{\partial}{\partial t}\rho u_i + \frac{\partial}{\partial x_j}(\rho u_i u_j) = \frac{\partial}{\partial x_j}\left(\tau_{ij} - \tilde{p}\delta_{ij}\right). \tag{2.38}$$

Proceeding with the energy conservation, it is convenient to first transform equation (2.13) into a transport equation for the sensible enthalpy h_s which is defined as

$$h_\mathrm{s} = h - \sum_{i=1}^{\mathrm{N_s}} h^0_{\mathrm{ref},i} Y_i\,, \tag{2.39}$$

using the relation between total energy and enthalpy, given in equation (2.18). Next, equation (2.36) is formulated in terms of h_s and introduced into the transport equation for h_s. Eliminating higher order pressure and viscous heating effects, and neglecting heat sources (e.g. electric sparks or radiative fluxes), leads to [57]

$$\frac{\partial}{\partial t}(\rho h_\mathrm{s}) + \frac{\partial}{\partial x_j}(\rho u_j h_\mathrm{s}) = -\frac{\partial}{\partial x_j} q_j + \dot{\omega}_T\,, \tag{2.40}$$

where $\dot{\omega}_T = -\sum_{i=1}^{\mathrm{N_s}} h^0_{\mathrm{ref},i}\dot{\omega}_i$ is the heat released due to combustion. Using relation (2.20), equation (2.40) is further transformed into a transport equation for temperature [57]

$$\rho c_\mathrm{p}\left(\frac{\partial}{\partial t}T + \frac{\partial}{\partial x_j}u_j T\right) = \dot{\omega}'_T + \frac{\partial}{\partial x_i}\left(\lambda\frac{\partial T}{\partial x_i}\right) - \left(\rho\sum_{i=1}^{N} c_{\mathrm{p},i} Y_i V_{i,j}\right)\frac{\partial}{\partial x_j}T\,, \tag{2.41}$$

where the source term $\dot{\omega}'_T$ is defined as

$$\dot{\omega}'_T = -\sum_{k=1}^{\mathrm{N_s}} h_k \dot{\omega}_k\,. \tag{2.42}$$

The advantage of solving a temperature equation instead of a conservation equation for energy or enthalpy is that the temperature is a direct solution of the problem. Hence, temperature dependent quantities, e.g. chemical source terms and thermodynamic quantities, can be easily computed. In contrast, solving any form of energy transport equation (for e_t,h or h_s) requires to iteratively determine the temperature from the current energy level, since the temperature is only an implicit solution in that case.

An important consequence of the low-Mach number formulation becomes obvious when equation (2.36) is introduced in the state law for ideal gases, which to leading order becomes

$$p_0 = \frac{\rho_0 \mathcal{R} T_0}{\langle W \rangle} . \tag{2.43}$$

It can be seen in this equation that the coupling between the hydrodynamic fluctuating pressure $\tilde{p}$ and the density is suppressed [79]. As a consequence, acoustic waves are neglected and the final set of equations that is solved for the subsequent analyses consists of equations (2.5), (2.38), (2.41) and (2.43). Note that upon introducing equation (2.36) into equation (2.5), to leading order, no simplifications of the species transport equation can be achieved.

2.4 Summary of governing equations

The governing equations that are solved in this work can be summarized as follows:

- Momentum

$$\frac{\partial}{\partial t}(\rho u_i) = -\frac{\partial}{\partial x_j}(\rho u_i u_j) + \frac{\partial}{\partial x_j}\left(\tau_{ij} - \tilde{p}\delta_{ij}\right) , \tag{2.44}$$

- Temperature

$$\frac{\partial}{\partial t} T = -u_j \frac{\partial}{\partial x_j} T + \frac{1}{\rho c_\mathrm{p}} \left[-\sum_{k=1}^{N} h_k \dot{\omega}_k + \frac{\partial}{\partial x_i}\left(\lambda \frac{\partial T}{\partial x_i}\right) - \left(\rho \sum_{i=1}^{N} c_{\mathrm{p},i} Y_i V_{i,j}\right) \frac{\partial}{\partial x_j} T \right] , \tag{2.45}$$

- Chemical Species

$$\frac{\partial}{\partial t}(\rho Y_i) = -\frac{\partial}{\partial x_j}(\rho u_j Y_i) - \frac{\partial}{\partial x_j}(\rho Y_i V_{i,j}) + \dot{\omega}_i , \tag{2.46}$$

2.5 Transport relations

This section briefly outlines the mathematical formalism used to evaluate the transport terms, μ, λ and $V_{i,j}$, appearing in the governing equations, cf. equations (2.44) to (2.46). Although in the pure species case expressions for these terms follow the standard kinetic theory [80, 81], the transport coefficients in multicomponent mixtures are not given explicitly by the kinetic theory [66, 82]. Indeed, their evaluation requires solving linear systems, referred to as transport linear systems. Several theories for the assembly and efficient solution of these linear systems exist [83–88]. However, a new class of transport algorithms was proposed by Ern and Giovangigli [89][90, 91] and implemented in the EGlib software package [92]. Exploiting important numerical properties of the transport linear systems and using iterative solution strategies [93], Ern and Giovangigli [94] demonstrated the benefits of EGlib compared to methods implemented in the software packages TRANSPORT [95] and Cantera [96].

In this work, transport coefficients are evaluated using the EGlib software package [92] and the following sections outline the most important relations used to evaluate multicomponent transport coefficients.

2.5.1 Shear viscosity

Viscosity is one of the most important terms that influences the character of the flow field significantly. To determine the viscosity of gas mixtures at moderate pressures the theory of Chapman and Enskog extended for multicomponent mixtures [81, 97, 98] can be used. Oftentimes, however, the solution of the transport linear system is omitted in favor of a semi-empirical formulation [80, 98–102]. Knowing the pure species viscosities μ_i, either from polynomial fits [103] or directly from the evaluation of kinetic theory relations [66, 89], Wilke's equation extended by Bird et al. [101] can be used to compute a mixture-averaged viscosity μ,

$$\mu = \sum_{i=1}^{\mathrm{N_s}} \frac{X_i \mu_i}{\sum_{j=1}^{\mathrm{N_s}} \Phi_{ij}}, \tag{2.47}$$

where the dimensionless quantity Φ_{ij} is defined as [101]

$$\Phi_{ij} = \frac{1}{\sqrt{8}} \left(1 + \frac{W_i}{W_j}\right)^{-1/2} \left[1 + \left(\frac{\mu_i}{\mu_j}\right)^{1/2} \left(\frac{W_j}{W_i}\right)^{1/4}\right]^2. \tag{2.48}$$

This approach is used in well known software packages like Cantera [96] and TRANSPORT [95]. However, based on the transport linear system associated with shear viscosity, Ern and Giovangigli [89] [66] derived a formulation which is ten times more accurate than equation (2.47) and cheaper to evaluate [90, 94],

$$\mu = \frac{\sum_{k=1}^{\mathrm{N_s}} \left(X_k^2 / \mathcal{H}_{kk}\right)^2}{\sum_{k=1}^{\mathrm{N_s}} \sum_{l=1}^{\mathrm{N_s}} X_k X_l \mathcal{H}_{kl} / (\mathcal{H}_{kk} \mathcal{H}_{ll})}, \tag{2.49}$$

where

$$\begin{aligned} \mathcal{H}_{kk} &= \sum_{\substack{l=1 \\ l \neq k}}^{\mathrm{N_s}} \frac{2\mathcal{K}_B T}{p \mathcal{D}_{kl}} \frac{X_k X_l}{W_k + W_l} \left[1 + \frac{3}{5} \frac{W_l}{W_k} \overline{A}_{kl}\right] + \frac{X_k^2}{\mu_k} \\ \mathcal{H}_{kl} &= \frac{2\mathcal{K}_B T}{p \mathcal{D}_{kl}} \frac{X_k X_l}{W_k + W_l} \left[-1 + \frac{3}{5} \overline{A}_{kl}\right], \end{aligned} \tag{2.50}$$

are the entries of the system matrix $\mathcal{H}$. Therein, $\mathcal{K}_B$ is the Boltzmann constant, $\mathcal{D}_{kl}$ are the binary diffusion coefficients and $\overline{A}_{kl} = \Omega_{kl}^{(2,2)} / \Omega_{kl}^{(1,1)}$ denotes the ratio of the collision integrals. Further details about the derivation of equations (2.49) and (2.50) can be found in [66, 89].

2.5.2 Diffusion velocities

In this section a brief overview of multicomponent diffusion velocities is given and further details can be found in [59, 66, 82, 89, 104]. The diffusion velocity of species i in the mixture, cf. equation (2.5), can be split into a molecular diffusion term and a term accounting for thermo-diffusion, also called Soret effect. It is generally expressed by [66, 81]

$$V_{i,j} = \underbrace{-\sum_{k=1}^{N_s} D_{ik}\, d_{k,j}}_{\text{Molecular diffusion}} \underbrace{-D_i^T \frac{\partial}{\partial x_j} \ln(T)}_{\text{Thermo diffusion}}, \tag{2.51}$$

where D_{ik} are the multi-component diffusion coefficients, depending on T, p and Y_k, and D_i^T is the termo-diffusion coefficient of species i. The multi-component diffusion coefficients are not given explicitly by the kinetic theory but can be obtained from the Stefan-Maxwell equations [59], for example by expanding D_{ik} in terms of convergent series [66, 89, 90, 92]. The diffusion driving force $d_{k,j}$ is defined by

$$d_{k,j} = \frac{\partial}{\partial x_j} X_k + (X_k - Y_k) \frac{1}{p} \frac{\partial}{\partial x_j} p + \frac{\rho}{p} \sum_{j=1}^{N_s} Y_k Y_j (b_j - b_k). \tag{2.52}$$

In this work, baro-diffusion (related to the pressure gradient) is neglected and external forces b_k are considered to act equally on all species. Hence, the diffusion driving force for species k reduces to

$$d_{k,j} = \frac{\partial}{\partial x_j} X_k. \tag{2.53}$$

Hirschfelder and Curtiss [105] pointed out the importance of molecular diffusion for combustion problems. However, due to high computational costs associated with the solution of the Stefan-Maxwell equations, even when the highly optimized algorithms of Ern and Giovangigli [89, 90, 92] are used, two simplifications are considered in this work

- Hirschfelder-Curtiss approximation,
- Unity Lewis number approximation.

Unless stated otherwise the Hirschfelder-Curtiss approximation, also known as mixture-average transport model, is used for all computations.

Hirschfelder-Curtiss approximation

The model of Hirschfelder and Curtiss [105][81] approximates the diffusion coefficient of species i in the mixture as

$$D_{i,m} = (1 - Y_i) \left(\sum_{k=1, k \neq i}^{\mathrm{N_s}} \frac{X_k}{\mathcal{D}_{ik}} \right)^{-1} , \tag{2.54}$$

where $\mathcal{D}_{ik}$ denotes the binary diffusion coefficients of species pair (i, k). It has been proven that this approximation is equivalent to keeping only the first term of the series expansion of the diffusion matrix D_{ik} [66, 89] and equation (2.54) is therefore also denoted as zeroth-order approximation [82]. Since this approximation only accounts for diagonal terms in the diffusion matrix, global mass conservation, cf. equation (2.7), is no longer ensured,

$$\sum_{i=1}^{N} Y_i V_{i,j} \neq 0 . \tag{2.55}$$

To overcome this problem, the diffusion velocity of the ith species is split into two parts [57, 106]

$$V_{i,j} = V_{i,j}^{*} + V_{c,j} , \tag{2.56}$$

where $V_{i,j}^{*}$ is a predictor and $V_{c,j}$ is a corrector. The predictor term is computed according to

$$V_{i,j}^{*} = -\frac{D_{i,m}}{X_i} d_{i,j} , \tag{2.57}$$

and the correction velocity $V_{c,j}$ is calculated such that, if all species equations are summed, the mass conservation is recovered

$$V_{c,j} = -\sum_{i=1}^{N} Y_i V_{i,j}^{*} . \tag{2.58}$$

Unity Lewis number diffusion

A simpler approach to compute species diffusion velocities is to assume that all species diffusivities are proportional to the thermal diffusivity, where the proportionality is expressed in terms of a species Lewis number Le_i

$$D_{i,m} = \frac{\lambda}{\rho c_{\mathrm{p}} \mathrm{Le}_i} . \tag{2.59}$$

This can be even further simplified if it is assumed that all Le_i are constant with $\mathrm{Le}_i = 1$, i.e.

$$D_{i,m} = D = \frac{\lambda}{\rho c_\mathrm{p}} \,. \tag{2.60}$$

In this case no species diffusion correction velocity is required and the diffusion velocity reads [57]

$$V_{i,j} = -\frac{D}{Y_i}\frac{\partial}{\partial x_j} Y_i \,. \tag{2.61}$$

2.5.3 Thermal Conductivity

An expression for the thermal conductivity of the mixture can be formulated based on the pure species thermal conductivities λ_i and the mole fractions X_i by [107, 108]

$$\lambda = \frac{1}{2}\left(\sum_{i=1}^{\mathrm{N_s}} X_i \lambda_i + \frac{1}{\sum_{i=1}^{\mathrm{N_s}} X_i/\lambda_i}\right). \tag{2.62}$$

This approach is applied by well known software packages like Cantera [96] and TRANSPORT [95] in case of the mixture-average species transport model.
On the other hand the EGlib software library [92] solves a transport linear system associated with thermal conductivity independently of the underlying species transport model. Details about the structure of the system and mathematical properties are skipped here for brevity, but details can be found in Ern and Giovangigli [89, 90]. Although, the solution of the transport linear system requires more computational resources, compared to equation (2.62), it is unrivalled in accuracy and will therefore be used for the following simulations.

2.6 Chemical kinetics relations

The species rates of production and related kinetic terms are generally defined as

$$\dot{\omega}_k = \sum_{i=1}^{\mathrm{N_r}} \nu_{ki} a_i \,, \tag{2.63}$$

where $\mathrm{N_r}$ is the number of reactions, ν_{ki} is the overall stoichiometric coefficient for species k in reaction i, and a_i is the rate-of-progress for reaction i. These rate determining quantities are defined by

$$\nu_{ki} = \nu''_{ki} - \nu'_{ki} \quad \text{and} \tag{2.64}$$

$$a_i = c_i R_i \,, \tag{2.65}$$

where ν''_{ki} and ν'_{ki} are the product and reactant stoichiometric coefficients (respectively) of species k in reaction i and c_i is a modification factor, explained later. Based on the molar concentration of species i, i.e.

$$[X_i] = \frac{\rho}{\langle W \rangle} X_i \,, \tag{2.66}$$

the principal rate-of-progress of the ith reversible reaction R_i is given by [10, 51, 109]

$$R_i = R_{f,i} - R_{r,i} \,, \tag{2.67}$$

$$R_{f,i} = k_{f,i} \prod_{j=1}^{\mathrm{N_s}} [X_j]^{\nu'_{ji}} \,, \tag{2.68}$$

$$R_{r,i} = k_{r,i} \prod_{j=1}^{\mathrm{N_s}} [X_j]^{\nu''_{ji}} \,. \tag{2.69}$$

Here, $k_{f,i}$ and $k_{r,i}$ are the forward and reverse reaction rate coefficients for the ith reaction, respectively. The forward reaction rate coefficient $k_{f,i}$ is given in Arrhenius form by

$$k_{f,i} = A_i T^{\beta_i} \exp\left(-\frac{T_{a,i}}{T}\right) , \tag{2.70}$$

where A_i is the pre-exponential factor, β_i is the temperature exponent, and $T_{a,i}$ is the activation temperature defined as $T_{a,i} = E_{a,i}/\mathcal{R}$. As demonstrated by Lu and Law [110], depending on the value of the Arrhenius parameters, $k_{f,i}$ can be calculated in different ways to minimize the computational cost [111]

$$k_{f,i} = \begin{cases} A_i & \text{if } \beta = 0 \text{ and } T_{a,i} = 0 \,, \\ \exp\left(\log A_i + \beta_i \log T\right) & \text{if } \beta_i \neq 0 \text{ and } T_{a,i} = 0 \,, \\ \exp\left(\log A_i + \beta_i \log T - T_{a,i}/T\right) & \text{if } \beta_i \neq 0 \text{ and } T_{a,i} \neq 0 \,, \\ \exp\left(\log A_i - T_{a,i}/T\right) & \text{if } \beta_i = 0 \text{ and } T_{a,i} \neq 0 \,, \text{ and} \\ A_i \prod^{\beta_i} T & \text{if } T_{a,i} = 0 \text{ and } \beta_i \in \mathbb{Z} \,, \end{cases} \tag{2.71}$$

where $\mathbb{Z}$ is the set of integers. The computation of the reverse reaction rate coefficients $k_{r,i}$ is not straight forward and details are given in appendix A.1.

The third-body/pressure modification, denoted c_i in equation (2.65), is given by [51, 112]

$$c_i = \begin{cases} 1 & \text{for elementary reactions,} \\ \displaystyle\sum_{j=1}^{\mathrm{N_s}} m_{ij} [X]_j & \text{for third-body enhanced reactions,} \\ \dfrac{P_{r,i}}{1 + P_{r,i}} F_i & \text{for unimolecular/recombination falloff reactions} \,, \end{cases} \tag{2.72}$$

where $P_{r,i}$ is the reduced pressure, and F_i is the falloff blending factor, see appendix A.2 for computational details. In case of a third-body enhanced reaction, principally all species contribute equally as third bodies and their corresponding efficiency factor is $m_{ij} = 1$. However, it is often the case that some species act more efficiently as third bodies than others do and in that case, m_{ij} can be different from unity. Further details about relations for chemical kinetics can be found in the textbook of Law [51].

3 Flamelet modeling

Flamelet models are widely used for turbulent non-premixed combustion modeling. The foundation of flamelet models was layed out more than forty years ago by Williams [113] and was essentially driven forward by Peters [22, 23]. They are based on the assumption that chemical reactions are fast and occur in thin confined layers around the reaction zone. If the characteristic length scale of these layers is smaller than that of the surrounding turbulent eddies, turbulence is unable to penetrate the reaction zone and the flame is assumed to be embedded in a quasi-laminar flow field [19]. With this notion, turbulent eddies can only stretch and strain the reaction zone. At the same time, this view of turbulent flame structures allows the complex chemical structures of the flame to be decoupled from the flow dynamics. Based on this asymptotic view of diffusion flames, Peters [22] introduced a coordinate transformation that eventually leads to a set of equations describing one-dimensional reactive-diffusive structures in the vicinity of the flame surface called flamelets [19].
The original flamelet model was derived based on boundary layer arguments for thin layers, and Peters [22] argued that derivatives tangential to the flame front are negligible compared to those in normal direction, which Peters [22] expressed in terms of the mixture fraction Z. However, in a recent study Scholtissek et al. [47] derived characteristic scaling ratios that relate flame thickness to curvature, which give some indication if curvature-induced flame-tangential effects must be considered. Scholtissek et al. [47] furthermore derived a new set of flamelet equations, which, compared to the original set of equations, accounts for curvature-induced flame-tangential transport effects.

In this chapter both the classical model of [22] and a modified version of the extended model of Scholtissek et al. [47] are introduced, where the structure is as follows. First the mixture fraction variable, essential for the subsequent derivations is introduced. Next, the classical flamelet model according to Peters [22] is presented. After that, the curvilinear coordinates used to derive an extended flamelet model in a Lagrangian manner are introduced, together with the rules for transforming the derivative operators appearing in the governing equations. The chapter closes with a presentation of the extended set of flamelet equations and the characteristic scaling ratios, used to assess curvature-induced transport effects.

3.1 The mixture fraction variable

One central quantity in the modeling of non-premixed combustion is the mixture fraction Z which was first introduced by Bilger [114]. It is used to determine the mixedness of the initially unmixed fuel and oxidizer streams. It can be related to chemical elements, e.g. C, O or H, by first writing a global reaction in the form

$$\nu_{\mathrm{C}}\mathrm{C} + \nu_{\mathrm{H}}\mathrm{H} + \nu_{\mathrm{O}}\mathrm{O} \rightarrow \text{products}\,, \tag{3.1}$$

where ν_C, ν_H, ν_O correspond to the number of elements C, H, O present in the reactants, respectively. Then the mass of an element j in the system is defined by

$$m_j = \sum_{i=1}^{N_s} \frac{a_{ij} W_j}{W_i} m_i \,, \tag{3.2}$$

where a_{ij} is the number of atoms of element j in species i. The mass fraction of element j is defined by

$$Z_j = \frac{m_j}{m} = \sum_{i=1}^{N_s} \frac{a_{ij} W_j}{W_i} Y_i \,. \tag{3.3}$$

Then, based on equation (3.3) a coupling function β is defined

$$\beta = \sum_{j=1}^{N_e} \gamma_j Z_j \,, \tag{3.4}$$

where N_e denotes the number of elements. In principle several different definitions of the weighting factors γ_j exist [115] but considering the choice by Bilger [114] yields

$$\beta = \frac{Z_C}{\nu_C W_C} + \frac{Z_H}{\nu_H W_H} - 2\frac{Z_O}{\nu_O W_O} \,. \tag{3.5}$$

Independent of the choice of γ_j the mixture fraction is determined by normalizing β with the constants β_1 and β_2

$$Z = \frac{\beta - \beta_2}{\beta_1 - \beta_2} \,, \tag{3.6}$$

where index 1 denotes the fuel stream and index 2 denotes the oxidizer stream, respectively. Finally, the mixture fraction according to Bilger [114] reads

$$Z = \frac{Z_C/(\nu_C W_C) + Z_H/(\nu_H W_H) + 2(Z_{O,2} - Z_O)/(\nu_O W_O)}{Z_{C,1}/(\nu_C W_C) + Z_{H,1}/(\nu_H W_H) + 2Z_{O,2}/(\nu_O W_O)} \,, \tag{3.7}$$

where $Z = 1$ denotes the pure fuel stream and $Z = 0$ denotes the pure oxidizer stream. This definition of the mixture fraction is commonly used in experiments.

According to Pitsch and Peters [116], definition (3.7) of the mixture fraction is problematic in terms of differential diffusion effects and an alternative definition of the mixture fraction is that of a conserved passive scalar [19, 116]

$$\frac{\partial}{\partial t}(\rho Z) = \frac{\partial}{\partial x_j}\left(\rho D_Z \frac{\partial}{\partial x_j} Z\right) - \frac{\partial}{\partial x_j}\left(\rho u_j Z\right) \,. \tag{3.8}$$

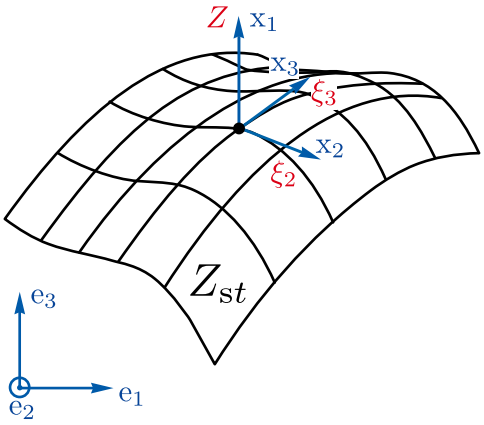

Figure 3.1.: Illustration of the orthogonal coordinate system (Z, ξ_2, ξ_3) attached to the stoichiometric mixture fraction iso-surface.

Peters [19] pointed out that equation (3.8) could be postulated, independently of any combinations of element mass fractions. Although in that case the diffusion coefficient D_Z is arbitrary, Peters [19] argues that choosing $D_Z = \lambda/(\rho c_\mathrm{p})$ is a reasonable choice, which results in a Lewis number of unity for the mixture fraction. It is definition (3.8) of the mixture fraction together with unity-Lewis number diffusion for Z that will be used in this work.

3.2 The flamelet model for non-premixed combustion

3.2.1 Steady laminar flamelet model

In the classical flamelet theory [22, 23], it is assumed that reactions are fast and occur in thin confined layers around the surface of stoichiometric mixture, determined by

$$Z(\mathbf{x}, t) = Z_{st}\,, \tag{3.9}$$

where Z_{st} denotes the stoichiometric mixture fraction. Then, a coordinate system can be introduced which is attached to the surface of stoichiometric mixture, where x_1 points normal to the surface $Z(\mathbf{x}, t) = Z_{st}$ and x_2 and x_3 lie within the surface. Further, replacing the coordinate x_1 with the mixture fraction Z, cf. figure 3.1, leads to a Crocco-type[1] transformation, $(t, x_1, x_2, x_3) \rightarrow (\tau, Z(t, \mathbf{x}), \xi_2, \xi_3)$, with the transformation rules [23]

$$\frac{\partial}{\partial t} = \frac{\partial}{\partial \tau} + \frac{\partial Z}{\partial t}\frac{\partial}{\partial Z} \tag{3.10}$$

$$\frac{\partial}{\partial x_1} = \frac{\partial Z}{\partial x_1}\frac{\partial}{\partial Z} \tag{3.11}$$

$$\frac{\partial}{\partial x_\alpha} = \frac{\partial}{\partial \xi_\alpha} + \frac{\partial Z}{\partial x_\alpha}\frac{\partial}{\partial Z}\,, \quad (\alpha = 2, 3) \tag{3.12}$$

[1] Crocco [117] expressed the temperature in a flat-plate boundary layer as functions of another dependent variable, the velocity.

Introducing this transformation into the governing equations (2.45) and (2.46) and assuming equal diffusivities for all quantities together with $\mathrm{Le}_i = 1$ yields [23]

$$\rho \frac{\partial Y_i}{\partial \tau} = \rho \frac{\chi}{2} \frac{\partial^2 Y_i}{\partial Z^2} + \dot{\omega}_i \tag{3.13}$$

$$\rho \frac{\partial T}{\partial \tau} = \rho \frac{\chi}{2} \frac{\partial^2 T}{\partial Z^2} - \frac{1}{c_\mathrm{p}} \sum_i^{\mathrm{N_s}} h_i \dot{\omega}_i + \rho \frac{\chi}{2c_\mathrm{p}} \left(\sum_i^{\mathrm{N_s}} c_{\mathrm{p},i} \frac{\partial Y_i}{\partial Z} + \frac{\partial c_\mathrm{p}}{\partial Z} \right) \frac{\partial T}{\partial Z} . \tag{3.14}$$

Due to the assumption of thin flame sheets, transport predominantly occurs perpendicular to the surface of stoichiometric mixture. Thus, terms in equations (3.13) and (3.14) that would involve derivatives into the ξ_α directions are of lower order compared to derivatives in the Z direction [22, 23]. Therefore, in equations (3.13) and (3.14) only the leading order terms with respect to Z are kept [23]. In equations (3.13) and (3.14), the scalar dissipation rate χ was introduced as

$$\chi = 2D_Z \left| \nabla Z \right|^2 . \tag{3.15}$$

It is an external parameter that incorporates effects of the three-dimensional flow field and links them to the one-dimensional flamelet equations. Due to its definition it can be regarded as the inverse of a characteristic diffusion time. Since the scalar dissipation rate involves three-dimensional gradient information, it appears as an unclosed term in equations (3.13) and (3.14). Thus, models for χ are required to solve equations (3.13) and (3.14). Among other derivations [118], Peters [23] showed that an analytical expression for $\chi(Z)$ can be derived for a one-dimensional mixing layer. In this case the scalar dissipation rate obeys [27]

$$\chi(Z) = \chi_\mathrm{st} \exp\left\{ 2 \left(\left[\mathrm{erfc}^{-1}(2Z_{st}) \right]^2 - \left[\mathrm{erfc}^{-1}(2Z) \right]^2 \right) \right\}, \tag{3.16}$$

where erfc^{-1} is the inverse error function complement and χ_st is the scalar dissipation rate at stoichiometric conditions. In the steady laminar flamelet model, it is assumed that the thermo-chemical state relaxes to a steady-state sufficiently fast. Hence, the time derivatives in equations (3.13) and (3.14) can be omitted and the flamelet equation reduce to a balance of reaction and diffusion.

3.2.2 Extended flamelet formulation

The classical flamelet concept as developed by Peters [22, 23] was a success story over the last decades. However, despite its success, it poses some limitations regarding the flame physics that can be represented.

For instance, the assumption that all species have diffusivities equal to the thermal diffusivity, i.e. $\mathrm{Le}_i = 1$, may have strong implications on the flame physics [31, 41, 116]. Contemporary after the initial publication of the flamelet model Mauß et al. [29] presented a formulation that accounts for different Le_i, thereby accounting for non-equal species diffusivities. However, the first consistent flamelet model incorporating differential diffusion effects was presented by Pitsch et al. [28]. As stated by the authors, a key point of their formulation is the definition of the mixture fraction

variable as a conserved scalar, which is only determined by the solution of a conservation equation for Z.

A second assumption of the classical flamelet model is that transport predominantly occurs perpendicular to flame sheets, while transport along the sheets (tangential transport) is considered to be of lower order and hence neglected. Already in the early days of the flamelet concept it was well known that curved flame fronts show significantly different physics than their flat counterparts [119–122]. Hence, in some flame configurations curvature-induced effects can appear, which cannot be captured by the classical flamelet approach. Kortschik et al. [44] were the first to overcome this shortcoming of the classical flamelet concept. Studying autoignition in corrugated counterflow mixing fields, they proposed a flamelet formulation including a correction term that explicitly accounts for curvature effects. After the initial publication of Kortschik et al. [44], the interest in extending the flamelet model to account for curvature effects continuously increased over the last years [45–47, 123–127].

Oijen et al. [123] analyzed DNS of a turbulent, stoichiometric and freely expanding spherical methane-air flame kernel. By employing a dimension-reduction technique called the flamelet-generated manifold (FGM) and comparing the FGM results to the DNS, by extracting various flamelets and computing profiles of the relevant variables along these paths, they showed that results differ from the ideal 1D flamelet behavior due to stretch and curvature. Similar to Oijen et al. [123] Verhoeven et al. [124] studied FGM but in the context of non-premixed laminar co-flow flames. Studying the applicability of premixed and non-premixed FGMs, they pointed out that especially near the burner axis significant deviations are observed due to curvature induced tangential diffusion effects. In an attempt to numerically model sooting tendencies, also Xuan and Blanquart [125] confirmed that especially near the flame centerline of a co-flow diffusion flame the classical flamelet model fails to reproduce the correct species profiles. They argued that the observed deviations are due to multi-dimensional convection and diffusion effects and rederived the flamelet equations for species mass fractions along the centerline.

Xu et al. [46] numerically investigated combustion of a single char particle in quiescent and convective environments. The authors performed a three-way comparison of the classical flamelet approach, fully resolved CFD simulations and an extended formulation that considers tangential diffusion effects. A budget analysis of the newly formulated equations revealed that curvature terms become relevant both for cases with unity and non-unity Lewis numbers, especially in the wake region of the particle. Furthermore, they pointed out that, independently of the transport model, only the improved flamelet formulation is able to accurately reproduce the CFD results.

Based on the aforementioned advances of the flamelet theory Scholtissek et al. [47] performed a multi-scale asymptotic scaling and regime analysis to verify the relevance of curvature induced effects. They derived a new set of generalized flamelet equations and proved the consistency to previous works [44–46]. Furthermore, their analysis yields characteristic scaling ratios dependent on the local curvature of the mixture fraction field, the scalar dissipation rate, and the flame thickness, which distinguish whether dominant transport effects are aligned with the flame-normal direction (thus, the mixture fraction gradient that further entails χ), or, if also curvature-induced

flame-tangential effects must be considered[2]. They developed a regime diagram and identified three regimes:

I *classical* flamelet regime,

II *curvature-affected* flamelet regime,

III *multi-dimensional* flamelet regime.

In addition to regime II, where differential diffusion of species and temperature along the flame tangential direction becomes influential, in regime III transport of species and temperature along mixture fraction iso-surfaces becomes relevant. While for regime II one-dimensional flamelet equations could be retained, though the curvature has to be considered as an additional flamelet parameter, in regime III the multi-dimensionality has to be accounted for.

It is one objective of this thesis to analyze the extended flamelet equations proposed by Scholtissek et al. [47] in the framework of a fully turbulent flow. Similar analyses were already performed by Chan et al. [128] and Scholtissek et al. [47]. However, both investigated turbulent flamelets on frozen snapshots of a direct numerical simulation, thereby neglecting transient effects. In this work however, flamelets are tracked in time and space facilitated by an on-the-fly tracking algorithm, which will be described later. Therefor, in this work the flamelet model as formulated by Scholtissek et al. [47] is utilized but reformulated in a Lagrangian manner [127], similar to the approach of Chan et al. [128]. Next, details of the derivation of the extended set of flamelet equations are given.

Curvilinear coordinate system

In order to describe multi-dimensional effects in the framework of the extended flamelet equations a curvilinear coordinate system is required. Similar to the classical flamelet transformation, cf. section 3.2.1, an orthogonal coordinate system (n, ξ_2, ξ_3) is introduced, cf. figure 3.2, that is locally attached to mixture fraction iso-surfaces. As indicated in figure 3.2, this coordinate system is allowed to develop with time, thereby representing a moving reference frame. This definition was similarly used by Cheatham and Matalon [129] for their asymptotic theory of diffusion flames, by Ida and Miksis [130] for their theory on the dynamics of thin films and by Yao and Stewart [131] for their analyses of multi-dimensional detonation dynamics.
The position of a point P in space, cf. figure 3.2 located on the mixture fraction iso-surface is described by a position vector $\mathbf{r}$ with respect to a fixed coordinate system $\mathbf{x} = (x_1, x_2, x_3)$ and time t, hence

$$\mathbf{r} = \mathbf{r}(\mathbf{x}, t)\,. \tag{3.17}$$

[2] Although Z is a conserved passive scalar, cf. equation (3.8), that is uncoupled from the local mixture, it is assumed that an element based Z_{st} still represents a sufficiently good approximation of the flame location [116], such that the terminology "flame-normal" and "flame-tangential" is justified when referring to the mixture fraction iso-surface.

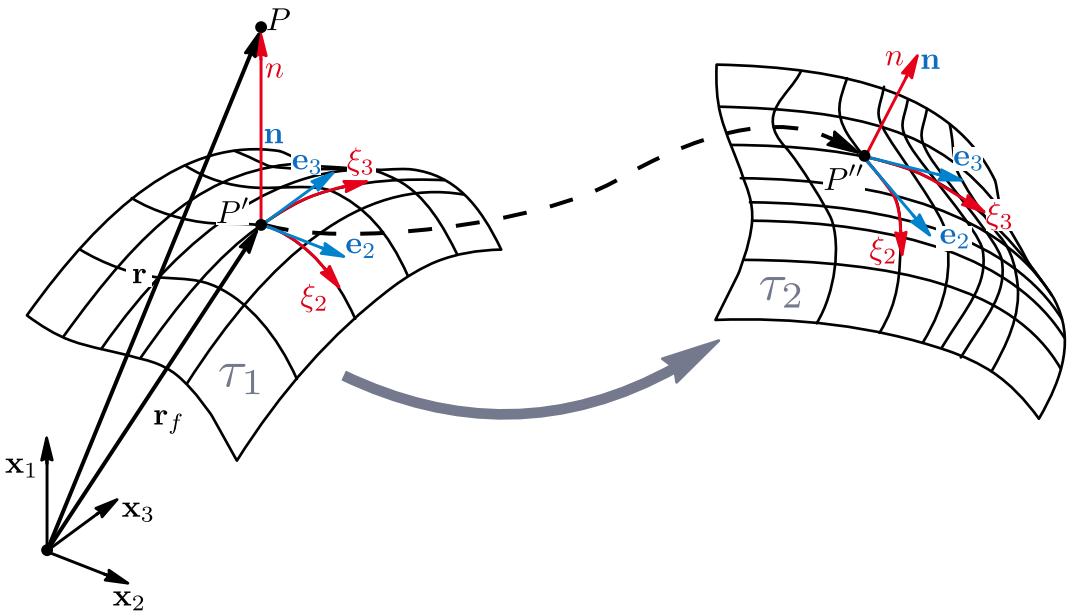

Figure 3.2.: Illustration of the orthogonal coordinate system $n(t,\mathbf{x}), \xi_2(t,\mathbf{x}), \xi_3(t,\mathbf{x})$ attached to the stoichiometric mixture fraction iso-surface. The schematic shows a hypothetical evolution of the surface sheet from Lagrangian time τ_1 to τ_2.

Alternatively the position of P may also be described as the sum of the distance vector $\mathbf{r}_f$ of the projection of P onto the mixture fraction iso-surface, P', and the distance n of P from the iso-surface [129]

$$\mathbf{r} = \mathbf{r}_f(\xi_2, \xi_3, t) + n\mathbf{n}(\xi_2, \xi_3, t)\,. \tag{3.18}$$

Here, $\xi_2(t,\mathbf{x})$ and $\xi_3(t,\mathbf{x})$ are intrinsic surface coordinates that are aligned with the principal directions of curvature at each point of the iso-surface and $\mathbf{n}$ denotes the unit normal vector. In order to ensure orthogonality of the curvilinear coordinate system, vectors $\mathbf{e}_2$ and $\mathbf{e}_3$ are introduced as unit vectors tangential to the parametric curves ξ_2 and ξ_3, hence

$$\mathbf{e}_2 = \frac{1}{a_2}\frac{\partial \mathbf{r}_f}{\partial \xi_2}, \quad \mathbf{e}_3 = \frac{1}{a_3}\frac{\partial \mathbf{r}_f}{\partial \xi_3}, \tag{3.19}$$

(3.20)

with

$$a_2 = \left|\frac{\partial \mathbf{r}_f}{\partial \xi_2}\right|, \quad a_3 = \left|\frac{\partial \mathbf{r}_f}{\partial \xi_3}\right|. \tag{3.21}$$

With this, $\mathbf{n}$, $\mathbf{e}_2$ and $\mathbf{e}_3$ form an orthogonal triad of unit vectors [129], such that

$$\mathbf{n} = \mathbf{e}_2 \times \mathbf{e}_3, \quad \mathbf{e}_2 = \mathbf{n} \times \mathbf{e}_3, \quad \mathbf{e}_3 = \mathbf{n} \times \mathbf{e}_2\,. \tag{3.22}$$

With these definitions, the gradient operator in the moving reference frame takes the form

$$\begin{aligned}\nabla &\rightarrow \mathbf{n}\frac{\partial}{\partial n} + \mathbf{e}_2\frac{1}{h_2}\frac{\partial}{\partial \xi_2} + \mathbf{e}_3\frac{1}{h_3}\frac{\partial}{\partial \xi_3} \\ \nabla &\rightarrow \mathbf{n}\frac{\partial}{\partial n} + \nabla_{\parallel} \\ \nabla &\rightarrow \nabla_{\perp} + \nabla_{\parallel}\,,\end{aligned} \tag{3.23}$$

where the scale factors h_i are expressed in terms of the principal curvatures of the mixture fraction iso-surface κ_i in the directions ξ_i [130]

$$h_2 = \left|\frac{\mathbf{r}}{\xi_2}\right| = a_2 + n\left|\frac{\partial}{\partial \xi_2}\mathbf{n}\right| = a_2 + n a_2 \kappa_2 \tag{3.24}$$

$$h_3 = \left|\frac{\mathbf{r}}{\xi_3}\right| = a_3 + n\left|\frac{\partial}{\partial \xi_3}\mathbf{n}\right| = a_3 + n a_3 \kappa_3\,. \tag{3.25}$$

In order to provide a clear distinction between normal ($\perp$) and tangential ($\parallel$) transport effects for the later following derivation of the flamelet equation in curvilinear coordinates, differential operations that appear in equation (3.23) are marked with their orientation to the mixture fraction iso-surface [126]. In equations (3.24) and (3.25) κ_2 and κ_3 are the principal curvatures of the mixture fraction iso-surface in the ξ_2 and ξ_3 direction, respectively. They are related to the total curvature of the mixture fraction iso-surface by

$$\kappa_Z = \kappa_2 + \kappa_3\,, \tag{3.26}$$

which renders κ_Z to be twice the mean curvature of the surface.

Flamelet transformation in curvilinear coordinates

Flamelet equations are now derived transforming equations (2.45) and (2.46) into mixture fraction space

$$(t, x_1, x_2, x_3) \rightarrow (\tau, Z, \xi_2, \xi_3)\,. \tag{3.27}$$

The coordinate Z is obtained by replacing the normal coordinate n according to $\mathrm{d}Z = |\nabla Z|\,\mathrm{d}n$ and ξ_2 and ξ_3 are curvilinear surface coordinates that span the mixture fraction iso-surface [127], cf. figure 3.2.

In order to find a transformation rule for the temporal derivative, first, a point P' on a mixture fraction iso-surface is considered which at the same time constitutes the origin of the curvilinear coordinate system, cf. figure 3.2. With respect to a fixed frame of reference ($\mathbf{x}_1$,$\mathbf{x}_2$,$\mathbf{x}_3$) this point moves on the surface with a velocity [132]

$$\mathbf{u}_s = \frac{\partial}{\partial \tau}\mathbf{r}_f \tag{3.28}$$

and remains on this iso-surface if the local kinematic condition holds [132, 133], i.e.

$$\frac{\partial}{\partial \tau} Z = \frac{\partial}{\partial t} Z + \mathbf{u}_s \cdot \nabla Z = 0\,, \tag{3.29}$$

where, τ represents the Lagrangian flamelet time. The velocity $\mathbf{u}_s$ is related to the flow velocity by [133, 134]

$$\mathbf{u}_s = \mathbf{u} - s_d \mathbf{n}\,, \tag{3.30}$$

where s_d is the displacement speed of the surface. Considering equation (3.8) together with equation (2.2), relation (3.29) implies

$$s_d = \frac{1}{\rho |\nabla Z|} \nabla \cdot (\rho D_Z \nabla Z)\,. \tag{3.31}$$

Hence, the transformation rules to be applied to an arbitrary scalar quantity ϕ can be formulated as

$$\begin{aligned} \frac{\partial \phi}{\partial t} &= \frac{\partial \phi}{\partial \tau} - \mathbf{u}_s \cdot \nabla \phi = \frac{\partial \phi}{\partial \tau} - (\mathbf{u} - s_d \mathbf{n}) \cdot \nabla \phi \\ &= \frac{\partial \phi}{\partial \tau} - \mathbf{u} \cdot \nabla \phi - \left(\frac{1}{\rho |\nabla Z|} \nabla \cdot (\rho D_Z \nabla Z) + \mathbf{u} \cdot \mathbf{n} - \mathbf{u} \cdot \mathbf{n} \right) \mathbf{n} \cdot \nabla \phi \\ &= \frac{\partial \phi}{\partial \tau} + \frac{\partial Z}{\partial t} \frac{\partial \phi}{\partial Z} - (\mathbf{u} - (\mathbf{u} \cdot \mathbf{n}) \mathbf{n}) \cdot \nabla \phi \end{aligned} \tag{3.32}$$

$$\nabla \phi = \nabla Z \frac{\partial \phi}{\partial Z} + \nabla_{\parallel} \phi\,, \tag{3.33}$$

The last term in equation (3.32) is characteristic for the flamelet transformation applied here and represents the Lagrangian flamelet velocity along the mixture fraction iso-surface. Without this term, the surface attached coordinate system would stay attached at all times, indeed, but would move along the surface with the velocity $\mathbf{u} - (\mathbf{u} \cdot \mathbf{n})\mathbf{n}$ [132]. Hence, the subtraction of this term ensures that the origin of the coordinate system is fixed on the iso-surface. In a previous work of Scholtissek et al. [47] this term was omitted since the time scale was chosen to be aligned with the Eulerian time t. As shall be seen later, transformation (3.32) introduced here allows flamelets to be tracked in time and space which is one essential part of this thesis.
In addition to equation (3.33) also the Laplacian operator, used in the formulation of diffusive transport processes, can be split as

$$\begin{aligned} \nabla^2 \phi = \nabla \cdot (\nabla \phi) &= \nabla \cdot \left(\mathbf{n} \frac{\partial \phi}{\partial n} + \nabla_{\parallel} \phi \right) \\ &= \mathbf{n} \cdot \nabla \left(\frac{\partial \phi}{\partial n} \right) + (\nabla \cdot \mathbf{n}) \frac{\partial \phi}{\partial n} + \nabla \cdot \left(\nabla_{\parallel} \phi \right) \\ &= \nabla_{\perp}^2 \phi - \kappa_Z \frac{\partial \phi}{\partial n} + \nabla \cdot \left(\nabla_{\parallel} \phi \right) \\ &= \nabla_{\perp}^2 \phi + \nabla_{\parallel}^2 \phi\,. \end{aligned} \tag{3.34}$$

where $\nabla^2_\perp \phi$ and $\nabla^2_\parallel \phi$ can be regarded as the diffusion of ϕ in directions normal and tangential to the mixture fraction iso-surfaces, respectively, and the curvature κ_Z is introduced as

$$\kappa_Z = -\nabla \cdot \mathbf{n} = -\nabla \cdot \frac{\nabla Z}{|\nabla Z|} = -\frac{\nabla^2 Z - \mathbf{n} \cdot \nabla(|\nabla Z|)}{|\nabla Z|} = -\frac{\nabla^2 Z - \mathbf{n} \cdot \nabla(\mathbf{n} \cdot \nabla Z)}{|\nabla Z|}. \tag{3.35}$$

According to equation (3.34), $\nabla^2_\perp \phi$ and $\nabla^2_\parallel \phi$ are defined as [127]

$$\nabla^2_\perp \phi = \mathbf{n} \cdot \nabla (\mathbf{n} \cdot \nabla \phi), \tag{3.36}$$

$$\nabla^2_\parallel \phi = \Gamma_\phi - \kappa_Z \frac{\partial \phi}{\partial n}, \tag{3.37}$$

where Γ_ϕ denotes a multi-dimensional term that is interpreted as transport along iso-surfaces of Z. Comparing equations (3.34) and (3.37) it is defined as

$$\begin{aligned} \Gamma_\phi &= \nabla \cdot (\nabla_\parallel \phi) = \nabla \cdot (\nabla \phi - \nabla_\perp \phi) \\ &= \nabla \cdot \left(\nabla \phi - \nabla Z \frac{\partial \phi}{\partial Z} \right). \end{aligned} \tag{3.38}$$

Scholtissek et al. [47] discussed the relation of Γ_ϕ to second derivatives of the scalar ϕ with respect to the coordinates ξ_2 and ξ_3. Hence, from their explanations it follows

$$\Gamma_\phi = \nabla \cdot (\nabla_\parallel \phi) = \frac{\partial^2 \phi}{\partial \xi_2^2} + \frac{\partial^2 \phi}{\partial \xi_3^2}. \tag{3.39}$$

From a computational point of view, however, it is advantageous to express the multi-dimensional diffusion term as

$$\begin{aligned} \Gamma_\phi = \nabla \cdot (\nabla_\parallel \phi) &= \nabla^2 \phi - \frac{\nabla Z}{|\nabla Z|} \cdot \nabla \left(\frac{\nabla Z}{|\nabla Z|} \cdot \nabla \phi \right) + \kappa_Z \frac{\nabla Z}{|\nabla Z|} \cdot \nabla \phi \\ &= \nabla^2 \phi + \frac{\nabla Z}{|\nabla Z|} \cdot \left(\kappa_Z \nabla \phi - \nabla \left(\frac{\nabla Z}{|\nabla Z|} \cdot \nabla \phi \right) \right), \end{aligned} \tag{3.40}$$

which in principal is a reformulation of equation (3.34). This way, derivatives can be directly computed in Cartesian space, thereby avoiding explicit computations in the curvilinear coordinate system.

In this section, the above expressions are used to formulate a flamelet model that explicitly includes both normal and tangential transport contributions. In order to maintain readability of the transformed equations, terms are grouped according to their physical effect [127], i.e.

$$\rho \frac{\partial \phi}{\partial \tau} = \Lambda^{\phi}_{trans} = \Lambda^{\phi}_{\mathrm{norm}} + \Lambda^{\phi}_{\mathrm{MD}} + \Lambda^{\phi}_{curv} + \Lambda^{\phi}_{src}\,, \tag{3.41}$$

where Λ^{ϕ}_{trans} denotes the transient term, Λ^{ϕ}_{src} the source term, $\Lambda^{\phi}_{\mathrm{norm}}$ accounts for flame-normal transport, and the flame-tangential transport is captured by $\Lambda^{\phi}_{\mathrm{MD}}$ and Λ^{ϕ}_{curv}, which represent multi-dimensional and curvature effects, respectively.
Introducing the transformations (3.32) to (3.34) to equation (2.45), the identities of the individual terms for the flamelet equation for the temperature T read

$$\begin{aligned}\Lambda^{T}_{\mathrm{norm}} = {} & \frac{\rho\chi}{2}\mathrm{Le}_Z \frac{\partial^2 T}{\partial Z^2} + \frac{\rho\chi}{2}\frac{\mathrm{Le}_Z}{c_p}\frac{\partial c_p}{\partial Z}\frac{\partial T}{\partial Z} + \frac{\rho\chi}{2c_p}\sum_{k=1}^{n}\frac{\mathrm{Le}_Z}{\mathrm{Le}_k}\left(\frac{\partial Y_k}{\partial Z} + \frac{Y_k}{\langle W\rangle}\frac{\partial \langle W\rangle}{\partial Z}\right)(c_{p,k}-c_p)\frac{\partial T}{\partial Z} \\ & + \frac{1}{4}\left[2\rho\chi\frac{\partial \mathrm{Le}_Z}{\partial Z} + (\mathrm{Le}_Z - 1)\left(\frac{\partial(\rho\chi)}{\partial Z} + \frac{\chi}{D_Z}\frac{\partial(\rho D_Z)}{\partial Z}\right)\right]\frac{\partial T}{\partial Z}\,,\end{aligned} \tag{3.42}$$

$$\Lambda^{T}_{\mathrm{MD}} = \mathrm{Le}_Z\,\rho D_Z\,\Gamma_T\,, \tag{3.43}$$

$$\Lambda^{T}_{curv} = (\mathrm{Le}_Z - 1)\,\rho\kappa_Z\sqrt{\frac{\chi D_Z}{2}}\frac{\partial T}{\partial Z}\,, \tag{3.44}$$

$$\Lambda^{T}_{src} = -\sum_{k=1}^{n}\frac{h_k}{c_p}\dot{\omega}_k\,. \tag{3.45}$$

It is emphasized that in case $\mathrm{Le}_Z = 1$, hence mixture fraction diffuses at the rate of heat, the curvature term Λ^{T}_{curv} vanishes in the temperature equation and only the curvature-induced multi-dimensional term remains, accounting for flame-tangential transport.
Using equations (3.32) to (3.34) to transform equation (2.46), the identities of the individual terms of the flamelet equation for the species mass fraction Y_i reads

$$\Lambda^{Y}_{src} = \dot{\omega}_i\,, \tag{3.46}$$

$$\Lambda^{Y}_{\mathrm{MD}} = \rho D_Z\frac{\mathrm{Le}_Z}{\mathrm{Le}_i}\Gamma_{Y_i} - \rho D_Z Y_i\sum_{k=1}^{n}\frac{\mathrm{Le}_Z}{\mathrm{Le}_k}\Gamma_{Y_k}\,, \tag{3.47}$$

$$\begin{aligned}\Lambda^{Y}_{curv} = {} & -\rho\kappa_Z\sqrt{\frac{\chi D_Z}{2}}\left[\left(\frac{\mathrm{Le}_Z}{\mathrm{Le}_i} - 1\right)\frac{\partial Y_i}{\partial Z} + \frac{\mathrm{Le}_Z}{\mathrm{Le}_i}\frac{Y_i}{\langle W\rangle}\frac{\partial \langle W\rangle}{\partial Z}\right. \\ & \left. + \rho\kappa_Z\sqrt{\frac{\chi D_Z}{2}}Y_i\sum_{k=1}^{n}\left(\frac{\mathrm{Le}_Z}{\mathrm{Le}_k}\frac{\partial Y_k}{\partial Z} + \frac{\mathrm{Le}_Z}{\mathrm{Le}_k}\frac{Y_k}{\langle W\rangle}\frac{\partial \langle W\rangle}{\partial Z}\right)\right],\end{aligned} \tag{3.48}$$

$$
\begin{aligned}
\Lambda^{Y}_{norm} = {} & \frac{\rho\chi}{2}\frac{\mathrm{Le}_Z}{\mathrm{Le}_i}\frac{\partial^2 Y_i}{\partial Z^2} + \frac{\rho\chi}{2}\frac{\mathrm{Le}_Z}{\mathrm{Le}_i}\frac{Y_i}{\langle W\rangle}\frac{\partial^2\langle W\rangle}{\partial Z^2} - \frac{\rho\chi}{2}Y_i\sum_{k=1}^{n}\left(\frac{\mathrm{Le}_Z}{\mathrm{Le}_k}\frac{\partial^2 Y_k}{\partial Z^2} + \frac{\mathrm{Le}_Z}{\mathrm{Le}_k}\frac{Y_k}{\langle W\rangle}\frac{\partial^2\langle W\rangle}{\partial Z^2}\right) \\
& + \frac{1}{4}\left[2\rho\chi\frac{\partial}{\partial Z}\left(\frac{\mathrm{Le}_Z}{\mathrm{Le}_i}\right) + \left(\frac{\mathrm{Le}_Z}{\mathrm{Le}_i} - 1\right)\left(\frac{\partial(\rho\chi)}{\partial Z} + \frac{\chi}{D_Z}\frac{\partial(\rho D_Z)}{\partial Z}\right)\right]\frac{\partial Y_i}{\partial Z} \\
& + \frac{1}{4}\left[2\rho\chi\frac{Y_i}{\langle W\rangle}\frac{\partial}{\partial Z}\left(\frac{\mathrm{Le}_Z}{\mathrm{Le}_i}\right) + \frac{\mathrm{Le}_Z}{\mathrm{Le}_i}\left(\frac{\partial}{\partial Z}\left(\rho\chi\frac{Y_i}{\langle W\rangle}\right) + \frac{\chi}{D_Z}\frac{\partial}{\partial Z}\left(\rho D_Z\frac{Y_i}{\langle W\rangle}\right)\right)\right]\frac{\partial\langle W\rangle}{\partial Z} \\
& - \frac{1}{4}\sum_{k=1}^{n}\left[2\rho\chi Y_i\frac{\partial}{\partial Z}\left(\frac{\mathrm{Le}_Z}{\mathrm{Le}_k}\right) + \frac{\mathrm{Le}_Z}{\mathrm{Le}_k}\left(\frac{\partial}{\partial Z}(\rho\chi Y_i) + \frac{\chi}{D_Z}\frac{\partial}{\partial Z}(\rho D_Z Y_i)\right)\right]\frac{\partial Y_k}{\partial Z} \\
& - \frac{1}{4}\sum_{k=1}^{n}\left[2\rho\chi Y_i\frac{Y_k}{\langle W\rangle}\frac{\partial}{\partial Z}\left(\frac{\mathrm{Le}_Z}{\mathrm{Le}_k}\right) + \frac{\mathrm{Le}_Z}{\mathrm{Le}_k}\left(\frac{\partial}{\partial Z}\left(\rho\chi Y_i\frac{Y_k}{\langle W\rangle}\right)\right.\right. \\
& \left.\left. + \frac{\chi}{D_Z}\frac{\partial}{\partial Z}\left(\rho D_Z Y_i\frac{Y_k}{\langle W\rangle}\right)\right)\right]\frac{\partial\langle W\rangle}{\partial Z}\,. \qquad (3.49)
\end{aligned}
$$

Comparing the above relations to the flamelet model that was presented by Scholtissek et al. [47] differences appear in the formulation of the normal transport terms, i.e. equations (3.42) and (3.49) and the source term of the temperature equation, i.e. equation (3.45). While in the formulation of Scholtissek et al. [47] temporal changes of the thermodynamic pressure are allowed ($\partial p/\partial\tau$), they are omitted here since in the low-Mach number analyses performed in this work, the thermodynamic pressure is considered as a constant background pressure and only fluid-dynamic perturbations are allowed, cf. section 2.3. Regarding the differences appearing in the $\Lambda^{(T|Y_i)}_{\mathrm{norm}}$ terms, Scholtissek et al. [47] neglected the gradient of the mean molecular mass, which has to be considered for diffusion models other than the unity-Lewis number model, since

$$
\mathbf{V}^{\mathbf{D},\mathbf{i}} = -\frac{D_{i,m}}{X_i}\nabla X_i = -\frac{D_{i,m}}{Y_i}\nabla Y_i - \frac{D_{i,m}}{\langle W\rangle}\nabla\langle W\rangle\,. \qquad (3.50)
$$

Furthermore, as pointed out earlier, Scholtissek et al. [47] aligned their time coordinate with the Eulerian time frame, which led to additional convective terms acting along the surface coordinates ξ_2 and ξ_3. As outlined in the previous section this form of convection is explicitly inhibited here because the coordinate system has to be fixed on the surface to facilitate the analyses presented later.

Characteristic scaling ratios

Inspecting the flamelet equations, presented in the previous section, there exist no conclusive evidence whether curvature induced transport effects are just a matter of rigorously transforming the governing equations or if they are actually important for flamelet modeling. In order to assess the impact of curvature induced transport effects, Scholtissek et al. [47] derived two asymptotic scaling ratios which in turn are based on three flame intrinsic length scales. These characteristic length scales are defined by [47]

$$
l_{\mathrm{m}} = \frac{\Delta Z}{|\nabla Z|_{p'}} \qquad (3.51)
$$

$$l_\chi = \frac{(\Delta Z)_\mathrm{R}}{|\nabla Z|_{P'}} \tag{3.52}$$

$$l_\kappa = \frac{1}{|\kappa_Z|_{P'}} \tag{3.53}$$

where l_m represents a mixing length [31], l_χ denotes a length scale related to the reaction zone thickness [19] and l_κ is a curvature related length scale [47]. In these definitions, the suffix $(\bullet)_{P'}$ refers to a point in the reaction zone, $(\Delta Z)_\mathrm{R}$ is the reaction zone thickness in mixture fraction space and ΔZ is the difference between the minimum and maximum value of Z of the corresponding flamelet. It is important to point out that, unlike in Scholtissek et al. [47], ΔZ is explicitly accounted for in the later following analyses since in turbulent flames individual flamelets generally do not span the whole range between $Z = 0$ and $Z = 1$. The reaction zone thickness $(\Delta Z)_\mathrm{R}$ can be estimated by [127]

$$(\Delta Z)_\mathrm{R} = \sqrt{\frac{\phi_\mathrm{max}}{\max(|\frac{\partial^2 \phi}{\partial Z^2}|)_\mathrm{R}}}, \tag{3.54}$$

where $\max(\bullet)_\mathrm{R}$ defines the maximum of the enclosed scalar quantity in the reaction zone. It is pointed out that the deductions drawn with the help of $(\Delta Z)_\mathrm{R}$ are sensitive to the chosen reference value ϕ [47]. To capture all influences of tangential diffusion on the overall flame structure, a rather conservative measure for $(\Delta Z)_\mathrm{R}$ is needed [47]. This is achieved by choosing a quantity that changes on the scale of the overall flame thickness and exists in multiple reaction-diffusion layers throughout the flame, e.g. the temperature or CO mass fraction.
The above relations are used to define two small parameters

$$\varepsilon = \frac{l_\chi}{l_\mathrm{m}} = \frac{(\Delta Z)_\mathrm{R}}{\Delta Z} \tag{3.55}$$

$$\nu = \frac{l_\kappa}{l_\mathrm{m}} = \frac{|\nabla Z|_{P'}}{\Delta Z\,|\kappa_Z|_{P'}}, \tag{3.56}$$

Based on these parameters two asymptotic scaling ratios, which determine whether multi-dimensional effects have to be considered in the flamelet equations, are derived [127]

$$\frac{\varepsilon}{\nu} = \frac{(\Delta Z)_R |\kappa_Z|_{P'}}{|\nabla Z|^2_{P'}} = (\Delta Z)_\mathrm{R} |\kappa_Z|_{P'} \sqrt{\frac{2D_Z}{\chi}}, \tag{3.57}$$

$$\frac{\varepsilon^3}{\nu^2} = \frac{(\Delta Z)^3_R |\kappa_Z|^2_{P'}}{|\nabla Z|_{P'}} = \frac{2(\Delta Z)^3_\mathrm{R} |\kappa_Z|^2_{P'} D_Z}{\chi \Delta Z}. \tag{3.58}$$

First, from the size of the characteristic ratio (3.57) two distinct limits can be deduced [47]. In case it is smaller than unity, the classical flamelet is sufficient to describe the flame physics since either the reaction zone thickness in mixture fraction space, $(\Delta Z)_\mathrm{R}$, or the curvature of the flame tend to zero. On the other hand for $\varepsilon/\nu > 1$, the considered flamelet is affected by curvature and the second ratio can be used to assess the impact of multi-dimensional diffusion. In case both ratios are larger than unity, both multi-dimensional and curvature-based effects influence the reaction zone of

Table 3.1.: The three flamelet regimes identified by Scholtissek et al. [47] for the extended flamelet model with differential diffusion ($\mathrm{Le}_i \neq 1$).

	regime	distinguished limit
Regime I	classical flamelet regime	$\varepsilon < \nu$
Regime II	curvature-affected flamelet regime	$\varepsilon > \nu$, $\varepsilon^3 < \nu^2$
Regime III	multi-dimensional flamelet regime	$\varepsilon > \nu$, $\varepsilon^3 > \nu^2$

the non-premixed flamelet. A summary of these asymptotic distinguished limits is given in table 3.1. In chapter 5 these regime classifications are used as a diagnostic tool for the analysis of flamelets that have been tracked on-the-fly in a turbulent reactive non-premixed jet flame.

4 Direct numerical simulation of turbulent reactive flows

The history of direct numerical simulation (DNS) began in the early 1970s with the pioneering work of Orszag and Patterson [135]. They demonstrated that it is possible to perform computer simulations of a fully developed turbulent flow without relying on any turbulence model to parameterize the influence of the turbulent eddies. The (direct) numerical solutions to the governing equations are correct to the accuracy of the embedded numerical methods [51]. DNS yields first-principal solutions free from turbulence modeling errors such that, with careful implementation of robust high-fidelity numerical methods, it serves as a valuable tool for the investigation of fluid dynamical problems. A comprehensive review of the contributions made by DNS studies to the understanding of turbulence and turbulent flows is given by Moin and Mahesh [136]. Comparing DNS with RANS or LES, it is the simplest approach, unrivalled in accuracy and in the level of detail provided [137]. DNS allows for detailed investigations of the multi-physics and multi-scale problems arising in turbulent reactive flows.

However, this accuracy comes at the expense of extremly high computational costs and the requirements increase so rapidly with the Reynolds number, such that the applicability of DNS is limited to flows of low to moderate Reynoldes numbers. The computational cost of a DNS is largely determined by the resolution requirements. A suitable resolution is given when the scales of turbulence are well-resolved and the largest and smallest eddies are captured by the numerical grid. For example, assuming that material properties are constant and that the computational domain is a cube of size L which is discretized such that the isotropic mesh has a spacing of Δx, the size of the computational domain must be large enough to represent the integral scales l_t of the flow ($L > l_t$) and the grid spacing must be small enough to resolve the smallest scales, connected to the Kolmogorov length scale η. Given the mean of the energy dissipation $\langle \epsilon \rangle$ and the mean of the viscosity $\langle \nu \rangle$, the Kolmogorov scales for length η, velocity u_η and time τ_η are given by [9]

$$\eta = \left(\frac{\langle \nu \rangle^3}{\langle \epsilon \rangle} \right)^{1/4} \tag{4.1}$$

$$u_\eta = \left(\langle \epsilon \rangle \langle \nu \rangle \right)^{1/4} \tag{4.2}$$

$$\tau_\eta = \left(\frac{\langle \nu \rangle}{\langle \epsilon \rangle} \right)^{1/2}. \tag{4.3}$$

Combining the previous expressions leads to an estimate for the number of grid points N required to resolve the DNS

$$\frac{l_t}{\eta} < N, \quad \frac{l_t}{\eta} = \frac{l_t}{(\nu^3/\epsilon)^{1/4}} = \mathrm{Re}_t^{3/4}, \quad \Rightarrow \quad N^3 > \mathrm{Re}_t^{9/4} \tag{4.4}$$

where Re is the Reynolds number [138], based on reference quantities $(\bullet)_{ref}$

$$\mathrm{Re} = \frac{u_{ref} L_{ref}}{\nu} . \tag{4.5}$$

The Reynolds number is a dimensionless quantity, often used to predict flow patterns in different fluid flow situations. The inequalities presented in equation (4.4) underline the enormeous computational costs of direct numerical simulation, since only a small increase in the Reynolds number leads to a tremendeous increase in the number of grid points required to resolve a three dimensional simulation. Besides the computational costs, a great challenge related to DNS studies is the development of stable, accurate and efficient numerical methods, especially for reactive flows, where due to chemical reactions an additional treatment of terms exhibiting large numerical stiffness is necessary.

In this work, direct numerical simulation serves as a tool to provide a highly resolved database of a temporally evolving jet flame which builds the foundation of the later following flamelet-based analyses. The chapter is structured as follows; first the high-fidelity DNS code *DINO* is described including details about the spatial discretization, temporal integration, the pressure velocity coupling and its parallel efficiency. Second a detailed description of the numerical simulation that has been conducted is presented including a description of the general setup, the initialization of all important quantities and finally results of the simulation are discussed.

4.1 DNS code DINO

In this work, all simulations were conducted with the direct numerical simulation (DNS) code *DINO* [139, 140]. The code is actively beeing developed by both the Institute of Fluid Dynamics and Thermodynamics at the Otto-von-Guericke University in Magdeburg and the Chair of Simulation of reactive Thermo-Fluid Systems at TU Darmstadt. The development began in 2013 as part of the Ph.D. of Abdelsamie [140] who at the same time is the main developer of the code. The goal behind theses collaborative efforts is to develop a multi-purpose DNS solver which is suitable for the simulation of low-Mach number reactive [126, 141–144] and non-reactive [145] as well as medical flows [146]. A working copy of *DINO* can be obtained on request by contacting the group of Prof. Thévenin at the Otto von Guericke University Magdeburg. As of November 2017, 7 groups from 5 different countries are already using *DINO* for their research.
Among many different submodules of the code, Abdelsamie [140] developed the core of the code including the implementation of the right-hand sides of equations (2.44) to (2.46), the finite differences and the pressure solver. Details about the core can be found in [140] and only key aspects will be recapitulated here. In addition, two newly implemented solvers are presented in conjunction with an approach to include analytical Jacobians within *DINO* and to ensure an optimal computation of chemical source terms. The section closes with a strong and weak scaling analysis of the newly implemented solvers.

Table 4.1.: Finite difference weights for first and second derivatives used in DINO [139]. Note, the values listed in the table should be divided by Δx^m, where Δx denotes the uniform grid spacing.

	order	weights α_i at grid point						
		x_{i-3}	x_{i-2}	x_{i-1}	x_i	x_{i+1}	x_{i+2}	x_{i+3}
$m=1$		Interior						
	6th	-1/60	3/20	-3/4	0	3/4	-3/20	1/60
		Boundary						
	5th	–	1/20	-1/2	-1/3	1	-1/4	1/30
	4th	–	–	-1/4	-10/12	3/2	-1/2	1/12
	3rd	–	–	–	-11/6	3	-3/2	1/3
$m=2$		Interior						
	6th	1/90	-3/20	3/2	-49/18	3/2	-3/20	1/90
		Boundary						
	3rd	–	-1/12	16/12	-30/12	16/12	-1/12	–
	3rd	–	–	11/12	-20/12	1/2	1/3	-1/12
	2nd	–	–	–	2	-5	4	-1

4.1.1 Spatial discretization - finite differences

For a uniform computational mesh, spatial derivatives are approximated by finite differences [147–149]

$$\left.\frac{\partial^m \phi}{\partial x^m}\right|_{x=x_i} \approx \frac{1}{\Delta x^m} \sum_{i=0}^{n} \alpha_{n,i}^m \phi_i \,, \tag{4.6}$$

where the discrete derivative at grid point x_i is described as a sum of weights α_i and discrete function values ϕ_i. The order of the derivative is denoted by m and Δx is the spacing of the computational mesh. In the interior of the simulation domain, sixth-order central finite differences are used. Towards domain boundaries, the order of finite differences is successively reduced down to third order to avoid numerical fluctuations. The corresponding coefficients used for the finite differences according to equation (4.6) are listed in table 4.1 [148].
The algorithm used for the computation of these weights was developed by [148] and examplary implementations are given in [147] and [150]. A detailed verification of the implementation in *DINO* and the achieved spatial accuracy is given in [139, 140].

4.1.2 Runge-Kutta time integration

Runge-Kutta (RK) time integration methods are widely accepted in the combustion community and have been employed in a variety of different DNS Codes during the last decades, e.g. *S3D* [151, 152], *SENGA* [153], *Parcomb* [58, 154, 155] and *DINO* [139]. The implemented schemes usually have an order of three to four, possess the low-storage property [156] and are explicit in nature. On the one hand fully explicit schemes have the advantage to be ideally parallelizable because they

require only a minimum of parallel communication. On the other hand they are limited to very small timesteps ($\mathcal{O}(10^{-9})$s) in order to cope with the numerical stiffness arising from the variety of different time scales of the chemical species. Usually for compressible combustion codes [151–154] this does not impose a severe limitation since they have to resolve acoustic (small) time scales anyway. However, for low-Mach number combustion simulation frameworks, like *DINO* [139], *Yales2* [157, 158], *AVBP* [159] and *NGA* [160] acoustic time scale restrictions do not apply and the feasible timestep is limited by combustion only. Therefore, semi-implicit time integration strategies are often used for low-Mach number combustion to achieve a computational speedup. Practical implementations of these methods include fractional-step schemes or additive semi-implicit schemes. In the fractional-step approach, also called timestep splitting or operator splitting, the individual types of processes are solved independently, and the changes resulting from the separate partial calculations are coupled (added) together [60]. These methods offer great flexibility in the choice of which algorithms are used to solve each type of process. However, for practical implementations the temporal accuracy is limited to second-order at most [161–163].
On the contrary, higher orders of accuracy can be "easily" achieved with additive semi-implicit methods, which solve the individual types of processes simultaneously. One important family of these methods are semi-implicit RK methods [164–167].

One aspect of this work is to extend the family of solvers implemented in *DINO* [139] by a low-storage semi-implicit Runge-Kutta (LSSIRK) [165, 168] scheme and a low-storage explicit Runge-Kutta (LSERK) [169, 170] scheme. In contrast to the already implemented explicit Runge-Kutta (ERK) [171] and semi-implicit Runge-Kutta (SIRK) solvers [164] both solvers require only 2N storage locations. This in turn significantly reduces the required memory per processor, which is an important computational resource for the large-scale direct numerical simulations conducted in this work. The technique of leaving useful information in the storage locations was already exploited in early works by Gill [172] and Blum [173] for a single fourth-order RK scheme. Later it was shown by Fyfe [156] and Williamson [174] that their ideas could be generalized leading to several new low-storage numerical integration schemes [165, 169, 175–178].
In the following, details about the newly implemented Runge-Kutta solvers are presented. While the LSERK scheme was used for cold-flow simulations, to verify the overall turbulent flow setup, the LSSIRK scheme was employed for the final simulation of a reactive flow, presented later in this chapter.

The general approach during the numerical integration is to first approximate the spatial derivatives appearing in the governing equations by finite differences, see section 4.1.1. This leads to a system of first-order ordinary differential equations

$$\frac{\partial}{\partial t}\mathbf{u} = F(\mathbf{u})\,. \tag{4.7}$$

Depending on the stiffness of the underlying physical problem, the right-hand side operator F is treated explicitly or implicitly.

Table 4.2.: Weights of the fourth-order five-stage explicit Runge-Kutta scheme [169, 170].

	coefficients		
i	α	β	γ
1	0	0	0.1496590219993
2	0.1496590219993	-0.4178904745	0.3792103129999
3	0.3704009573644	-1.192151694643	0.8229550293869
4	0.6222557631345	-1.697784692471	0.6994504559488
5	0.9582821306748	-1.514183444257	0.1530572479681

Explicit Runge-Kutta

In case of cold-flow simulations, used to verify the overall turbulent flow setup, the governing equations are considerd as non-stiff and the integration is performed by an explicit fourth-order five-stage RK scheme (LSERK4(5)). The general approach how the low-storage property can be achieved for conventional RK schemes is outlined in [169] and is just shown for the sake of completeness. An r-stage explicit RK algorithm reads

$$t^i = t^{i-1} + \alpha^i \Delta t \tag{4.8}$$

$$t^{i+1} = t^{i-1} + \alpha^{i+1} \Delta t \tag{4.9}$$

$$\mathbf{k}^i = \beta^i \mathbf{k}^{i-1} + \Delta t F(\mathbf{u}^i) \tag{4.10}$$

$$\mathbf{u}^i = \mathbf{u}^{i-1} + \gamma^i \mathbf{k}^i \qquad (i = 1, \cdots, r), \tag{4.11}$$

where t^i is the physical time at stage i. The symbols $\mathbf{u}$ and $\mathbf{k}$ denote the two storage locations and store the solution and right-hand side, respectively . The numerical time step is denoted by Δt. Further details about a proper choice of Δt are given in section 4.1.4. The corresponding coefficients $\alpha^i, \beta^i, \gamma^i$ that were used for the implementation are given in table 4.2. A verification of the implementation in *DINO* is presented in appendix B.1.

Semi-implicit Runge-Kutta

In case of the reacting flow DNS, analyzed later in this work, the governing equations of temperature and species mass fractions are considerd as stiff and the integration is performed by a semi-implicit third-order three-stage RK scheme (LSSIRK3(3)) [165]. In the semi-implicit discretization approach, the right-hand side of equation (4.7) is additively split into non-stiff terms $f(\mathbf{u})$ and stiff terms $g(\mathbf{u})$

$$\frac{\partial}{\partial t}\mathbf{u} = f(\mathbf{u}) + g(\mathbf{u}), \tag{4.12}$$

Table 4.3.: Weights of the third-order low-storage semi-implicit Runge-Kutta scheme [165].

	coefficients				
i	α	β	γ	δ	$\tilde{\delta}$
1	0	0	1/3	0	2.267596813284564
2	1/3	−5/9	15/16	−1.143097033946135	2.685297589634163
3	3/4	−153/128	8/15	−2.031219208388789	2.309749357551431
4	1	–	–	–	–

where $\mathbf{u}$ is the vector of variables exhibiting a stiff right-hand side, i. e. $\mathbf{u} = (T, Y_1, Y_2, \cdots, Y_{\mathrm{N_s}})$. During each stage i of the r-stage RK method the following linear system has to be solved [165]

$$\mathbf{A}^i\mathbf{k}^i = \Delta t\left[f(\mathbf{u}^{i-1}) + g(\mathbf{u}^{i-1} + \tilde{\delta}^i\mathbf{k}^{i-1})\right] + \beta^i\mathbf{A}^i\mathbf{k}^{i-1} \qquad (i = 1, \cdots, r) \tag{4.13}$$

where the system matrix $\mathbf{A}^i$ is defined through

$$\mathbf{A}^i = \left[\mathcal{I} - \Delta t\,\delta^i\mathbf{J}(\mathbf{u}^{i-1} + \tilde{\delta}^i\mathbf{k}^{i-1})\right]. \tag{4.14}$$

Here, $\mathcal{I}$ is the identity matrix and $\mathbf{J} = \partial g(\mathbf{u})/\partial\mathbf{u}$ is the chemical Jacobian matrix. The coefficients $\alpha, \beta, \gamma, \delta, \tilde{\delta}$ required during the integration were derived by Yoh and Zhong [165] and are given in table 4.3. Since stiffness is primarily induced by chemistry, only the Jacobian of the chemical source term is evaluated, and the other terms are treated explicitly. Also the integration of the momentum equation, cf. equation (2.8), is done explicitely. Finally, after solving the linear system (4.13) (for $\mathbf{k}^i$), the solution is advanced to an intermediate time level i by equation (4.11), where the time at level i and $i+1$ is given by equations (4.8) and (4.9), respectively. A verification of the solver is presented in appendix B.2.

4.1.3 Evaluation of the Jacobian matrix and chemical kinetics

The semi-implicit algorithm described above requires the computation of the Jacobian matrix $\mathbf{J}$ of the chemical source term. The evaluation of the Jacobian can be performed either numerically or analytically. In *DINO* the standard way of evaluating $\mathbf{J}$ is numerically by forward finite differences

$$J_{i,j} = \frac{\partial g_i}{\partial \Phi_j} \approx \frac{g_i(\Phi_j + \delta_j) - g_i(\Phi_j)}{\delta_j}, \tag{4.15}$$

where δ_j represents a small increment. This approach is expensive due to repeated evaluations of chemical source terms, scales quadratically with the number of species and reactions ($\mathrm{N_s} \cdot \mathrm{N_r}$) and dominates the computational costs even for small to moderate-sized mechanisms [110]. On the other hand, as stated by Lu and Law [110], evaluation of the analytic Jacobian for the species chemical source term is less expensive. Therefore, in this work the capabilities of computing Jacobian matrices were extended in *DINO* by coupling it to the analytical Jacobian generator

pyJac [111, 179]. PyJac is capable of generating subroutines for the computation of species production rates, thermodynamical expressions and analytical chemical Jacobian matrices both for CPU operation via C/C++ and GPU operation via CUDA [180]. These subroutines are then directly compiled into *DINO* and are accessed via the interface described in appendix C.1. Detailed explanations how to compute the different entries of the Jacobian matrix are given in [111, 181, 182] and the correctness and the general computational performance of the generated code for various mechanisms is demonstrated in [111, 183]. It turns out that for the setup considered here, see section 4.2 for details, the utilization of *pyJac* leads to an overall speedup of the simulation by a factor of two compared to the standard approach implemented in *DINO* . This speedup is not only the result of using *pyJac* for the evaluation of the chemical Jacobian but also using it for the computation of chemical source terms $\dot{\omega}_i$ and thermodynamic quantities like $c_{\mathrm{p},i}$ and h_i, which is a novelty related to this work.

4.1.4 Numerical timestep

In *DINO* the maximum feasible time step is estimated based on time scales of advective and diffusive processes. For advective processes the Courant-Friedrich-Lewy (CFL) condition [184] states that information can only travel a fraction of the grid size Δx in one time step Δt. For a n-dimensional low-Mach number simulation it is expressed by

$$\Delta t_{\mathrm{adv}} \leq \mathrm{CFL}_{\mathrm{lim}}^{\mathrm{adv}} \cdot \left(\sum_{i=1}^{n} \frac{|u_i|}{\Delta x_i} \right)^{-1} , \tag{4.16}$$

where $\mathrm{CFL}_{\mathrm{lim}}^{\mathrm{adv}}$ denotes a limiting, problem dependent constant. In contrast to a fully-compressible formulation, where also the local speed of sound has to be considered through $(|u_i| + c)/\Delta x_i$, the low-Mach number approach allows for significantly higher advective timesteps and thereby the overall computing time is significantly reduced.
In diffusively controlled regimes, however, the time step is restricted by

$$\Delta t_{\mathrm{diff}} \leq \mathrm{CFL}_{\mathrm{lim}}^{\mathrm{diff}} \cdot \left(\frac{\max[D_i, \nu, \alpha]}{\min[\Delta x^2]} \right)^{-1} . \tag{4.17}$$

In equation (4.17) $\alpha = \lambda/(\rho c_{\mathrm{p}})$ denotes the thermal diffusivity, ν the kinematic viscosity and D_i is the diffusion coefficient of species i. The final timestep that is taken by the numerical scheme is

$$\Delta t = \min[\Delta t_{\mathrm{adv}}, \Delta t_{\mathrm{diff}}] \tag{4.18}$$

4.1.5 Coupling of pressure and velocity

Due to the low-Mach number approximation, acoustic waves are neglected and the coupling between fluctuating pressure and density is suppressed. Therefore, a specific procedure is required

to determine the hydrodynamic pressure. In the *DINO* code, a pressure free projection method [185–187] is applied, which leads to solve equation (2.38) in two consecutive steps.
At each Runge-Kutta stage, starting from the known momentum value at step n, considering a constant pressure, an approximation of the momentum at an intermediate time instant is predicted by

$$(\rho u_i)^* = (\rho u_i)^n + \gamma^i \Delta t \left[-\frac{\partial}{\partial x_j}(\rho u_i u_j) + \frac{\partial}{\partial x_j}\tau_{ij} \right]. \tag{4.19}$$

Now, the solution at the time level $(n+1)$ is obtained in a subsequent corrector step

$$(\rho u_i)^{n+1} = (\rho u_i)^* - \gamma^i \Delta t \frac{\partial}{\partial x_i}\tilde{p}\,. \tag{4.20}$$

This procedure involves the solution of a Poisson equation for the fluctuating pressure $\tilde{p}$ which can be derrived by taking the divergence of equation (4.20)

$$\frac{\partial^2}{\partial x_i^2}\tilde{p} = \frac{1}{\gamma^i \Delta t}\left[\frac{\partial}{\partial x_i}(\rho u_i)^* - \frac{\partial}{\partial x_i}(\rho u_i)^{n+1} \right]. \tag{4.21}$$

While for non-reactive incompressible flows the divergence of the momentum at time level $(n+1)$ is zero [185, 186], this methodology is an extension to reactive flows [187–189] since the dilatation due to heat release has to be considered. Although the dilatation at $(n+1)$ is not directly available, it can be assessed by using the continuity equation such that equation (4.21) transforms into

$$\frac{\partial^2}{\partial x_i^2}\tilde{p} = \frac{1}{\gamma^i \Delta t}\left[\frac{\partial}{\partial x_i}(\rho u_i)^* + \left(\frac{\partial}{\partial t}\rho\right)^{n+1} \right]. \tag{4.22}$$

Since the temperature and species mass fraction fields are advanced first (during the numerical integration procedure), the equation of state can be used to compute the density at level $(n+1)$. Then a backward discretization for the time derivative of density can be used to assess the second term on the right-hand side of equation (4.22). As argued by Nicoud [190] this backward discretization has to be at least second order accurate for consistency. Here, a third order backward finite difference approximation with non-constant step size according to Bowen and Smith [149] was used to estimate the derivative at $n+1$

$$\begin{aligned}\left(\frac{\partial}{\partial t}\rho\right)^{n+1} = {} & \frac{\alpha_2\alpha_3 + \alpha_2\alpha_4 + \alpha_3\alpha_4}{(\alpha_1-\alpha_2)(\alpha_1-\alpha_3)(\alpha_1-\alpha_4)}\rho^{n+1} + \frac{\alpha_1\alpha_3 + \alpha_1\alpha_4 + \alpha_3\alpha_4}{(\alpha_2-\alpha_1)(\alpha_2-\alpha_3)(\alpha_2-\alpha_4)}\rho^{n} \\ & + \frac{\alpha_1\alpha_2 + \alpha_1\alpha_4 + \alpha_2\alpha_4}{(\alpha_3-\alpha_1)(\alpha_3-\alpha_2)(\alpha_3-\alpha_4)}\rho^{n-1} + \frac{\alpha_1\alpha_2 + \alpha_1\alpha_3 + \alpha_2\alpha_3}{(\alpha_4-\alpha_1)(\alpha_4-\alpha_2)(\alpha_4-\alpha_3)}\rho^{n-2},\end{aligned} \tag{4.23}$$

where $\alpha_i = t^i - t$, and t is the time at the end of the current Runge-Kutta stage.
Nicoud [190] demonstrated that the finite difference approximation can lead to numerical errors and other techniques have been proposed in the literature. For example a velocity divergence

constraint can be derived from the continuity equation and introduced in a Poisson equation with variable coefficients [191, 192]. However this approach is not pursued in favor of the computational more efficient finite difference approach. Further, as observed by Charentenay and Ern [187] in reactive simulations the error introduced by the numerical approximation of $(\partial\rho/\partial t)^{n+1}$ is negligible compared to the magnitude of physical effects.

4.1.6 Poisson solver

As outlined in the previous section a pressure Poisson equation has to be solved during each Runge-Kutta integration stage. Therefore, it is crucial to have an efficient solution strategy that also scales in parallel computations. There are two fundamental classes of algorithms that are generally used to solve equation (4.22): direct and iterative methods. In many situations iterative techniques can outperform direct solvers, especially in cases where memory restrictions exist or where the solution only gradually changes and rapid convergence can be achieved. However, their parallel performance greatly depends on the desired accuracy and with that on the number of iterations required. On the other hand if the "condition" of the underlying problem is unknown direct solvers stand out due to their robustness.
Spectral methods belong to the family of direct solvers which are only seldomly used because usually they are restricted to rectangular, periodic and equidistant, though not necessarily isotropic, domains. In *DINO* , however, the Poisson equation is solved by a spectral approach, even when the boundary conditions of the domain are not periodic. Despite the higher memory consumption, compared to iterative methods, and a possibly larger parallel communication overhead, it turned out that the spectral solver is the fastest and most accurate alternative to other well known solver packages [139], e.g. HYPRE [193]. The Poisson solver described in detail in [139, 140] is an extension of that described in [194–197], where pre- and post-processing steps are applied both in physical and in spectral space and the Poisson equation is solved on a staggered grid. On the contrary, the algorithm implemented in *DINO* [139] needs only one pre- and post-processing step in the physical space and solves for the pressure on a collocated grid. In both approaches the pre- and postprocessing steps are required to account for non-periodic boundary conditions. Finally, the algorithm implemented in DINO for solving the Poisson equation $\nabla^2 p = F$ can be summarized as follows:

1. Pre-process the right-hand side F, details can be found in [139, 140]

2. Apply standard three dimensional fast Fourier transform (FFT) to pre-processed system

$$\mathcal{F}\left\{\frac{\partial^2}{\partial x^2}+\frac{\partial^2}{\partial y^2}+\frac{\partial^2}{\partial z^2}\right\}\hat{p}=\hat{F} \quad \rightarrow \quad \hat{p}=-\frac{\hat{F}}{(\kappa_x^2+\kappa_y^2+\kappa_z^2)} \tag{4.24}$$

3. Apply standard IFFT routine to equation (4.24), obtaining the pressure in physical space

4. Post-process solution p. During this step mainly the memory is rearranged to match the data structures within *DINO*

The three dimensional forward and backward fast Fourier transforms are performed using `2DECOMP&FFT` [198], which itself is linked to the highly optimized fast Fourier transform library `FFTW3` [199].

4.1.7 Parallelization and parallel efficiency

The computational domain has to be decomposed into subdomains in order to allow for massive-parallel computations on distributed memory platforms. Keeping in mind that the Poisson solver is based on discrete Fourier transformations the decomposition strategy must guarantee that the data along a global grid line is accessible for each corresponding computational process. For cartesian topologies typically two different strategies exist, the 1D slab decomposition and the 2D pencil decomposition. Because the slab decomposition exhibits severe limitations in the number of usable processors, the pencil decomposition is used for the simulations presented later. An example of a 2D distribution is given in figure 4.1.
Besides efficient parallel communication patterns for 3D discrete Fourier transforms *DINO* also requires the exchange of ghost cells for the inter-processor computation of spatial derivatives via finite differences, c.f. section 4.1.1. Implementing highly scalable inter-processor communication can be a very demanding task. Here, the high performance decomposition library `2DECOMP&FFT` [198] is used. Besides the decomposition algorithm, Li and Laizet [198] also implemented a 3D interface for discrete Fourier transforms and ghost cell exchange. The applicability and general scalability of the library on a variety of platforms was already demonstrated in [139, 194, 195, 200]. However,

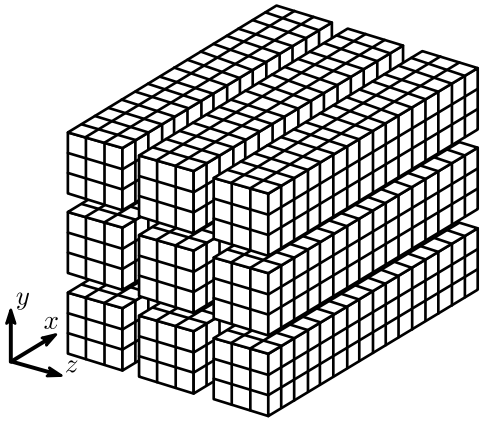

Figure 4.1.: Example of a two dimensional pencil decomposition used in *DINO* . The data is distributed between processors in the y and z direction.

a detailed scaling analysis for the implemented solvers presented in section 4.1.2 was missing until now. Therefore, a benchmark case consisting of a temporally evolving jet flame [201] at two different spatial resolutions was simulated. The governing equations were integrated for one time step using both solvers presented in section 4.1.2 and explicit 6th order finite differences. Initial conditions and the chemical kinetic scheme were the same as in [201]. In order to get reliable timings this procedure was repeated 10 times for each configuration listed in table 4.4. As can be seen from table 4.4 and figures 4.2a and 4.2b, both solvers show an excellent strong scaling behavior. It seems that for the small scale benchmark case even a super-linear scaling can be achieved by both solvers. For the large scale case, only the explicit solver shows super-linear scaling. The typical

Table 4.4.: Strong scaling and strong scaling efficiency of the Runge-Kutta solvers presented in section 4.1.2. The scaling runs were performed on SuperMUC phase 1 at Leibniz Supercomputing Centre. Each island of phase 1 of SuperMUC consists of 512 nodes each of which is equipped with 2 Intel Xeon E5-2680 (8 cores at 2.7GHz).

		$256 \times 513 \times 512$				$1024 \times 2049 \times 2048$			
		Explicit		Semi-Implicit		Explicit		Semi-Implicit	
Islands	cores	time	efficiency	time	efficiency	time	efficiency	time	efficiency
1	128	33.04	100.00	39.74	100.00	–	–	–	–
1	256	16.56	99.722	19.85	100.07	–	–	–	–
1	512	7.78	106.13	9.66	102.82	–	–	–	–
1	1024	3.69	111.90	4.78	103.91	–	–	–	–
1	2048	1.61	127.81	2.32	106.81	–	–	–	–
1	4096	0.86	119.15	1.28	96.61	–	–	–	–
1	8192	0.53	97.02	0.67	92.06	–	–	–	–
2	16384	–	–	–	–	19.88	100.00	22.49	100.00
4	32768	–	–	–	–	9.23	107.67	11.79	95.36
8	65536	–	–	–	–	4.59	108.06	6.63	84.82

reason for super-linear speedup is that decomposition of the fixed-size data set has become small enough per core to fit into local cache.

A subsequent decrease of the efficiency can be attributed to a parallel communication overhead. This overhead increases even further when going to more islands[1] because of the established inter-island network topology[2]. The decrease in efficiency also becomes evident looking at the weak scaling behavior of both solvers, c.f. figures 4.2a and 4.2b. Investigations of the weak scaling of the code were performed keeping the work load per computational core constant at 524288 grid points.

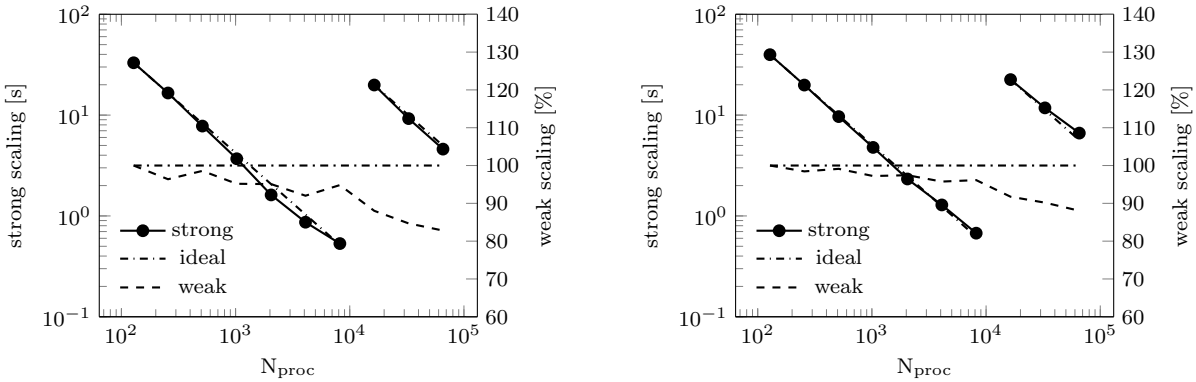

(a) Explicit **(b)** Semi-Implicit

Figure 4.2.: Strong and weak scaling of the Runge-Kutta solvers presented in section 4.1.2.

[1] Within an island compute nodes are connected via a fully non-blocking Infiniband network.

[2] At SuperMUC inter-island communication is handled by a pruned-tree 4:1 configuration. This means that one node communicating with another node in another island has to share its link with 3 other nodes. A complete description of the SuperMUC system can be found at `https://www.lrz.de/services/compute/supermuc/systemdescription/`

4.2 Reactive temporally evolving jet flame

In this section the direct numerical simulation (DNS) setup used for the analysis in the subsequent chapters is described. It is based on a well-established DNS setup [202–208] of a temporally evolving syngas jet flame that was originally proposed by Hawkes et al. [201].
The physical setup presented in detail in the following was already used in Refs. [127, 144], but is revisited here with a higher resolution to increase the accuracy of the later following on-the-fly tracking and dissipation element (DE) analysis. Furthermore, statistics with respect to the flame structure are presented and phenomenological aspects of the jet are discussed.

4.2.1 General setup

In this work a temporally evolving jet configuration was selected rather than a spatial jet because it allows for more significant flame-turbulence interaction within a given computational domain, thereby potentially creating a more wrinkled flame surface through intense turbulent mixing. Also from a computational point of view it is often advantagous to consider a temporally evolving jet rather than a spatially evolving jet because spatial jets must be run for several flow times because otherwise artifacts from the initial conditions may pollute the results.
For the analyses, carried out later, a temporal jet configuration similar to that by Hawkes et al. [201] was chosen. The governing equations that were solved correspond to equations (2.44) to (2.46). In addition, also a transport equation for the mixture fraction, according to equation (3.8), was solved. The temporal jet setup can be parameterized by the initial jet height H_0, the initial velocity difference $\Delta U_0 = U_{\text{fuel}} - U_{\text{oxidizer}}$, where U_{fuel} and U_{oxidizer} denote the velocity of the counter-flowing fuel and oxidizer streams, respectively, and the cold-flow kinematic viscosity ν_{fuel} of the pure fuel stream. The jet time t_{jet} and the jet Reynolds number Re_{jet} are given by

$$t_{\text{jet}} = \frac{H_0}{\Delta U_0}\,, \tag{4.25}$$

$$\text{Re}_{\text{jet}} = \frac{\Delta U_0 H_0}{\nu_{\text{fuel}}}\,. \tag{4.26}$$

As indicated in figure 4.3 the boundary conditions are periodic in the stream-wise (z) and span-wise (x) direction, while zero-gradient boundary conditions are imposed in the cross-stream (y) direction. The domain size was chosen as $L_x = 10H_0$ in span-wise direction, $L_y = 20H_0$ in cross-stream direction and $L_z = 16H_0$ in stream-wise direction, whereas the initial jet height was set to $H_0 = 1.37\,\text{mm}$. The number of grid points across H_0 was set to $N_{H_0} = 96$. Thus, the total number of points required for the simulation is $N_{\text{tot}} \approx 2.8 \times 10^9$. This case was simulated on the supercomputer SuperMUC[3] and required more than 2 MCPUh running on 23 904 cores. While in the original study by Hawkes et al. [201] the simulation was carried out on an isotropic mesh with a grid spacing of $\Delta x = \Delta y = \Delta z = 19.03 \times 10^{-6}\,\mu\text{m}$ the current simulation has a resolution of $\Delta x = \Delta y = \Delta z = 14.27 \times 10^{-6}\,\mu\text{m}$. This increased resolution is required to facilitate the later

[3] System description (2017): `https://www.lrz.de/services/compute/supermuc/systemdescription/`

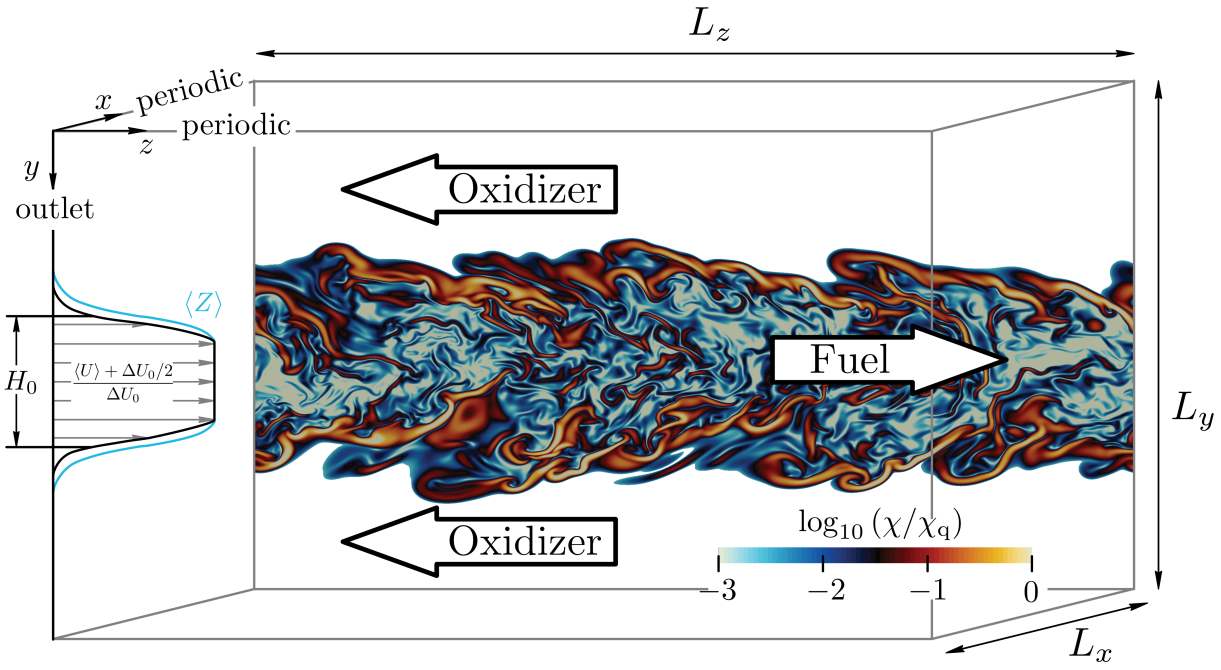

Figure 4.3.: Setup of the direct numerical simulation together with a sketch of the initial profiles of $\langle Z \rangle$ and $\langle U \rangle$. The domain size is denoted by L_x, L_y and L_z. The contours show the logarithm of the scalar dissipation rate χ normalized by its value near extinction χ_q.

following analyses of dissipation elements (DE) [48, 144, 209], cf. chapter 6. According to Wang and Peters [48] the ratio of grid resolution and Kolmogorov scale should be $\Delta x/\eta < 1$ to obtain a sufficient accuracy for DE analyses. However, in order to meet this criterion a resolution of at least $\Delta x = 11.41 \times 10^{-6}\,\mu\text{m} = 0.8 \cdot \Delta x$ is required, see figure 4.4a, which would correspond to $N_{H_0} = 120$. Therefore, the chosen resolution represents a compromise between the criteria of Wang and Peters [48] and Pope [137]. Despite the resolution required to perform a DE analysis the DNS itself is very well resolved. As Pope [137] pointed out, sufficient resolution exists if the criteria $\Delta x/\eta \leq 2.1$ and $\kappa_{max}\eta \geq 1.5$ are fulfilled, where κ_{max} denotes the maximum wavenumber that can be resolved on the grid. As it is shown in figure 4.4 both criteria are fulfilled during the whole course of the simulation.

4.2.2 Initialization of mean profiles

All mean velocities are initially set to zero, except the stream-wise velocity which is described by

$$\langle U \rangle_y = U_{\text{fuel}} \left(-1 + \frac{2}{1 + \Delta R_U} \right) \tag{4.27}$$

where the radial increment ΔR_U is determined through

$$\Delta R_U = \left| \frac{y - 0.5 \cdot L_y}{r_U} \right|^{s_U} . \tag{4.28}$$

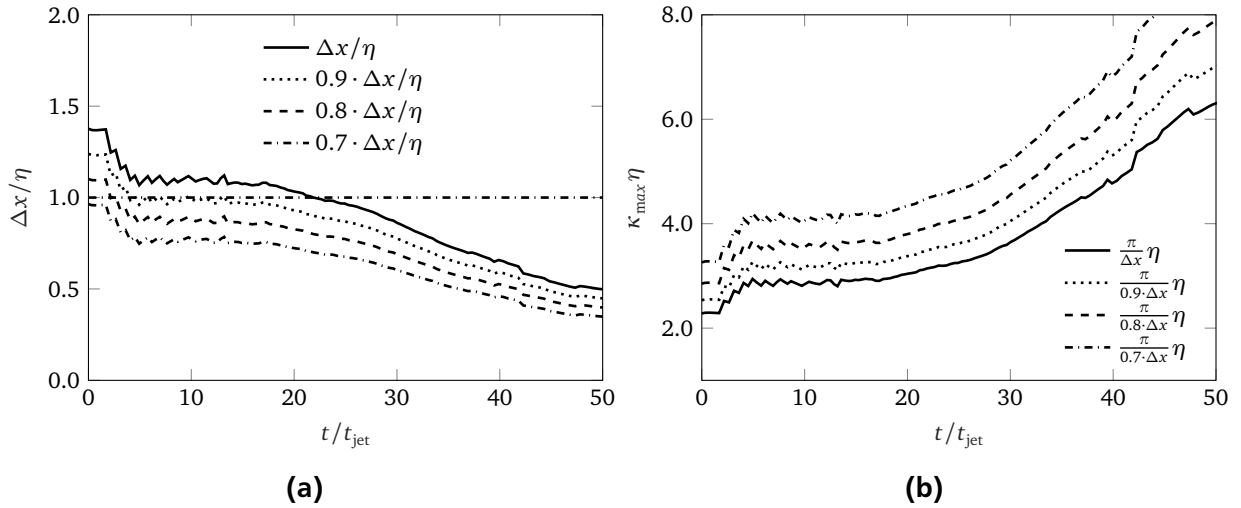

Figure 4.4.: Evolution of two different resolution criteria: (a) $\Delta x/\eta$ and (b) $\kappa_{\max}\eta$. For resolutions $\Delta x/\eta < 2.1$ and $\kappa_{\max}\eta > 1.5$ the simulation can be considered as well resolved [137].

The initial velocity of the fuel stream is set to $U_{\text{fuel}} = 138\,\text{m}\,\text{s}^{-1}$. At the same time the description through equation (4.27) fixes the velocity of the oxidizer stream to $U_{\text{oxidizer}} = -U_{\text{fuel}}$. The resulting initial maximum Mach number is Ma ≈ 0.4 which successively decreases towards later times of the jet. The other parameters in equation (4.27), s_U and r_U, control the stiffness and width of the initial profile, respectively. They were set to $s_U = 10$ and $r_U = H_0/2$.
The chemistry is initialized in a similar fashion based on the mean mixture fraction profile

$$\langle Z \rangle = \left(\frac{1}{1 + \Delta R_Z} \right), \tag{4.29}$$

which is unity in the central fuel stream and zero in the counterflowing oxidizer streams. The radial increment ΔR_Z is determined through

$$\Delta R_Z = \left| \frac{y - 0.5 \cdot L_y}{r_Z} \right|^{s_Z} . \tag{4.30}$$

Here, s_Z and r_Z control the stiffness and width of the initial profile, respectively, and were set to $s_Z = 7$ and $r_Z = 0.000\,918\,\text{mm}$. Both initial profiles of $\langle Z \rangle_y$ and $\langle U \rangle_y$ are illustrated in figure 4.5.

4.2.3 Initialization of chemistry

The chemical kinetic scheme employed for the study is a skeletal scheme that was reduced by Hawkes et al. [201] specifically for the purpose of their DNS. It was reduced from a complete C1 mechanism that was originally published by Li [210]. The same chemical kinetic scheme is used for the present DNS simulation. As in the original publication [201] the central fuel stream consists 50% CO, 10% H_2 and 40% N_2 by volume and the counter-flowing oxidizer streams consists of 25% O_2 and 75% N_2. This results in an element based stoichiometric mixture fraction of $Z_{st} = 0.42$. The initial temperature of both streams is $T_{\text{fuel}} = T_{\text{oxidizer}} = 500\text{K}$. The initial distribution of species mass

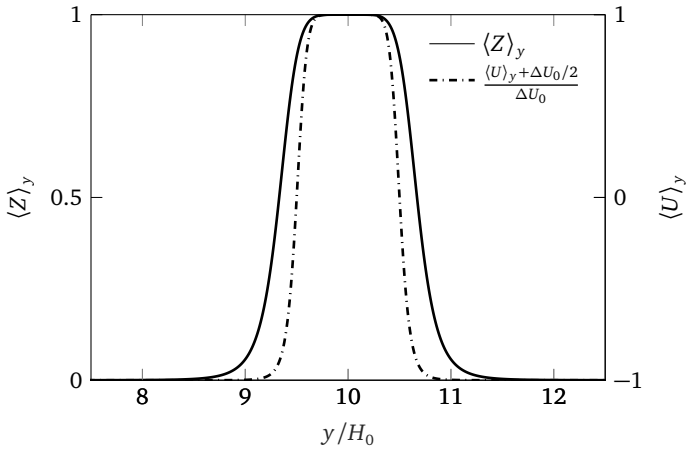

Figure 4.5.: Initial mean profile of mixture fraction and stream-wise velocity, for $U_{\text{fuel}} = 1$.

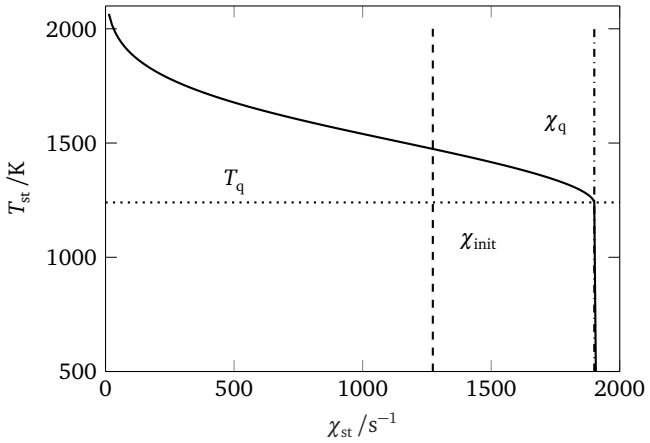

Figure 4.6.: Evolution of temperature with scalar dissipation rate at stoichiometric conditions. The temperature near extinction (T_q) is estimated at the point where the temperature abruptly drops. At the same time this also states the scalar dissipation rate near extinction (χ_q). The scalar dissipation rate χ_{init} is assumed to be representative for the conditions under which the turbulent flame resides and it was set to $\chi_{init} = 0.67\chi_q$.

fractions and temperature is obtained by linear interpolation from a flamelet table which was generated for one specific scalar dissipation rate χ_{init}. This χ_{init} was assumed to be representative for the conditions under which the turbulent flame resides and it was set to $\chi_{init} = 0.67\chi_q$. In order to estimate the scalar dissipation rate near extinction χ_q, a series of steady laminar flamelet calculations (cf. section 3.2.1), varying χ_{st}, was conducted using an inhouse laminar flame solver [211] and the corresponding temperature at stoichiometry T_{st} was extracted. Figure 4.6 shows a plot of T_{st} versus the stoichiometric scalar dissipation rate. The scalar dissipation rate near extinction is then obtained at the point where the temperature abruptly drops. Here, it is estimated at $\chi_q = 1901\text{s}^{-1}$. At the same time this procedure also allows to assess the temperature near extinction, which is estimated at $T_q = 1241\,\text{K}$.

Solution from the flamelet table for the above mentioned conditions for Y_{CO}, Y_{H_2}, Y_{OH},Y_{O_2} and the temperature T are shown in figure 4.7a. After the interpolation procedure the initial profiles of the species mass fractions and the temperature in physical space are depicted in figure 4.7b. Note, that for the sake of clarity not all initial profiles are shown.

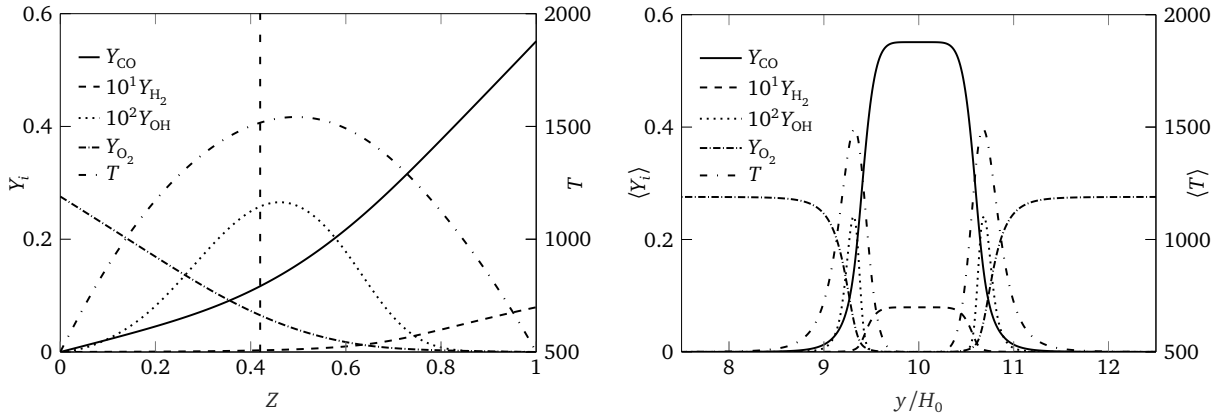

(a) flamelet space **(b)** physical space

Figure 4.7.: Initial profiles of temperature, Y_{H_2}, Y_{OH}, Y_{CO} and Y_{O_2} in: (a) flamelet space and (b) physical space. Note that for the sake of clarity not all initial profiles are shown.

4.2.4 Initialization of turbulence

In order to trigger the transition to a fully turbulent jet, solenoidal isotropic velocity fluctuations $\mathbf{u}'$ are superimposed upon the initial velocity mean profiles $\langle \mathbf{U} \rangle$

$$\mathbf{U} = \langle \mathbf{U} \rangle + \mathbf{u}' \qquad \langle \mathbf{u}' \rangle = 0\,, \tag{4.31}$$

whereat $\mathbf{u}'$ is spatially confined to the jet region using the same profile as in equation (4.27). In the literature different approaches are available for the generation of initial or inflow conditions, namely the Kraichnan technique [212], digital filtering [213], or random noise diffusion [214]. However, due to the employed domain decomposition library (`2DECOMP&FFT` [198]) it is reasonable to use a different approach based on inverse fast Fourier transforms (IFFT). In the IFFT approach a prescribed energy spetrum of Passot-Pouquet type [215] is used

$$E(|\kappa|) = \frac{16u'^2}{\kappa_0}\sqrt{\frac{2}{\pi}}\left(\frac{|\kappa|}{\kappa_0}\right)^4 \exp\left[-2\left(\frac{|\kappa|}{\kappa_0}\right)^2\right], \tag{4.32}$$

together with the input parameters κ_0 and u' to prescribe the three velocity components in spectral space [216]. While κ_0 is the wavenumber that corresponds to the integral scale of the turbulent flow field, u' characterizes its intensity. They were set to $u' = 0.05\Delta U_0$ and $\kappa_0 = 8\pi/H_0$. Note that this approach is not restricted to spectra of Passot-Pouquet type but could also be applied using any other kind of analytical spectrum function, e.g. the Von Kármán spectrum [217] with Paó correction [218].

Three dimensional solenoidal velocity fluctuations are then obtained by applying Rogallo's method [216]. The initial profiles of scalar variables, i. e. mixture fraction, temperature and species mass fractions, remain unperturbed.

4.2.5 Results of the DNS

The analyses were carried out based on a three dimensional direct numerical simulation of a turbulent reactive syngas jet flame under atmospheric conditions which was simulated with the DNS code *DINO* [139]. The initial conditions and the domain were chosen according to the explanations in the previous sections. Based on that, the initial cold flow Reynolds number of the central fuel jet is $\mathrm{Re}_{\mathrm{jet}} = 9075$, where ν_{f} denotes the kinematic viscosity of the pure fuel. In addition to the ordinary governing equations (2.44) to (2.46) for reactive flows an additional transport equation for the mixture fraction, cf. equation (3.8), was solved assuming unity-Lewis number diffusion for Z, i.e. $D_Z = \lambda/(\rho c_{\mathrm{p}})$. On the contrary, the species diffusion velocities were computed according to the Hirschfelder-Curtiss approximation, cf.section 2.5.2, thereby neglecting thermo diffusion. All transport properties required for the integration of the governing equations, i.e. μ, λ and $\mathcal{D}_{ij}$, were obtained using the high-fidelity software library EGlib [92]. For the computation of the chemical source terms, enthalpies and specific heat capacities the source code generator *pyJac* in conjunction with the interface presented in appendix C.1 was employed. The equations were discretized using 6th order finite differences in space. After the verification of the flow setup, the 3rd order semi-implicit Runge-Kutta scheme, presented in section 4.1.2, was used for time integration.

Phenomenology of the syngas jet flame

In order to get an impression of the turbulence in the jet, it is instructive to visualize some turbulent fields obtained by the direct numerical simulation. Figures 4.8 and 4.9 show yOz-planes, taken at $L_x/2$, of the mixture fraction, the scalar dissipation rate, the temperature and the OH mass fraction at four instants in time. According to [219] the evolution of the jet can be divided into three different regimes:

I shear layer development and flame-turbulence interaction,

II local flame extinction with mixing of fuel, oxidizer and combustion products,

III reignition of the turbulent flame.

These regimes are also apparent from figures 4.8 and 4.9. Beginning with the inspection of figure 4.8, fields relevant for the flamelet model, namely Z and χ, are shown for times $t/t_{\mathrm{jet}} = 10, 20, 30, 40$. While transitioning to a fully turbulent field, the mixture fraction field reveals coherent structures of roughly constant scalar value, though the maximum mixture fraction decreases due to mixing. These structures are separated by sharp highly convoluted boundaries at which, in turn, the scalar dissipation rate χ reaches high values. To accentuate the wide range of the scalar dissipation, plots of χ/χ_q are shown on a logarithmic scale, where χ_q was obtained from steady laminar flamelet calculations. In contrast to the mixture fraction, the scalar dissipation is characterized by filamented structures. It is a highly intermittent quantity and regions of high χ are confined in localized regions of space. While these are ordinary observations for scalar mixing, see Gauding [220], additional information regarding turbulence-chemistry interaction is gained from figure 4.9.

As an indicator for a burning flame both the temperature and the OH mass fraction must sufficiently exceed their quench limits, $T_q = 1241\,\mathrm{K}$ and $\mathrm{OH}_q = 1.17 \cdot 10^{-3}$, respectively. Beginning at the stage of shear layer evolution (regime I), $t/t_{\mathrm{jet}} = 10$, a stable burning flame seems to exist, which gets gradually weaker as the jet evolves. An illustration of the causal chain is given in figure 4.10. As turbulence evolves, mostly compressive (negative) strain ($a = \mathbf{n} \cdot \nabla\mathbf{u} \cdot \mathbf{n}$) acts (top), which leads to an increase in the scalar dissipation rate (middle). In regions where the scalar dissipation rate is above the critical limit, $\chi > \chi_q$, the temperature will drop below the quench temperature (bottom) which eventually leads to local extinction. At $t/t_{\mathrm{jet}} = 20$, the temperature and OH mass fraction field are highly contorted and regions of burning and extinguished regimes coexist (regime II), though the flame seems to be globally extinguished. However, due to small pockets of high temperature and radicals, the jet approaches the onset of reignition at $t/t_{\mathrm{jet}} = 30$ (regime III) and a stable burning flame emerges.
Besides the visual inspection of the turbulent fields, the extent to which extinction occurs is assessed by analyzing statistics and flame structures of the jet in the next section.

Statistics and flame structure of the jet

First results are presented for some characteristic quantities of the turbulent reactive jet. Therefore, ensemble-averages conditioned on a small band, $0.8Z_{st} \leq Z \leq 1.2Z_{st}$, centered around the surface of stoichiometric mixture fraction were computed and are denoted by $\langle \bullet \rangle_{\mathrm{st}}$. The evolution in terms of a nondimensionalized time, t/t_{jet}, of the mean turbulent kinetic energy $\langle k \rangle_{\mathrm{st}}$ and the mean dissipation $\langle \varepsilon \rangle_{\mathrm{st}}$

$$\langle \varepsilon \rangle_{\mathrm{st}} \equiv 2 \left\langle \nu S_{ij} S_{ij} \right\rangle_{\mathrm{st}} \tag{4.33}$$

$$\langle k \rangle_{\mathrm{st}} \equiv \frac{1}{2} \langle u_i u_i \rangle_{\mathrm{st}} \,, \tag{4.34}$$

together with the jet width H is shown in figure 4.11, where H was measured at the point where the mean velocity profile reaches half its maximum. All quantities are normalized accordingly by the initial values ΔU_0 and H_0.

After an initial transient phase, where turbulence starts to evolve, the jet shows evidence of self-similarity after $t/t_{\mathrm{jet}} \approx 10$. The property of self-similarity is well known for fully developed turbulence [221] and can be further investigated by looking at the nondimensionalized mean stream-wise velocity profile, depicted in figure 4.12. By scaling large-scale quantities, like $\langle u_z \rangle_y$, with the mean centerline velocity, u_c, statistical profiles at different times collapse onto a single curve, which is an indicator for self-similarity. The average of the stream-wise velocity u_z was determined by

$$\langle u_z \rangle_y (y) = \frac{1}{2N_x N_z} \sum_{i=1}^{N_x} \sum_{k=1}^{N_z} (u_z(i, y, k) + u(i, -y, k)) \,, \tag{4.35}$$

where the coordinate system is shifted to $L_y/2$ prior to the computation of $\langle u_z \rangle_y (y)$. At the same time u_c is determined as $u_c = \langle u_z \rangle_y (0)$. As can be seen in figure 4.12, the jet shows indications of a self-similar behavior. Hence, after $t/t_{\mathrm{ref}} \approx 10$ the jet can be considered fully turbulent. After this

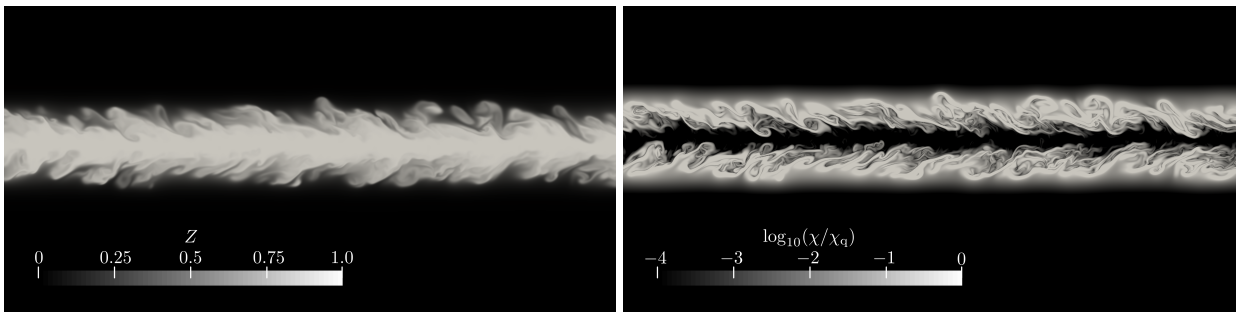

(a) $t/t_{\text{jet}} = 10$

(b) $t/t_{\text{jet}} = 10$

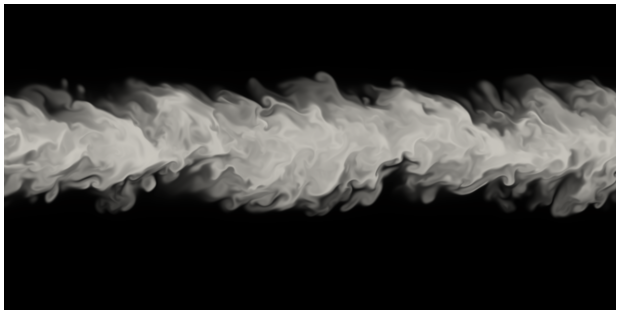

(c) $t/t_{\text{jet}} = 20$

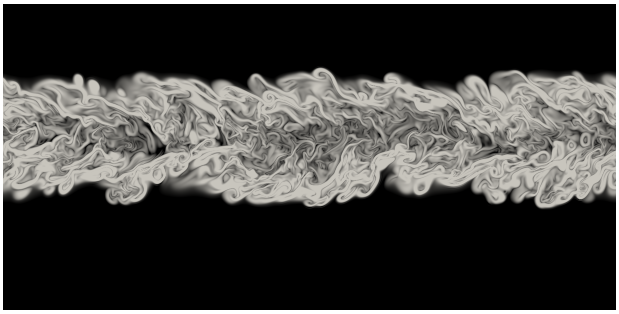

(d) $t/t_{\text{jet}} = 20$

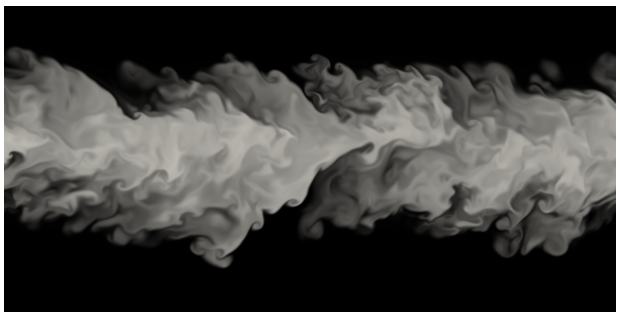

(e) $t/t_{\text{jet}} = 30$

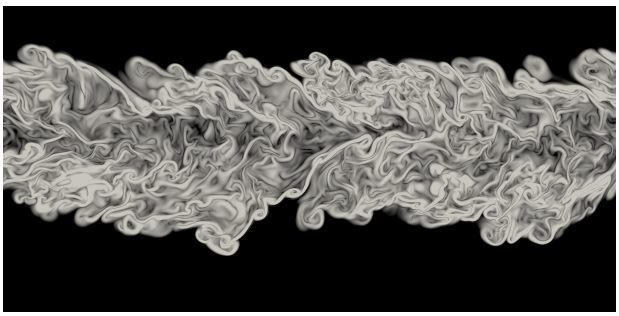

(f) $t/t_{\text{jet}} = 30$

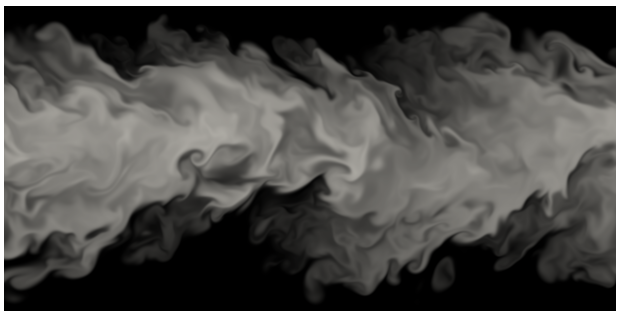

(g) $t/t_{\text{jet}} = 40$

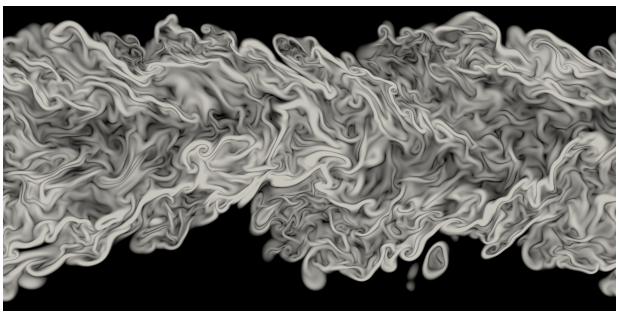

(h) $t/t_{\text{jet}} = 40$

Figure 4.8.: Evolution of the temporally evolving syngas jet for $t/t_{\text{jet}} = 10, 20, 30, 40$ for: (a), (c), (e), (g) the mixture fraction and (b), (d), (f), (h) $\log_{10}(\chi/\chi_{\text{q}})$

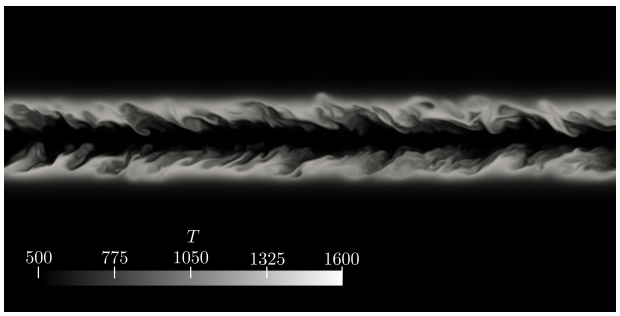

(a) $t/t_{\text{jet}} = 10$

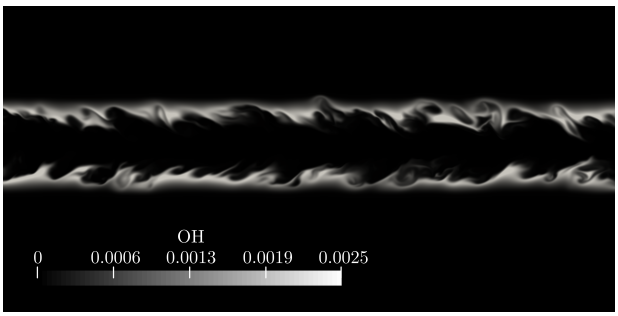

(b) $t/t_{\text{jet}} = 10$

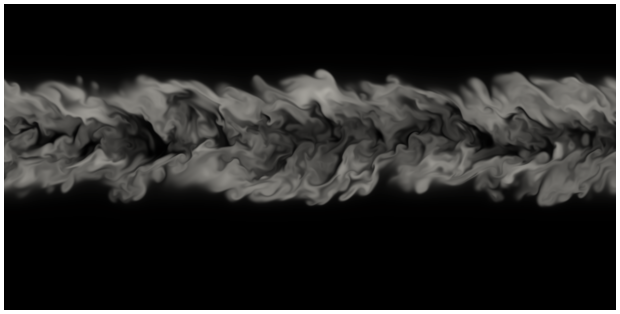

(c) $t/t_{\text{jet}} = 20$

(d) $t/t_{\text{jet}} = 20$

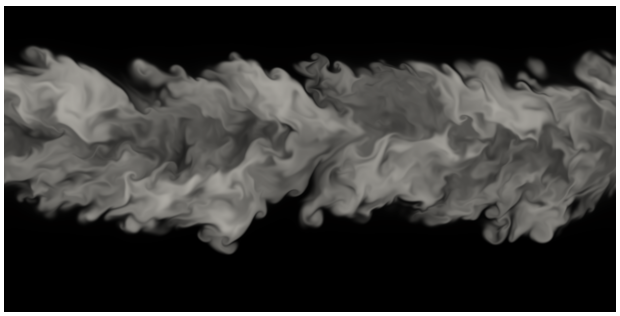

(e) $t/t_{\text{jet}} = 30$

(f) $t/t_{\text{jet}} = 30$

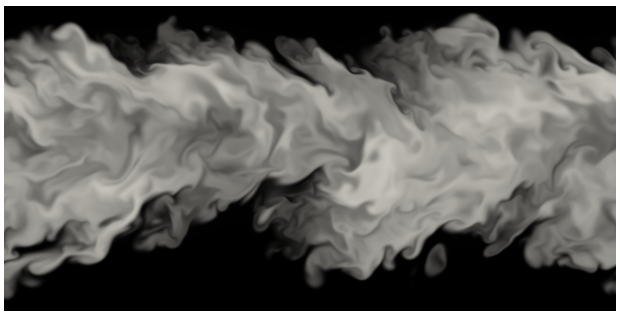

(g) $t/t_{\text{jet}} = 40$

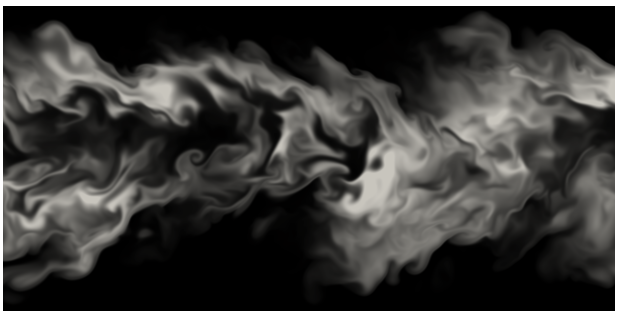

(h) $t/t_{\text{jet}} = 40$

Figure 4.9.: Evolution of the temporally evolving syngas jet for $t/t_{\text{jet}} = 10, 20, 30, 40$ for: (a), (c), (e), (g) the temperature and (b), (d), (f), (h) the mass fraction of OH.

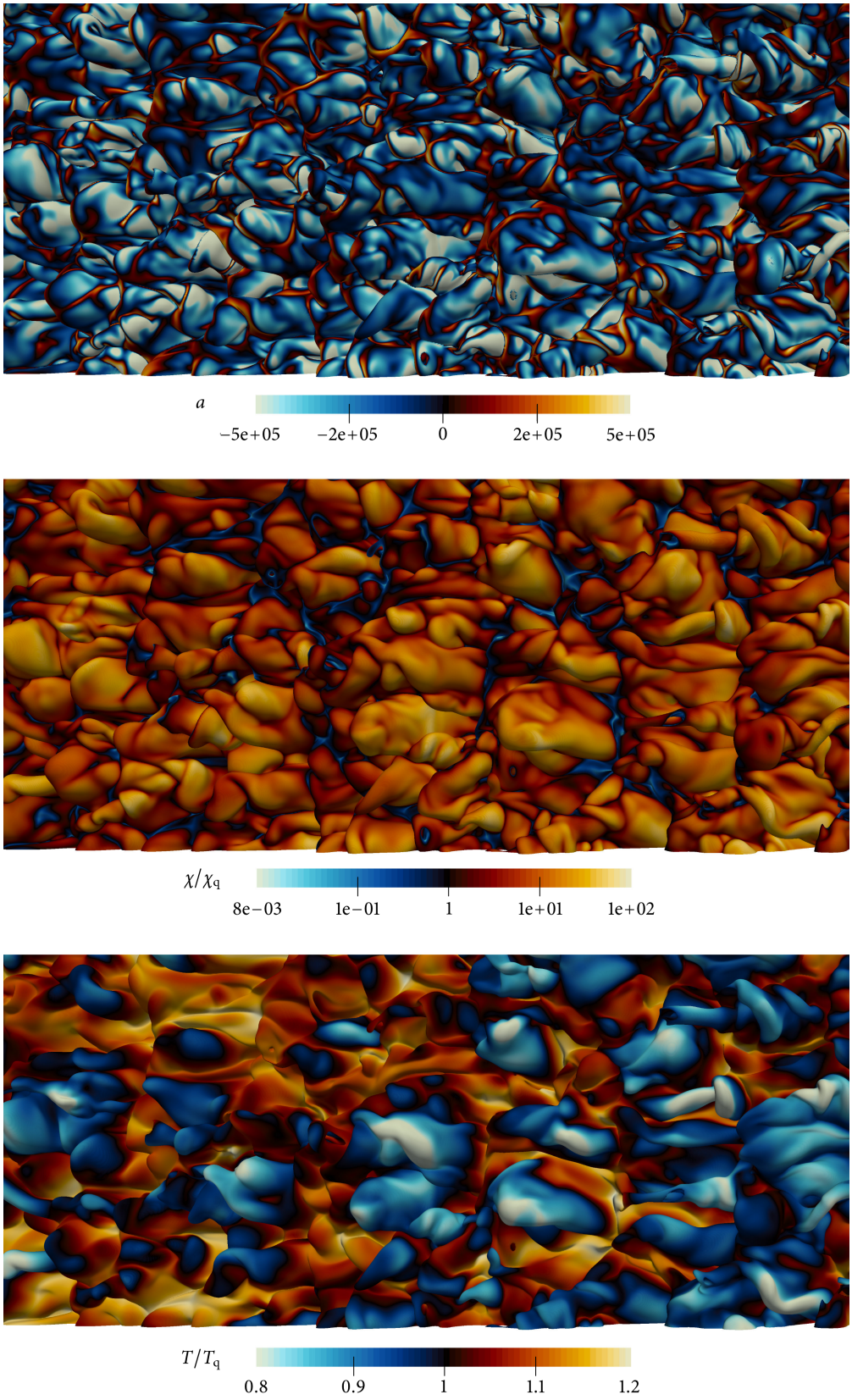

Figure 4.10.: View on top of the center-plane xOz. The causal chain that leads to local extinction is visualized. Compressive (negative) strain ($a = \mathbf{n} \cdot \nabla\mathbf{u} \cdot \mathbf{n}$) causes increased scalar dissipation rates which inturn causes a decrease in temperature.

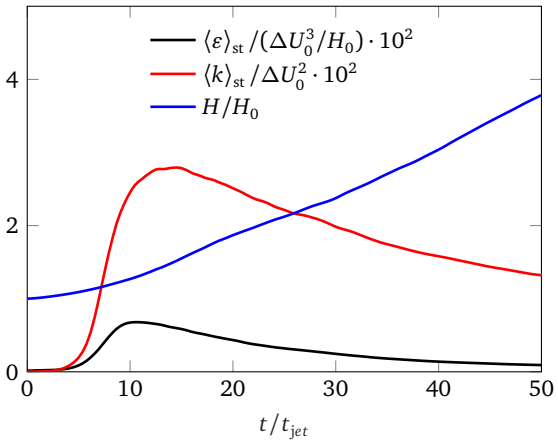

Figure 4.11.: Temporal evolution of important flow quantities. After $t/t_{\text{jet}} \approx 10$ the jet shows evidence of self-similarity since $\langle k\rangle_{\text{st}}$ and $\langle\varepsilon\rangle_{\text{st}}$ start to gradually decay while the jet width exhibits a linear growth, which is to be expected for self-similarly evolving mixing layers [221].

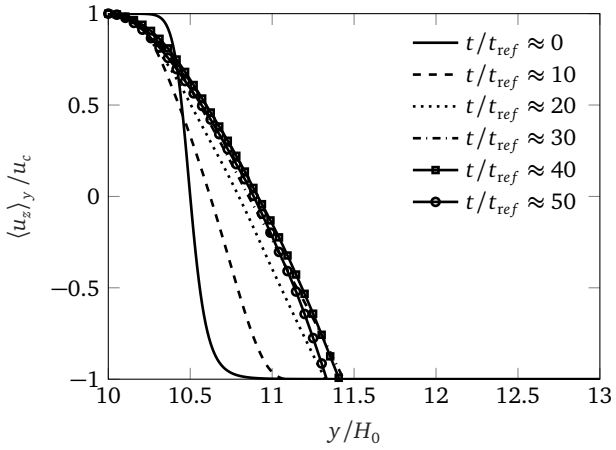

Figure 4.12.: Profiles of the mean stream-wise velocity normalized by the streamwise mean centerline velocity. After $t/t_{\text{jet}} \approx 10$ the jet shows evidence of self-similarity as the profiles collapse.

initial transient, $\langle k\rangle_{\text{st}}$ and $\langle\varepsilon\rangle_{\text{st}}$ start to gradually decay while the jet width exhibits a linear growth, which is to be expected for self-similarly evolving mixing layers [221].

A second important property, specific to this DNS case, is that the simulated flame exhibits strong flame–turbulence interactions resulting in local extinction followed by re-ignition [201]. This phenomenon is illustrated in figure 4.13, where the temporal evolution of the mean temperature around stoichiometry is plotted. To allow for a better comparison against quenched conditions, the curve is normalized with the quenching temperature, obtained from steady laminar flamelet calculations, cf. section 4.2.3. It can be clearly seen that at $t/t_{\text{jet}} \approx 12$ the temperature drops below the quench limit and reaches maximum extinction (lowest temperature) at $t/t_{\text{jet}} \approx 25$, followed by a subsequent reignition. A similar behavior was also reported by Vo et al. [222], although they obtained a slightly different extinction curve, which is possibly due to a different averaging procedure for the temperature.

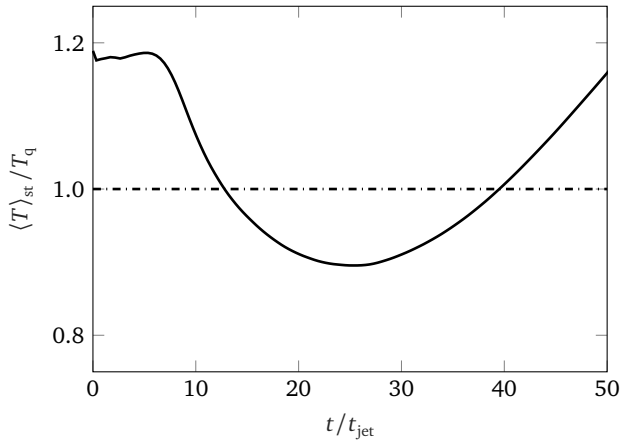

Figure 4.13.: Temporal evolution of the mean temperature around stoichiometry normalized by the temperature near extinction T_q. The jet exhibits significant local extinction between $t/t_{jet} \approx 12$ and $t/t_{jet} \approx 40$.

Although, figure 4.13 gives a first indication of the level of extinction in the jet, figure 4.14 demonstrates this fact more comprehensively. Figure 4.14 shows the joint propability density functions (jpdf) of temperature and mixture fraction, $P(T, Z)$, and the OH mass fraction and mixture fraction, $P(Y_{OH}, Z)$, at four different instants in time. In addition, also the corresponding conditional mean and quenching values are plotted.

While in the early stages of the flame, up to $t/t_{jet} = 10$, the flame starts to evolve and most of the samples near stoichiometry are well above the quenching limit, extinction events are clearly visible at times $t/t_{jet} = 20, 30$. As first indications were given in figure 4.13, highest extinction occurs around $t/t_{jet} = 20$, where most of the samples of both temperature and OH mass fraction drop fairly below the quench limit. At the onset of reignition, around $t/t_{jet} = 30$, the conditional means are still below the quench limit, however, more and more samples near stoichiometry begin to exceed the quench limit. Although at $t/t_{jet} = 40$ the case is not yet fully reignited, the OH radical pool has already started to build up again and also most of the temperature samples are well above the quench limit.

Serving as a reference for the later following discussion of turbulent flame structures, figure 4.15 shows mean values of Y_{OH}, Y_{CO}, Y_{H_2} and Y_{O_2} conditioned on the mixture fraction Z (right) together with the joint propability of $\log_{10}(\chi/\chi_q)$ and mixture fraction (left). Again χ is taken on a logarithmic scale to accentuate the wide range of different scalar dissipation rates. First, the joint pdfs of the scalar dissipation rate underline the reignition propability of the jet with time, since the majority of samples around stoichiometry gradually move below the quench limit. Note, that for these plots the quench limit is marked by the zero-line and values above zero indicate values higher than the quenching limit. A second observation is that the flame seems to be shifted from the lean side of the flame, during the early jet times, to the rich side, for later jet times, where $\langle Y_{OH}|Z \rangle$ serves as a marker for the flame position. This finding is also supported by figure 4.14 where not only most of the samples of $P(Y_{OH}, Z)$ undergo this shift but also $P(T, Z)$ and the mean temperature conditioned on Z support this finding. Furthermore, figure 4.15 shows evidence of a significant leakage of fuel (Y_{CO} and Y_{H_2}) and oxidizer for the turbulent syngas flame.

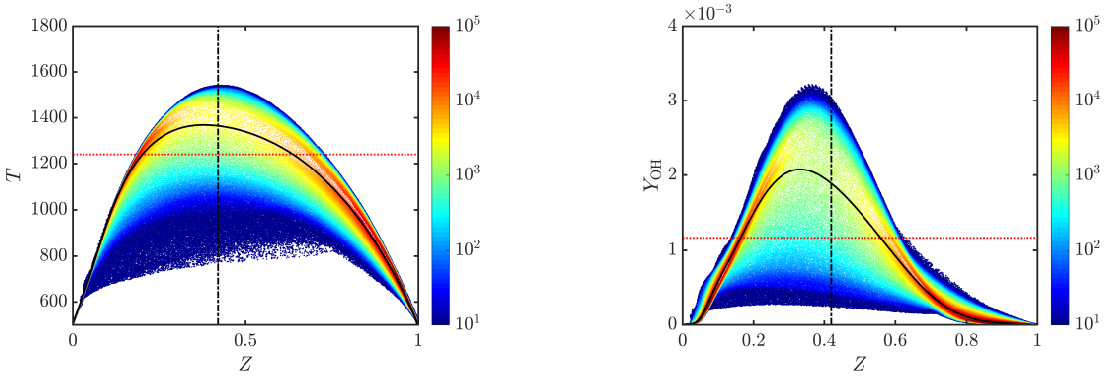

(a) $t/t_{\mathrm{ref}} = 10$

(b) $t/t_{\mathrm{ref}} = 10$

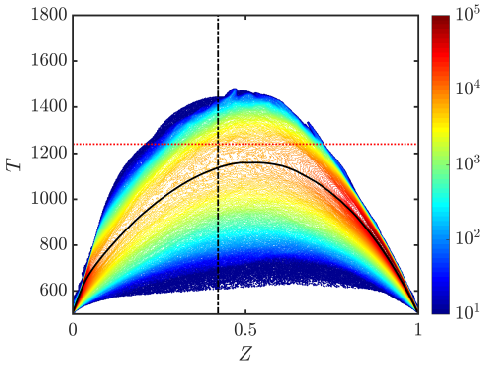

(c) $t/t_{\mathrm{ref}} = 20$

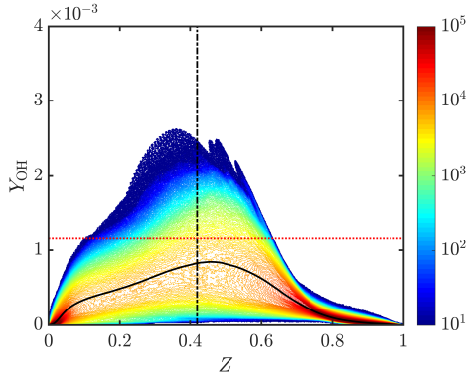

(d) $t/t_{\mathrm{ref}} = 20$

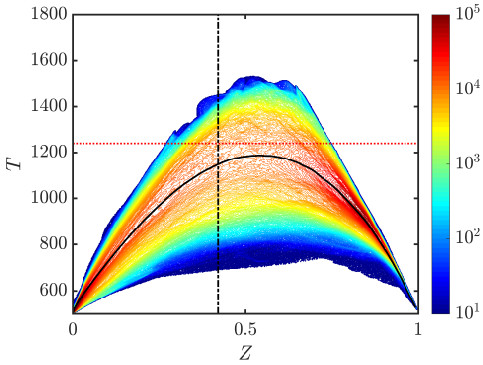

(e) $t/t_{\mathrm{ref}} = 30$

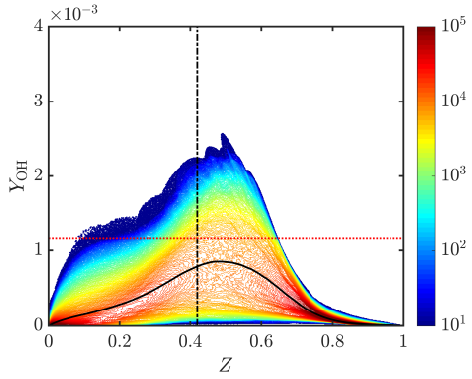

(f) $t/t_{\mathrm{ref}} = 30$

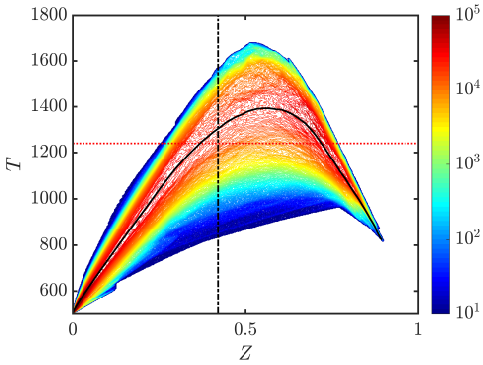

(g) $t/t_{\mathrm{ref}} = 40$

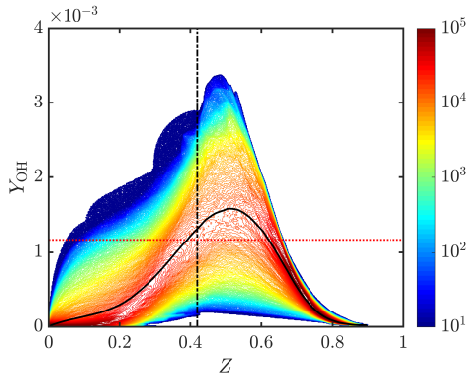

(h) $t/t_{\mathrm{ref}} = 40$

Figure 4.14.: Joint probability density functions for $t/t_{\mathrm{jet}} = 10, 20, 30, 40$ for: (a), (c), (e), (g) temperature and mixture fraction and (b), (d), (f), (h) OH mass fraction and mixture fraction. The black solid line and red dashed line indicate the conditional mean and quenching value, respectively. The vertical dash-dotted line indicates Z_{st}.

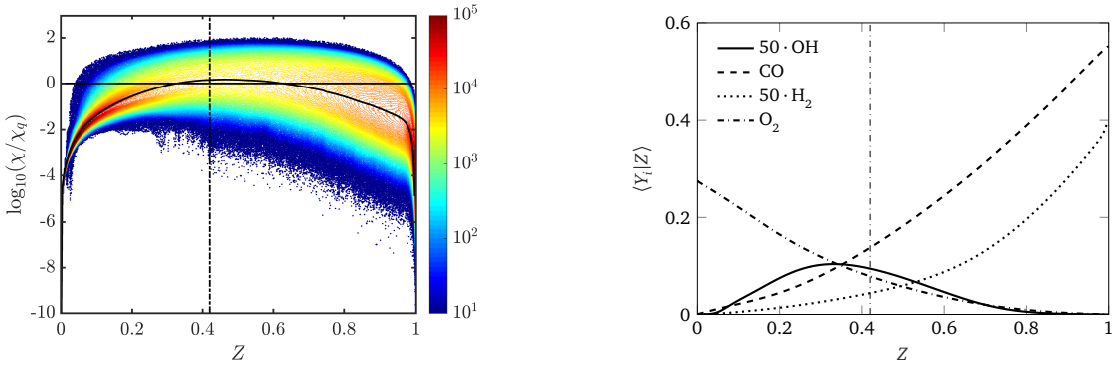

(a) $t/t_{\text{ref}} = 10$

(b) $t/t_{\text{ref}} = 10$

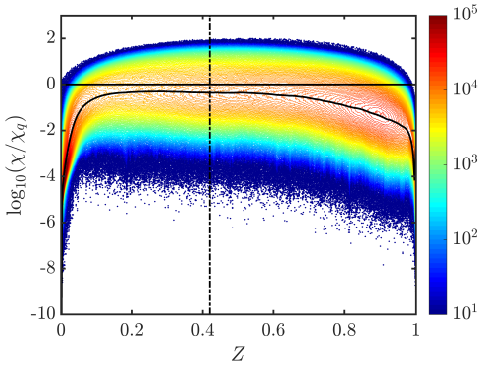

(c) $t/t_{\text{ref}} = 20$

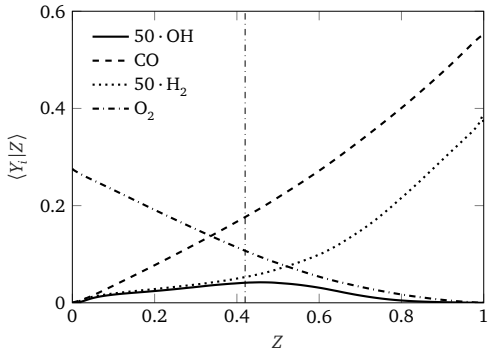

(d) $t/t_{\text{ref}} = 20$

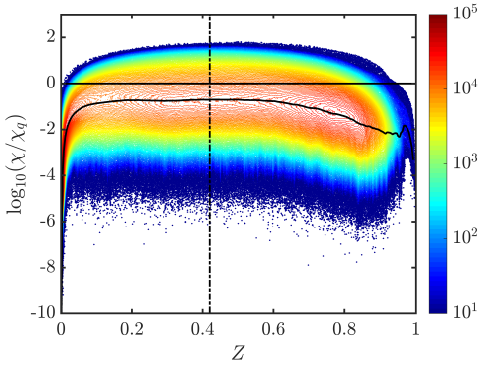

(e) $t/t_{\text{ref}} = 30$

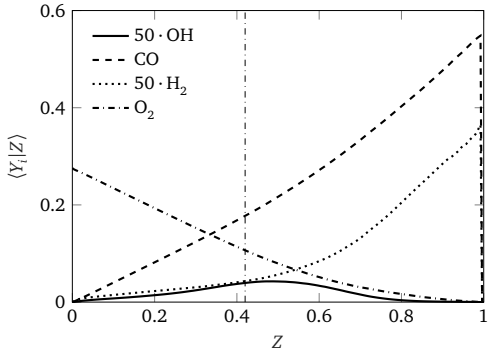

(f) $t/t_{\text{ref}} = 30$

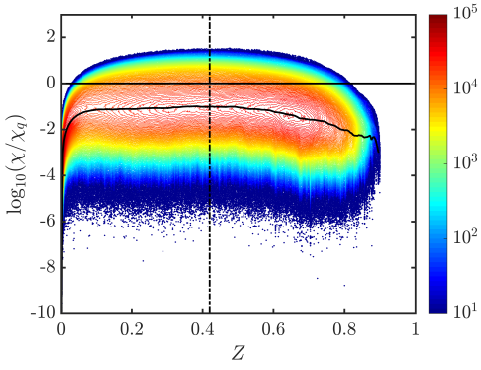

(g) $t/t_{\text{ref}} = 40$

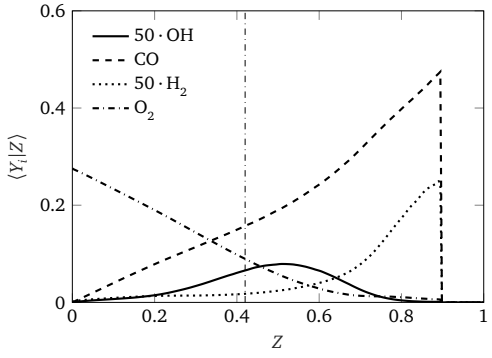

(h) $t/t_{\text{ref}} = 40$

Figure 4.15.: Flame structure statistics for $t/t_{\text{jet}} = 10, 20, 30, 40$ for: (a), (c), (e), (g) the joint pdf of $\log_{10}(\chi/\chi_q)$ and mixture fraction and (b), (d), (f), (h) the mean values of Y_{H_2}, Y_{CO}, Y_{OH}, Y_{O_2} conditioned on mixture fraction. The vertical dash-dotted line indicates Z_{st}.

5 On-The-Fly tracking of flamelet structures

In the past, several authors have proposed new sets of flamelet equations, extended by curvature induced (tangential) transport effects [45–47, 125–128]. In these studies, the extended flamelet formulations have been analyzed by means of

1. steady-state laminar flames [45–47, 125, 126],
2. unsteady laminar flames [45],
3. averaged snapshots of DNS of a jet in crossflow [128] and
4. a single snapshot of a DNS of a spatially evolving jet [47].

While most of these studies were carried out for steady-state laminar flames, also DNS databases of two different turbulent flame configurations were investigated [47, 128]. In these DNS studies, flamelet equations similar to equation (3.41) for the temperature and species mass fractions were analyzed. However, both DNS studies were conducted on single or averaged snapshots of a DNS, and the transient terms in the flamelet equations were not assessable. Furthermore, due to the lack of transient information, budgets of the extended flamelet equations (presented by Scholtissek et al. [47] and Chan et al. [128]) were presented in unclosed form and the impact of the transient term was assessed based on the budgets by implicitly assuming that the extended flamelet equations are closed.

In this work, flamelets are tracked in time and space to explicitly address this shortcoming. The study is facilitated by an on-the-fly tracking algorithm that was developed within the scope of Ref. [127], where the terminology implies that the tracking happens while the simulation is running. Besides restart files for the DNS, only the final trajectories are dumped to disk, which significantly reduces the amount of disk spaces required to study the transient behavior of flamelets. Furthermore, the methodology presented here in detail, allows full flamelet histories to be reconstructed from a DNS and helps to assess the extended unsteady flamelet equations, cf. section 3.2.2.
The chapter is structured as follows: first, a detailed description of the algorithm applied to the DNS of a temporally evolving syngas jet flame is given. Thereafter, the history of three flamelets is recomputed by means of a stand-alone flamelet solver, where all relevant flamelet parameters are extracted from the DNS. The chapter closes with a budget analysis of the extended flamelet equations.

5.1 Tracking algorithm

5.1.1 Principles behind the algorithm

For the description of the tracking algorithm, first figure 3.2 is revisited. Based on the surface attached coordinate system, outlined in section 3.2.2, a reference point P' on a mixture fraction iso-

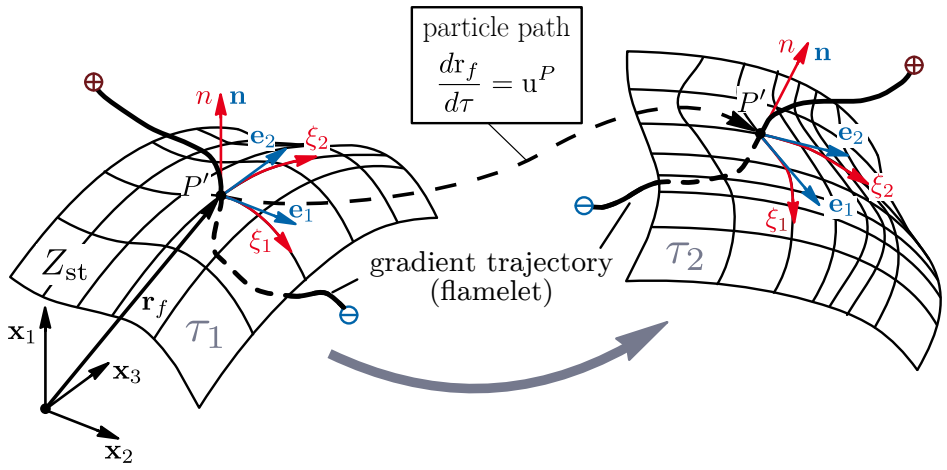

Figure 5.1.: Illustration of the orthogonal coordinate system $n(t,\mathbf{x}), \xi_2(t,\mathbf{x}), \xi_3(t,\mathbf{x})$ attached to the stoichiometric mixture fraction iso-surface. The schematic shows a hypothetical evolution of the surface sheet from Lagrangian time τ_1 to τ_2 together with the corresponding path of the reference point P', marked by the black dashed line.

surface is introduced which denotes the origin of the coordinate system, cf. figure 5.1. In principal P' could be placed on any iso-surface of Z, however, since flamelets are usually associated with the reaction zone, which is located in the vicinity of the iso-surface of stoichiometric mixture [223], the surface of Z_{st} is chosen here. Then, the trajectory of the gradient of Z can be constructed through P' by integrating

$$\mathrm{d}\mathbf{x} = \mathbf{n}\,\mathrm{d}n\,, \tag{5.1}$$

where n is the coordinate aligned with the normalized mixture fraction gradient $\mathbf{n}$. At the same time this definition of a trajectory constitutes a flamelet in three-dimensional space, cf. figure 5.1. Furthermore, since these flamelets shall be tracked in a transient direct numerical simulation, surfaces and thereby also the reference point P' are allowed to move within the computational domain. The position of P' is measured in the laboratory coordinates according to equation (3.17) and thereby the velocity of P' can be computed by

$$\frac{\mathrm{d}\mathbf{r}_f}{\mathrm{d}\tau} = \mathbf{u}^P\,. \tag{5.2}$$

Due to definitions (5.1) and (5.2) the velocity $\mathbf{u}^P$ is associated with the velocity of the iso-scalar surface which according to Gibson [134] is given by

$$\mathbf{u}^P = \mathbf{u} - D\nabla^2 Z \frac{\nabla Z}{|\nabla Z|^2}\,. \tag{5.3}$$

However, this definition is only valid for flows of constant density and constant scalar diffusivity. Thus, for reacting flows, where both parameters are inherently non-constant, the velocity of P' has to be rederived. Revisiting equation (3.32) and using equation (3.8) it can be written

$$\begin{aligned}\frac{\partial \phi}{\partial \tau} &= \frac{\partial \phi}{\partial t} - \frac{\partial Z}{\partial t}\frac{\partial \phi}{\partial Z} + (\mathbf{u} - (\mathbf{u}\cdot\mathbf{n})\mathbf{n})\cdot\nabla\phi \\ &= \frac{\partial \phi}{\partial t} + \mathbf{u}\cdot\nabla\phi - \left(\frac{1}{\rho}\nabla\cdot(\rho D_Z \nabla Z) - \mathbf{u}\cdot\nabla Z\right)\frac{\mathbf{n}}{|\nabla Z|}\cdot\nabla\phi - (\mathbf{u}\cdot\mathbf{n})(\mathbf{n}\cdot\nabla\phi) \\ &= \frac{\partial \phi}{\partial t} + \left(\mathbf{u} - \frac{1}{\rho|\nabla Z|}\nabla\cdot(\rho D_Z \nabla Z)\,\mathbf{n}\right)\cdot\nabla\phi\,, \end{aligned} \tag{5.4}$$

which constitutes the velocity $\mathbf{u}^P$

$$\mathbf{u}^P = \mathbf{u} - \frac{1}{\rho|\nabla Z|}\nabla\cdot(\rho D_Z \nabla Z)\mathbf{n}\,. \tag{5.5}$$

This formulation accounts for both transport due to the convection of the flow field and the molecular diffusion of the iso-scalar surface.
With the definition of the curvilinear coordinate system and its velocity within three-dimensional space, the tracking of multi-dimensional flamelet structures is a straight forward approach. The on-the-fly tracking procedure is based on a technique called flame element tracking which was already proposed by Sripakagorn et al. [224]. In their work, flame elements denote single points on the surface of stoichiometric mixture, which were used by the authors to evaluate local flame characteristics, including different extinction and reignition scenarios. Furthermore, they were also able to access the time history of the individual flame elements. In this work, the concept of flame element tracking is extended to not only track single points in space, but complete flamelet-like structures. The algorithm can be split into three phases which will be described in more detail in the following.

Initialization phase

First, during phase I, the initialization of the algorithm, massless particles are randomly distributed across the stoichiometric surface $Z(t,\mathbf{x}) = Z_{st} = 0.42$. Note that it is not possible to attach the particles directly to the stoichiometric surface, because, due to the numerical discretization the stoichiometric surface may reside on the subgrid, i.e. between computational cells. However, the particles were initially distributed within a narrow band of $0.95 \cdot Z_{st} = 0.40$ and $1.05 \cdot Z_{st} = 0.44$, to ensure that they are close to the reaction zone. Thereby, it is assumed that the reaction zone can be represented by the instantaneous stoichiometric surface [116]. Furthermore, the band width of $0.40 < Z < 0.44$ was chosen to be well below the reaction zone thickness $(\Delta Z)_\mathrm{R} = 0.25$, where $(\Delta Z)_\mathrm{R}$ was estimated from steady laminar flamelet calculations with the help of equation (3.54) with $\phi = T$. A snapshot of the initialization is shown in figure 5.2. Note, that the tracking procedure is not started from the very beginning of the DNS since turbulence has to be evolved before useful information can be gained from the tracking procedure. It is rather initiated after the turbulent

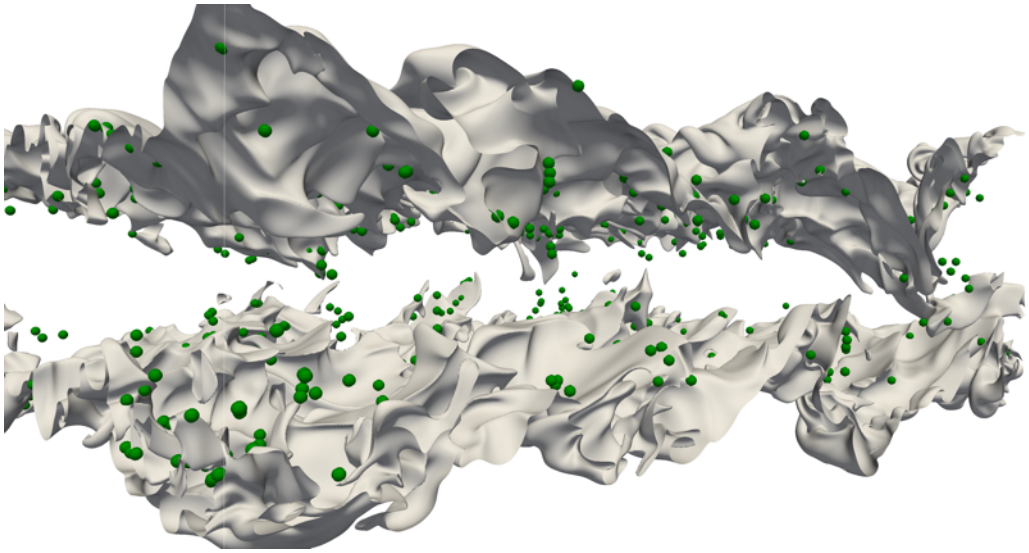

Figure 5.2.: Snapshot of the stoichiometric iso-scalar surface of mixture fraction together with randomly distributed particles. These particles are used during the on-the-fly tracking procedure.

flow field has reached a self similar state, see section 4.2.5. After each particle has been assigned a unique identifier that is fixed for all times the algorithm proceeds to phase II, the actual tracking procedure.

Tracking phase

The second phase can be seen as a twofold process that involves the temporal advancement of particles and the subsequent emission of gradient trajectories. For the first process, figure 5.1 shows a hypothetical evolution of the stoichiometric surface sheet from Lagrangian time τ_1 to τ_2 together with the corresponding path of a particle P'. Since Z_{st} is defined as the thermo-chemical reference state for the flamelet analyses and a Lagrangian flamelet formulation according to equation (3.32) is used, it must be ensured that particles stay on their initial surface. Therefore, revisiting equation (5.5) the positions of particles are updated by integrating the equations of motion for each single particle, i.e.

$$\mathbf{x}^P_{n+1} = \mathbf{u}^P \Delta t + \mathbf{x}^P_n \,, \tag{5.6}$$

which corresponds to a simple explicit Euler forward integration. The integration step (5.6) is executed after a Runge-Kutta step for the Eulerian phase is completed, that is all flow field quantities have been advanced to the next time level.

For serial simulations the integration of equation (5.6) is trivial. However, in parallel simulation frameworks, like *DINO* , it has to be considered that particles do not necessarily reside on the same processor during the course of the simulation. Hence, particles may cross processor boundaries, which has to be accounted for by providing a dedicated parallel communication infrastructure. This communication layer is build on top of the Message Passing Interface (MPI), which allows to

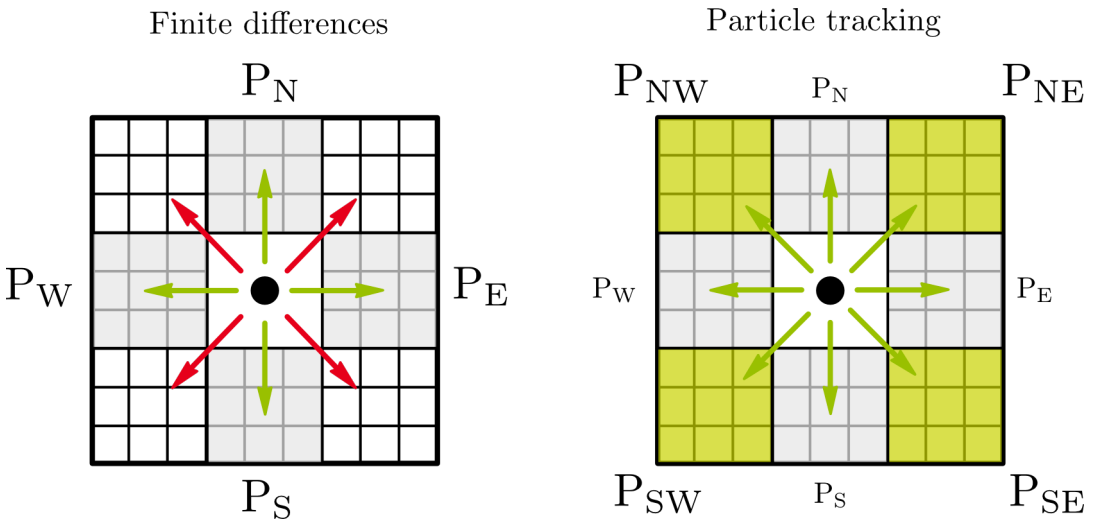

Figure 5.3.: Illustration of ghost cell communication patterns. The schematic illustrates the difference between the approaches for finite difference computations and the particle tracking algorithm employed here. The processors are marked by their location with respect to the sending processor. Arrows indicate possible communication patterns.

build up a layer of ghost cells[1] around each processor. These ghost cells are used to access data that resides on a neighbouring processor. The parallel decomposition of the domain is the same for both, the Eulerian and the Lagrangian phase, see figure 4.1. This principle of parallelization, by statically assigning components of the mesh (blocks) to processors, is also referred to as static allocation principal [225]. During the course of the simulation the path of each particle is integrated, according to equation (5.6) until it leaves the block owned by the current processor. As each particle is allowed to move between blocks, it is communicated to the processor that owns the block in which it currently resides. This communication is based on the non-blocking MPI collectives `MPI_ISend` and `MPI_IRecv`, where the data to be transmitted is repacked into a buffer vector. During this procedure all processors maintain a globally communicated particle counter, so that all processors may monitor how many particle paths have yet to be integrated. Once this counter reaches zero, all particles have been successfully advanced and the tracking algorithm proceeds with the next step. Although *DINO* is already built on top of `2DECOMP&FFT`, that allows for parallel communication, an additional communication layer is required to access data on diagonally adjacent processors as illustrated in figure 5.3. In contrast to “standard” ghost cell communication used for finite difference computations, the new communication pattern allows particles to also leave processors towards the corners of their respective domain. This step is crucial for the particle tracking procedure, since otherwise particles would get lost which would lead to an inconsistent flamelet history. Processors that are located at the physical domain boundary, communicate with processors at the opposite site of the domain, which corresponds to periodic boundary conditions for the particle (Lagrangian) phase. Note, that this definition of boundary conditions is independent from the choice of boundary conditions for the Eulerian phase and was chosen for the sake of simplicity. Furthermore, it is pointed out that these conditions do not influence the later following analyses of flamelet structures since particles that would leave the domain towards the cross-stream direction are in a non-burning

[1] Ghost cells are also often referred to as halo cells.

environment which is of no interest for the analyses.
Though the integration of equation (5.6) seems to be a straight forward approach, there are, however, non-trivial numerical difficulties to be overcome. During the integration procedure particles traverse points located in the subgrid, which requires to have an accurate interpolation of $\mathbf{u}^P$ at these locations. According to Yeung and Pope [226] an accurate interpolation in the context of particle tracking is a difficult task, since the Eulerian velocity fields vary greatly in space in a nonlinear manner. Due to the diffusive nature of turbulence, numerical errors in particle tracking grow rapidly in time. It is thus imperative to have an accurate interpolation scheme [226]. Therefore, a tricubic interpolation procedure [227, 228] is used to accurately determine velocity data at the subgrid positions. The additional CPU time spent for the interpolation of the velocity data and the integration of particle paths is only a small fraction of the time taken for the evaluation of the right-hand sides of equations (2.44) to (2.46) in the Eulerian framework. Hence, the computational overhead due to particle tracking is negligible.

After all particles have been successfully advanced onto their new positions, the emission of gradient trajectories (flamelets) is triggered, where particles serve as an initial point (seed point) for the subsequent tracking of flamelets. At the same time this method ensures that flamelets could be uniquely identified over time by using the particle identifier mentioned earlier. The principals behind the flamelet tracking are the same as for the particle tracking if each point of the flamelet is regarded as a hypothetical particle position. Hence, the same computational methods, like ghost cell communication, integration and interpolation, could be employed. Also the `MPI`-collectives for sending and receiving trajectories between processors are the same, though the underlying data structures (buffers) are different. However, particles are advanced in the time domain, while trajectories (flamelets) are advanced in the spatial domain. Hence, the flamelets are advanced through the gradient of Z, as already outlined by equation (5.1). The integration for one step reads

$$\mathbf{x}^F_{n+1} = \mathbf{n}\Delta x^F + \mathbf{x}^F_n = \frac{\nabla Z}{|\nabla Z|}\Delta x^F + \mathbf{x}^F_n\,, \tag{5.7}$$

where Δx^F denotes a fraction of the computational mesh and is set to $\Delta x^F = 0.1\min(\Delta x, \Delta y, \Delta z)$ to capture critical points, possibly located in the subgrid. For the later following flamelet analyses these critical points are required to be local extremal points of the mixture fraction field and the integration (5.7) is performed until both, the local minimum and maximum for each trajectory were reached.
In principle all points of the scalar field Z could be characterized as either critical or non-critical. While at non-critical points trajectories will smoothly advance along the gradient of Z, the gradient of Z vanishes at critical points and $\mathbf{n}$ becomes undefined, which requires a special detection criterion for critical points. Within the tracking algorithm, it is assumed that a critical point is reached as soon as the absolute value of the scalar gradient becomes smaller than a given threshold value $\epsilon_{|\nabla Z|}$, which is set to $\epsilon_{|\nabla Z|} = 50$ for the present study. However, for the proper detection of local extremal points, speaking in mathematical terms, this is only a necessary but not a sufficient condition and an additional evaluation of the eigenvalues of the Hessian of Z is required. In case these eigenvalues are either all positive (minimum point) or all negative (maximum point) at a

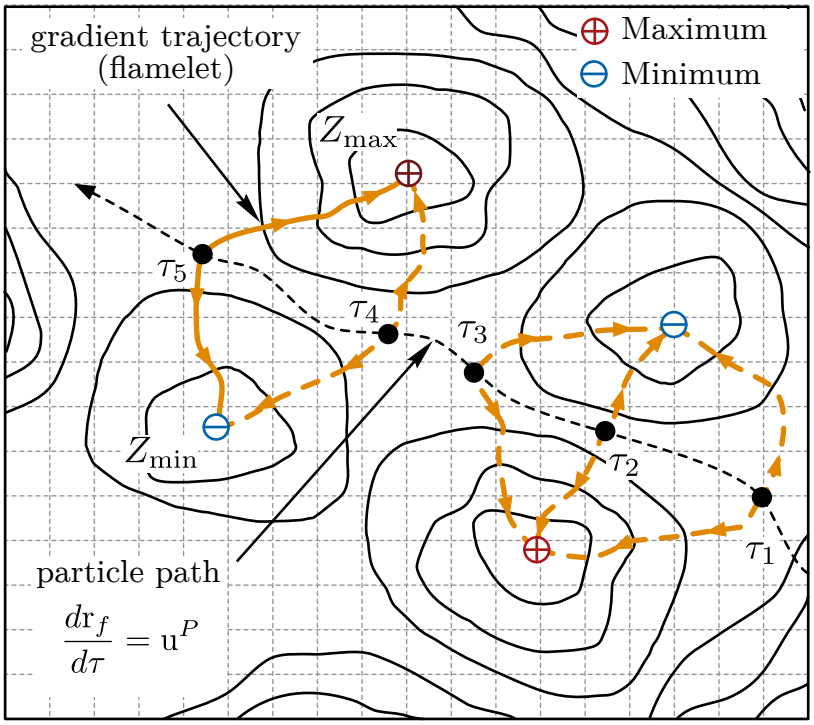

Figure 5.4.: Schematic of the gradient trajectory tracking algorithm. The particle, that emits the trajectory, is marked with a black dot. Local maxima and minima are represented by a red plus and blue minus, respectively. Furthermore, hypothetical trajectories are shown for five different instants in time.

critical point, then this renders the critical point to be a local extremum. In case there exist both negative and positive eigenvalues, the critical point is a saddle point which would requires further treatment.[2] Saddle points, however, are difficult to address in the tracking framework, since a decision has to be made in which direction the algorithm should proceed to reach the actual local extremum. A random-walk strategy [229] seems to be a promising approach to avoid the evaluation of the Hessian and to surmount saddle points. For this technique, once a trajectory approaches a saddle point, its direction will be randomly diverted and forced to advance with a small pace in some random direction. However, in a `MPI`-parallelized framework random-walks are unfeasible since for each walk, according to equation (5.7), multiple `MPI`-collectives are possibly triggered, if the trajectory leaves the current processor which eventually leads to a tremendous communication overhead. Therefore, due to the computational and numerical complexity associated with saddle points, they are not specifically treated by the algorithm, which might lead to a false detection of local extremal points.

Due to numerical accuracy, sometimes certain degenerated cases might occur, when approaching extremal points. In these cases trajectories do not strictly follow the gradient towards extremal points, but rotate infinitely around the extremal point and $|\nabla Z|$ falls never short of the predefined threshold value $\epsilon_{|\nabla Z|}$. This infinite looping may appear whether the local extremum is located in the subgrid or directly on a grid point and needs a secondary condition after which the tracking is aborted. In addition to the $\epsilon_{|\nabla Z|}$ criterion the tracing is forcedly stopped after 5000 data points were

[2] In case there exist eigenvalues which are zero at a critical point, further treatment is necessary before a decision could be made.

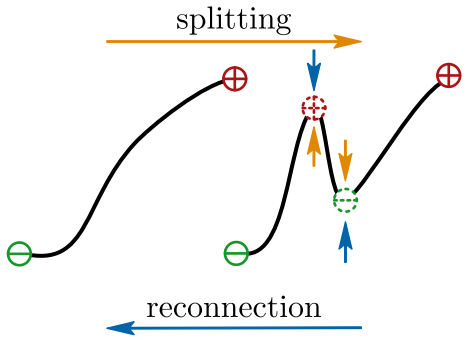

Figure 5.5.: Simplified illustration of a splitting and reconnection event in one-dimensional space.

gathered for one trajectory. Both threshold values were determined empirically and were found to be a good compromise between accuracy and computational effort.
A schematic of the trajectory tracking is given in figure 5.4, where 5 hypothetical particle positions together with the corresponding trajectories are shown. From this illustration it is obvious that a trajectory and, hence, also the flamelet might change its connectivity to the local extremal points. This change in connectivity might happen due to two reasons. First, since the particles move in space, the connectivity changes due to their proximity to different extrema. Second, extremal points are either annihilated due to molecular diffusion or they are created due to turbulent motion [230, 231]. This process, also known as splitting and reconnection [134, 229], is further illustrated in figure 5.5.
While the change in connectivity has no meaning for the trajectory itself, it has important implications for the flamelet analyses, as will be discussed later. To give a visual impression of the results of the tracking algorithm, figure 5.6 shows results of the application to the three-dimensional DNS discussed in [127]. Furthermore, figure 5.7 shows two exemplary trajectories giving an indication of the diversity with which trajectories appear in DNS of turbulent reactive flows.

Postprocessing phase

The analyses of the extended flamelet equations, require additional data from the DNS which has been pre-computed and interpolated during the tracing of trajectories. Once all trajectories have been tracked until they met one of the stopping criteria mentioned earlier, the trace of each trajectory together with the data is dumped to disk. Since the data resides on different processors and writing the data in a serialized manner is particularly inefficient for large scale DNS, the tracking algorithm has a parallel IO layer build on top of `HDF5` [232]. The total disk space required for trajectories tracked in the present DNS is nearly 4.5 TB ($\approx$ 400 trajectories). Although, the number of tracked flamelets seems to be small, it has to be envisioned that the whole tracking procedure (phases I-III) has to be conducted during each single DNS time step in order to capture all relevant thermo-chemical effects.

5.2 Application to the reactive syngas jet

In this section the on-the-fly tracking procedure is applied to the direct numerical simulation presented in section 4.2.5. The tracking algorithm is coupled to the DNS solver *DINO* and the

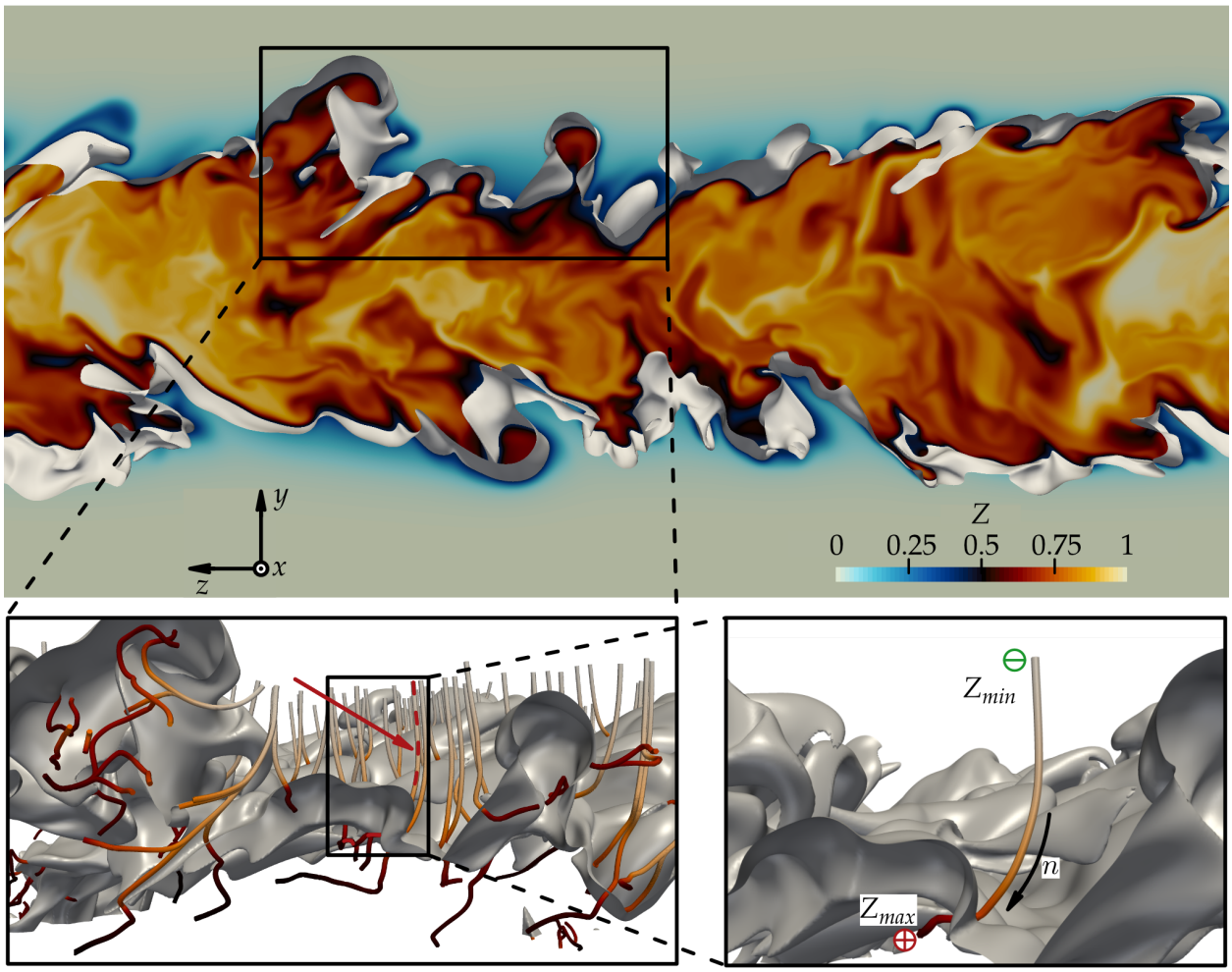

Figure 5.6.: Top: Snapshot of the direct numerical simulation conducted in [127] together with the stoichiometric mixture fraction iso-surface ($Z = Z_{st}$). Bottom left: gradient trajectories (flamelets) that intersect the stoichiometric mixture fraction iso-surface. Bottom right: realization of a single flamelet.

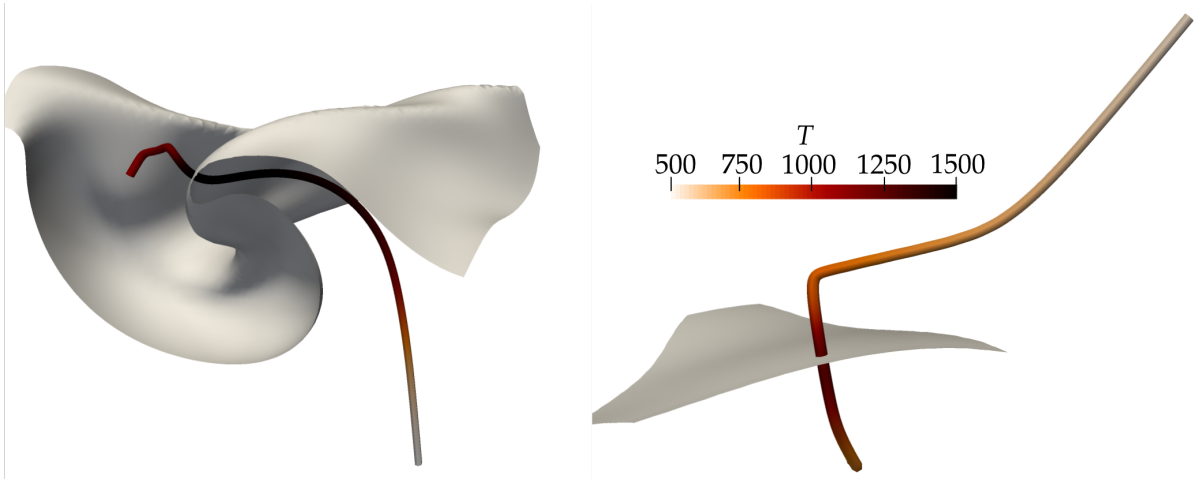

Figure 5.7.: Two exemplary trajectories that were tracked in a direct numerical simulation [127]. While both trajectories intersect the surface of stoichiometric mixture fraction, they are colored according to the temperature field.

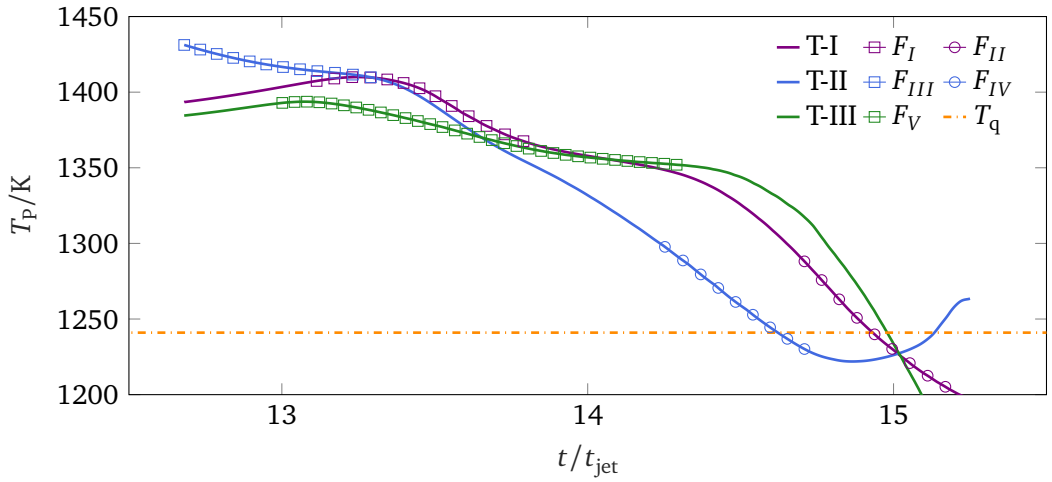

Figure 5.8.: Evolution of temperature T_P of the tracer particle for three exemplary trajectories T-I, T-II and T-III. Along these trajectories, five flamelet identities F_I to F_V are identified, which are examined in detail in this section. One marker represents at least 30 data points, to improve clarity in the figure. The dash-dotted line marks the temperature near extinction obtained from a representative steady laminar flamelet calculation.

simulation is restarted after the jet has reached $t/t_\mathrm{jet} \approx 12.5$. While nearly 400 trajectories are tracked in the simulation, special attention is paid to trajectories that satisfy the following criteria:

1. the flame temperature is above the flame temperature at extinction T_q at least once during the tracking period and

2. the temperature range observed at stoichiometry is larger than $\Delta T = 150\,K$.

The latter condition ensures a certain dynamic in the thermo-chemical state of the flamelet to be analyzed. According to these criteria three exemplary trajectories, T-I, T-II and T-III, have been extracted and the evolution of temperature at their respective seed point is shown in figure 5.8. Further, for each trajectory, flamelet identities that have been identified are highlighted by symbols. At this point it is important to make a clear distinction between the different terminologies used so far. While the terms flamelet and gradient trajectory could be used interchangeably, flamelet identities are different by conception. In the previous section it has been outlined that trajectories might change their connectivity to the local extremal points due to morphological changes of the underlying scalar field (splitting and reconnection of extremal points). Although the trajectories still run along the ascending and descending gradient until local maxima are reached, sudden changes in the connectivity also causes a change in the boundary conditions to be imposed for the flamelet equations. Hence, each time a sudden event (splitting or reconnection) is detected, a new flamelet identity is created. However, slow changes due to continuous homogenization of the scalar fields by turbulent mixing can be accounted for by applying an additional transformation to equation (3.41). According to Pitsch [27], moving boundaries can be accounted for if the flamelet equations are transformed into (τ, ζ) space, where ζ varies between 0 and 1 and is defined as

$$\zeta = \frac{Z - Z_\mathrm{min}}{Z_\mathrm{max} - Z_\mathrm{min}} = \frac{Z - Z_\mathrm{min}(\tau)}{\Delta Z(\tau)}. \tag{5.8}$$

Here, $Z_{\min}$ and ΔZ change with time, such that the transformation introduces additional convective terms into the flamelet equations. Details about the additional transformation steps can be found in [127] and are skipped her for brevity. To distinguish between fast and slow changes of the boundary conditions, the relative change of ΔZ, $\delta_{r,\Delta Z}$, between two consecutive time steps serves as a measure. For the present study $\delta_{r,\Delta Z}$ was set to $\delta_{r,\Delta Z} = 0.02$. According to this criterion five flamelet identities, F_I to F_V, are identified and are marked by the symbols in figure 5.8.

Applying the tracking procedure to the turbulent reactive syngas jet facilitates detailed analyses of the flamelet equations, since additional information from the DNS is required for that purpose. In the remainder of this chapter the individual flamelet identities F_I to F_V, see figure 5.8, will be analyzed with respect to their transient behavior and the impact of curvature induced transport is assessed.

5.2.1 Analysis of flamelet histories

The history of the flamelet identities F_I to F_V is analyzed by means of a flamelet solver that is part of the solver package *ULF* [211]. Based on the transient data extracted along the gradient trajectories, the history of the individual flamelet identities is reconstructed by solving the extended flamelet equations (3.41) for the temperature T and the species mass fractions Y_i. To this end, the flamelet parameters that require three-dimensional gradient information, i.e χ, κ_Z and the multi-dimensional terms Γ_T and Γ_{Y_i}, are provided as an input to the flamelet solver.
The importance of curvature induced flame-tangential transport for the individual flamelet identities is assessed by considering three scenarios:

1. FLT: flame-tangential effects are neglected (terms Λ^T_{MD}, Λ^Y_{MD}, $\Lambda^Y_{\mathrm{curv}}$); classical flamelet,
2. FLT-C: only the curvature-based effect $\Lambda^Y_{\mathrm{curv}}$ is considered,
3. FLT-MD: curvature-based and multi-dimensional effects are considered.

While in the first scenario, the extended formulation (3.41) simplifies to the flamelet model proposed by Pitsch [27], the last scenario considers all effects contained in the extended formulation.

Flamelet identities are recomputed according to the scenarios FLT, FLT-C and FLT-MD, where the flamelet solver is restarted for each integration step. While the quantities χ, κ_Z, Γ_T and Γ_{Y_i} are updated according to the extracted trajectory data of the current time instant, the temperature T and mass fractions Y_i are solutions of this procedure. The time step taken to advance the flamelet equations is the same as in the DNS.

Figure 5.9 shows the temporal evolution of the temperature of the seed point, T_P, of the three gradient trajectories T-I, T-II and T-III. In addition, the flamelet identities, which were identified according to the criterion mentioned above, are highlighted by the symbols. Among other flamelet identities found along the temporal evolution of the trajectories, these are chosen according to a certain "lifetime". To give an impression of what is meant by "lifetime", an example of a trajectory having a long "lifetime" is given in figure 5.9c. The horizontal dash-dotted line marks the temperature

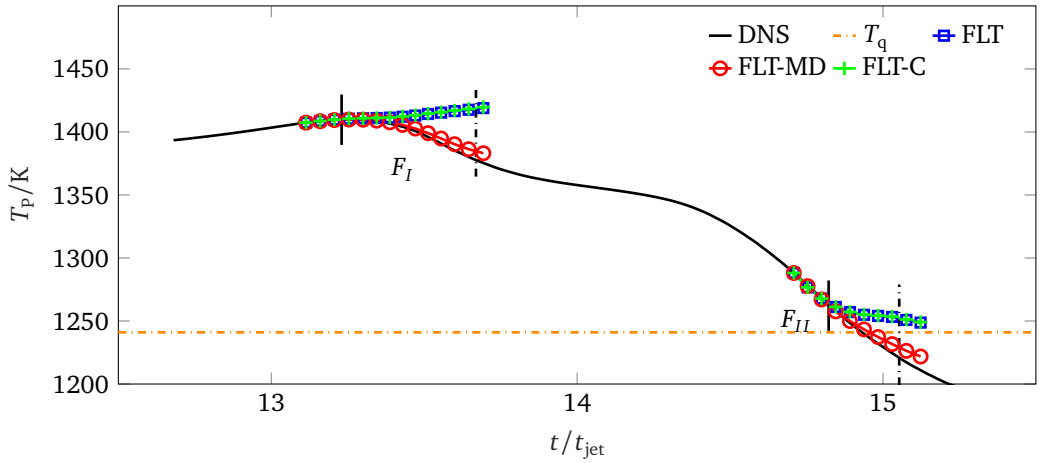

(a) T-I

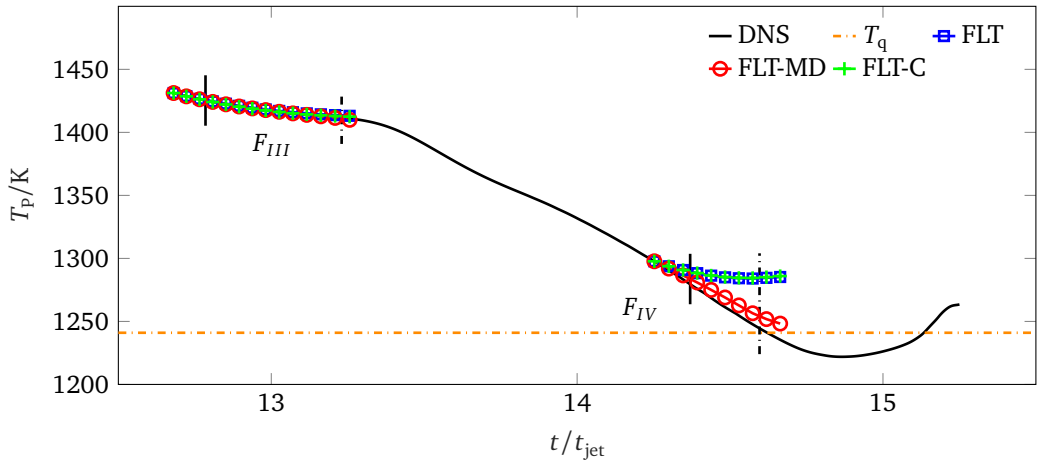

(b) T-II

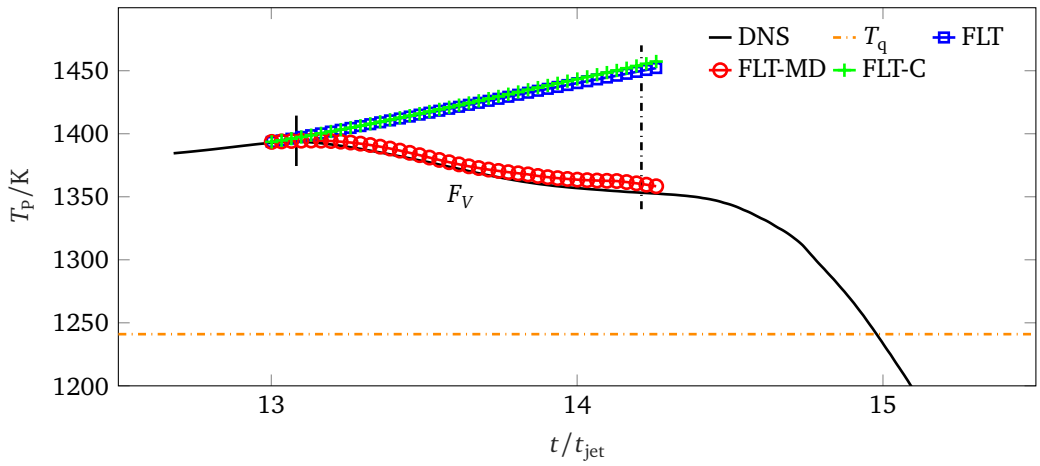

(c) T-III

Figure 5.9.: Time history of the seed point temperature of the gradient trajectories T-I, T-II and T-III. Recomputed flamelet identities are marked by symbols, where squares and pluses mark the flamelet solution according to scenarios 1 and 2, respectively. The circles indicate solutions that were obtained with the complete set of extended flamelet equations.

near extinction, $T_q = 1241\,\mathrm{K}$, obtained from steady laminar flamelet calculations, see section 4.2.3. This temperature only serves as a reference value and could be different for the individual flamelet identities, since changes in Z_{min}, Z_{max}, the χ-profile and the initial thermo-chemical state could lead to different temperatures at extinction.

A first general observation for all trajectories is that their seed point temperature T_P initially resides well above the quench temperature and shows a decrease towards T_q. Eventually T_P drops below T_q for all trajectories, indicating a process of local extinction which also agrees with the statistics obtained from the DNS, see section 4.2.5. Although, T-II seems to traverse a region of reignition at the end of its tracking, around $t/t_{\mathrm{ref}} \approx 15$. Furthermore, the slope with which the temperature decreases is significantly different between the trajectories, indicating that T-I to T-III traverse through regions with different straining and mixing intensities. At the same time, this ensures a certain diversity in the flamelet identities to be analyzed.
Having a look at the identities F_I and F_{II} and comparing them to the trajectory history extracted from the DNS, it is noted that for both identities the FLT and FLT-C approach fail to reproduce the flamelet history. Only during the early stages of the identities they are able to follow the slope. Towards later times, at the point where FLT and FLT-C start to diverge from the DNS data, both approaches even predict a temperature increase. This can be attributed to the neglection of the multidimensional terms, since, on the other hand, the FLT-MD model (including curvature and multi-dimensional effects) closely follows the original data. Only, towards the end of the flamelet identities some slight deviations occur, which might be attributed to numerical issues. Similar observations could be made for the flamelet identities F_{IV} and F_V found along the trajectories T-II and T-III, respectively. In contrast, for F_{III} also the FLT and FLT-C model are able to reproduce the temperature evolution, suggesting that the multi-dimensional terms are negligible in the vicinity of stoichiometry for F_{III}.
Giving an intermediate summary, these observations indicate that although regions exist where the classical flamelet model is able to reproduce the DNS results, there exist multi-dimensional effects in the setup and only the FLT-MD model is able to accurately reproduce all flamelet identities. Although this is to be expected, since all external flamelet parameters (χ, κ and $\Gamma^{(T,Y_i)}$) are extracted from the DNS, these results confirm the validity of the tracking algorithm, cf. section 5.1, and the procedure of extracting data along gradient trajectories by tricubic interpolation [227, 228].

The analyses of flamelet histories is complemented by having a closer look onto variables in flamelet space. Therefore, figures 5.10 to 5.12 show the flame structure (top), the scalar dissipation rate χ and the curvature κ_Z (middle), and a regime classification according to explanations given in section 3.2.2 (bottom). The results were obtained by directly extracting the data from trajectories T-I, T-II and T-III without any interposed flamelet solver. Due to the transient nature of the flamelet identities, also the corresponding profiles in mixture fraction space evolve with time. To better illustrate this temporal evolution, each plot in figures 5.10 to 5.12 shows two instants in time (solid and dash-dotted lines). The corresponding time instants are marked by the vertical solid and dash-dotted line in figure 5.9. They were chosen to allow for a direct comparison of the profiles in mixture fraction space at the beginning and ending of each flamelet identity.

A first general inspection of the flame structures reveals, that the overall shape of the turbulent flamelet identities is similar to conditional means shown in figure 4.15 and to the laminar flamelet profiles depicted in figure 4.7a, which was used to initialize the DNS. All identities show a temperature maximum near Z_{st}, although, compared to the laminar flamelet, the peak is shifted towards the oxidizer. Further, deviations from the laminar flame structure exist for F_{II}, F_{IV} and the later instant of time of F_V, cf. figures 5.10b, 5.11b and 5.12a. At the same time, for F_{IV} and F_V, the fuel side boundary is shifted towards Z_{st} (indicated by the dashed vertical line), resulting in $Z_{\max} < 1$. It is further interesting to note, by comparing identities F_{III} and F_{IV}, cf. figures 5.11a and 5.11b, lying on the same trajectory T-II, that within ≈ 1.5 dimensionless times the position of the fuel side boundary has shifted by almost 15 % in mixture fraction space, which again highlights the importance of defining different flamelet identities.

Next the profiles of scalar dissipation rate and curvature together with the regime classification according to section 3.2.2 are analyzed in detail. First, having a look at the flamelet identities F_I and F_{II}, situated on T-I, figures 5.10c and 5.10d show the development of χ and κ_Z in mixture fraction space. Although, the flame structures of F_I and F_{II} show similarities to laminar flamelet solutions, the scalar dissipation rate profiles look significantly different to what is usually obtained for laminar counterflow flames. To better illustrate the differences, a χ-profile obtained from equation (3.16) which was scaled with χ_{st} from the DNS is also plotted in figures 5.10c and 5.10d for reference and is denoted by $\chi_{\text{erfc}^{-1}}$. Further, the value of the scalar dissipation rate near extinction, $\chi_{\text{q,st}}$, is also marked in the plots. Similar to the temperature near extinction T_{q}, the value of $\chi_{\text{q,st}}$ serves as a reference and could be different for the individual flamelet identities.
Both, F_I and F_{II} exhibit a peak in the χ-profile that exceeds the scalar dissipation rate near extinction by nearly one order of magnitude and is shifted towards the fuel side. At the same time, the curvature profile peaks in regions where the scalar dissipation rate is small. This opposing trend in the χ and κ_Z-profiles is also clearly deducible from the regime classification in figures 5.10e and 5.10f. Both flamelet identities show a regime transition from R-I (classical flamelet regime) to R-III (multi-dimensional flamelet regime) around stoichiometry and F_I shows a second transition on the fuel rich side, where the different regimes are identified based on the limits given in table 3.1. The asymptotic parameter ε, used for the regime detection, is determined with the help of equation (3.55) and the temperature as the reference quantity. It was estimated at $\varepsilon = 0.25$, based on laminar flamelet calculations. The locations at which the regime transitions occur clearly coincide with the locations at which χ becomes small and κ_Z increases. Furthermore, it can be noted that the transitions itself exhibit a sharp interface between regimes R-I and R-III, such that R-II barely exists in the small corridor highlighted by the dashed horizontal lines in figures 5.10e and 5.10f. This emphasizes that, in case curvature is present, multi-dimensional effects (FLT-MD) are dominant over other curvature terms in the flamelet equations. This also might explain why the FLT-C approach in figure 5.9 performs equally poor as FLT for all flamelet identities, except for F_{III}. Applying the same analyses to the flamelet identity F_{III}, different characteristics are found which are in agreement with the findings from the flamelet results shown in figure 5.9b. Figure 5.9b suggests that the multi-dimensional terms are negligible for F_{III}, hence, F_{III} is supposed to be a *classical* flamelet (FLT). Having a look at the corresponding χ and κ_Z-profiles, the peak value of χ

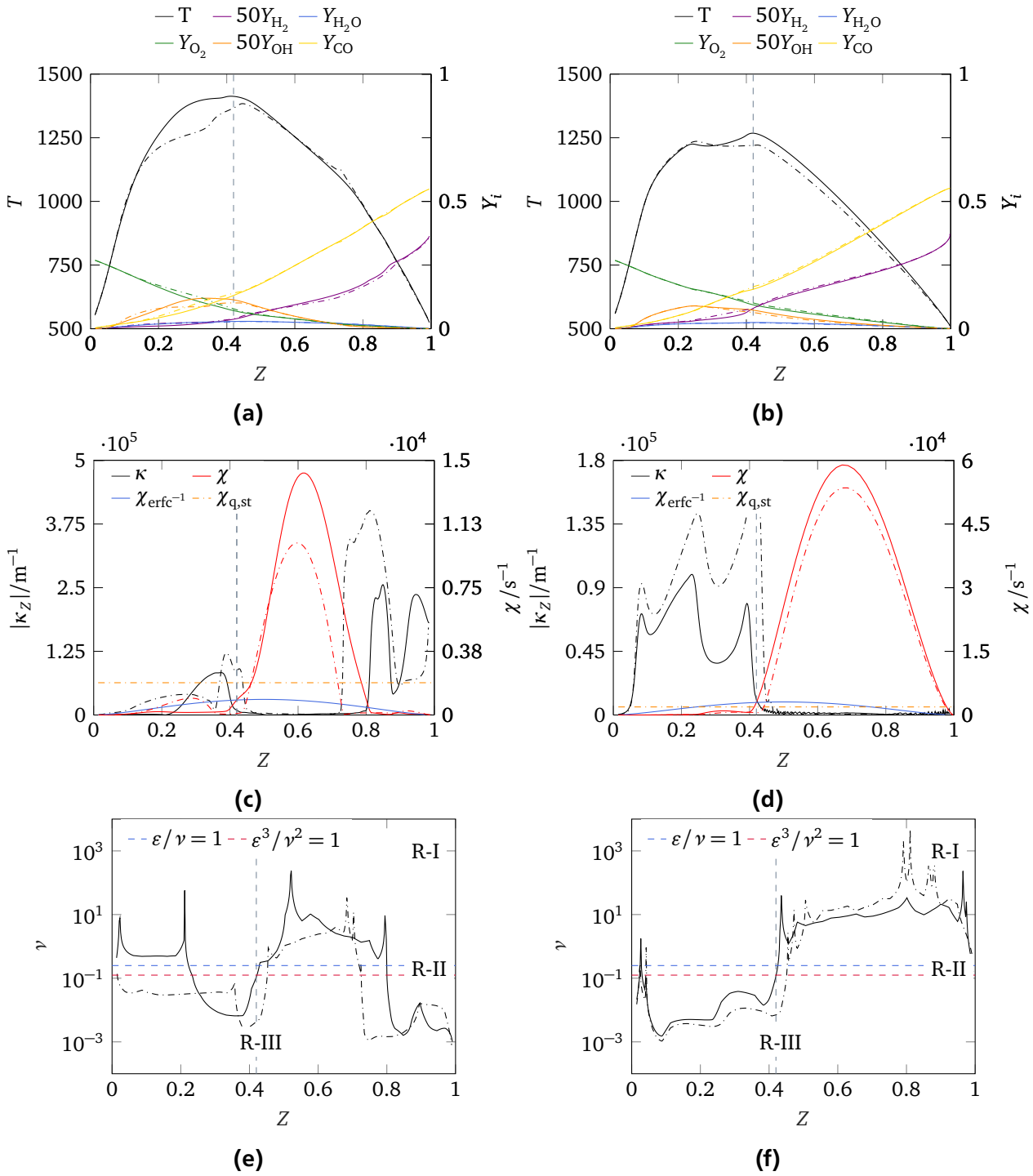

Figure 5.10.: Flame structures and regime classification for the two flamelet identities F_I (left) and F_{II} (right) of the gradient trajectory T-I. Each plot shows two instants in time, marked by the solid and dash-dotted vertical line in figure 5.9a, where the solid line corresponds to an early stage of the corresponding flamelet identity and the dash-dotted line to a later one. In all plots the vertical dashed line marks Z_{st}.

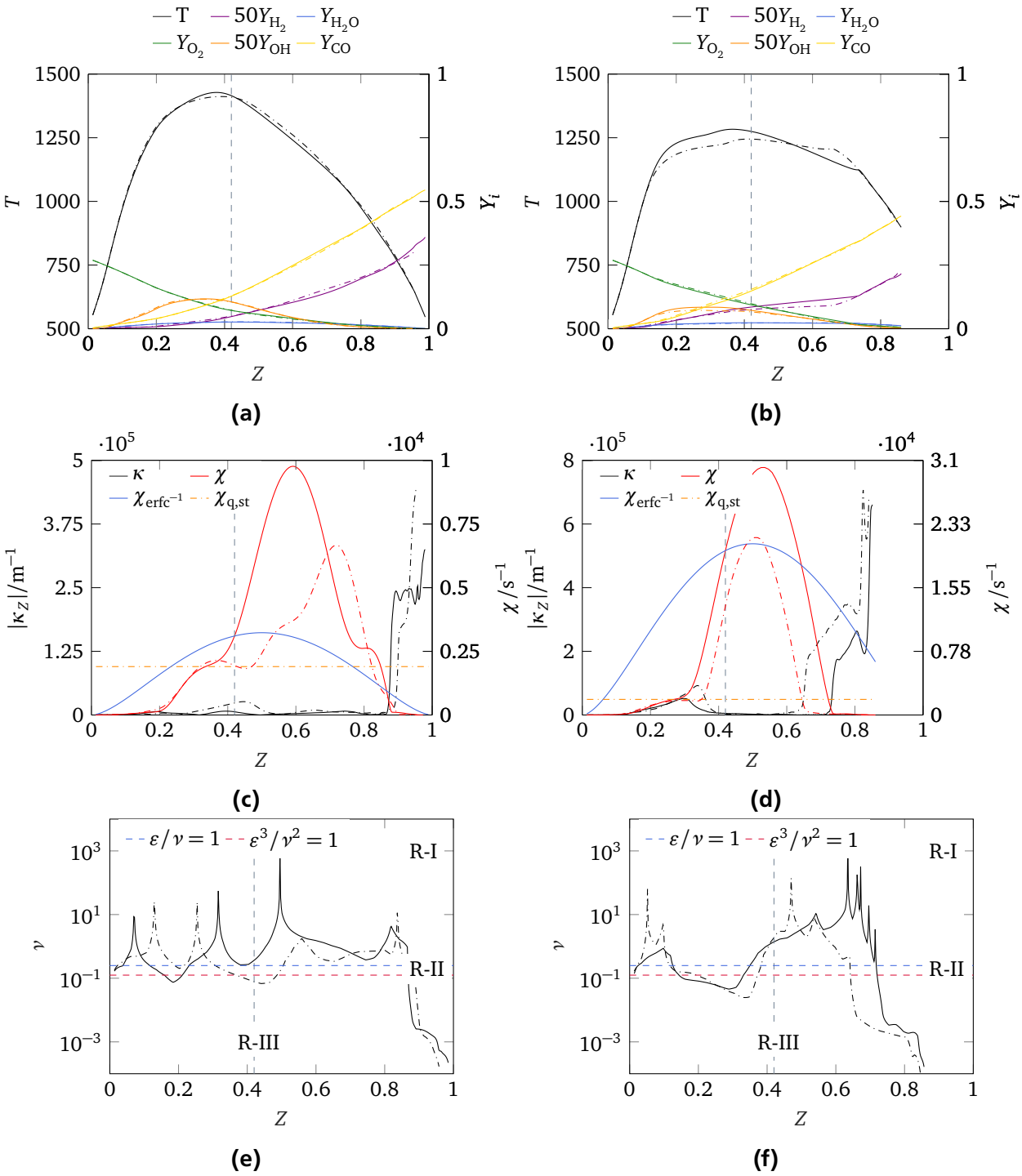

Figure 5.11.: Flame structures and regime classification for the two flamelet identities F_{III} (left) and F_{IV} (right) of the gradient trajectory T-II. Each plot shows two instants in time, marked by the solid and dash-dotted vertical line in figure 5.9b, where the solid line corresponds to an early stage of the corresponding flamelet identity and the dash-dotted line to a later one. In all plots the vertical dashed line marks Z_{st}.

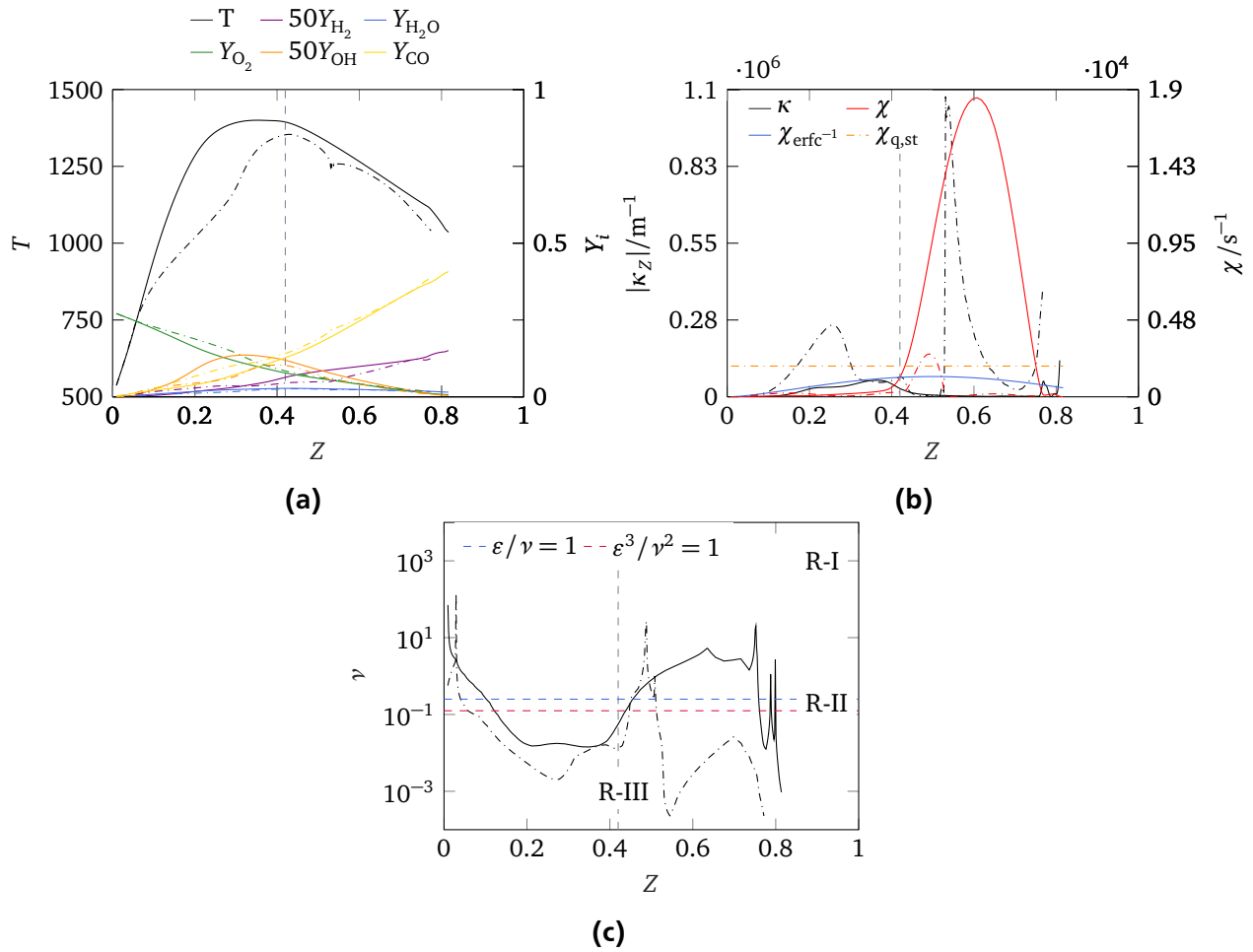

Figure 5.12.: Flame structures and regime classification for the flamelet identity F_V of the gradient trajectory T-III. The plot shows two instants in time, marked by the solid and dash-dotted vertical line in figure 5.9c, where the solid line corresponds to an early stage of the flamelet identity and the dash-dotted line to a later one. In all plots the vertical dashed line marks Z_{st}.

significantly exceeds $\chi_{q,st}$ for both time instants, while κ_Z is almost negligible over the whole range, except towards the right boundary of F_{III}. While this is only a first indication of F_{III} being a classical flamelet, the regime plot also supports this characterization. Looking at figure 5.11e hardly any regime transitions can be observed, which finally proves F_{III} to be a classical flamelet. In contrast, F_{IV} shows a distinct regime transition left of Z_{st} which also coincides with the small curvature peaks seen in figure 5.11f. This, in conjunction with the regime transition towards the right boundary and the corresponding curvature increase leads to the conclusion that relevant multi-dimensional terms are active along F_{IV} which can only be properly captured by the FLT-MD approach, as can be seen in figure 5.9b.

Last, flamelet F_V is examined in more detail. Due to its long "lifetime", cf. figure 5.9c, it is most affected by multi-dimensional effects compared to the other flamelet identities. In the early stage of F_V the profiles of χ, κ_Z and the regime characterization, cf. figures 5.12b and 5.12c, are similar to profiles obtained for F_I, F_{II} and F_{IV}. The scalar dissipation rate has a peak on the fuel side and the curvature similarily on the oxidizer side. Also the regime diagram shows a distinct transition

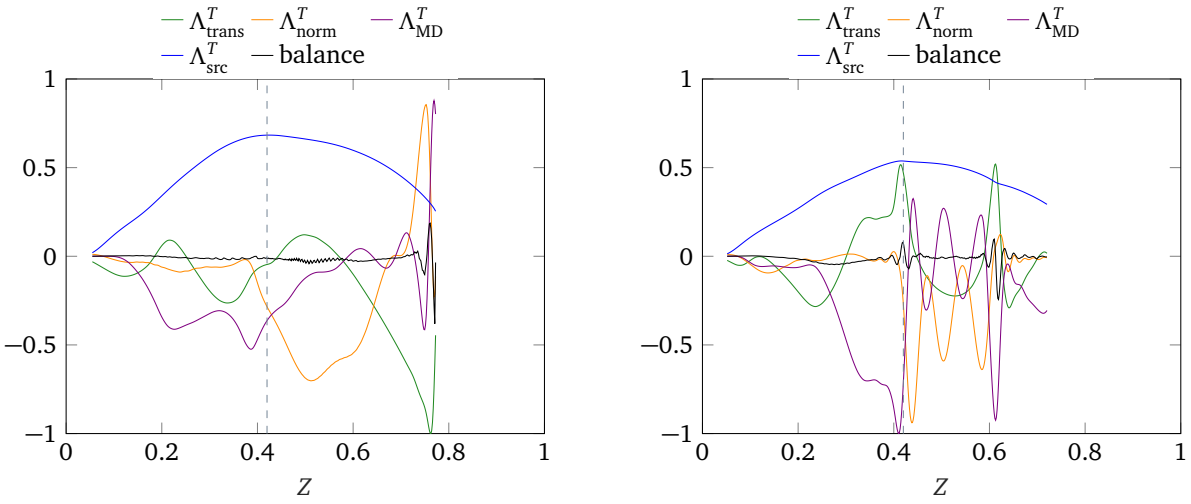

(a) $T - t_1$ **(b)** $T - t_2$

Figure 5.13.: Budgets of the extended flamelet temperature equation for two instants in time: early (left) and late (right). The budgets are evaluated for the flamelet identity F_V according to the time instants marked in figure 5.9c. All budgets are normalized by the maximum of all terms and "balance" (black line) denotes the sum of all budget terms.

from regime I to regime III near stoichiometry. However, towards the later stages of the flamelet identity, F_V seems to be completely dominated by multi-dimensional effects. While figure 5.9c already suggests the impact of multi-dimensional terms, the regime classification in figure 5.12c reveals that F_V largely resides in regime III and only a small part around stoichiometry resides in regime I. Consequently, only a small peak of the scalar dissipation rate is observed around Z_{st}.

5.2.2 Budget analysis of flamelet equations

The previous study of the temporal evolution of different flamelet identities already provided some important insights which are further extended here by inspecting budgets of the extended flamelet equations. The study, presented in the following, extends the analysis of equations (3.41) compared to the previous work of Scholtissek et al. [47]. In their study they evaluated budgets based on single snapshots of a direct numerical simulation. While the impact of curvature induced transport processes could be evaluated using single snapshots, contributions of the transient term can only be assessed when the complete time history is available. Since their investigation was restricted to frozen snapshots of the DNS, the transient term was not assessable and was obtained from the budgets by implicitly assuming that their extended flamelet equations (3.41) are closed.

In this work, based on the data extracted along the gradient trajectories, the budgets are computed by evaluating each of the single terms appearing in equation (3.41), where the contributions are named according to their physical interpretation. All terms appearing in the expanded form of equation (3.41) are directly evaluated in mixture fraction space, except for the multi-dimensional and the transient terms. They, however, require information about the three-dimensional gradient and the temporal evolution of equations (2.45), (2.46) and (3.8) which are additionally provided by the tracking procedure. The temporal evolution is provided by means of the righ-hand-side

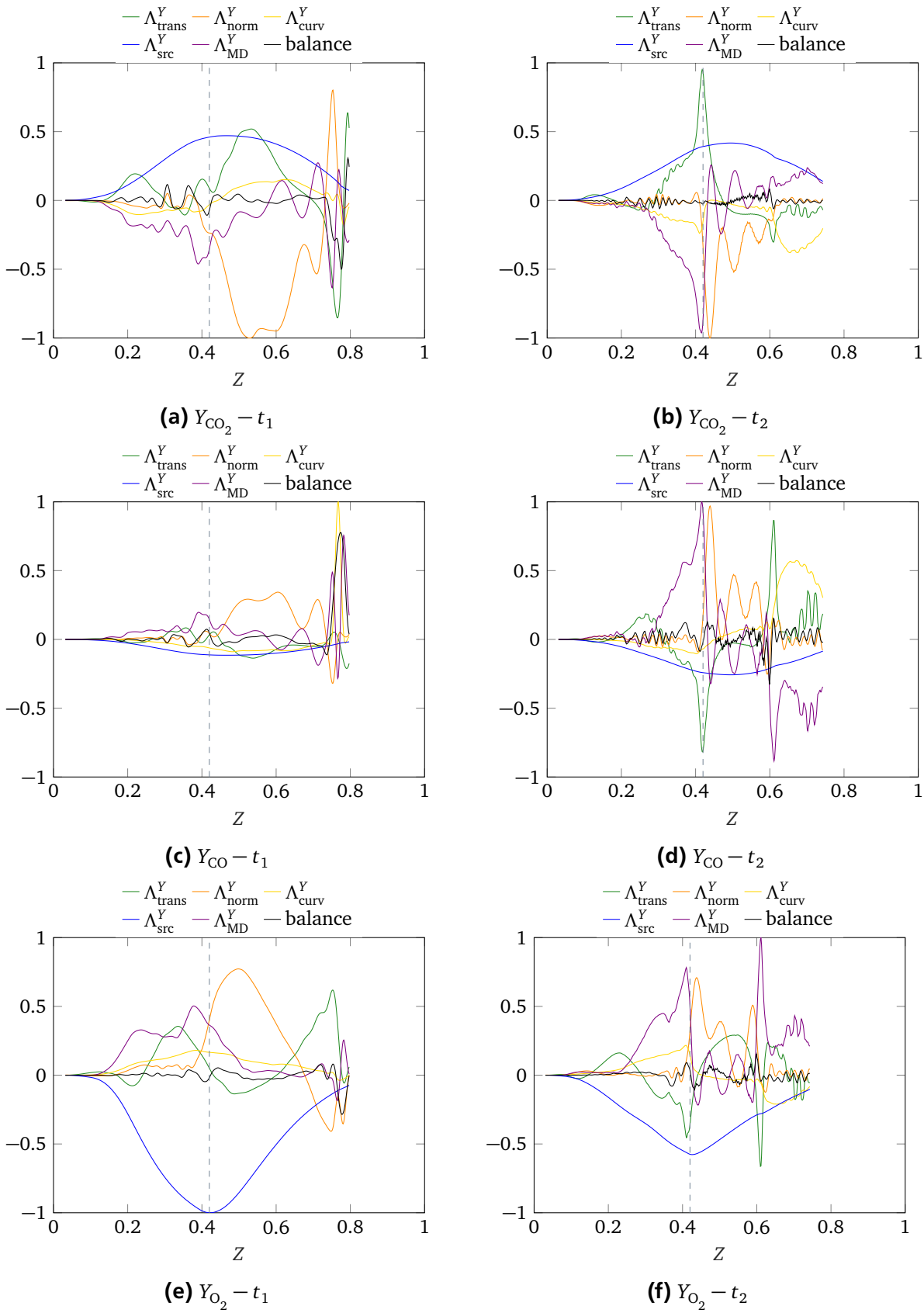

(a) $Y_{\text{CO}_2} - t_1$ **(b)** $Y_{\text{CO}_2} - t_2$

(c) $Y_{\text{CO}} - t_1$ **(d)** $Y_{\text{CO}} - t_2$

(e) $Y_{\text{O}_2} - t_1$ **(f)** $Y_{\text{O}_2} - t_2$

Figure 5.14.: Budgets of the extended flamelet species equations of CO_2, CO and O_2 for two instants in time: early (left) and late (right). The budgets are evaluated for the flamelet identity F_V according to the time instants marked in figure 5.9c. All budgets are normalized by the maximum of all terms and "balance" (black line) denotes the sum of all budget terms.

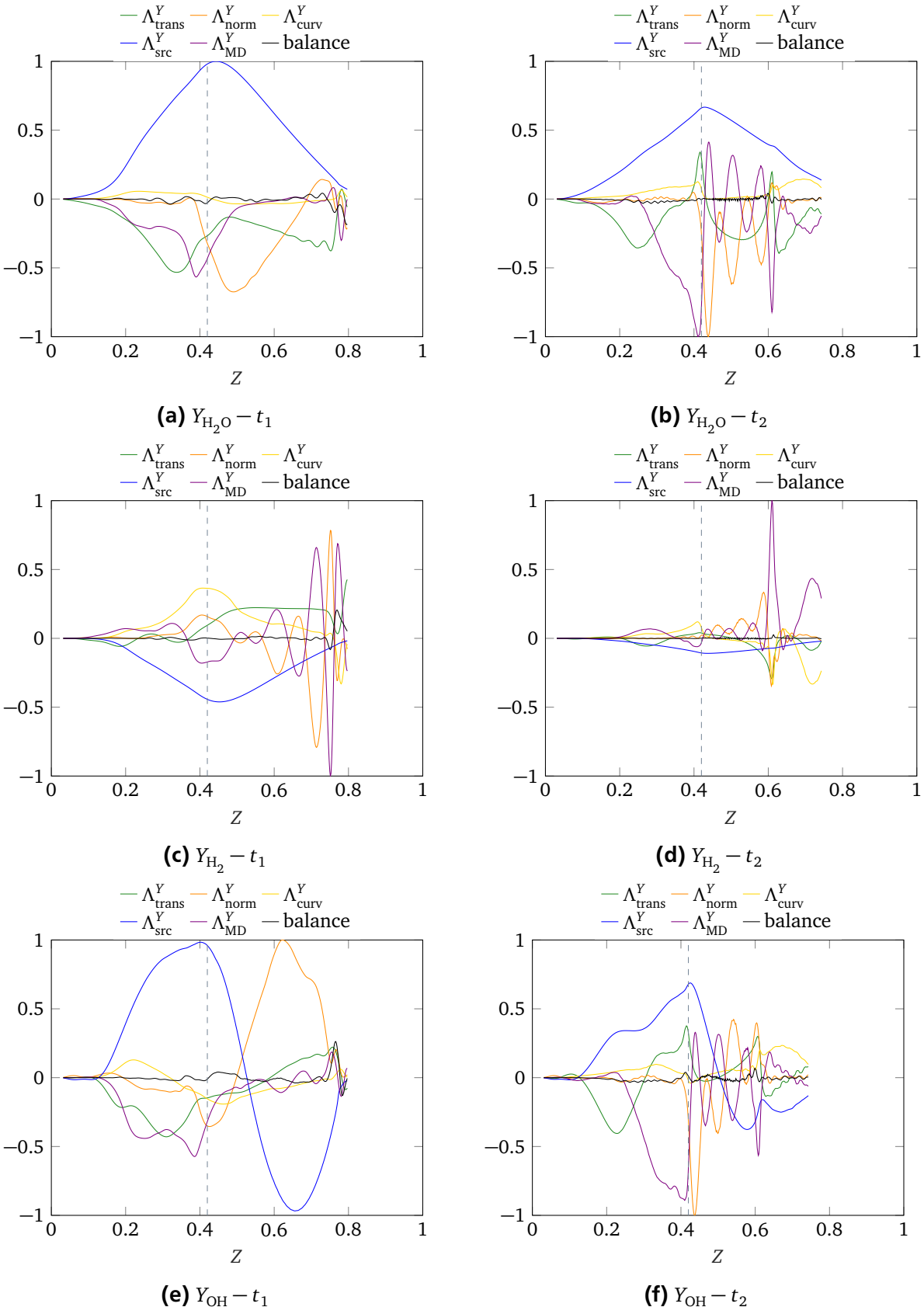

(a) $Y_{\text{H}_2\text{O}} - t_1$ **(b)** $Y_{\text{H}_2\text{O}} - t_2$

(c) $Y_{\text{H}_2} - t_1$ **(d)** $Y_{\text{H}_2} - t_2$

(e) $Y_{\text{OH}} - t_1$ **(f)** $Y_{\text{OH}} - t_2$

Figure 5.15.: Budgets of the extended flamelet species equations of H_2O, H_2 and OH for two instants in time: early (left) and late (right). The budgets are evaluated for the flamelet identity F_V according to the time instants marked in figure 5.9c. All budgets are normalized by the maximum of all terms and "balance" (black line) denotes the sum of all budget terms.

of equations (2.45), (2.46) and (3.8), interpolated onto the tracked flamelets.
The flamelet identity F_V was tagged to be significantly influenced by multi-dimensional terms. To support these findings, figures 5.13 to 5.15 show the budget plots for the temperature T and the species mass fractions of CO_2, CO, O_2, H_2O, H_2 and OH, evaluated for the flamelet identity F_V for the two time instants highlighted in figure 5.9c. In each plot the single contributions are normalized by the maximum of all terms and "balance" denotes the sum of all terms.
First, the temperature budget is investigated in figure 5.13. For the first time instant, cf. figure 5.15e, clearly all terms of the extended flamelet equation for the temperature show contributions to the overall balance, though for $Z < 0.7$ mainly flame-normal transport, multi-dimensional transport and the source term are active. As predicted by the regime classification, cf. figure 5.12, multi-dimensional terms and flame-normal terms are confined to the oxidizer and fuel side, respectively, where the transition occurs around $Z = Z_{st}$. Looking at the later time instant, cf. figure 5.13b, transient terms become more influential around $Z = Z_{st}$ and the zone of transition between multi-dimensional transport and flame-normal transport narrows down around $Z = Z_{st}$, while the appearance of flame-normal transport for $Z > 0.5$, contradicts predictions from the regime plot. The source term remains of leading order also for the later time.
To further expand these observations the flamelet-budgets for the species mass fractions of CO_2, CO, O_2, H_2O, H_2 and OH are shown in figures 5.14 and 5.15. All budgets exhibit a comparably dominant source term over the complete interval for both time instants. First, having a closer look at the first instant of time, all species, except for H_2, show a similar spatial division of flame-normal (on the fuel side) and multidimensional transport (on the oxidizer side) compared to the temperature budget for that time. The point of transition is again located around $Z = Z_{st}$. The balance term is further complemented by significant transient effects, while the influence of the curvature term is less distinct. For H_2, however, the curvature term dominates over multi-dimensional and flame-normal transport for almost the entire mixture fraction space. For the later instant of time similar observations as for the temperature budget can be made, although for CO_2 and CO the transient term plays a more dominant role near Z_{st} compared to the temperature budget.
This closes the study on the temporal evolution of flamelet identities found along gradient trajectories tracked in the DNS of a reactive syngas jet. Both diagnostic tools, the budget analyses and the regime characterization, agree very well, except smaller discrepancies for the later instant of time. However, keeping in mind that the regime analysis is relevant only to the order-of-magnitude of the scaling parameters, ε and ν, with uncertainties of about the same order, the results agree remarkably well. At the same time this, demonstrates the robustness of the regime characterization in conjunction with the underlying tracking algorithm and the associated numerical methods. In summary, the results show that in the present case multi-dimensional and unsteady effects can become influential for flamelets. The omission of such effects, as in the case of the classical flamelet model, may introduce modeling errors with respect to flame structure or extinction and reignition characteristics in the reactive flow.

6 Dissipation element analysis of turbulent non-premixed combustion

In the previous chapter, flamelets have been analyzed by means of an on-the-fly tracking procedure to assess the influence of transient and curvature effects on single flamelets in a fully turbulent environment. While this methodology helps to get a principle understanding of the nature of turbulent flamelets and the corresponding set of extended flamelet equations, the equations are still given in unclosed form, i.e. a model for the multi-dimensional term is required. Although the on-the-fly procedure could serve as a tool to assess model assumptions, the development of closure strategies should be based on statistical grounds to account for the inherently non-deterministic nature of turbulence. To complement the study presented in the previous chapter, here, a statistical approach based on the concept of dissipation elements [48] is applied to the direct numerical simulation presented in section 4.2.5. Classically applied to non-reactive flows [48, 233–236], this concept might also provide insightful details for reactive flows [235].

Within the theory of Wang and Peters [48] a geometrical description of the fluctuating scalar field is sought by decomposing it into small coherent regions of finite size within which the scalar field varies monotonically. These regions are identified by tracing gradient trajectories (GT) from every grid point in the domain along the ascending and descending gradient until a local minimum or local maximum point is reached. Then, according to Wang and Peters [48], the ensemble of grid points from which the same pair of local minimum and maximum points is reached defines a dissipation element (DE).
A schematic arrangement of four dissipation elements is given in figure 6.1, where the DE are highlighted in green. Once a gradient trajectory is emitted from an initial point, it inevitably will reach a local extremal point. A dissipation element satisfies the properties of completeness and uniqueness, required for a self-contained geometrical decomposition, according to Wang and Peters [234]. This means that each material point is included once and only once during the analyses. At the same time this ensures that DEs are space-filling and geometrically non-arbitrary. Although, dissipation elements might appear as quite irregularly shaped objects, they are unambiguously defined [233], which eventually allows for a statistical characterization of turbulent flame physics. An example of a dissipation element is given in figure 6.2, which was found by applying the gradient trajectory search algorithm of Wang [229] to the DNS of the reactive syngas jet explained earlier. Clearly, the complex morphology of a dissipation element intersecting an iso-scalar surface of the mixture fraction can be seen.
In what follows, dissipation elements will be sought on the mixture fraction field Z, similar to the on-the-fly tracking procedure presented in the last chapter. However, in contrast to the on-the-fly tracking procedure, the DE analysis is meant as a post-processing tool and is therefore only applied to single snapshots of the DNS. Furthermore, with the DE analysis all gradient trajectories can be identified. Although, the principle behind the DE analyses is the same as for the on-the-fly procedure, more sophisticated methods regarding the detection of local extrema and saddle points are involved.
The chapter is structured as follows: first, after a brief description of the differences between

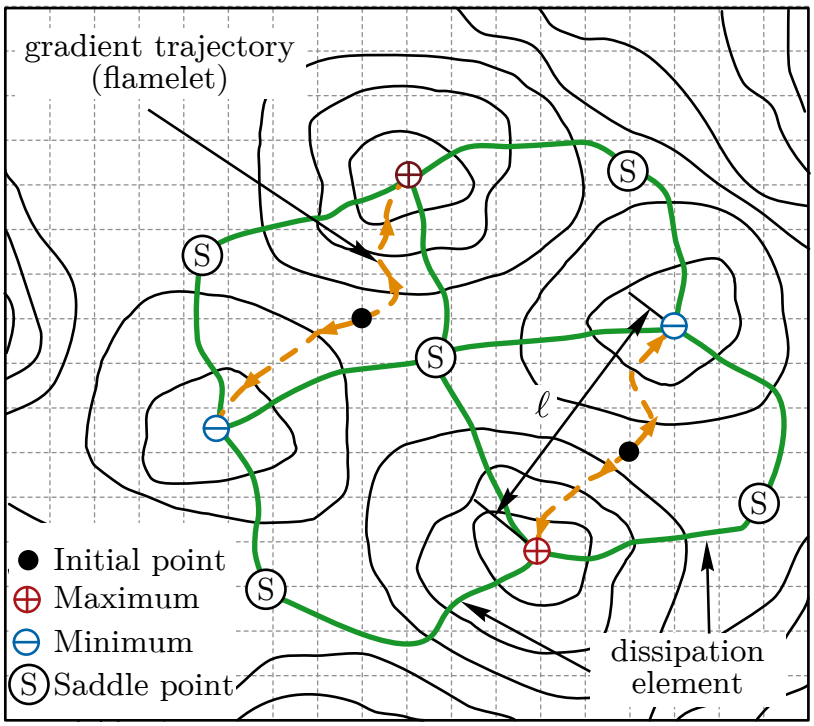

Figure 6.1.: Schematic of a scalar field including two hypothetical trajectories (orange) originating from an initial point to their respective minimum and maximum points. The green solid lines correspond to dissipation elements, enclosing all trajectories that end at the same minimum and maximum point.

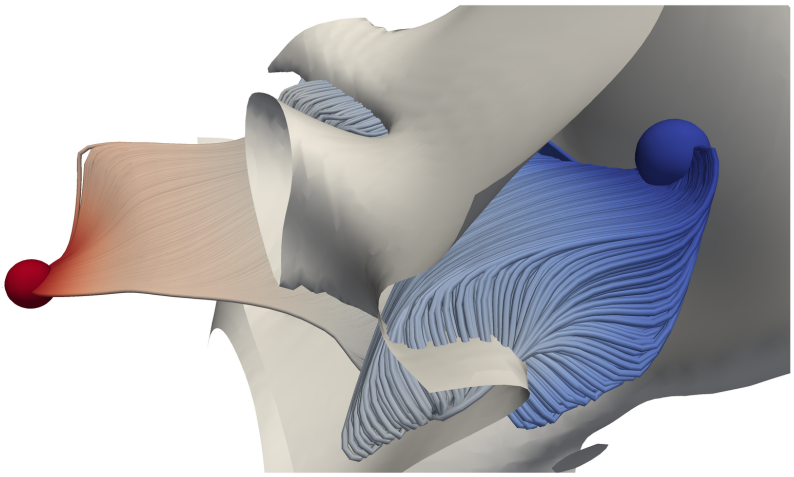

Figure 6.2.: Exemplary representation of a dissipation element within a three-dimensional direct numerical simulation. The blue bullet constitutes a local minimum, while the red bullet is a local maximum. The local extrema are connected through gradient trajectories which are colored with respect to the underlying scalar field.

the algorithm of Wang [229] and the on-the-fly tracking, a parametrization approach for DE is presented [144]. Thereafter, a regime classification for DE in the context of turbulent reactive jet flows is proposed [144]. The chapter closes with a discussion of statistics of parameters related to dissipation elements, obtained by applying the procedure of Wang [229] to the reactive syngas jet.

6.1 Numerical method

For the analyses presented later, the algorithm of Wang [229] is used. First, revisiting figure 6.1, the procedure of extracting data along gradient trajectories is conceptually similar to the on-the-fly tracking. However, the seed points are now directly located at grid points of the computational domain and trajectories are emitted from each grid point instead of just using a few points distributed across the surface of stoichiometric mixture. Furthermore, as described in [229] scalar gradients are first interpolated on a staggered mesh before tracing the trajectories. Except for regions around critical points, the algorithm advances trajectories with a step size $< 0.1\Delta x$, where Δx denotes the mesh size of the isotropic computational mesh.
In contrast to the on-the-fly tracking algorithm, the DE search algorithm has a more sophisticated numerical treatment near critical points. As already explained during the description of the on-the-fly tracking algorithm, cf. section 5.1, the scalar gradient vanishes at critical points and the direction of gradient trajectories becomes undetermined. Hence, a special procedure is required to distinguish between saddle points and actual extremal points. Wang [229] utilizes the fact that, mathematically, saddle points are unstable and extremal points are stable with respect to small perturbations. In the vicinity of a critical point, where the trajectory can not proceed further, due to a scalar gradient being smaller than a given threshold value, the algorithm of Wang [229] creates a small spherical surface enclosing this point. Then the six normal vectors on the intersections of the Cartesian axes with the sphere, $\mathbf{n}_x^+$, $\mathbf{n}_x^-$, $\mathbf{n}_y^+$, $\mathbf{n}_y^-$, $\mathbf{n}_z^+$ and $\mathbf{n}_z^-$, are computed and the curvature around the critical point is estimated by

$$\nabla \cdot \mathbf{n} \approx (\mathbf{n}_x^+ - \mathbf{n}_x^-) + (\mathbf{n}_y^+ - \mathbf{n}_y^-) + (\mathbf{n}_z^+ - \mathbf{n}_z^-)\,. \tag{6.1}$$

In the ideal case where the extremal point is directly located in the center of the sphere equation (6.1) yields -6 for local maxima and $+6$ for local minima. In case of a saddle point equation (6.1) yields $-2 \leq \nabla \cdot \mathbf{n} \leq 2$. With respect to numerical accuracy, critical points with $\nabla \cdot \mathbf{n} > 3.5$ are treated as minima and points with $\nabla \cdot \mathbf{n} < -3.5$ are treated as maxima. All other points are handled as saddle points by the numerical procedure which require further treatment. For saddle points, Wang [229] proposes a random-walk strategy. Once a trajectory hits a saddle point, its direction will be randomly diverted and the tracking is forced to proceed with small step sizes until a local extreme point is reached.
In order to apply the algorithm to the reactive syngas jet, small adaptions had to be made. The original study considered homogeneous isotropic turbulence in a triply periodic box. However, in this work a turbulent jet flow is analyzed which reveals an inhomogenity and requires to have an outlet boundary condition in the cross-stream direction. Furthermore, the jet has a complex flow morphology with a fully developed inner turbulent core region adjacent to a non-turbulent

outer region. Problems arise if gradient trajectories, originating from the inner region, proceed towards the outer irrotational region without reaching a local extremal point. Hence, the tracing of a trajectory is forcedly stopped if it enters the irrotational outer region, assumed for $Z \leq 0.05$.

6.2 Parametrization of dissipation elements

In order to study geometrical objects, like DE, apart from phenomenological observations, it is crucial for model development to have quantitative theories based on statistical grounds. Further, one should also aim for a reduction of the complexity of the underlying problem to grasp the cause and effect of different phenomena in a turbulent reactive flow. Hence, to find a statistical description of highly irregularly shaped objects, like DE, and to reduce the amount of information gained from DE analyses it is important to have simple parameters at hand, which can capture the mixing characteristics of the turbulent reactive flows. Furthermore, Wang and Peters [209] have shown that based on the space filling property of DE statistical properties of the entire scalar field can be reconstructed from mean values of dissipation elements. To this end the properties of dissipation elements need to be parameterized. Therefore, in this section a parametric description of dissipation elements that solely relies on information at the ending points is presented.
According to Wang [229], elements are elongated in one direction and thin in the other two and therefore it seems natural to pick the Euclidean distance ℓ between the local extremal points. A second quantity [229] proposed, is the scalar difference between the maximum and the minimum point, cf. figure 6.1,

$$\Delta Z = Z_{\mathrm{max}} - Z_{\mathrm{min}} \,. \tag{6.2}$$

This characterization can be interpreted as the fluctuation intensity of the scalar field Z at the length scale ℓ. A second property, also related to the scalar values, is the arithmetic mean of Z with respect to the ending points. Initially introduced by Peters and Trouillet [237], Z_{m}, defined as

$$Z_{\mathrm{m}} = \frac{Z_{\mathrm{max}} + Z_{\mathrm{min}}}{2} \,, \tag{6.3}$$

in conjunction with ΔZ helps to draw conclusions about the location of gradient trajectories in mixture fraction space. From a statistical point of view, the three parameters ℓ, ΔZ and Z_{m} contain most of the information of the mixture fraction field. However, especially for mixing processes the scalar gradient plays an important role and apart from the above parametrization, also a dissipation element based mean mixture fraction gradient g can be defined,

$$g = \frac{\Delta Z}{\ell} \,, \tag{6.4}$$

which in turn is closely related to the scalar dissipation rate. On dimensional grounds, it can be concluded that [229]

$$\chi \propto 2 D g^2 \,. \tag{6.5}$$

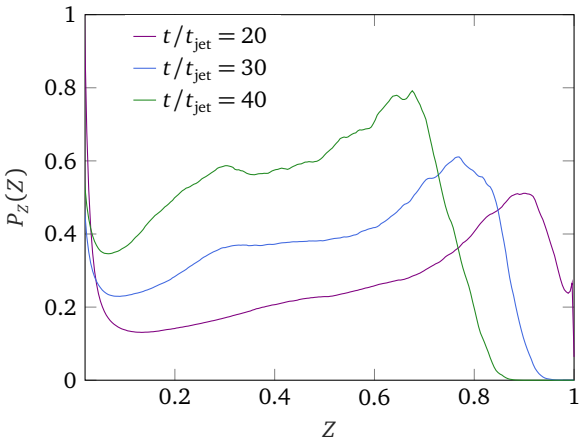

Figure 6.3.: Marginal probability distribution of the mixture fraction P(Z) at three instants in time. All pdfs exhibit a bimodal shape with minima located at $Z = 0.13$, $Z = 0.09$ and $Z = 0.07$ for ascending t/t_{jet}, respectively.

For the later following analyses the definitions (6.2) to (6.4) are non-dimensionalized with respect to the initial values H_0 and ΔZ_0. Hence,

$$g^* = \frac{g}{\Delta Z_0/\mathrm{H}_0}, \quad \ell^* = \frac{\ell}{\mathrm{H}_0}, \quad \Delta Z^* = \frac{\Delta Z}{\Delta Z_0}, \quad Z_{\mathrm{m}}^* = \frac{Z_{\mathrm{m}}}{\Delta Z_0}, \tag{6.6}$$

where $\Delta Z_0 = 1$ and $H_0 = 1.37\,\mathrm{mm}$, cf. section 4.2.1. Based on the above parametrization, DE analyses facilitates a general decomposition of the turbulent mixture fraction field into regions with equal mixing properties, thereby allowing to deduce statistics for characteristic regions of the flow as will be shown next.

6.3 Application to the reactive syngas jet

6.3.1 Regime classification

A turbulent jet flow can principally be partitioned into a fully turbulent inner core region and an irrotational outer region, where both regions are separated by an interfacial layer, called the turbulent/non-turbulent (T/NT) interface [238, 239]. In addition, the reactive syngas jet under consideration features a second interface, namely the reaction zone, which is located in the vicinity of the stoichiometric mixture fraction, thereby dividing the mixture fraction field into a fuel lean and a fuel rich region. Both layers, the T/NT and the reaction zone, give rise to define a regime classification for dissipation elements, where DE are classified based on the location of their ending points. A first attempt in this regard was made by Mellado et al. [236] who partitioned the flow field into three zones: a turbulent zone, a turbulence interface and quasi-laminar diffusion layers. By partitioning the flow into these zones Mellado et al. [236] were able to compute conditional zonal statistics investigating the role of external intermittency[1].

[1] The concept of external intermittency describes the segregation of a turbulent jet into two disjoint sub-volumes with fully developed turbulence and nearly laminar flow [240].

In this work, a regime classification based on the reaction zone is proposed. Therefore, the flow is partitioned into three zones, based on the value of the mixture fraction at the ending points gradient trajectories. It is important to note that all gradient trajectories ending at the same points, thereby defining a DE, belong to the same regime. The advantage of this partitioning is that it allows to distinguish between ensembles of trajectories that are subject to chemical reaction and those that are mainly subject to turbulent mixing. Before going into detail about the regime classification, the T/NT-interface has to be characterized first in order to be able to estimate where regions of turbulence mixing occur. Thereby, it is important to find the location of the T/NT with respect to the mixture fraction variable, since Z is the scalar the DE analysis is based on.
Two general approaches exist in the literature to detect the interface position, where it could be either detected based on a vorticity criterion or a scalar criterion. The different detection approaches were examined qualitatively and quantitatively in terms of the interface position by Gampert et al. [241]. They computed the probability density function of the mean location of the T/NT interface from both criteria and did a detailed comparison of the two methods, where they observed a very good agreement.
In this work, the location of the interface is detected based on the scalar criterion because, as already said, the location is required in mixture fraction space. Therefore the procedure of Prasad and Sreenivasan [242] is used, who identified the location based on the probability density function (pdf) of the mixture fraction variable $P(Z)$. This pdf usually exhibits a bimodal shape and the threshold value at which the interface is located corresponds to the minimum of the probability density function. For the present simulation, the pdf of Z for three time instants is shown in figure 6.3 and the bimodal shape can be clearly seen, resulting in threshold values of $Z = 0.13$ for $t/t_{\text{jet}} = 20$, $Z = 0.09$ for $t/t_{\text{jet}} = 30$ and $Z = 0.07$ for $t/t_{\text{jet}} = 40$.
By knowing the location of the T/NT it is obvious that for the present case the surface of stoichiometric mixture, $Z = Z_{st} = 0.42$, is located in the fully developed turbulent part of the jet flow. With this the three regimes are identified as follows:

Regime I

In the first regime gradient trajectories do not cross the surface of stoichiometric mixture due to the condition that the mixture fraction at both ending points of the trajectory is above Z_{st}, i.e. $Z_{\text{max}} \geq Z_{\text{min}} \geq Z_{st}$. With this definition, GT from regime I are confined to the inner fuel rich core region of the jet, where turbulent mixing outweighs chemical reactions.

Regime II

In the second regime gradient trajectories cross the surface of stoichiometric mixture since the values of Z at the ending points enclose Z_{st}, i.e. $Z_{\text{max}} \geq Z_{st} \geq Z_{\text{min}}$. Due to this condition, trajectories are captured in regime II that are subject to both chemical reaction and turbulent mixing. Because of the nature of these trajectories, connecting a maximum point at the fuel rich side with $Z_{\text{max}} > Z_{\text{st}}$ and a minimum point at the fuel lean side with $Z_{\text{min}} < Z_{\text{st}}$, they may provide information about the flame structure in the vicinity of the stoichiometric surface. Furthermore, the non-local (two-point) character of gradient trajectories provides additional information whether points in the reaction zone are connected through a diffusive layer with points located away from Z_{st}.

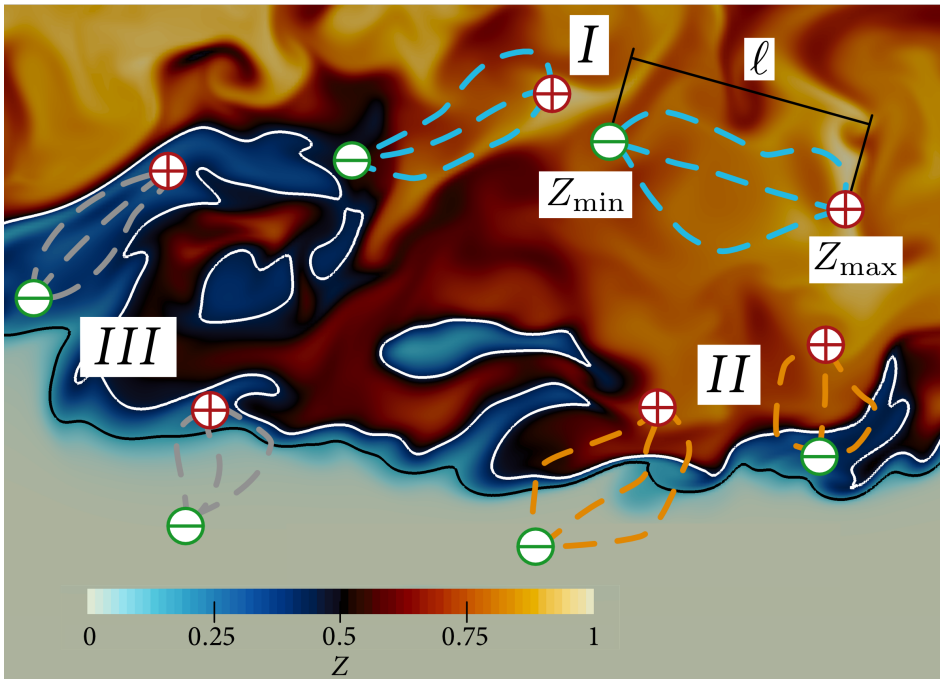

Figure 6.4.: Two-dimensional slice of the instantaneous mixture fraction field Z in the xOz plane at $t/t_{\mathrm{ref}} \approx 20$. Gradient trajectories are schematically shown in the different regimes by colored solid lines. The white line indicates the location of stoichiometric mixture fraction and the black line indicates the location of the turbulent/non-turbulent interface.

Regime III

Similar to the first regime, in the third regime gradient trajectories do not cross the surface of stoichiometric mixture due to the condition that the mixture fraction at both ending points of the trajectory is below Z_{st}, i.e. $Z_{st} \geq Z_{\max} \geq Z_{\min}$. While being located on the fuel lean side of the flame, both regions of turbulent mixing and quasi laminar regions are embraced.

Figure 6.4 shows a representative slice through the mixture fraction field in the $x0z$ plane. The white line indicates the surface of stoichiometric mixture, while the T/NT is marked by the black line. Trajectories in the different regimes are illustrated schematically by bold colored lines. To conclude the regime classification, it can be said that only trajectories from regimes II and III can cross the T/NT eventually ending in the quasi laminar outer flow. In contrast, only trajectories in regime I exhibit turbulent mixing over their whole length. A more profound analysis of the location of gradient trajectories in mixture fractions space with respect to the different regimes is given in the next section.

6.3.2 Joint statistics of Z_{m}^* and ΔZ^*

It has already been demonstrated that gradient trajectories based on the mixture fraction field constitute flamelets in terms of the flamelet theory. In the present simulation, these flamelets are subject to turbulent mixing processes. In order to assess the impact of turbulent mixing and to estimate the location of flamelets in mixture fraction space a statistical analysis of ΔZ^* and Z_{m}^* is insightful. Figure 6.5 shows the joint probability density function (jpdf) of both quantities

$P(Z_{\mathrm{m}}^*, \Delta Z^*)$ for three jet times, where the instants of time were chosen with respect to the quasi self-similar state of the jet, which is reached for $t/t_{\mathrm{jet}} > 10$, cf.section 4.2.5.
Based on equations (6.2) and (6.3) simple kinematic relations for the motion of extremal points in scalar turbulence can be derived which give a first impression on the temporal evolution of Z_{m} and ΔZ. The substantial changes of Z_{m} and ΔZ can be written as

$$\frac{\mathrm{d}Z_{\mathrm{m}}}{\mathrm{d}t} = \frac{1}{2}\left(\frac{\mathrm{d}Z_{\mathrm{max}}}{\mathrm{d}t} + \frac{\mathrm{d}Z_{\mathrm{min}}}{\mathrm{d}t}\right), \tag{6.7}$$

and

$$\frac{\mathrm{d}\Delta Z}{\mathrm{d}t} = \frac{\mathrm{d}Z_{\mathrm{max}}}{\mathrm{d}t} - \frac{\mathrm{d}Z_{\mathrm{min}}}{\mathrm{d}t} < 0\,. \tag{6.8}$$

Equation (6.8) indicates that ΔZ will always decrease with time, because diffusivity requires

$$\frac{\mathrm{d}Z_{\mathrm{max}}}{\mathrm{d}t} < 0\,, \text{and} \quad \frac{\mathrm{d}Z_{\mathrm{min}}}{\mathrm{d}t} > 0\,. \tag{6.9}$$

A similar restriction for Z_{m} does not exist and Z_{m} either increases or decreases with time. However, the temporal evolution of dissipation elements is more complex than implied by eqs. (6.7) and (6.8). Schäfer et al. [230] showed that the evolution of dissipation elements is affected by slow and fast changes. Slow changes are responsible for a continuous evolution, while fast changes describe processes where the connectivity of dissipation elements changes abruptly due to a topology change of the mixture fraction field. An abrupt topology change results in a discrete change of ΔZ and ℓ and occurs when zero gradient points disappear due to diffusion or new zero gradient points appear due to the folding mechanism of turbulent flows. Schäfer et al. [230] discriminated between two fast processes. By a reconnection process two initially independent dissipation elements are merged and a new dissipation element with a larger ΔZ is created. This is the only mechanism for ΔZ to increase with time. A secondary splitting process on the other hand would generate new zero gradient points resulting in shorter dissipation elements and an abrupt decrease of ΔZ. Figure 5.5 illustrates an example of a cutting and reconnection process by means of a one-dimensional dissipation element.

The joint pdf of Z_{m} and ΔZ exhibits a triangular shape as can be seen in figure 6.5. In addition, the three regimes introduced earlier are marked together with the two corresponding boundaries between regime I and II (dash-dotted line) and between regime II and III (dashed line). Due to their definition the regime borders solely depend on the stoichiometric scalar dissipation rate Z_{st} and can formally be expressed in terms of Z_{m} and ΔZ

$$\text{regime I}\rightarrow\text{II:} \qquad Z_{\mathrm{m}}^*(\Delta Z^*) = \frac{\Delta Z^*}{2} + Z_{\mathrm{st}} \tag{6.10}$$

$$\text{regime II}\rightarrow\text{III:} \qquad Z_{\mathrm{m}}^*(\Delta Z^*) = -\frac{\Delta Z^*}{2} + Z_{\mathrm{st}}\,. \tag{6.11}$$

On the other hand, due to the temporal decay of the jet, the boundaries of the joint pdf change with time as indicated by the black solid lines in figure 6.5, though the overall triangular shape persists.

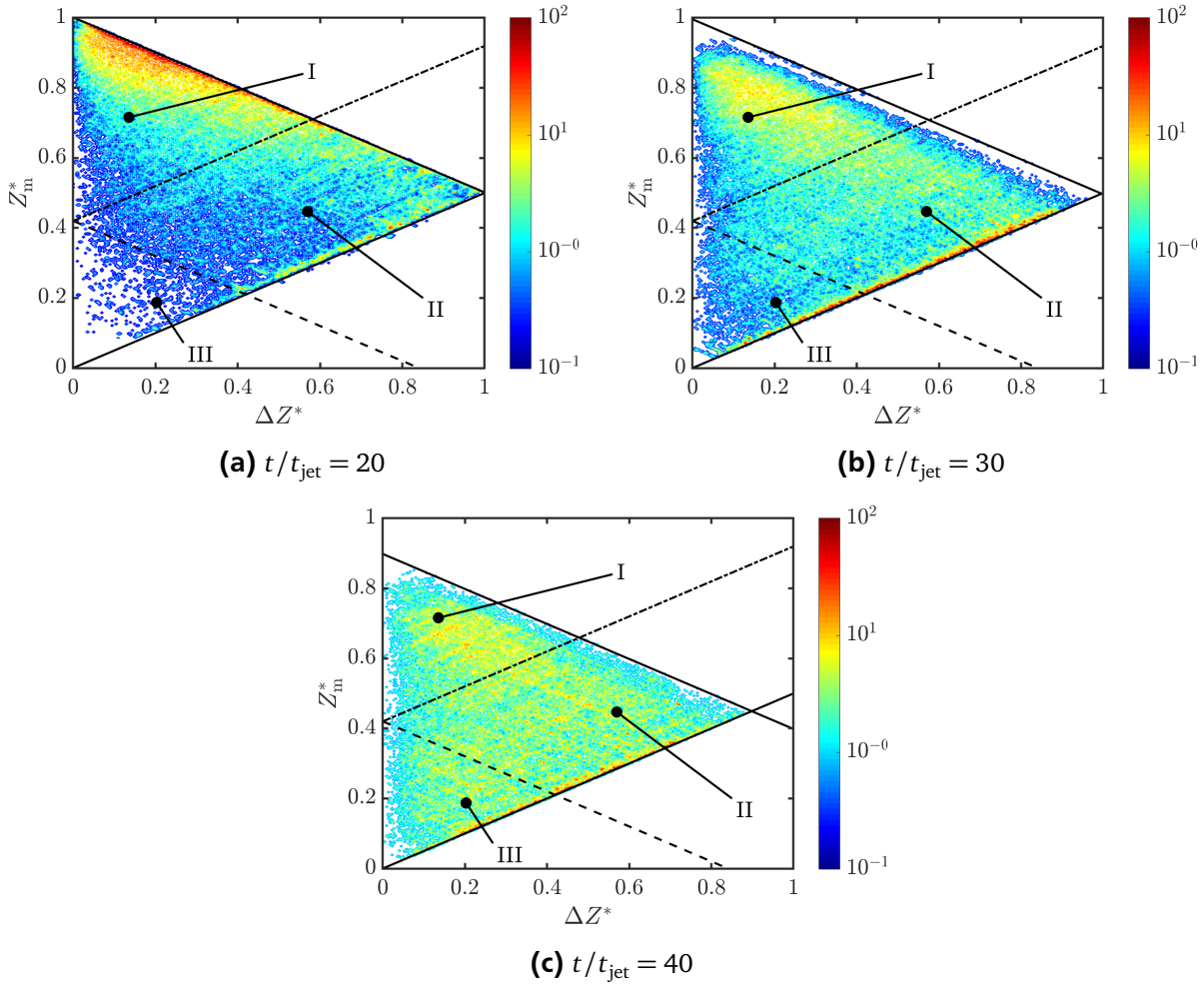

(a) $t/t_{jet} = 20$ **(b)** $t/t_{jet} = 30$

(c) $t/t_{jet} = 40$

Figure 6.5.: Joint probability density function of Z^*_m and ΔZ^* for three dimensionless times. The different regimes and also their corresponding regime boundaries are highlighted. The probability is indicated by colors and scaled logarithmically.

During the decay the maximum mixture fraction Z_{max} decreases from $Z_{max} = 1.0$ for $t/t_{jet} = 20$ to $Z_{max} = 0.89$ for $t/t_{jet} = 40$. The intersection of both solid lines indicates an upper limit for ΔZ^*, which moves to lower values during the decay eventually resulting in a singular jpdf for $t \to \infty$. The joint pdfs for the different instants of time clearly show a change in the morphology of flamelets with time. For $t/t_{jet} = 20$, cf. figure 6.5a, a distinct maximum of $P(Z^*_m, \Delta Z^*)$ occurs in the intervals of $0.1 < \Delta Z^* < 0.3$ and $0.85 < Z^*_m < 0.95$ indicating that most trajectories are situated in the fuel rich region of the jet, i.e. $Z_m > Z_{st}$. Furthermore, with respect to flamelet space, most of the trajectories occupy only parts of the fuel rich side, indicated by the relatively small scalar difference. However, there exist also trajectories situated in the vicinity of Z_{st} spanning nearly the whole flamelet space, i.e. $\Delta Z^* \approx 1$. Only a rare occurrence of trajectories on the fuel lean side (regime III) can be observed which might be due to the proximity of Z_{st} and the T/NT ($Z = 0.13$) at that time.For the second instant of time, cf. figure 6.5b, the distinct maximum in regime I disappeared and it seems that the majority of trajectories is located in regime II at the lower boundary of $P(Z^*_m, \Delta Z^*)$, though a significant amount of trajectories is still located in regime I. At the lower boundary all trajectories have a $Z_{min} = 0$, according to equations (6.2) and (6.3), thereby connecting regions of

pure oxidizer with the reaction zone. Furthermore, it can be noted that due to shift of the T/NT towards a lower mixture fraction value ($Z = 0.09$) more trajectories are situated in regime III. During the later stages of the jet, cf. figure 6.5c, gradient trajectories are homogeneously distributed without any distinct maximum in $P(Z^*_{\mathrm{m}}, \Delta Z^*)$. At the same time this is also an indicator for the state of mixing during later jet times. The state of mixing could be further assessed by investigating the joint distribution of the scalar difference ΔZ^* and the length scale ℓ^* which is done in the next section.

6.3.3 Joint statistics of ΔZ^* and ℓ^*

The joint distribution of the mixture fraction difference ΔZ^* and the length scale ℓ^*, $P(\Delta Z^*, \ell^*)$, complements the study of $P(Z^*_{\mathrm{m}}, \Delta Z^*)$ by providing additional information about the local structure of the mixture fraction field. The joint pdf is plotted for all regimes in figure 6.6 for $t/t_{\mathrm{jet}} = 20$ (left) and $t/t_{\mathrm{jet}} = 40$ (right) in conjunction with the conditional mean $\langle \Delta Z^* | \ell^* \rangle$, indicated by the black circles. In addition, also $P(\Delta Z^*, \ell^*)$ for all gradient trajectories independent of their regime is shown.

The plots of $P(\Delta Z^*, \ell^*)$ clearly show that the scalar difference and the length scale ℓ^* exhibit a strong correlation independent of the regime classification. All joint distributions show distinct maxima near the origin and indicate that with increasing ℓ^* also ΔZ^* increases. This finding is further supported by the conditional mean value which increases monotonously with ℓ^*. From a theoretical point of view [234] the probability near the origin vanishes because at very small scales, extremal points may rapidly be annihilated owing to molecular diffusion which prohibits the existence of very small ΔZ^* and ℓ^* at the same time.

First, having a closer look at the joint probabilities for $t/t_{\mathrm{jet}} = 20$ further insights into the state of mixing can be obtained. Poor mixed regions are represented by probabilities in the upper left corner of $P(\Delta Z^*, \ell^*)$, where ℓ^* is small but ΔZ^* has already large values. On the other hand, well mixed regions are represented by probabilities in the lower left corner, where ΔZ^* is small at finite length scales ℓ^*. Both, regime I and II have a distinct peak in $P(\Delta Z^*, \ell^*)$ which is located near $\ell^* \approx 0.3$. However, according to the location of the peak with respect to ΔZ^* they are different in the state of mixing. While regime I exhibits a peak at $\Delta Z^* \approx 0.1$, thereby showing indications of well mixedness, regime II seems to be poorly mixed since the peak occurs at $\Delta Z^* \approx 0.6$. Furthermore, this shows that trajectories in regime II have a tendency to connect extremal points with large scalar differences. Regime III allows no clear conclusion due to a lack of samples at that time.

Next, analyzing the second instant of time at $t/t_{\mathrm{jet}} = 40$, cf. figure 6.6 (right), the state of mixing clearly changed. A first observation is that for all regimes the probability of having long elements with smaller scalar difference increased, which is an indicator for well mixedness. While for $t/t_{\mathrm{jet}} = 20$ the longest elements exhibit a length of $\ell^* \approx 2$, this length increases to $\ell^* \approx 3$ for $t/t_{\mathrm{jet}} = 40$. Also the distinct maxima of regimes I and II are shifted. Comparing them to the corresponding earlier instant of time, the maximum for regime I is shifted to $\ell^* \approx 0.5$, while having nearly the same scalar difference as for $t/t_{\mathrm{jet}} = 20$. In contrast the maximum of $P(\Delta Z^*, \ell^*)$ for regime II is shifted to $\ell^* \approx 0.5$ and $\Delta Z^* \approx 0.4$ which is a decrease in the scalar difference by 0.2.

Since scalar mixing and the occurrence of scalar gradients are strongly connected, it is of interest at which length scale large mean gradients g will occur. This will be the topic of the next section.

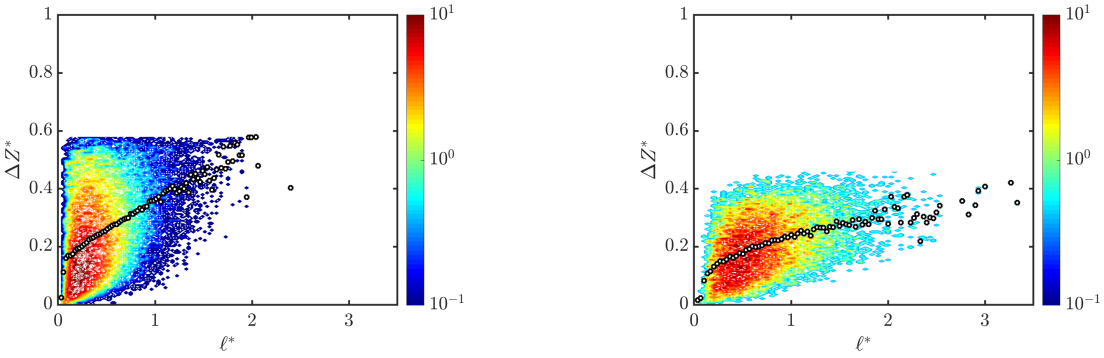

(a) Regime I

(b) Regime I

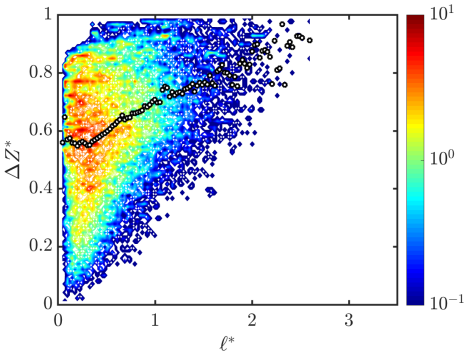

(c) Regime II

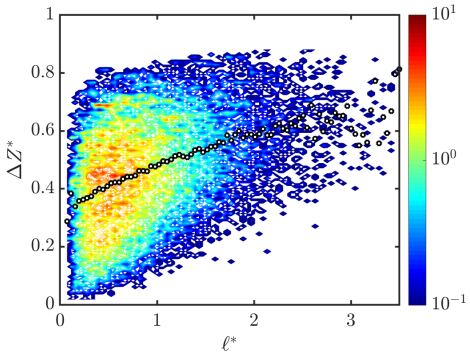

(d) Regime II

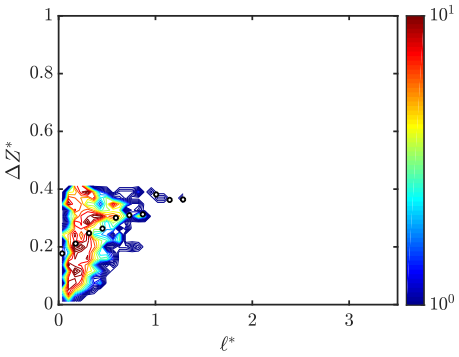

(e) Regime III

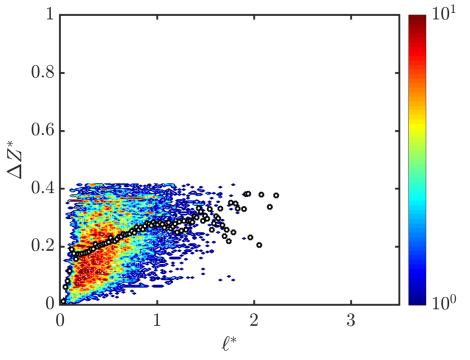

(f) Regime III

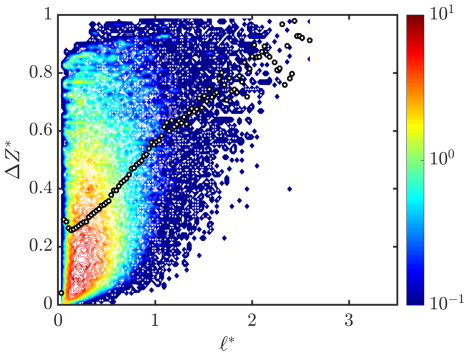

(g) All

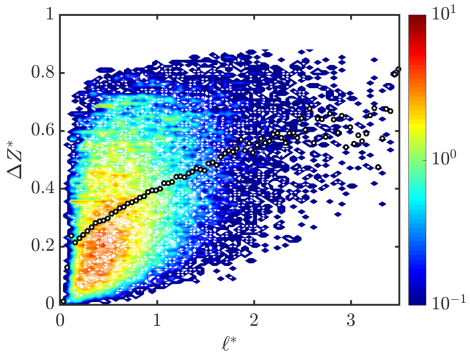

(h) All

Figure 6.6.: Joint distribution of ΔZ^* and ℓ^* together with the conditional mean $\langle \Delta Z^* | \ell^* \rangle$ (black circles) for two instants of time $t/t_{\text{jet}} = 20$ (left) and $t/t_{\text{jet}} = 40$ (right). From top to bottom the different regimes are shown with $P(\Delta Z^*, \ell^*)$ of all trajectories at the bottom. The probability is indicated by colors and scaled logarithmically.

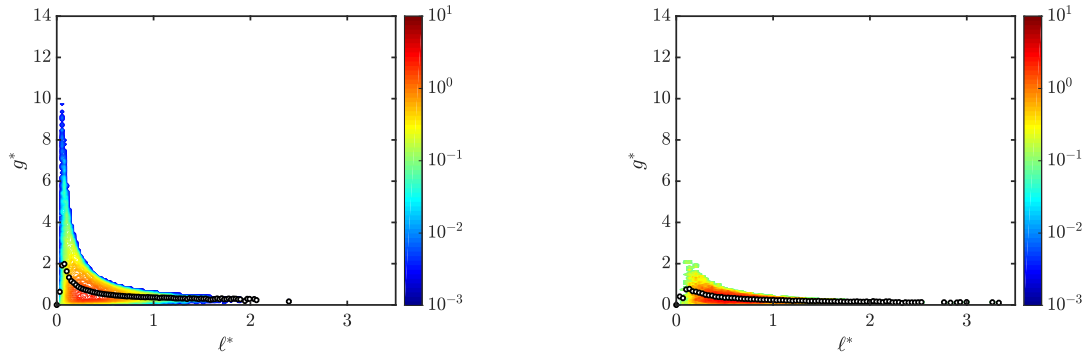

(a) Regime I

(b) Regime I

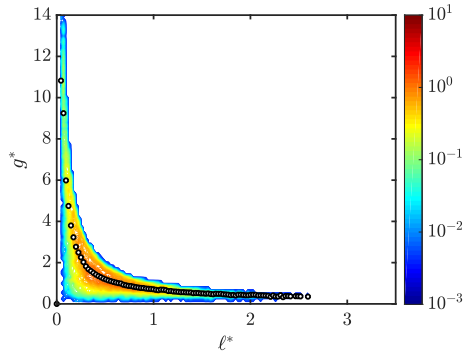

(c) Regime II

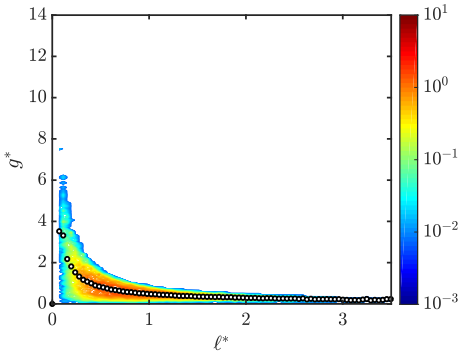

(d) Regime II

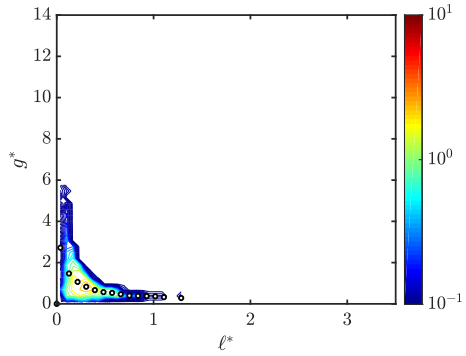

(e) Regime III

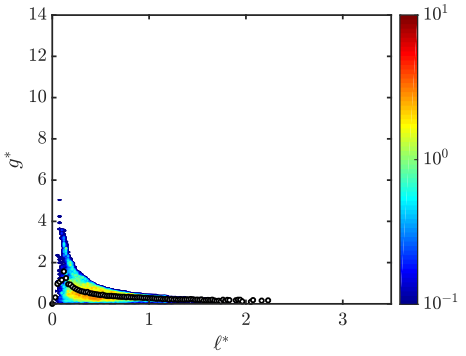

(f) Regime III

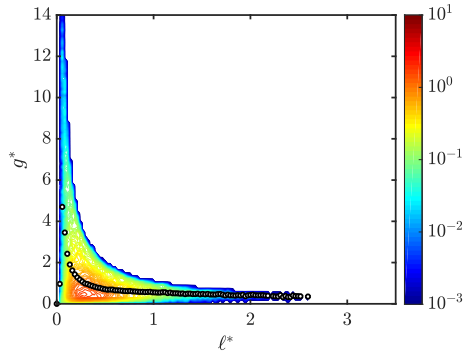

(g) All

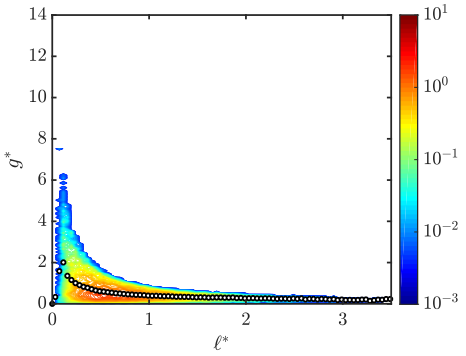

(h) All

Figure 6.7.: Joint distribution of g^* and ℓ^* together with the conditional mean $\langle g^*|\ell^*\rangle$ (black circles) for two instants of time $t/t_{\text{jet}} = 20$ (left) and $t/t_{\text{jet}} = 40$ (right). From top to bottom the different regimes are shown with $P(g^*, \ell^*)$ of all trajectories at the bottom. The probability is indicated by colors and scaled logarithmically.

6.3.4 Joint statistics of g^* and ℓ^*

In the theory of Wang and Peters [48] the scalar difference ΔZ^* and ℓ^* are the most important parameters, since they allow to reconstruct fundamental statistics of the scalar field [209]. However, based on these two quantities a third quantity providing an approximation for the normalized mean scalar gradient g^* of a gradient trajectory can be derived which in turn can be related to the scalar dissipation rate χ, cf. equation (6.5). While the scalar dissipation rate can be interpreted as the local rate of mixing of the scalar field, g^* provides additional scale-dependent information due to the non-local character of ΔZ^* and ℓ^*. Therefore, in this section the joint pdf of g^* and ℓ^*, $P(g^*, \ell^*)$, is studied. The joint pdf is plotted for all regimes in figure 6.7 for $t/t_{\text{jet}} = 20$ (left) and $t/t_{\text{jet}} = 40$ (right) in conjunction with the conditional mean of both quantities $\langle g^*|\ell^*\rangle$, indicated by the black circles. In addition, also $P(g^*, \ell^*)$ for all gradient trajectories independent of their regime is shown. For the first instant of time at $t/t_{\text{jet}} = 20$ the joint pdfs of regime I and II exhibit a long tail at length scales $\ell^* \approx 0.5$ but not for $\ell^* \to 0$. It might seem surprising that the largest gradients do not occur for $\ell^* \to 0$, however, ΔZ^* and ℓ^* are not independent and ΔZ^* is affected by molecular damping at the smallest scales. The tail is most pronounced for regime II and exceeds the reference value $\Delta Z_0/H_0$ by almost a factor of 14. This corresponds to the upper left region in the joint pdf $P(\Delta Z^*, \ell^*)$, where relatively large values of ΔZ^* occur at small length scales ℓ^*. The largest excursion from the conditional mean value $\langle g^*|\ell^*\rangle$ is observed for regime I, where g^* exceeds $\langle g^*|\ell^*\rangle$ by almost a factor of 5. This phenomenon is also known as small-scale intermittency in the literature [243].

According to Gauding et al. [244] large gradients g^* at moderate length scales ℓ^* can be interpreted as steep jumps in the mixture fraction field which manifest themselves as cliff-like structures, caused by compressive strain acting on the mixture fraction field. Strong molecular transport occurs predominantly over these cliffs where the width of these structures could be interpreted as a length scale over which mixing predominantly occurs. On average, this width corresponds to the length scale ℓ^* at which the maximum of $\langle g^*|\ell^*\rangle$ occurs, which is at $\ell^* \approx 0.1$ independently of the regime. On the other hand, the lower right tails of $P(\Delta Z^*, \ell^*)$ can be interpreted as ramp-like structures, where the scalar difference ΔZ^* varies monotonously over a length scale up to $\ell^* = 2$, resulting in low values for g^*. For the later instant of time, $t/t_{\text{jet}} = 40$, ramp-like structures get more pronounced while at the same time cliff-like structures are significantly reduced.

6.3.5 Inner structure of dissipation elements

According to the flamelet theory, chemical reactions mostly take place in thin confined layers around the surface of stoichiometric mixture fraction, where diffusion is the rate controlling process. The dissipation element approach, due to its non-local nature, in conjunction with the regime classification can be used to provide further insights into the inner structure of these diffusively controlled regions. To this end, statistics for the temperature T and the species mass fraction OH are computed based on information extracted along gradient trajectories, rather than using data at the ending points. Based on the regime classification, cf. section 6.3.1, the analyses are restricted to gradient trajectories belonging to regime II, since only these gradient trajectories intersect the

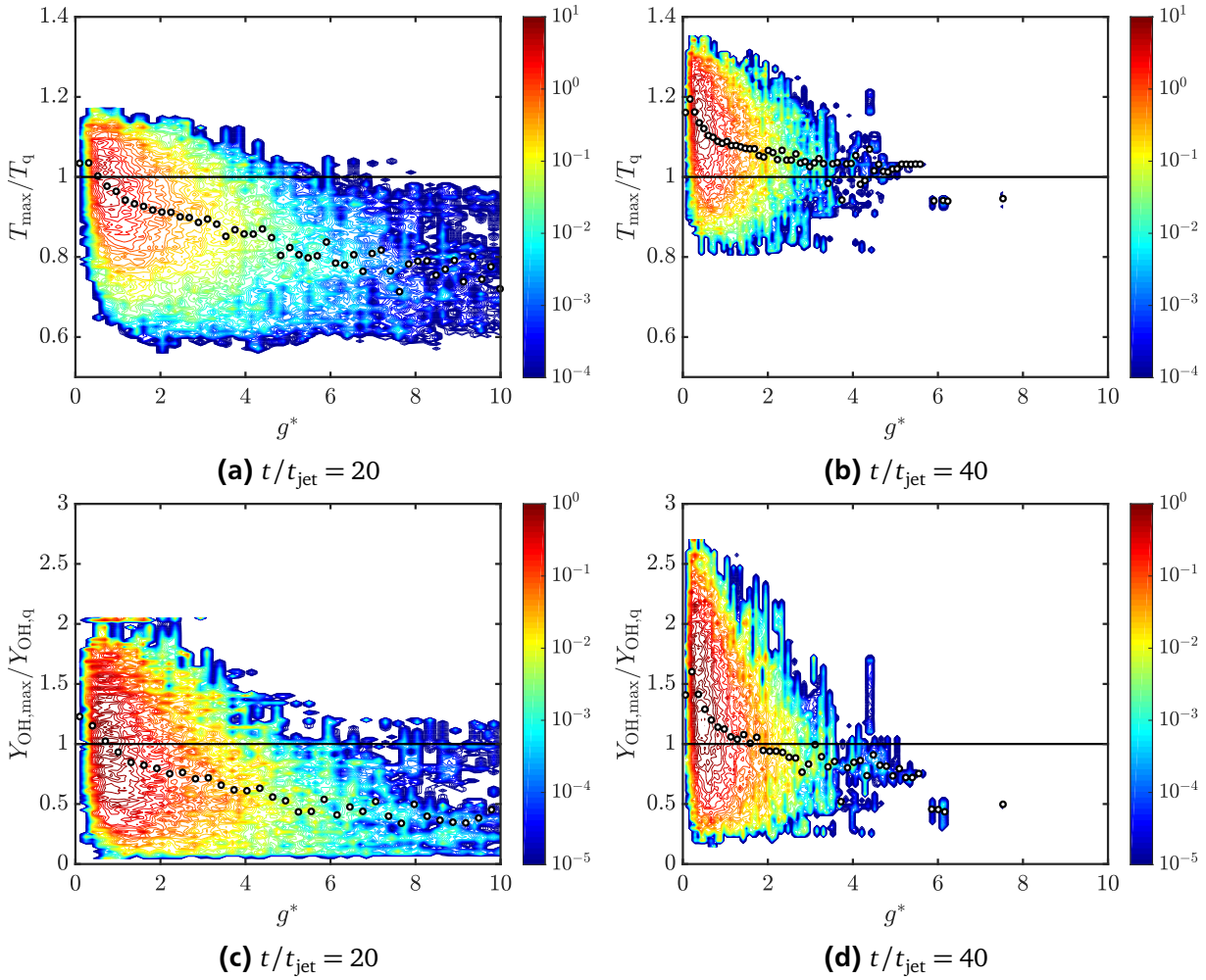

Figure 6.8.: Joint distributions of T_{max}/T_q (top) and $Y_{OH,max}/Y_{OH,q}$ (bottom) with respect g^* for two instants of time $t/t_{jet} = 20$ (left) and $t/t_{jet} = 40$ (right), together with their conditional mean values $\langle T_{max}/T_q|g^*\rangle$ and $\langle Y_{OH,max}/Y_{OH,q}|g^*\rangle$, indicated by black circles. The probability is indicated by colors and scaled logarithmically.

surface of stoichiometric mixture fraction and are subject to chemical reactions.

Figure 6.8 shows the joint distributions of T_{max}/T_q and $Y_{OH,max}/Y_{OH,q}$ with respect to the normalized gradient g^* for two instants of time, $t/t_{jet} = 20$ and $t/t_{jet} = 40$, together with their conditional mean values $\langle T_{max}/T_q|g^*\rangle$ and $\langle Y_{OH,max}/Y_{OH,q}|g^*\rangle$, indicated by black circles. The subscript $(\bullet)_{max}$ denotes the maximimum value of the respective quantity that has been extracted along individual gradient trajectories. Both stoichiometric quantities have been normalized by their corresponding value near extinction, $(\bullet)_q$, which were estimated at $T_q = 1241\,\mathrm{K}$ and $Y_{OH,q} = 0.00117$, respectively. These values are obtained from steady laminar flamelet calculations, cf. section 3.2.1. First, examining the joint distribution of T_{max}/T_q and g^* for $t/t_{jet} = 20$, cf. figure 6.8a, it turns out that strong fluctuations around the conditional mean exist. The joint distribution has a peak value near $g^* \approx 1$ and $T_{max}/T_q \approx 1$, thereby indicating that a significant number of trajectories is at the edge of extinction (indicated by the horizontal line), which is also in agreement with $\langle T\rangle_{st}$ at that time, cf. figure 4.13. A trajectory is defined to by extinguished if $T_{max}/T_q < 1$. Although the conditional mean clearly shows a trend towards a quenched state of trajectories for $g^* > 1$, there is

a significant number of burning trajectories for $1 < g^* < 4$. Similar observations can be made for $P(Y_{\mathrm{OH,max}}/Y_{\mathrm{OH,q}}, g^*)$, cf. figure 6.8c, although the peak in the vicinity of $g^* \approx 1$ is less distinct.
Inspecting the second instant of time $t/t_{\mathrm{jet}} = 40$, cf. figures 6.8b and 6.8d, the jet seems to be mostly reignited. This is most apparent for the normalized temperature, cf. figure 6.8b, where the conditional mean $\left\langle T_{\mathrm{max}}/T_{\mathrm{q}} | g^* \right\rangle$ completely lies above the quench limit (indicated by the horizontal line). This finding agrees also well with $\langle T \rangle_{\mathrm{st}}$ at that time, cf. figure 4.13. Although, there still exist strong fluctuations around the conditional mean, the majority of samples is above the extinction value. Similarly, the conditional mean of the normalized OH mass fraction indicates a reignition of the jet, cf. figure 6.8d. However, compared to the earlier instant of time, for small gradients g^* stronger fluctuations around the conditional mean exist. Nevertheless, the peak of the joint distribution $P(Y_{\mathrm{OH,max}}/Y_{\mathrm{OH,q}}, g^*)$ is well above the critical value.

7 Summary and conclusion

This thesis presents two methodologies for analyzing a direct numerical simulation (DNS) of a turbulent reactive jet flow with respect to flamelet modeling. Based on a reference case from the literature, a highly resolved DNS of a temporally evolving syngas jet flame was conducted with the direct numerical flow solver *DINO*, where the mixture fraction was transported as an additional passive scalar. All transport properties except for the mixture fraction were computed based on a mixture-averaged formulation and were provided by the high-performance multi-component transport library EGlib. The temporal integration was performed with a third-order semi-implicit low-storage Runge-Kutta solver, where the Jacobian matrix of the chemical source terms was provided in analytical form by means of pre-generated source code. The source code was generated with the help of *pyJac* and directly compiled into *DINO*.

Based on this DNS, a recently published extended flamelet formulation, that explicitly accounts for curvature-induced flame-tangential transport, is assessed by means of a novel on-the-fly gradient trajectory tracking algorithm, which was conceived as part of this dissertation. To this end, gradient trajectories are tracked on the mixture fraction field, which renders them as flamelets in terms of the flamelet theory. The newly developed framework is coupled to the DNS solver *DINO* and several gradient trajectories are tracked simultaneously in space and time. In order to identify flamelets over time, tracer particles serve as seed points from which gradient trajectories are emitted and traced along the ascending and descending gradient until a local extremal point of the mixture fraction field is reached. This identification procedure allows a full reconstruction of unsteady flamelet histories in the turbulent reactive flow, which forms the basis for assessing the extended flamelet model. This is in contrast to previous studies where flamelets were extracted in a postprocessing step, neglecting transient influences. With the help of the on-the-fly procedure, for the first time, transient terms can be accurately computed and their effect on the temporal evolution of the entire flamelet structure can be analyzed. For that purpose, flamelet histories are recomputed for five flamelet identities by means of a flamelet solver, considering three different flamelet regimes: (i) the classical flamelet regime (FLT), (ii) the curvature-affected flamelet regime (FLT-C) and (iii) the multi-dimensional flamelet regime (FLT-MD). Here, a flamelet identity is defined as a gradient trajectory whose connectivity to the local extremal points does not change within a period of time during the tracking. This distinction is crucial, since abrupt changes in the connectivity might occur due to the splitting or reconnection of extremal points. These changes in connectivity lead to abrupt changes in the boundary conditions, which in turn lead to the formation of a new flamelet identity. During the recomputation of flamelet histories, terms that are originally unclosed in the extended flamelet formulation, i.e. the scalar dissipation rate and multi-dimensional diffusion terms, are computed from the data extracted along gradient trajectories.
The time histories are evaluated in terms of the temperature at the seed point of each trajectory. Comparing the results of the recomputed histories with the DNS, it is evident that the FLT and FLT-C approaches mostly fail to reproduce the DNS results. The temperature was only accurately recomputed for one flamelet identity. On the other hand, the full extended FLT-MD approach

agrees very well with the DNS for all identities considered, indicating that curvature-induced flame-tangential transport is an important aspect to consider in flamelet modeling. The study of recomputed temperature histories is complemented by a budget analysis of instantaneous flamelet identities, verifying the finding that significant multi-dimensional effects are present. Furthermore, only by means of the tracking procedure the complete budgets can be evaluated, including an accurate representation of the transient terms. It is successfully shown that transient terms significantly contribute to the overall balance of the equations.
The methodology of analyzing flamelets in a direct numerical simulation of a turbulent reactive jet, facilitated by an on-the-fly tracking procedure, is only a first step and further research is necessary to develop a fully self-contained extended flamelet model. First and foremost, suitable closure strategies for the multi-dimensional transport term should be developed. Next, a proper tabulation strategy, also to be developed, should be evaluated in a priori and a posteriori test scenarios.

In the second part of the thesis, the method of dissipation elements is applied to the DNS, which (in contrast to the on-the-fly methodology) serves as a postprocessing tool able to identify all gradient trajectories (flamelets) present in the flow. With this framework the mixture fraction field is decomposed into small subunits called “dissipation elements”. The identification of dissipation elements works similarly to the on-the-fly tracking, by tracing gradient trajectories until local extremal values are reached. However, in contrast to the on-the-fly procedure, they are emitted from every grid point within the computational domain. The ensemble of all trajectories that end at the same local extremal points form a dissipation element eventually leading to a geometrical decomposition of the mixture fraction field.
Based on this geometrical decomposition, a parametrization solely based on the endpoints is introduced. It considers the scalar difference ΔZ, the arithmetic mean Z_{m} and an approximate gradient $g = \Delta Z/\ell$ which in turn includes additional information about the Euclidean distance ℓ between the endpoints. Furthermore, the gradient g can be related to the scalar dissipation rate. Apart from this parametrization, a regime classification based on the stoichiometric mixture fraction is proposed which distinguishes between: (i) a fuel rich regime , (ii) a stoichiometric regime and (iii) a fuel lean regime. This classification in conjunction with the two-point character of dissipation elements allows conclusions to be drawn about the connectivity of different regions of the jet, e.g. the connection between the reaction zone and the turbulent core. Based on these regimes, dissipation elements are classified according to the location of their endpoints and various statistics of the above parameters are computed.
First, joint probabilities of Z_{m} and ΔZ are presented. The distribution of these two quantities allows conclusions to be drawn about the mixing process and the location of dissipation elements in mixture fraction space. It is observed that most dissipation elements initially lie in the fuel rich regime. During later jet times, dissipation elements are homogeneously distributed without any distinct maximum of the joint distribution of Z_{m} and ΔZ.
Next, investigating the conditional mean of ΔZ and ℓ reveals that long dissipation elements exhibit large scalar differences on average. The joint probability of these quantities further reveals, that independently of the regime, high probabilities occur for dissipation elements having a length of roughly $1/3$ of the initial jet width. At the same time, the probabilities of the scalar difference at

this length scale varies between the regimes.
The impact of g is studied by analyzing joint statistics of the temperature and the species mass fraction of OH for the stoichiometric regime. It is shown that with an increasing mean gradient, both the temperature and Y_{OH} decrease, although the joint probability reveals large fluctuations around the mean, especially for small gradients.

The analysis of turbulent reactive flows by means of dissipation elements complements the on-the-fly analysis by providing a statistical characterization of flamelet-related parameters. This statistical analysis in turn could be used to develop possible closure strategies for the extended flamelet equations by providing further insights into the topology of the mixture fraction field. Finding proper expressions for curvature in terms of dissipation-element-based quantities could be the first step in this regard. Then, the interplay of the scalar dissipation rate (related to g) and the curvature could be thoroughly analyzed, possibly allowing conclusions to be drawn on the interplay of normal and multi-dimensional transport.

References

[1] International Energy Outlook 2017. Technical report DOE/EIA-0484(2017), U.S. Energy Information Administration, 2017.

[2] R. F. Sawyer. Science based policy for addressing energy and environmental problems. *Proc. Combust. Inst.*, 32(1), 2009.

[3] IPCC. Climate Change 2014: Synthesis Report. Contribution of Working Groups I, II and III to the Fifth Assessment Report of the Intergovernmental Panel on Climate Change. Technical report IPCC AR5, Intergovernmental Panel on Climate Change (IPCC), Geneva, Switzerland, 2014.

[4] A Roadmap for moving to a competitive low carbon economy in 2050. Technical report COM(2011), European Comission, Burssels, 2011.

[5] R. S. Barlow. Laser diagnostics and their interplay with computations to understand turbulent combustion. *Proc. Combust. Inst.*, 31(1), 2007.

[6] E. R. Hawkes, O. Chatakonda, H. Kolla, A. R. Kerstein, and J. H. Chen. A petascale direct numerical simulation study of the modelling of flame wrinkling for large-eddy simulations in intense turbulence. *Combust. Flame*, 159(8), 2012.

[7] J. H. Chen. Petascale direct numerical simulation of turbulent combustion—fundamental insights towards predictive models. *Proc. Combust. Inst.*, 33(1), 2011.

[8] L. F. Richardson. *Weather Prediction by Numerical Process*. Cambridge Mathematical Library. Cambridge University Press, 1922.

[9] A. N. Kolmogorov. The local structure of turbulence in incompressible viscous fluid for very large Reynolds numbers. In *Dokl. Akad. Nauk SSSR*, volume 30 of number 4, 1941.

[10] S. R. Turns. *An Introduction to Combustion: Concepts and Applications*. McGraw-Hill, 3rd edition, 2012.

[11] C. Meneveau and J. Katz. Scale-Invariance and Turbulence Models for Large-Eddy Simulation. *Annu. Rev. Fluid Mech.*, 32(1), 2000.

[12] M. Lesieur and O. Métais. New Trends in Large-Eddy Simulations of Turbulence. *Annu. Rev. Fluid Mech.*, 28(1), 1996.

[13] D. C. Wilcox. *Turbulence Modeling for CFD*. DCW Industries, 2nd edition, 1994.

[14] S. B. Pope. Small scales, many species and the manifold challenges of turbulent combustion. *Proc. Combust. Inst.*, 34(1), 2013.

[15] H. Pitsch. Large-Eddy simulation of turbulent combustion. *Annu. Rev. Fluid Mech.*, 38(1), 2006.

[16] D. Veynante and L. Vervisch. Turbulent combustion modeling. *Prog. Energy Combust. Sci.*, 28(3), 2002.

[17] T. Echekki and E. Mastorakos. *Turbulent Combustion Modeling*. T. Echekki and E. Mastorakos, editors, volume 95 of *Fluid Mechanics and Its Applications*. Springer Netherlands, Dordrecht, 2011.

[18] R. O. Fox. *Computational Models for Turbulent Reacting Flows*. Cambridge Series in Chemical Engineering. Cambridge University Press, 2003.

[19] N. Peters. *Turbulent Combustion*. Cambridge University Press, 2004.

[20] S. B. Pope. PDF methods for turbulent reactive flows. *Prog. Energy Combust. Sci.*, 11(2), 1985.

[21] D. C. Haworth. Progress in probability density function methods for turbulent reacting flows. *Prog. Energy Combust. Sci.*, 36(2), 2010.

[22] N. Peters. Local Quenching Due to Flame Stretch and Non-Premixed Turbulent Combustion. *Combust. Sci. Technol.*, 30(1-6), 1983.

[23] N. Peters. Laminar diffusion flamelet models in non-premixed turbulent combustion. *Prog. Energy Combust. Sci.*, 10(3), 1984.

[24] S. Weise, S. Popp, D. Messig, and C. Hasse. A Computationally Efficient Implementation of Tabulated Combustion Chemistry based on Polynomials and Automatic Source Code Generation. *Flow, Turbul. Combust.*, 100(1), 2017.

[25] S. Weise and C. Hasse. Reducing the memory footprint in Large Eddy Simulations of reactive flows. *Parallel Comput.*, 49, 2015.

[26] S. Weise, D. Messig, B. Meyer, and C. Hasse. An abstraction layer for efficient memory management of tabulated chemistry and flamelet solutions. *Combust. Theory Model.*, 17(3), 2013.

[27] H. G. Pitsch. *Modellierung der Zündung und Schadstoffbildung bei der dieselmotorischen Verbrennung mit Hilfe eines interaktiven Flamelet-Modells*. PhD thesis, Technische Hochschule Aachen, Aachen, 1998.

[28] H. Pitsch, M. Chen, and N. Peters. Unsteady flamelet modeling of turbulent hydrogen-air diffusion flames. *Symp. Combust.*, 27(1), 1998.

[29] F. Mauß, D. Keller, and N. Peters. A lagrangian simulation of flamelet extinction and re-ignition in turbulent jet diffusion flames. *Symp. Combust.*, 23(1), 1991.

[30] B. Cuenot, F. Egolfopoulos, and T. Poinsot. An unsteady laminar flamelet model for non-premixed combustion. *Combust. Theory Model.*, 4(1), 2000.

[31] H. Pitsch and H. Steiner. Large-eddy simulation of a turbulent piloted methane/air diffusion flame (Sandia flame D). *Phys. Fluids*, 12(10), 2000.

[32] C. Hasse and N. Peters. A two mixture fraction flamelet model applied to split injections in a DI Diesel engine. *Proc. Combust. Inst.*, 30(2), 2005.

[33] M. Ihme and Y. C. See. LES flamelet modeling of a three-stream MILD combustor: Analysis of flame sensitivity to scalar inflow conditions. *Proc. Combust. Inst.*, 33(1), 2011.

[34] E. M. Doran, H. Pitsch, and D. J. Cook. A priori testing of a two-dimensional unsteady flamelet model for three-feed combustion systems. *Proc. Combust. Inst.*, 34(1), 2013.

[35] C. D. Pierce and P. Moin. Progress-variable approach for large-eddy simulation of non-premixed turbulent combustion. *J. Fluid Mech.*, 504, 2004.

[36] M. Ihme, C. M. Cha, and H. Pitsch. Prediction of local extinction and re-ignition effects in non-premixed turbulent combustion using a flamelet/progress variable approach. *Proc. Combust. Inst.*, 30(1), 2005.

[37] M. Ihme and H. Pitsch. Prediction of extinction and reignition in nonpremixed turbulent flames using a flamelet/progress variable model: 1. A priori study and presumed PDF closure. *Combust. Flame*, 155(1), 2008.

[38] M. Ihme and H. Pitsch. Modeling of radiation and nitric oxide formation in turbulent nonpremixed flames using a flamelet/progress variable formulation. *Phys. Fluids*, 20(5), 2008.

[39] H. Barths, N. Peters, N. Brehm, A. Mack, M. Pfitzner, and V. Smiljanovski. Simulation of pollutant formation in a gas-turbine combustor using unsteady flamelets. *Symp. Combust.*, 27(2), 1998.

[40] V. Mittal, D. J. Cook, and H. Pitsch. An extended multi-regime flamelet model for IC engines. *Combust. Flame*, 159(8), 2012.

[41] K. Claramunt, R. Cònsul, D. Carbonell, and C. Pérez-Segarra. Analysis of the laminar flamelet concept for nonpremixed laminar flames. *Combust. Flame*, 145(4), 2006.

[42] M. Ihme and H. Pitsch. Prediction of extinction and reignition in nonpremixed turbulent flames using a flamelet/progress variable model: 2. Application in LES of Sandia flames D and E. *Combust. Flame*, 155(1), 2008.

[43] D. Messig, F. Hunger, J. Keller, and C. Hasse. Evaluation of radiation modeling approaches for non-premixed flamelets considering a laminar methane air flame. *Combust. Flame*, 160(2), 2013.

[44] C. Kortschik, S. Honnet, and N. Peters. Influence of curvature on the onset of autoignition in a corrugated counterflow mixing field. *Combust. Flame*, 142(1), 2005.

[45] Y. Xuan, G. Blanquart, and M. E. Mueller. Modeling curvature effects in diffusion flames using a laminar flamelet model. *Combust. Flame*, 161(5), 2014.

[46] H. Xu, F. Hunger, M. Vascellari, and C. Hasse. A consistent flamelet formulation for a reacting char particle considering curvature effects. *Combust. Flame*, 160(11), 2013.

[47] A. Scholtissek, W. L. Chan, H. Xu, F. Hunger, H. Kolla, J. H. Chen, M. Ihme, and C. Hasse. A multi-scale asymptotic scaling and regime analysis of flamelet equations including tangential diffusion effects for laminar and turbulent flames. *Combust. Flame*, 162(4), 2015.

[48] L. Wang and N. Peters. The length-scale distribution function of the distance between extremal points in passive scalar turbulence. *J. Fluid Mech.*, 554, 2006.

[49] H. G. Pitsch and P. Trisjono. Can Combustion Models be Developed from DNS Data? In *Proc. 19th Australas. Fluid Mech. Conf.* Melbourne, 2014.

[50] P. Trisjono and H. Pitsch. Systematic Analysis Strategies for the Development of Combustion Models from DNS: A Review. *Flow, Turbul. Combust.*, 95(2-3), 2015.

[51] C. K. Law. *Combustion Physics*. Cambridge University Press, 2006.

[52] E. Strohmaier, H. W. Meuer, J. Dongarra, and H. D. Simon. The TOP500 List and Progress in High-Performance Computing. *Computer (Long. Beach. Calif).*, 48(11), 2015.

[53] M. Schmitt, C. E. Frouzakis, Y. M. Wright, A. G. Tomboulides, and K. Boulouchos. Investigation of cycle-to-cycle variations in an engine-like geometry. *Phys. Fluids*, 26(12), 2014.

[54] R. W. Grout, A. Gruber, H. Kolla, P.-T. Bremer, J. C. Bennett, A. Gyulassy, and J. H. Chen. A direct numerical simulation study of turbulence and flame structure in transverse jets analysed in jet-trajectory based coordinates. *J. Fluid Mech.*, 706, 2012.

[55] C. S. Yoo, R. Sankaran, and J. H. Chen. Three-dimensional direct numerical simulation of a turbulent lifted hydrogen jet flame in heated coflow: flame stabilization and structure. *J. Fluid Mech.*, 640, 2009.

[56] Y. Minamoto and J. H. Chen. {DNS} of a turbulent lifted {DME} jet flame. *Combust. Flame*, 169, 2016.

[57] T. Poinsot and D. Veynante. *Theoretical and Numerical Combustion, Second Edition*. 3. Edition, editor. R.T. Edwards, Inc., 2nd edition, 2005.

[58] G. Fru. *Direct Numerical Simulation of Turbulent Flames on Super-Computers and PC-Clusters*. PhD thesis, Otto-von-Guericke Universität, Magdeburg, 2011.

[59] F. A. Williams. *Combustion Theory*. Addison-Wesley, 2nd edition, 1985.

[60] E. S. Oran and J. P. Boris. *Numerical Simulation of Reactive Flow*. 2nd edition, 2001.

[61] K. K. Kuo. *Principles of combustion*. Wiley New York et al., 2nd edition, 2005.

[62] G. Fru, G. Janiga, and D. Thévenin. Impact of Volume Viscosity on the Structure of Turbulent Premixed Flames in the Thin Reaction Zone Regime. *Flow, Turbul. Combust.*, 88(4), 2012.

[63] G. Billet, V. Giovangigli, and G. D. Gassowski. Impact of volume viscosity on a shock-hydrogen-bubble interaction. *Combust. Theory Model.*, 12(2), 2008.

[64] V. Giovangigli. Multicomponent transport in laminar flames. *Proc. Combust. Inst.*, 35(1), 2015.

[65] G. Prangsma, A. Alberga, and J. Beenakker. Ultrasonic determination of the volume viscosity of N2, CO, CH4 and CD4 between 77 and 300 K. *Physica*, 64(2), 1973.

[66] V. Giovangigli. *Multicomponent Flow Modeling*. Birkhäuser Boston, 1999.

[67] A. H. Shapiro. *The dynamics and thermodynamics of compressible fluid flow*, volume 1. The Ronald Press Company, 1953.

[68] P. Atkins and J. De Paula. *Atkins' physical chemistry*. Oxford University Press, 8th edition, 2006.

[69] A. Burcat and B. Ruscic. Third millennium ideal gas and condensed phase thermodynamical database for combustion. Technical report TAE 960, Technion Aerospace Engineering (TAE), 2001.

[70] D. R. Stull and H. Prophet. JANAF thermochemical tables. Technical report NSRDS-NBS-37, US National Bureau of Standard, 1971.

[71] S. Gordon and B. J. McBride. Computer Program for Calculation of Complex Chemical Equilibrium Compositions, Rocket Performance, Incident and Reflected Shocks, and Chapman-Jouguet Detonations. Technical report NASA SP-273, NASA Lewis Research Center, Cleveland, 1971.

[72] H. D. Baehr and S. Kabelac. *Thermodynamik*. Springer-Lehrbuch. Springer Berlin Heidelberg, Berlin, Heidelberg, 15th edition, 2012.

[73] P. Stephan, K. Schaber, K. Stephan, and F. Mayinger. *Thermodynamik*. Springer-Lehrbuch. Springer Berlin Heidelberg, Berlin, Heidelberg, 15th edition, 2010.

[74] G. Volpe. On the use and the accuracy of compressible flow codes at low Mach numbers. In *22nd Fluid Dyn. Plasma Dyn. Lasers Conf.* Reston, Virigina. American Institute of Aeronautics and Astronautics, 1991.

[75] R. Pletcher and K. H. Chen. On solving the compressible Navier-Stokes equations for unsteady flows at very low Mach numbers. In *11th Comput. Fluid Dyn. Conf.* Reston, Virigina. American Institute of Aeronautics and Astronautics, 1993.

[76] A. Majda and J. Sethian. The Derivation and Numerical Solution of the Equations for Zero Mach Number Combustion. *Combust. Sci. Technol.*, 42(3-4), 1985.

[77] S. Klainerman and A. Majda. Compressible and Incompressible Fluids. *Commun. Pure Appl. Math.*, XXXV, 1982.

[78] B. Müller. Low Mach Number Asymptotics of the Navier-Stokes Equations and Numerical Implications. In *30th Comput. Fluid Dyn.* von Karman Institute for Fluid Dynamics, 1999.

[79] J. D. Charentenay, D. Thévenin, and B. Zamuner. Comparison of direct numerical simulations of turbulent flames using compressible or low-Mach number formulations. *Int. J. Numer. Methods Fluids*, 39(6), 2002.

[80] S. Chapman and T. G. Cowling. *The Mathematical Theory of Non-uniform Gases: An Account of the Kinetic Theory of Viscosity, Thermal Conduction and Diffusion of Gases*. Cambridge University Press, 1953.

[81] J. O. Hirschfelder, C. F. Curtiss, and R. B. Bird. *Molecular theory of gases and liquids*, volume 26. Wiley New York, 1954.

[82] R. Hilbert, F. Tap, H. El-Rabii, and D. Thévenin. Impact of detailed chemistry and transport models on turbulent combustion simulations. *Prog. Energy Combust. Sci.*, 30(1), 2004.

[83] L. Monchick, K. S. Yun, and E. A. Mason. Formal Kinetic Theory of Transport Phenomena in Polyatomic Gas Mixtures. *J. Chem. Phys.*, 39(3), 1963.

[84] G. Dixon-Lewis. Flame Structure and Flame Reaction Kinetics. II. Transport Phenomena in Multicomponent Systems. *Proc. R. Soc. London A Math. Phys. Eng. Sci.*, 307(1488), 1968.

[85] C. S. Wang Chang, J. D. Boer, G. W. Ford, and G. E. Uhlenbeck. Studies in statistical mechanics. In J. D. Boer and G. E. Uhlenbeck, editors, *Stud. Stat. Mech.* Volume 5. North-Holland, 2nd edition, 1970.

[86] L. Waldmann. Transporterscheinungen in Gasen von mittlerem Druck. In S. Flügge, editor, *Thermodyn. der Gase / Thermodyn. Gases*. Volume 3, Handbuch der Physik / Encyclopedia of Physics. Springer Berlin Heidelberg, Berlin, Heidelberg, 1958.

[87] E. A. Mason and L. Monchick. Heat Conductivity of Polyatomic and Polar Gases. 36(6), 1962.

[88] W. Wangard, D. S. Dandy, and B. J. Miller. A Numerically Stable Method for Integration of the Multicomponent Species Diffusion Equations. *J. Comput. Phys.*, 174(1), 2001.

[89] A. Ern and V. Giovangigli. *Multicomponent Transport Algorithms*, volume 24 of *Lecture Notes in Physics Monographs*. Springer Berlin Heidelberg, Berlin, Heidelberg, 1994.

[90] A. Ern and V. Giovangigli. Thermal conduction and thermal diffusion in dilute polyatomic gas mixtures. *Phys. A Stat. Mech. its Appl.*, 214(4), 1995.

[91] A. Ern and V. Giovangigli. Structure of transport linear systems in dilute isotropic gas mixtures. *Phys. Rev. E*, 53(1), 1996.

[92] A. Ern and V. Giovangigli. EGLIB: a General-Purpose Fortran Library for Multicomponent Transport Property Evaluation. Technical report, CERMICS, 1996.

[93] V. Giovangigli. Convergent iterative methods for multicomponent diffusion. *IMPACT Comput. Sci. Eng.*, 3(3), 1991.

[94] A. Ern and V. Giovangigli. Optimized Transport Algorithms for Flame Codes. *Combust. Sci. Technol.*, 118(4-6), 1996.

[95] R. J. Kee, G. Dixon-Lewis, J. Warnatz, M. E. Coltrin, J. A. Miller, and H. K. Moffat. A Fortran Computer Code Package For The Evaluation Of Gas-Phase, Multicomponent Transport Properties. Technical report SAND86-8246, Sandia National Laboratories, 1998.

[96] D. G. Goodwin, H. K. Moffat, and R. L. Speth. Cantera: An Object-oriented Software Toolkit for Chemical Kinetics, Thermodynamics, and Transport Processes. http://www.cantera.org, 2017.

[97] C. F. Curtiss and J. O. Hirschfelder. Transport Properties of Multicomponent Gas Mixtures. *J. Chem. Phys.*, 17(6), 1949.

[98] B. E. Poling, J. M. Prausnitz, and J. P. O'Connell. *The properties of gases and liquids*, volume 5. McGraw-Hill New York, 5th edition, 2001.

[99] R. S. Brokaw. Approximate Formulas for the Viscosity and Thermal Conductivity of Gas Mixtures. II. *J. Chem. Phys.*, 42(4), 1965.

[100] C. R. Wilke. A Viscosity Equation for Gas Mixtures. *J. Chem. Phys.*, 18(4), 1950.

[101] R. B. Bird, W. E. Stewart, and E. N. Lightfoot. *Transport phenomena*. John Wiley & Sons, 2nd edition, 2002.

[102] J. Kestin, H. E. Khalifa, and W. A. Wakeham. Viscosity of multicomponent mixtures of four complex gases. *J. Chem. Phys.*, 65(12), 1976.

[103] R. J. Kee, M. E. Coltrin, and P. Glarborg. *Chemically Reacting Flow : Theory and Practice*. John Wiley & Sons, Ltd., 1st edition, 2003.

[104] R. B. Bird and D. J. Klingenberg. Multicomponent diffusion—A brief review. *Adv. Water Resour.*, 62, 2013.

[105] J. Hirschfelder and C. Curtiss. Theory of propagation of flames. Part I: General equations. *Symp. Combust. Flame, Explos. Phenom.*, 3(1), 1948.

[106] K. K. Kuo and R. Acharya. *Fundamentals of Turbulent and Multiphase Combustion*. John Wiley & Sons, Inc., 2012.

[107] S. Mathur, P. Tondon, and S. Saxena. Thermal conductivity of binary, ternary and quaternary mixtures of rare gases. *Mol. Phys.*, 12(6), 1967.

[108] J. Burgoyne and F. Weinberg. A method of analysis of a plane combustion wave. *Symp. Combust.*, 4(1), 1953.

[109] J. Warnatz, U. Maas, and R. W. Dibble. *Combustion: Physical and Chemical Fundamentals, Modeling and Simulation, Experiments, Pollutant Formation*. Springer, softcover edition, 2010.

[110] T. Lu and C. K. Law. Toward accommodating realistic fuel chemistry in large-scale computations. *Prog. Energy Combust. Sci.*, 35(2), 2009.

[111] K. E. Niemeyer, N. J. Curtis, and C.-J. Sung. pyJac: Analytical Jacobian generator for chemical kinetics. *Comput. Phys. Commun.*, 2017.

[112] R. J. Kee, F. M. Rupley, E. Meeks, and J. A. Miller. CHEMKIN-III: A fortran chemical kinetics package for the analysis of gas-phase chemical and plasma kinetics. Technical report SAND96-8216, Sandia National Laboratories, 1996.

[113] F. A. Williams. *Recent Advances in Theoretical Descriptions of Turbulent Diffusion Flames*. In *Turbul. Mix. Nonreact. React. Flows*. S. N. B. Murthy, editor. Springer New York, Boston, MA, 1975.

[114] R. Bilger. The structure of turbulent nonpremixed flames. *Symp. Combust.*, 22(1), 1988.

[115] J. C. Sutherland, P. J. Smith, and J. H. Chen. Quantification of differential diffusion in nonpremixed systems. *Combust. Theory Model.*, 9(2), 2005.

[116] H. Pitsch and N. Peters. A Consistent Flamelet Formulation for Non-Premixed Combustion Considering Differential Diffusion Effects. *Combust. Flame*, 114(1-2), 1998.

[117] L. Crocco. Sulla trasmissione del calore da una lamina piana a un fluido scorrente ad alta velocita. *L'Aerotecnica*, 12, 1932.

[118] J. S. Kim and F. A. Williams. Structures of Flow and Mixture-Fraction Fields for Counterflow Diffusion Flames with Small Stoichiometric Mixture Fractions. *SIAM J. Appl. Math.*, 53(6), 1993.

[119] S. Ishizuka. On the behavior of premixed flames in a rotating flow field: Establishment of tubular flames. *Symp. Combust.*, 20(1), 1985.

[120] P. Clavin and G. Joulin. *Flamelet Library for Turbulent Wrinkled Flames*. In *Turbul. React. Flows*. R. Borghi and S. N. B. Murthy, editors. Springer US, New York, NY, 1989.

[121] K. Yoshida and T. Takagi. Transient local extinction and reignition behavior of diffusion flames affected by flame curvature and preferential diffusion. *Symp. Combust.*, 27(1), 1998.

[122] H. G. Im, C. Law, and R. L. Axelbaum. Opening of the Burke-Schumann flame tip and the effects of curvature on diffusion flame extinction. *Symp. Combust.*, 23(1), 1990.

[123] J. A. V. Oijen, R. J. M. Bastiaans, and L. P. H. D. Goey. Low-dimensional manifolds in direct numerical simulations of premixed turbulent flames. *Proc. Combust. Inst.*, 31(1), 2007.

[124] L. M. Verhoeven, W. J. S. Ramaekers, J. A. V. Oijen, and L. P. H. D. Goey. Modeling non-premixed laminar co-flow flames using flamelet-generated manifolds. *Combust. Flame*, 159(1), 2012.

[125] Y. Xuan and G. Blanquart. Numerical modeling of sooting tendencies in a laminar co-flow diffusion flame. *Combust. Flame*, 160(9), 2013.

[126] A. Scholtissek, R. Pitz, and C. Hasse. Flamelet budget and regime analysis for non-premixed tubular flames. *Proc. Combust. Inst.*, 36(1), 2017.

[127] A. Scholtissek, F. Dietzsch, M. Gauding, and C. Hasse. In-situ tracking of mixture fraction gradient trajectories and unsteady flamelet analysis in turbulent non-premixed combustion. *Combust. Flame*, 175, 2017.

[128] W. L. Chan, H. Kolla, J. H. Chen, and M. Ihme. Assessment of model assumptions and budget terms of the unsteady flamelet equations for a turbulent reacting jet-in-cross-flow. *Combust. Flame*, 161(10), 2014.

[129] S. Cheatham and M. Matalon. A general asymptotic theory of diffusion flames with application to cellular instability. *J. Fluid Mech.*, 414, 2000.

[130] M. P. Ida and M. J. Miksis. The Dynamics of Thin Films I: General Theory. *SIAM J. Appl. Math.*, 58(2), 1998.

[131] J. Yao and D. S. Stewart. On the dynamics of multi-dimensional detonation. *J. Fluid Mech.*, 309, 1996.

[132] M. Matalon. On Flame Stretch. *Combust. Sci. Technol.*, 31(3-4), 1983.

[133] J. V. Oijen, A. Donini, R. Bastiaans, J. ten Thije Boonkkamp, and L. D. Goey. State-of-the-art in premixed combustion modeling using flamelet generated manifolds. *Prog. Energy Combust. Sci.*, 57, 2016.

[134] C. H. Gibson. Fine Structure of Scalar Fields Mixed by Turbulence. I. Zero-Gradient Points and Minimal Gradient Surfaces. *Phys. Fluids*, 11(11), 1968.

[135] S. A. Orszag and G. S. Patterson. Numerical Simulation of Three-Dimensional Homogeneous Isotropic Turbulence. *Phys. Rev. Lett.*, 28(2), 1972.

[136] P. Moin and K. Mahesh. Direct numerical simulation: A Tool in Turbulence Research. *Annu. Rev. Fluid Mech.*, 30(1), 1998.

[137] S. B. Pope. *Turbulent Flows*. Cambridge University Press, 2000.

[138] O. Reynolds. On the Dynamical Theory of Incompressible Viscous Fluids and the Determination of the Criterion. *Philos. Trans. R. Soc. London A Math. Phys. Eng. Sci.*, 186(0), 1895.

[139] A. Abdelsamie, G. Fru, T. Oster, F. Dietzsch, G. Janiga, and D. Thévenin. Towards direct numerical simulations of low-Mach number turbulent reacting and two-phase flows using immersed boundaries. *Comput. Fluids*, 131, 2016.

[140] A. Abdelsamie. *Direct Numerical Simulations of Turbulent Flow and Spray Combustion*. PhD thesis, University of Magdeburg "Otto von Guericke", 2017.

[141] A. Abdelsamie and D. Thévenin. Direct numerical simulation of spray evaporation and autoignition in a temporally-evolving jet. *Proc. Combust. Inst.*, 36(2), 2017.

[142] R. Schießl, V. Bykov, U. Maas, A. Abdelsamie, and D. Thévenin. Implementing multi-directional molecular diffusion terms into Reaction Diffusion Manifolds (REDIMs). *Proc. Combust. Inst.*, 36(1), 2017.

[143] A. Abdelsamie, D. O. Lignell, and D. Thévenin. Comparison Between ODT and DNS for Ignition Occurrence in Turbulent Premixed Jet Combustion: Safety-Relevant Applications. *Zeitschrift für Phys. Chemie*, 231(10), 2017.

[144] M. Gauding, F. Dietzsch, J. H. Goebbert, D. Thévenin, A. Abdelsamie, and C. Hasse. Dissipation element analysis of a turbulent non-premixed jet flame. *Phys. Fluids*, 29(8), 2017.

[145] A. Abdelsamie, G. Janiga, C. Chi, and D. Thévenin. *Turbulence Structure Analysis of DNS Data Using DMD and SPOD: Mixing Jet and Channel Flow*. In *Proc. iTi Conf. Turbul. 2016*. Springer International Publishing, Cham, 2017.

[146] L. Daróczy, A. Abdelsamie, G. Janiga, and D. Thévenin. State detection and hybrid simulation of biomedical flows. In *Tenth Int. Symp. Turbul. Shear Flow Phenom.* 2017.

[147] B. Fornberg. Classroom Note:Calculation of Weights in Finite Difference Formulas. *SIAM Rev.*, 40(3), 1998.

[148] B. Fornberg. Generation of finite difference formulas on arbitrarily spaced grids. *Math. Comput.*, 51(184), 1988.

[149] M. Bowen and R. Smith. Derivative formulae and errors for non-uniformly spaced points. *Proc. R. Soc. London A Math. Phys. Eng. Sci.*, 461(2059), 2005.

[150] R. J. LeVeque. *Finite Difference Methods for Ordinary and Partial Differential Equations*. Steady-State and Time-Dependent Problems. Society for Industrial and Applied Mathematics, 2007.

[151] E. R. Hawkes, R. Sankaran, J. C. Sutherland, and J. H. Chen. Direct numerical simulation of turbulent combustion: fundamental insights towards predictive models. *J. Phys. Conf. Ser.*, 16(1), 2005.

[152] J. H. Chen, A. Choudhary, B. D. Supinski, M. DeVries, E. R. Hawkes, S. Klasky, W. K. Liao, K. L. Ma, J. Mellor-Crummey, N. Podhorszki, R. Sankaran, S. Shende, and C. S. Yoo. Terascale direct numerical simulations of turbulent combustion using S3D. *Comput. Sci. Discov.*, 2(1), 2009.

[153] K. W. Jenkins and R. S. Cant. *Direct Numerical Simulation of Turbulent Flame Kernels*. In *Recent Adv. DNS LES*. D. Knight and L. Sakell, editors. Volume 54. Fluid Mechanics and its Applications. Springer Netherlands, Dordrecht, 1999.

[154] D. Thévenin, F. Behrendt, U. Maas, B. Przywara, and J. Warnatz. Development of a parallel direct simulation code to investigate reactive flows. *Comput. Fluids*, 25(5), 1996.

[155] G. Fru, G. Janiga, and D. Thévenin. Direct Numerical Simulations of the Impact of High Turbulence Intensities and Volume Viscosity on Premixed Methane Flames. *J. Combust.*, 2011, 2011.

[156] D. J. Fyfe. Economical Evaluation of Runge-Kutta Formulae. *Math. Comput.*, 20(95), 1966.

[157] V. Moureau, P. Domingo, and L. Vervisch. Design of a massively parallel CFD code for complex geometries. *Comptes Rendus Mécanique*, 339(2-3), 2011.

[158] V. Moureau, P. Domingo, and L. Vervisch. From Large-Eddy Simulation to Direct Numerical Simulation of a lean premixed swirl flame: Filtered laminar flame-PDF modeling. *Combust. Flame*, 158(7), 2011.

[159] T. Schoenfeld and M. Rudgyard. Steady and Unsteady Flow Simulations Using the Hybrid Flow Solver AVBP. *AIAA J.*, 37(11), 1999.

[160] O. Desjardins, G. Blanquart, G. Balarac, and H. Pitsch. High order conservative finite difference scheme for variable density low Mach number turbulent flows. *J. Comput. Phys.*, 227(15), 2008.

[161] S. MacNamara and G. Strang. Operator Splitting. In R. Glowinski, S. J. Osher, and W. Yin, editors, *Split. Methods Commun. Imaging, Sci. Eng.* Scientific Computation. Springer International Publishing, 2016.

[162] G. Strang. On the Construction and Comparison of Difference Schemes. *SIAM J. Numer. Anal.*, 5(3), 1968.

[163] R. Leveque and H. Yee. A study of numerical methods for hyperbolic conservation laws with stiff source terms. *J. Comput. Phys.*, 86(1), 1990.

[164] X. Zhong. Additive Semi-Implicit Runge–Kutta Methods for Computing High-Speed Nonequilibrium Reactive Flows. *J. Comput. Phys.*, 128(1), 1996.

[165] J. J.-i. Yoh and X. Zhong. Low-storage semi-implicit Runge-Kutta methods for reactive flow computations. In *36th AIAA Aerosp. Sci. Meet. Exhib.* Aerospace Sciences Meetings, Reston, Virigina. American Institute of Aeronautics and Astronautics, 1998.

[166] G. J. Cooper and A. Sayfy. Additive Methods for the Numerical Solution of Ordinary Differential Equations. *Math. Comput.*, 35(152), 1980.

[167] G. J. Cooper and A. Sayfy. Additive Runge-Kutta Methods for Stiff Ordinary Differential Equations. *Math. Comput.*, 40(161), 1983.

[168] J. J.-i. Yoh and X. Zhong. Semi-implicit Runge-Kutta schemes for stiff multi-dimensional reacting flows. In *35th Aerosp. Sci. Meet. Exhib.* Aerospace Sciences Meetings. American Institute of Aeronautics and Astronautics, 1997.

[169] M. H. Carpenter and C. A. Kennedy. Fourth-order 2N-storage Runge-Kutta schemes. Technical report NASA-TM-109112, NASA Langley Research Center, 1994.

[170] C. Canuto, M. Y. Hussaini, A. Quarteroni, and T. A. Zang. *Spectral Methods*. Scientific Computation. Springer Berlin Heidelberg, 2006.

[171] J. D. Charentenay. *Simulation numérique découlements réactifs instationnaires a faibles nombres de Mach*. PhD thesis, Ecole Centrale Paris, 2001.

[172] S. Gill. A process for the step-by-step integration of differential equations in an automatic digital computing machine. *Math. Proc. Cambridge Philos. Soc.*, 47(1), 1951.

[173] E. K. Blum. A Modification of the Runge-Kutta Fourth-Order Method. *Math. Comput.*, 16(78), 1962.

[174] J. H. Williamson. Low-storage Runge-Kutta schemes. *J. Comput. Phys.*, 35(1), 1980.

[175] C. A. Kennedy, M. H. Carpenter, and R. Lewis. Low-storage, explicit Runge–Kutta schemes for the compressible Navier–Stokes equations. *Appl. Numer. Math.*, 35(3), 2000.

[176] S. J. Ruuth. Global optimization of explicit strong-stability-preserving Runge-Kutta methods. *Math. Comput.*, 75(253), 2005.

[177] S. Gottlieb. On high order strong stability preserving Runge-Kutta and multi step time discretizations. *J. Sci. Comput.*, 25(1-2), 2005.

[178] S. Gottlieb, C.-W. Shu, and E. Tadmor. Strong Stability-Preserving High-Order Time Discretization Methods. *SIAM Rev.*, 43(1), 2001.

[179] K. E. Niemeyer and N. J. Curtis. {pyJac} v1.0.4, 2017.

[180] J. Nickolls, I. Buck, M. Garland, and K. Skadron. Scalable Parallel Programming with CUDA. *Queue*, 6(2), 2008.

[181] F. Perini, E. Galligani, and R. D. Reitz. An Analytical Jacobian Approach to Sparse Reaction Kinetics for Computationally Efficient Combustion Modeling with Large Reaction Mechanisms. *Energy & Fuels*, 26(8), 2012.

[182] C. Safta, H. N. Najm, and O. Knio. TChem - A Software Toolkit for the Analysis of Complex Kinetic Models. Technical report, Sandia National Laboratories, Livermore, 2011.

[183] K. Niemeyer, N. J. Curtis, and C.-J. Sung. Initial investigation of pyJac: an analytical Jacobian generator for chemical kinetics. *Fall 2015 Meet. West. states Sect. Combust. Inst.*, 2016.

[184] R. Courant, K. Friedrichs, and H. Lewy. Über die partiellen Differenzengleichungen der mathematischen Physik. *Math. Ann.*, 100(1), 1928.

[185] J. Kim and P. Moin. Application of a fractional-step method to incompressible Navier-Stokes equations. *J. Comput. Phys.*, 59(2), 1985.

[186] D. L. Brown, R. Cortez, and M. L. Minion. Accurate Projection Methods for the Incompressible Navier–Stokes Equations. *J. Comput. Phys.*, 168(2), 2001.

[187] J. D. Charentenay and A. Ern. Multicomponent transport impact on turbulent premixed H2/O2 flames. *Combust. Theory Model.*, 6(3), 2002.

[188] H. N. Najm, P. S. Wyckoff, and O. M. Knio. A Semi-implicit Numerical Scheme for Reacting Flow. *J. Comput. Phys.*, 143(2), 1998.

[189] O. M. Knio, H. N. Najm, and P. S. Wyckoff. A Semi-implicit Numerical Scheme for Reacting Flow. *J. Comput. Phys.*, 154(2), 1999.

[190] F. Nicoud. Conservative High-Order Finite-Difference Schemes for Low-Mach Number Flows. *J. Comput. Phys.*, 158(1), 2000.

[191] M. S. Day and J. B. Bell. Numerical simulation of laminar reacting flows with complex chemistry. *Combust. Theory Model.*, 4(4), 2000.

[192] J. B. Bell, M. S. Day, C. A. Rendleman, S. E. Woosley, and M. A. Zingale. Adaptive low Mach number simulations of nuclear flame microphysics. *J. Comput. Phys.*, 195(2), 2004.

[193] R. D. Falgout and U. M. Yang. *hypre: A Library of High Performance Preconditioners*. In *ICCS Int. Conf. Comput. Sci.* P. M. A. Sloot, A. G. Hoekstra, C. J. K. Tan, and J. J. Dongarra, editors. Springer Berlin Heidelberg, Berlin, Heidelberg, 2002.

[194] S. Laizet, E. Lamballais, and J. Vassilicos. A numerical strategy to combine high-order schemes, complex geometry and parallel computing for high resolution DNS of fractal generated turbulence. *Comput. Fluids*, 39(3), 2010.

[195] S. Laizet and N. Li. Incompact3d: A powerful tool to tackle turbulence problems with up to O(105) computational cores. *Int. J. Numer. Methods Fluids*, 67(11), 2011.

[196] J. Cooley, P. Lewis, and P. Welch. The fast Fourier transform algorithm: Programming considerations in the calculation of sine, cosine and Laplace transforms. *J. Sound Vib.*, 12(3), 1970.

[197] P. N. Swarztrauber. Symmetric FFTs. *Math. Comput.*, 47(175), 1986.

[198] N. Li and S. Laizet. 2DECOMP&FFT-A highly scalable 2D decomposition library and FFT interface. In *Cray User Gr. Conf.* Edinburgh, 2010.

[199] M. Frigo and S. G. Johnson. The Design and Implementation of FFTW3. *Proc. IEEE*, 93(2), 2005.

[200] S. Aseeri, O. Batrasev, M. Icardi, B. Leu, A. Liu, N. Li, B. K. Muite, E. Müller, B. Palen, M. Quell, H. Servat, P. Sheth, R. Speck, M. Van Moer, and J. Vienne. Solving the Klein-Gordon Equation Using Fourier Spectral Methods: A Benchmark Test for Computer Performance. In *Proc. Symp. High Perform. Comput.* HPC '15, San Diego, CA, USA. Society for Computer Simulation International, 2015.

[201] E. R. Hawkes, R. Sankaran, J. C. Sutherland, and J. H. Chen. Scalar mixing in direct numerical simulations of temporally evolving plane jet flames with skeletal CO/H2 kinetics. *Proc. Combust. Inst.*, 31(1), 2007.

[202] S. Vo, O. Stein, A. Kronenburg, and M. Cleary. Assessment of mixing time scales for a sparse particle method. *Combust. Flame*, 179, 2017.

[203] Y. Yang, H. Wang, S. B. Pope, and J. H. Chen. Large-eddy simulation/probability density function modeling of a non-premixed CO/H2 temporally evolving jet flame. *Proc. Combust. Inst.*, 34(1), 2013.

[204] A. Krisman, J. C. Tang, E. R. Hawkes, D. O. Lignell, and J. H. Chen. A DNS evaluation of mixing models for transported PDF modelling of turbulent nonpremixed flames. *Combust. Flame*, 161(8), 2014.

[205] J. C. Bennett, V. Krishnamoorthy, Shusen Liu, R. W. Grout, E. R. Hawkes, J. H. Chen, J. Shepherd, V. Pascucci, and P.-T. Bremer. Feature-Based Statistical Analysis of Combustion Simulation Data. *IEEE Trans. Vis. Comput. Graph.*, 17(12), 2011.

[206] L. Wang, E. R. Hawkes, and J. H. Chen. Flame edge statistics in turbulent combustion. *Proc. Combust. Inst.*, 33(1), 2011.

[207] B. A. Sen, E. R. Hawkes, and S. Menon. Large eddy simulation of extinction and reignition with artificial neural networks based chemical kinetics. *Combust. Flame*, 157(3), 2010.

[208] E. R. Hawkes, R. Sankaran, J. H. Chen, S. A. Kaiser, and J. H. Frank. An analysis of lower-dimensional approximations to the scalar dissipation rate using direct numerical simulations of plane jet flames. *Proc. Combust. Inst.*, 32(1), 2009.

[209] L. Wang and N. Peters. A compensation-defect model for the joint probability density function of the scalar difference and the length scale of dissipation elements. *Phys. Fluids*, 20(6), 2008.

[210] J. Li. *Experimental and Numerical Studies of Ethanol Chemical Kinetics*. PhD thesis, Princeton University, 2004.

[211] A. Zschutschke, D. Messig, A. Scholtissek, and C. Hasse. Universal Laminar Flame Solver (ULF). 2017. URL: `https://figshare.com/articles/ULF%7B%5C_%7Dcode%7B%5C_%7Dpdf/5119855`.

[212] R. H. Kraichnan. Diffusion by a Random Velocity Field. *Phys. Fluids*, 13(22), 1970.

[213] M. Klein, A. Sadiki, and J. Janicka. A digital filter based generation of inflow data for spatially developing direct numerical or large eddy simulations. *J. Comput. Phys.*, 186(2), 2003.

[214] A. Kempf, M. Klein, and J. Janicka. Efficient Generation of Initial- and Inflow-Conditions for Transient Turbulent Flows in Arbitrary Geometries. *Flow, Turbul. Combust.*, 74(1), 2005.

[215] T. Passot and A. Pouquet. Numerical simulation of compressible homogeneous flows in the turbulent regime. *J. Fluid Mech.*, 181(-1), 1987.

[216] R. S. Rogallo. Numerical experiments in homogeneous turbulence. Technical report NASA-TM-81315, NASA Ames Research Center, 1981.

[217] T. V. Karman. Progress in the Statistical Theory of Turbulence. *Proc. Natl. Acad. Sci. U. S. A.*, 34(11), 1948.

[218] Y.-H. Pao. Structure of Turbulent Velocity and Scalar Fields at Large Wavenumbers. *Phys. Fluids*, 8(6), 1965.

[219] D. O. Lignell, J. H. Chen, and H. A. Schmutz. Effects of Damköhler number on flame extinction and reignition in turbulent non-premixed flames using DNS. *Combust. Flame*, 158(5), 2011.

[220] M. Gauding. *Statistics and scaling laws of turbulent scalar mixing at high Reynolds numbers*. PhD thesis, RWTH Aachen university, 2014.

[221] M. M. Rogers and R. D. Moser. Direct simulation of a self-similar turbulent mixing layer. *Phys. Fluids*, 6(2), 1994.

[222] S. Vo, A. Kronenburg, O. T. Stein, and E. R. Hawkes. *Direct Numerical Simulation of Non-premixed Syngas Combustion Using OpenFOAM*. In *High Perform. Comput. Sci. Eng. '16*. W. E. Nagel, D. H. Kröner, and M. M. Resch, editors. Springer International Publishing, Cham, 2016.

[223] H. Pitsch. Unsteady flamelet modeling of differential diffusion in turbulent jet diffusion flames. *Combust. Flame*, 123(3), 2000.

[224] P. Sripakagorn, S. Mitarai, G. Kosály, and H. Pitsch. Extinction and reignition in a diffusion flame: a direct numerical simulation study. *J. Fluid Mech.*, 518, 2004.

[225] D. Pugmire, H. Childs, C. Garth, S. Ahern, and G. H. Weber. Scalable computation of streamlines on very large datasets. In *Conf. High Perform. Comput. Networking, Storage Anal.* New York, New York, USA. IEEE, 2009.

[226] P. K. Yeung and S. B. Pope. An algorithm for tracking fluid particles in numerical simulations of homogeneous turbulence. *J. Comput. Phys.*, 79(2), 1988.

[227] F. Lekien and J. Marsden. Tricubic interpolation in three dimensions. *Int. J. Numer. Methods Eng.*, 63, 2005.

[228] E. Kreyszig. *Advanced engineering mathematics*. John Wiley & Sons, Inc., 10th edition, 2011.

[229] L. Wang. *Geometrical description of homogeneous shear turbulence using dissipation element analysis*. PhD thesis, Aachen, Techn. Hochsch., 2008.

[230] P. Schäfer, M. Gampert, L. Wang, and N. Peters. Fast and slow changes of the length of gradient trajectories in homogeneous shear turbulence. In *Adv. Turbul. XII Proc. 12th EUROMECH Eur. Turbul. Conf.* Springer, Berlin, Heidelberg, 2009.

[231] P. Schaefer, M. Gampert, M. Gauding, N. Peters, and C. Treviño. The secondary splitting of zero-gradient points in a scalar field. *J. Eng. Math.*, 71(1), 2011.

[232] The HDF Group. Hierarchical Data Format, version 5. 2017. URL: `http://www.hdfgroup.org/HDF5/`.

[233] L. Wang and N. Peters. Length-scale distribution functions and conditional means for various fields in turbulence. *J. Fluid Mech.*, 608, 2008.

[234] L. Wang and N. Peters. A new view of flow topology and conditional statistics in turbulence. *Philos. Trans. R. Soc. London A Math. Phys. Eng. Sci.*, 371(1982), 2012.

[235] N. Peters and L. Wang. The central role of the scalar dissipation rate in non-premixed combustion. In *5th US Combust. Meet.* Curran, 2007.

[236] J. P. Mellado, L. Wang, and N. Peters. Gradient trajectory analysis of a scalar field with external intermittency. *J. Fluid Mech.*, 626, 2009.

[237] N. Peters and P. Trouillet. On the role of quasi-one-dimensional dissipation layers in turbulent scalar mixing. *Cent. Turbul. Stanford Univ. Annu. Res. Briefs*, 2002.

[238] J. Westerweel, T. Hofmann, C. Fukushima, and J. Hunt. The turbulent/non-turbulent interface at the outer boundary of a self-similar turbulent jet. *Exp. Fluids*, 33(6), 2002.

[239] C. B. D. Silva, J. C. Hunt, I. Eames, and J. Westerweel. Interfacial Layers Between Regions of Different Turbulence Intensity. *Annu. Rev. Fluid Mech.*, 46(1), 2014.

[240] C. Ansorge and J. P. Mellado. Analyses of external and global intermittency in the logarithmic layer of Ekman flow. *J. Fluid Mech.*, 805, 2016.

[241] M. Gampert, J. Boschung, F. Hennig, M. Gauding, and N. Peters. The vorticity versus the scalar criterion for the detection of the turbulent/non-turbulent interface. *J. Fluid Mech.*, 750, 2014.

[242] R. R. Prasad and K. R. Sreenivasan. Scalar interfaces in digital images of turbulent flows. *Exp. Fluids*, 7(4), 1989.

[243] Z. Warhaft. Passive Scalars in Turbulent Flows. *Annu. Rev. Fluid Mech.*, 32(1), 2000.

[244] M. Gauding, J. H. Goebbert, C. Hasse, and N. Peters. Line segments in homogeneous scalar turbulence. *Phys. Fluids*, 27(9), 2015.

[245] F. A. Lindemann, S. Arrhenius, I. Langmuir, N. R. Dhar, J. Perrin, and W. C. McC. Lewis. Discussion on "the radiation theory of chemical action". *Trans. Faraday Soc.*, 17(0), 1922.

[246] R. G. Gilbert, K. Luther, and J. Troe. Theory of Thermal Unimolecular Reactions in the Fall-off Range. II. Weak Collision Rate Constants. *Berichte der Bunsengesellschaft für Phys. Chemie*, 87(2), 1983.

[247] J. H. Goebbert and M. Gauding. Direct Numerical Simulations of Fluid Turbulence at Extreme Scale with psOpen. In D. Brömmel, W. Frings, and B. J. N. Wylie, editors, *JUQUEEN Extrem. Scaling Work. 2015*. Jülich Supercomputing Center, 2015.

[248] T. Ishida, P. A. Davidson, and Y. Kaneda. On the decay of isotropic turbulence. *J. Fluid Mech.*, 564, 2006.

[249] K. Yamamoto and I. Hosokawa. A Decaying Isotropic Turbulence Pursued by the Spectral Method. *J. Phys. Soc. Japan*, 57(5), 2013.

[250] E. T. Spyropoulos and G. A. Blaisdell. Evaluation of the dynamic model for simulations of compressible decaying isotropic turbulence. *AIAA J.*, 34(5), 1996.

[251] G. P. Smith, D. M. Golden, M. Frenklach, N. W. Moriarty, B. Eiteneer, M. Goldenberg, C. T. Bowman, R. K. Hanson, S. Song, W. C. G. Jr., V. V. Lissianski, and Z. Qin. GRI-Mech 3.0. 1999. URL: `http://www.me.berkeley.edu/gri%7B%5C_%7Dmech/`.

A Additional chemical kinetic relations

A.1 Reverse rate coefficient

For reversible reactions, the reverse rate coefficient is determined in one of two ways [51]:

1. evaluate explicit reverse Arrhenius parameters, similar to equation (2.70), or
2. evaluate the ratio of $k_{f,i}$ and $K_{c,i}$, i.e. the equilibrium constant.

$$k_{r,i} = \frac{k_{f,i}}{K_{c,i}}\,, \tag{A.1}$$

$$K_{c,i} = K_{p,i}\left(\frac{p_{\text{atm}}}{\mathcal{R}T}\right)^{\sum_{k=1}^{\text{N}_\text{s}} \nu_{ki}}\,, \text{ and} \tag{A.2}$$

$$K_{p,i} = \exp\left(\frac{\Delta S_i^\circ}{\mathcal{R}} - \frac{\Delta H_i^\circ}{\mathcal{R}T}\right) = \exp\left(\sum_{k=1}^{\text{N}_\text{s}} \nu_{ki}\left(\frac{S_k^\circ}{\mathcal{R}} - \frac{H_k^\circ}{\mathcal{R}T}\right)\right)\,, \tag{A.3}$$

Combining the expressions for $K_{c,i}$ and $K_{p,i}$ yields

$$K_{c,i} = \left(\frac{p_{\text{atm}}}{\mathcal{R}}\right)^{\sum_{k=1}^{\text{N}_\text{s}} \nu_{ki}} \exp\left(\sum_{k=1}^{\text{N}_\text{s}} \nu_{ki} B_k\right)\,, \tag{A.4}$$

where, expanding the polynomial expressions for S_k° and H_k° from Eqs. equation (2.26) and equation (2.25) leads to

$$B_k = a_{6,k} - a_{0,k} + a_{0,k}\ln T + T\left(\frac{a_{1,k}}{2} + T\left(\frac{a_{2,k}}{6} + T\left(\frac{a_{3,k}}{12} + \frac{a_{4,k}}{20}T\right)\right)\right) - \frac{a_{5,k}}{T}\,. \tag{A.5}$$

A.2 Falloff reactions

Unlike elementary and third-body reactions, falloff reactions exhibit a pressure dependence described as a blending of rates at low- and high-pressure limits. The corresponding rate coefficients for the low-pressure- ($k_{0,i}$) and high-pressure-limit ($k_{\infty,i}$) are each expressed in Arrhenius form following equation (2.70). Then, the ratio of the coefficients $k_{0,i}$ and $k_{\infty,i}$, combined with the third-body concentration defines a reduced pressure $P_{r,i}$ given by

$$P_{r,i} = \frac{k_{0,i}}{k_{\infty,i}} \sum_{j=1}^{\text{N}_\text{s}} m_{ij}[X]_j\,. \tag{A.6}$$

The falloff blending factor F_i used in Eq. (2.72) is determined based on one of two representations [51, 112]:

$$F_i = \begin{cases} 1 & \text{Lindemann [245], or} \\ F_{\text{cent}}^{\left(1+\left(\frac{A_{\text{Troe}}}{B_{\text{Troe}}}\right)^2\right)^{-1}} & \text{Troe [246]}\,. \end{cases} \tag{A.7}$$

The variables for the Troe representation are given by

$$F_{\text{cent}} = (1-a)\exp\left(-\frac{T}{T^{***}}\right) + a\cdot\exp\left(-\frac{T}{T^{*}}\right) + \exp\left(-\frac{T^{**}}{T}\right)\,, \tag{A.8}$$

$$A_{\text{Troe}} = \log_{10} P_{r,i} - 0.67\log_{10} F_{\text{cent}} - 0.4\,, \text{and} \tag{A.9}$$

$$B_{\text{Troe}} = 0.806 - 1.1762\log_{10} F_{\text{cent}} - 0.14\log_{10} P_{r,i}\,, \tag{A.10}$$

where a, T^{***}, T^{*}, and T^{**} are parameters that are specified in the chemical mechanism. The final parameter T^{**} is optional, and, if it is not present, the final term of F_{cent} is omitted.

B Validation cases

B.1 Decaying homogeneous isotropic turbulence

The simulation of decaying homogeneous isotropic turbulence (HIT) serves as a well suited test case to validate the implemented solution strategy, consisting of finite-difference approximation, cf. section 4.1.1, Runge-Kutta solver, cf. section 4.1.2 and the fractional step algorithm, cf. section 4.1.5. The reference data was generated with a pseudo-spectral code that was developed by Gauding [220] and Goebbert and Gauding [247]. Details about the numerical solution strategy can be found in [220]. Simulations were performed on a cubic isotropic mesh with an edge length of 2π and 1024 grid points in each direction. Periodic boundary conditions were imposed everywhere. Similarly to [248–250] both DNS were initialized with a prescribed energy spectrum

$$E = A_0 \cdot \frac{\kappa^4}{\kappa_0^5} \exp\left(-2\left(\frac{\kappa}{\kappa_0}\right)^2\right), \tag{B.1}$$

where κ denotes the wavenumber. The peak of the spectrum (in wavenumber space) is denoted by $\kappa_0 = 10$ and the amplitude is $A_0 = 100$. figure B.1a shows the three dimensional energy spectrum computed from velocity fluctuations generated with the help of equation (B.1).

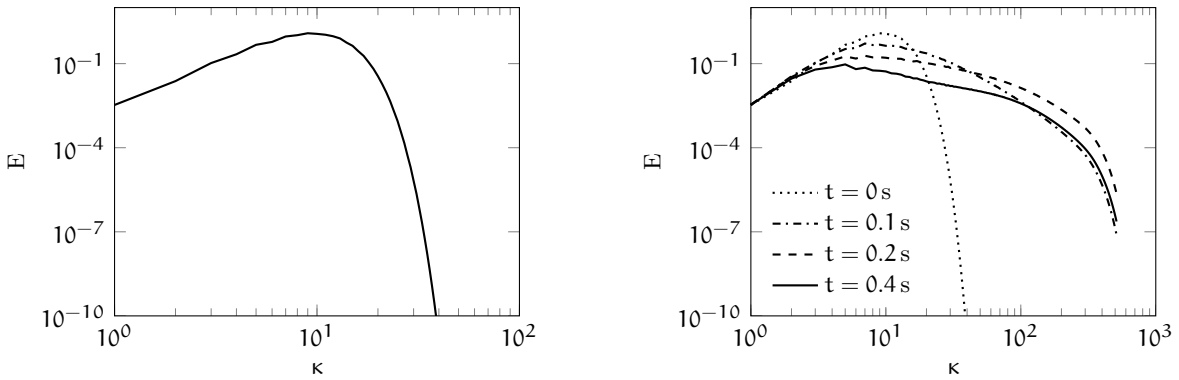

Figure B.1.: Illustration of the initial three dimensional energy spectrum (a) and evolution of the spectrum b computed from velocity fluctuations generated with (B.1). The initial spectrum peaks at the prescribed wavenumber $\kappa_0 = 10$.

The evolution of the energy spectrum is shown in figure B.1a. Furthermore, it can be seen from figure B.2 that after an initial transition phase both $\langle k \rangle$ and $\langle \varepsilon \rangle$ decay as a power law, as expected. The corresponding rates of decay agree well with values reported in [137]. Note, that almost no differences between the spectral DNS code and DINO exist.

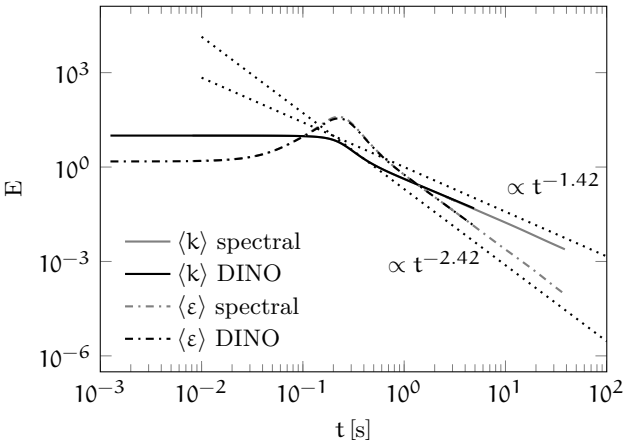

Figure B.2.: Self similar decay of mean kinetic energy $\langle k \rangle$ (solid line) and mean dissipation $\langle \varepsilon \rangle$ (dash-dotted line). In addition the theoretical decay rates are illustrated by the dotted lines.

B.2 Homogeneous reactor

In order to validate the different time integration strategies discussed in section 4.1.2 and the computation of kinetic parameters, cf. section 2.6, a homogeneous reactor setup is used. The initial value problem to be solved, in the context of a single homogeneous reacting system (e.g., autoignition, perfectly stirred reactor), is described using an ordinary differential equation for the thermochemical composition vector

$$\Phi = \left\{ T, Y_1, Y_2, \ldots, Y_{\mathrm{N_s}-1} \right\}^{\mathsf{T}} , \tag{B.2}$$

where T is the temperature, Y_i are the species mass fractions, and $\mathrm{N_s}$ is the number of species. The system of ODEs governing the time change in thermochemical composition corresponding to equation (B.2) is then $f = \partial\Phi/\partial t$:

$$f = \frac{\partial}{\partial t}\Phi = \left\{ \frac{\partial}{\partial t}T, \frac{\partial}{\partial t}Y_1, \frac{\partial}{\partial t}Y_2, \ldots, \frac{\partial}{\partial t}Y_{\mathrm{N_s}-1} \right\}^{\mathsf{T}} , \tag{B.3}$$

where

$$\frac{\partial}{\partial t}T = \frac{-1}{\rho c_p}\sum_{k=1}^{\mathrm{N_s}} h_k W_k \dot{\omega}_k \tag{B.4}$$

$$\frac{\partial}{\partial t}Y_k = \frac{W_k}{\rho}\dot{\omega}_k \quad k = 1, \ldots, \mathrm{N_s}-1 \tag{B.5}$$

where c_p is the mass-averaged constant-pressure specific heat, h_k is the enthalpy of the kth species in mass units, and $\dot{\omega}_k$ is the overall production rate of the kth species. The right hand sides of equations (B.4) and (B.5) were computed with the help of *pyJac* [179], a software package

specifically designed for the generation of analytical jacobian matrices and chemical source terms. The initial conditions for equations (B.4) and (B.5) were set to

$$Y_{H_2} = 0.027226\,, Y_{O_2} = 0.216085\,, Y_{N_2} = 0.756689\,, T = 1001\,\mathrm{K} \tag{B.6}$$

whereat all other species mass fractions were set to 0. The chemical kinetic scheme used for the computations was the `GRI-MECH 3.0` [251]. Two different low-storage Runge-Kutta solvers were benchmarked, namely a fully explicit fourth-order five-stage solver (LSERK4(5)) [169] and a low-storage semi-implicit third-order three-stage solver (LSSIRK3(3)) [165], see section 4.1.2. The time step used for the integration was fixed to $\Delta t = 6 \cdot 10^{-9}$ s for the explcit solver and $\Delta t = 1 \cdot 10^{-7}$ s for the semi-implicit solver. Both solvers were validated against solutions obtained with the in-house universal laminar flame solver (*ULF* [211]). As can be seen in figure B.3 both solvers achieve

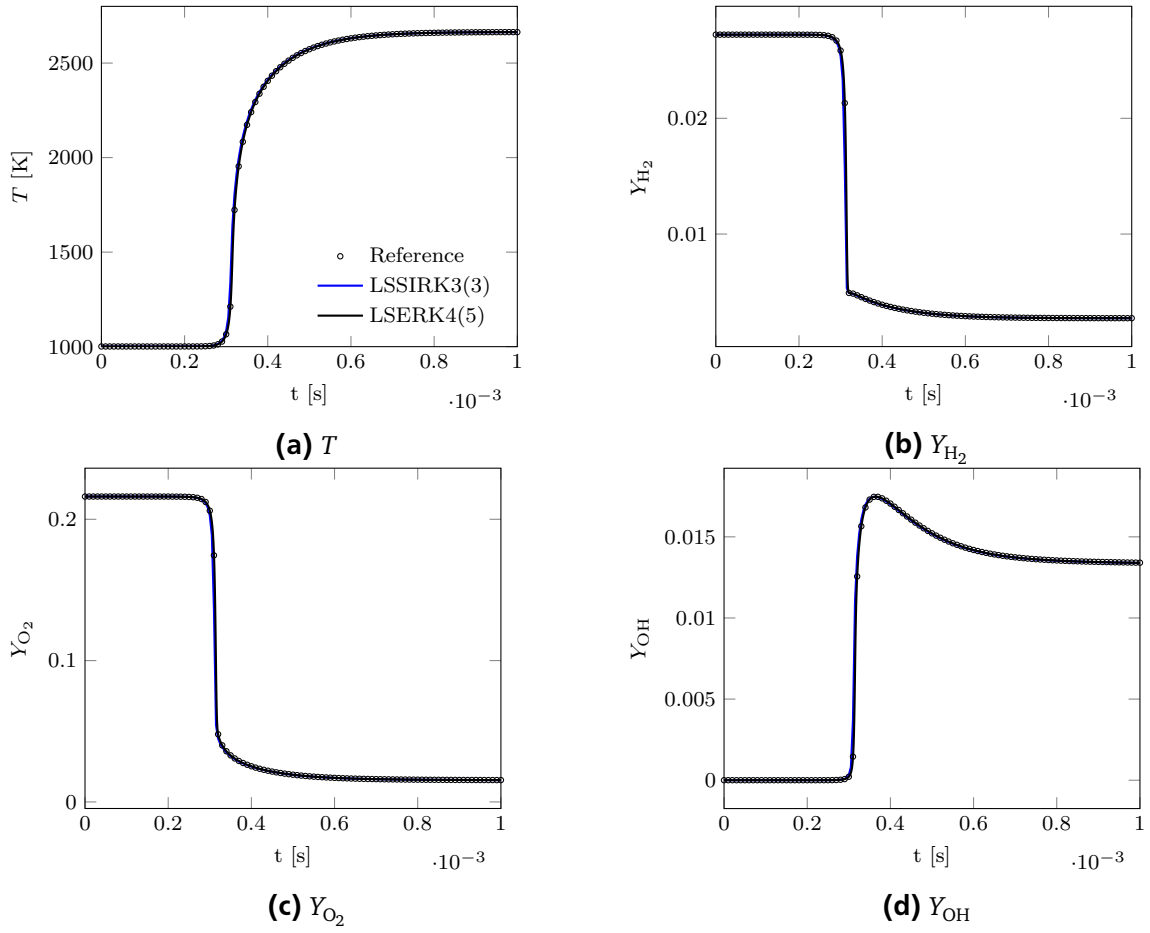

(a) T **(b)** Y_{H_2} **(c)** Y_{O_2} **(d)** Y_{OH}

Figure B.3.: Solutions of equations (B.4) and (B.5) obtained with different time integration strategies, cf. section 4.1.2.

solutions which agree very well with the reference solution. It should be noted that the timestep for the semi-implicit solver was about 17 times higher than that for the fully explicit solver. Although the evaluation of the jacobian (required for the LSSIRK3) requires a significant amount of time per timestep the overall runtime of the simulation was reduced by a factor of 5.

C Code listings

C.1 Fortran interface to *pyJac*

With the current version of *pyJac* [179] only C code can be generated, which requires a special interface to be useable within *DINO* . The interface, used in this work is presented in the following.

Listing C.1: Fortran interface to the *pyJac* library [111, 179].

```
module pyjac_mod
  use iso_c_binding
  interface
    subroutine compute_hi(T,h) bind(c,name='eval_h')
      use iso_c_binding
      ! value keyword important, because usually
      ! fortran passes by reference, but pyjac
      ! requires value to be passed
      real(kind=c_double), intent(in   ), value :: T
      real(kind=c_double) :: h(*)
    end subroutine compute_hi
  end interface

  interface
    subroutine compute_cpi(T,cp) bind(c,name='eval_cp')
      use iso_c_binding
      real(kind=c_double), intent(in   ), value :: T
      real(kind=c_double) :: cp(*)
    end subroutine compute_cpi
  end interface

  interface
    subroutine convert_x2y(X,Y) bind(c,name='mole2mass')
      use iso_c_binding
      real(kind=c_double), intent(in   ) :: X(*)
      real(kind=c_double) :: Y(*)
    end subroutine convert_x2y
  end interface

  interface
    subroutine convert_y2x(Y,X) bind(c,name='mass2mole')
      use iso_c_binding
```

```
      real(kind=c_double), intent(in   ) :: Y(*)
      real(kind=c_double) :: X(*)
    end subroutine convert_y2x
  end interface

  interface
    real(c_double) function computeDensity(T,P,X) bind(c,name='getDensity')
      use iso_c_binding
      real(kind=c_double), intent(in   ), value :: T
      real(kind=c_double), intent(in   ), value :: P
      real(kind=c_double), intent(in   ) :: X(*)
    end function computeDensity
  end interface

  interface
    subroutine reaction_rates(T,P,Y,omega) bind(c,name='dydt')
      use iso_c_binding
      real(kind=c_double), intent(in   ), value :: T
      real(kind=c_double), intent(in   ), value :: P
      real(kind=c_double), intent(in   ) :: Y(*)
      real(kind=c_double) :: omega(*)
    end subroutine reaction_rates
  end interface

  interface
    subroutine jacobian(T,P,Y,jac) bind(c,name='eval_jacob')
      use iso_c_binding
      real(kind=c_double), intent(in   ), value :: T
      real(kind=c_double), intent(in   ), value :: P
      real(kind=c_double), intent(in   ) :: Y(*)
      real(kind=c_double) :: jac(*)
    end subroutine jacobian
  end interface

end module pyjac_mod
```